

# Dispersive production of vector mesons in Deep Inelastic Scattering within $k_t$ -factorization approach

Dissertation  
zur  
Erlangung des Doktorgrades (Dr. rer. nat.)  
der  
Mathematisch-Naturwissenschaftlichen Fakultät  
der  
Rheinischen Friedrich-Wilhelms-Universität Bonn

vorgelegt von

Igor Ivanov  
aus  
Russland

Bonn 2002

Angefertigt am Institut für Kernphysik  
des Forschungszentrums Jülich GmbH

mit Genehmigung der Mathematisch-Naturwissenschaftlichen Fakultät der  
Rheinischen Friedrich-Wilhelms-Universität Bonn

1. Referent: Prof. Dr. J. Speth

2. Referent: Prof. Dr. H. R. Petry

Tag der Promotion:

## Abstract

In this work we give a theoretical description of the elastic vector meson production in diffractive DIS developed within the  $k_t$ -factorization formalism. Since the  $k_t$ -factorization scheme does not require large values of  $Q^2 + m_V^2$ , we conduct an analysis that is applicable to all values of  $Q^2$  from photo- up to highly virtual production of vector mesons. The basic quantity in this approach — the unintegrated gluon structure function — was for the first time extracted from the experimental data on  $F_{2p}$ , thoroughly investigated, and consistently used in the vector meson production calculation. Moreover, by limiting ourselves to the lowest Fock state of the vector meson, we were able to construct in a closed form the theory of spin-angular coupling in the vector meson. This allowed us for the first time to address the production of a vector meson in a given spin-angular state. We performed an extensive analytical and numerical investigation of the properties of 1S, 2S, and D-wave vector meson production reactions. Treating the physical ground state vector mesons as purely 1S states, we observed a good overall agreement with all available experimental data on vector meson production. For the excited states, our analysis predicts a picture which is remarkably different from 1S-state, so that such reactions can be regarded as potential sources of new information on the structure of excited states in vector mesons.

to

C laudia I

and

C laudia II

# Contents

1	Introduction	9
1.1	Di ractive processes and Pom eron	10
1.2	Vector meson production in di ractive DIS	11
1.3	The strategy of the thesis	13
I	Basics of $k_t$ -factorization schem e	14
2	The virtual Compton scattering	15
2.1	Modeling virtual photoabsorption in QCD	15
2.2	Details of calculation	17
2.3	Denom inator and trace evaluation	19
2.4	G luon density	21
2.4.1	Di erential density of gauge bosons: the QED primer	22
2.4.2	Di erential density of photons in a positronium	22
2.4.3	Di erential gluon density in a proton	24
2.5	Final expressions	24
2.6	The virtual Compton amplitude in the in pact param eter space	25
2.6.1	D ipole cross section	26
3	DGLAP vs. $k_t$ factorization	28
3.1	How DGLAP and $k_t$ factorization approaches meet at high $Q^2$	28
3.2	The di erent evolution paths: soft-to-hard di usion and vice versa	30
II	Derivation of vector meson production amplitudes	32
4	Description of a vector meson	33
4.1	Bound states in QFT	33
4.2	LCWF and vertex factor	34
4.3	Light cone form alism	35
4.4	Spin structure of a vector particle	37
4.5	Vector meson LCWF norm alization	38
4.5.1	Naive $qqV$ vertex	39
4.5.2	Norm alization for S wave vector meson	41
4.5.3	Norm alization for D wave vector meson	41
4.6	Decay constant	42

4.7	Ansatz for LCWF . . . . .	43
4.7.1	Suppressed Coulomb wave functions . . . . .	43
4.7.2	Oscillator type LCWF . . . . .	44
5	Vector meson production amplitudes . . . . .	45
5.1	Preliminary notes . . . . .	45
5.2	Notation and helicity amplitudes . . . . .	46
5.3	General amplitude . . . . .	48
5.4	Color factor . . . . .	48
5.5	Scalarization of upper and lower parts . . . . .	49
5.6	Denominator evaluation . . . . .	50
5.7	O <sup>-</sup> -forward gluon density . . . . .	51
5.8	Final results for the naive vertex . . . . .	53
5.9	Final results for S and D wave amplitudes . . . . .	54
6	Analysis for heavy quarkonia . . . . .	56
6.1	Twist expansion . . . . .	56
6.2	Twist expansion for S wave type mesons . . . . .	57
6.3	Twist expansion for D {type vector mesons . . . . .	57
6.4	Final results for S wave mesons . . . . .	58
6.4.1	S wave: $\langle p \rangle$ averaging . . . . .	58
6.4.2	S wave: answers for $L \rightarrow L$ up to differential cross section . . . . .	59
6.4.3	S wave: the other amplitudes . . . . .	60
6.5	Final results for D wave . . . . .	61
6.5.1	D wave: $\langle p \rangle$ averaging for $L \rightarrow L$ amplitude . . . . .	61
6.5.2	D wave: the other amplitudes . . . . .	62
6.6	S wave vs. D wave comparison . . . . .	63
III	Numerical analysis . . . . .	64
7	Determination of the unintegrated gluon structure function of the proton: DGD 2000 analysis . . . . .	65
7.1	The Ansatz for differential gluon structure function . . . . .	66
7.2	The parameters of DGSF for different DGLAP inputs . . . . .	69
7.3	The description of the proton structure function $F_{2p}(x;Q^2)$ . . . . .	70
7.4	Real photoabsorption cross section $\sigma^p$ . . . . .	74
8	Properties of differential gluon structure function . . . . .	76
8.1	DGSF in the momentum space . . . . .	76
8.1.1	Soft/hard decomposition of DGSF . . . . .	76
8.1.2	Soft/hard decomposition of the integrated gluon structure function . . . . .	77
8.1.3	Soft/hard decomposition of the proton structure function $F_2(x;Q^2)$ . . . . .	78
8.2	DGSF in the x-space: effective intercepts and hard-to-soft diffusion . . . . .	79
8.3	How the gluon densities of $\sim$ -factorization differ from DGLAP gluon densities . . . . .	84
8.4	How different observables probe the DGSF . . . . .	86

9	Improved determination of the differential glue in proton: DGD 2002 analysis	91
9.1	Fitting procedure and parameters of DGSF	91
9.2	The properties of the gluon structure function	94
9.3	The observables	96
9.3.1	Structure function $F_{2p}$ and its derivatives	96
9.3.2	Structure function $F_L$	100
9.3.3	Real photoabsorption cross section	100
10	Numerical analysis of the vector meson production	103
10.1	$1S$ states: a brief look	103
10.1.1	Absolute values of cross sections and scaling phenomenon	103
10.1.2	The energy and $t$ -dependence	103
10.1.3	The level of accuracy	105
10.2	The meson production	107
10.2.1	$Q^2$ dependence	107
10.2.2	$L$ - $T$ decomposition	113
10.2.3	Energy dependence	114
10.2.4	$t$ -dependence	115
10.2.5	Helicity amplitudes	118
10.3	mesons	120
10.4	$J=$ and mesons	121
10.5	Production of excited states	123
11	The $T$ puzzle	137
11.1	The Coulomb tail of the wave function	137
11.1.1	The strategy	138
11.1.2	The quantum mechanics of the Coulomb tail	139
11.1.3	Derivation of $C_{Coul}$	139
11.1.4	The large $Q^2$ asymptotics of $T$ : analytical result	142
11.2	The $S=D$ wave mixing	144
11.2.1	Cooking up vertex	144
11.2.2	Impact of $S=D$ wave mixing on meson production	146
12	Conclusion	148
A	Denominator evaluation: details	155
A.1	Forward Compton scattering	155
A.1.1	The $s$ -channel diagram: all details	155
A.1.2	The other three $s$ -channel diagrams	158
A.1.3	The $u$ -channel diagrams	159
A.1.4	The same integral in the $\bar{t}$ -representation technique	160
A.2	Vector meson production: the fully $o$ -forward case	161

B	Helicity amplitude technique	163
B.1	Photon vertex amplitudes . . . . .	169
B.2	Vector meson vertex amplitudes . . . . .	169
B.3	Final trace calculation . . . . .	170



# Chapter 1

## Introduction

In the past 30 years the particle physics theory has proved numerous times to provide a good, consistent, unified description of the great variety of nuclear, low and high energy particle physics experiments. Being based on the ideas of QFT applicability, gauge approach to fundamental interactions, symmetry and naturalness considerations, the Standard Model managed to explain virtually all phenomena in electromagnetic, weak and strong interactions, to predict new particles and effects. Though the questions of fundamental origin lie beyond the scope of the Standard Model, its precision in description, for instance, QED phenomena reaches the magnitude of  $10^{-10}$ .

However, the current situation is not that optimistic in the domain of strong interactions. The gauge-based formulation — the Quantum Chromodynamics (QCD) — seems to offer reasonably good description only of the energetic enough processes (more accurately: only when every vertex involves at least one highly virtual particle) thanks to the famous asymptotic freedom. The major difficulty lies in the behavior of the QCD coupling constant:  $\alpha_s(Q^2)$  exhibits infrared growth and becomes comparable to unity at  $Q^2 \sim 1 \text{ GeV}^2$ . The net result is that the perturbation theory — the only prolific universal treatment of various high-energy processes — fails to give even qualitative description of low-energy, essentially non-perturbative phenomena. Additional difficulties arise from the non-abelian nature of QCD, chiral symmetry breaking, non-trivial QCD vacuum, instantons etc.

On the other hand, many separate concepts have been developed, which do not cling to the perturbative QCD (pQCD) and provide reasonably good description of phenomena in their applicability regions. The fundamental problem of the theory of strong interactions is that these heterogeneous approaches do not match<sup>1</sup>. They do not comprise a unified picture of strong interactions. Given such a lack of universal, rigorously derived results, one must admit that the subject of our investigation belongs to the realm of phenomenology rather than rigorous theory.

---

<sup>1</sup>Just a few examples of poor accordance among various approaches: the quark generated ladder diagrams do not appear to correspond uniquely to any of experimentally observed Regge trajectories. Another example is the vague status of  $\alpha_s = \text{const}$  BFKL results in true QCD.

## 1.1 D i r a c t i v e p r o c e s s e s a n d P o m e r o n

In the light of these problems, the careful examination of regions where two or more approaches overlap (or visa versa, where neither of the concepts exhausts the interaction) are of great interest. D i r a c t i v e D e e p I n e l a s t i c S c a t t e r i n g (D D I S) is exactly one of these fields.

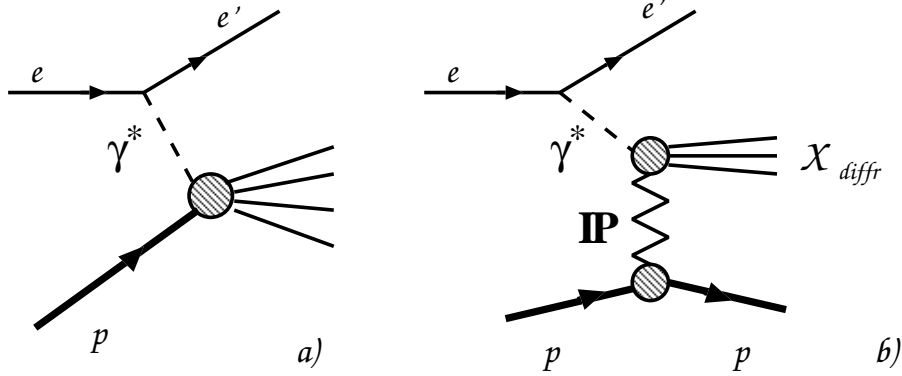


Figure 1.1: Examples of deep inelastic scattering process: (a) hard D I S and (b) d i r a c t i v e D I S. In the latter case  $M_{diff}^2$  is small and the process proceeds via pomeron t-channel exchange.

A typical hard D I S process (Fig.1.1a) occurs when a virtual photon<sup>2</sup> strikes a proton to produce a hard system X with large invariant mass<sup>3</sup> and large enough multiplicity, final state hadrons being distributed over whole rapidity range approximately smoothly.

However, as it was noted long ago, sometimes the proton survives, being only slightly dected, and a virtual photon turns into a so-called d i r a c t i v e system  $X_{diff}$  with invariant mass  $M_{diff}^2$  is small. In this process the proton and the d i r a c t i v e system are naturally separated by a large rapidity gap and a condition which appears necessary for the rapidity gap formation is  $Q^2$  is small, or in terms of Bjorken x

$$x = \frac{Q^2}{s} \ll 1 : \quad (1.1)$$

This is one of the most common cases of d i r a c t i v e D I S (D D I S) processes. In fact, the class of d i r a c t i v e processes is not confined within D I S; it is much broader. There are many other reactions which possess the generic features | the rapidity gap and smallness of  $M_{diff}^2$  | and therefore can be classified as d i r a c t i v e processes (for a recent review see [1]).

How can a typical d i r a c t i v e process occur? Certainly, it must be kind of a peripheral interaction: if the photon struck directly one of the valence quarks, the proton would 'explode', providing no way for the large rapidity gap formation. What remains is the possibility of the t-channel exchange by not-too-energetic 'particle' (Fig.1.1b), which would be a natural mechanism of the experimentally observed weak proton dected and small  $M_{diff}^2$ . Further experimental features suggest that this 'particle' should be chargeless and colorless, its interaction with other particles should be of strong (not EM or weak) nature, its 'propagation'

<sup>2</sup>We will always imply that the virtual photon is emitted by an electron, which means the photon is always space-like: if  $q$  is photon momentum, then  $Q^2 = -q^2 > 0$ .

<sup>3</sup>In hard D I S phenomenology this quantity is usually labeled as  $W^2$ . However, for simplicity we will use notations.

should be independent of the specific process ( $p, \bar{p}, pp, \bar{p}\bar{p}$ , etc), and it should be of spin 1 (due to approximately s(=constant) pp cross section). In the early 60s this ‘particle’ was dubbed Pomeron (symbol  $\mathbb{P}$ ).

Further properties come from combining the Regge picture and BFKL results with experimental observations (for a detailed review of Regge theory see [2]). They include, first of all, the asymptotic equality of total pp and  $\bar{p}p$  cross sections (the Pomanchuk theorem). Formulated long ago, it was experimentally verified only recently. Then, the Regge theory predicts the power-like s-dependence of the total pp cross section  $\propto s^{2(\alpha_{\mathbb{P}}-1)}$ , which has also been experimentally observed, with intercept  $\alpha_{\mathbb{P}} = 1.08$ . On the other hand, the BFKL equation [3, 4] succeeded in reproducing such power-like dependence in QCD, but in a simplified case  $\alpha_s = \text{const}$ . In this approach the hard pomeron is treated as two reggeized gluons – an ansatz used currently in diffraction phenomenology with great success. However, the predictive power of the BFKL approach for the numerical value of the pomeron intercept is still limited and not all issues with sensitivity of the result to the infrared region have been understood. For further reading on pomerons, a topic very intriguing by itself, we refer to [5].

## 1.2 Vector meson production in diffractive DIS

There are several possible final states  $X$  in a typical diffractive DIS (DDIS) process  $p + \gamma^* \rightarrow X + p$ : system  $X$  can be a real photon, a qq continuum pair forming two jets or qq bound state, for example, a vector meson. Let us now focus specifically on exclusive vector meson production in diffractive DIS. This reaction has been studied extensively at fixed target DIS experiments at CERN and FNAL and more recently by the H1 and ZEUS collaborations at HERA.

Despite the great deal of theoretical work on vector meson production in diffractive DIS [6, 7, 8, 9], there is a number of issues that have not yet been seriously analyzed and still need a closer investigation.

One of them concerns the vector meson production in a seeming soft region, namely, at small values of  $Q^2$  and  $m_V^2$  (or, to put it short, at small values of  $Q^2 + m_V^2$ ). Indeed, the majority of early calculations treated the vector meson productions within the DGLAP-inspired approach, the production amplitudes being expressed in terms of the integrated gluon density  $G(x; Q^2)$ . Certainly, this line of calculation is not applicable at small enough values of  $Q^2 + m_V^2$ , say at  $Q^2 + m_V^2 < 1 \text{ GeV}^2$ . However it is necessary to understand that the DGLAP-based approach not only can be avoided but also should be avoided when one studies diffractive scattering. Indeed, at high energies and small to moderate values of  $Q^2$  the dynamics of the amplitudes is governed by large logarithms of  $\log(1/x)$  rather than  $\log(Q^2)$ , and the correct and the most natural method to treat processes in this kinematical region is  $k_t$ -factorization approach. This approach does not place any restriction on the value of  $Q^2$  as long as one works at large enough energies.

Although the strategy of the evaluation of the vector meson production amplitudes within the  $k_t$ -factorization approach is essentially clear, performing reliable numerical prediction is not a straightforward task. The impediment consists in presence of purely soft, non-perturbative quantities in the calculation, namely, the gluon content of the proton and the wave function of the vector meson.

The presence of the former quantity is a specific feature of the particular final state we

investigate, however, the unintegrated gluon density

$$F(x; Q^2) = \frac{\partial G(x; Q^2)}{\partial \log Q^2}; \quad (1.2)$$

is the basic quantity in all  $k_t$ -factorization calculations. Unfortunately, no reliable Ansatz or parametrization has been developed, and this gap needs to be filled.

Another issue that has never been brought under scrutiny is the spin-angular coupling inside the vector meson. In an  $o$ -forward scattering  $q\bar{q} \rightarrow V$ , the  $s$ -channel helicity flip amplitudes can be non-vanishing. Because of the well known quark helicity conservation in high energy QCD scattering, such a helicity flip is possible only due to the internal motion and spin{angular momentum coupling of quarks in a vector meson. This issue was accurately analyzed only in very recent papers [6, 7], where it was shown that helicity non-conserving amplitudes are not negligible, as they had been thought before. Thus, as such, the helicity flip amplitudes would offer a great deal of unique information of internal constituent motion and spin{angular momentum structure of vector mesons, inaccessible in other experiments. In addition, the vector meson decays are self-analyzing and the full set of helicity amplitudes can be measured experimentally. For unpolarized incident leptons, the angular distribution of decay products is parameterized in terms of 15 spin-density matrix elements, which can be calculated via  $\sqrt{2}$  helicity conserving plus three helicity violating  $\sqrt{2}$  basic helicity amplitudes [10].

Certainly, the helicity structure of the vector meson production amplitudes must be analyzed only along with a careful treatment of the spinorial structure of the  $q\bar{q} \rightarrow V$  transition. It is thus rather surprising that the above issue of sensitivity of the production amplitudes to the spin-angular momentum coupling has not been addressed before. Namely, in a typical vector meson production calculation, a vector meson has been implicitly taken as 1S state and at the same time an unjustified ansatz was used for  $q\bar{q} \rightarrow V$  transition spinorial structure, namely, of  $u\bar{u} \rightarrow V$  type. Being a mere analogy of  $q\bar{q}$  vertex, this ansatz in fact corresponds neither to pure S nor to pure D wave state but rather to their certain mixture. Only in [11] the cases of 1S and 2S vector mesons were compared and the necessity of similar calculation for D wave states was stressed. Such calculations however have been missing in literature until now.

In addition to purely theoretical needs, there are more issues that call upon a thorough analysis of the D-wave effects. For instance, different spin properties of the S- and D-wave production may resolve the long standing problem of the D-wave vs. 2S-wave assignment for the  $\phi(1480)$  and  $\phi(1700)$  mesons (as well as the  $\omega^0$  and  $\phi^0$  mesons). Furthermore, the deuteron which is a spin{1 ground state in the pn system is known to have a substantial D wave admixture, which mostly derives from the tensor forces induced by pion exchange between nucleons. Recently, there has been much discussion [12] of the nonperturbative long-range pion exchange between light quarks and antiquarks in a vector meson, which is a natural source of the S-D mixing in the ground state  $\rho$  and  $\omega$  mesons.

In the present work we addressed both issues. We performed an accurate determination of the unintegrated gluon density from the experimental data on the structure function  $F_{2p}$  and gave its convenient and ready-to-use parametrizations. Besides, we constructed the consistent description of the vector mesons with spin-angular coupling taken into account, which enabled us to calculate diffractive production amplitudes for pure S-wave and D-wave states as well

as for an arbitrary  $S=D$  wave mixture. This resulted in a complete theory of the vector meson production in diffractive DIS within the  $k_t$ -factorization approach.

### 1.3 The strategy of the thesis

The guideline of the thesis is the following. The main text is comprised of three Parts. Part I is an introduction to the  $k_t$ -factorization approach. Here we calculate some basic scattering processes, such as the virtual Compton scattering, and introduce the concept of the differential densities of partons. The discussion on the similarities and distinctions between the DGLAP-motivated description and  $k_t$ -factorization description of diffractive processes can also be found here.

In Part II we turn to the vector meson production amplitudes. These are preceded by the theory of vector meson structure within the truncated Fock space, that is, when the vector meson is assumed to be a bound state of  $q\bar{q}$  pair only. Upon obtaining the closed analytical expressions for vector meson production amplitudes, we perform the twist expansion and illustrated some of the most salient properties of the  $S$ -wave and  $D$ -wave vector meson amplitudes.

Part III contains the numerical analysis of the expressions obtained and the concrete prediction to various experimentally observed quantities. At first we perform an extraction of the differential gluon density of the proton and thoroughly investigate its properties. Having brought the differential glue under control, we turn to the vector meson production amplitudes and give a large number of predictions for  $1S$ ,  $2S$ , and  $D$ -wave states. Whenever the experimental results are available, we confront our predictions with the data. This Part is concluded with a detailed consideration of the effect of the Coulomb tail of the vector meson wave function and of the  $S=D$ -wave mixing.

Finally, we summarize our main findings in Conclusions. Some lengthy calculations can be found in Appendices.

All the results presented in this thesis were derived by the author. The text is based on publications [13] and [14], and on the works in progress [15]. Preliminary results have been presented as talks at [16, 17].

## Part I

### Basics of $k_t$ -factorization scheme

## Chapter 2

### The virtual Compton scattering

We start our acquaintance with the  $k_t$ -factorization scheme with calculation of the imaginary part of the forward virtual Compton scattering amplitude. By means of optical theorem it is related with the total photoabsorption cross section and with the structure functions of the proton.

The purpose to get started with this quantity is twofold. First, during this calculation we will follow all steps and discuss all major feature of the  $k_t$ -factorization scheme of calculations. Being rather simple, the Compton scattering amplitude will keep us from being distracted by inessential technical complications, which would arise in other diffractive reactions.

The second purpose is to derive the well-known expression for the structure function  $F_{2p}$  in terms of unintegrated gluon density of the proton: the basic quantity in any  $k_t$ -factorization calculation. These expressions will be used later, when we discuss the determination of the unintegrated glue from the experimental data.

The third aim is to use the simplicity of this amplitude to gain as much insight into the dynamics of photon-proton peripheral interactions. This information will be used later in deriving the vector meson production amplitudes thanks to a remarkable similarity between the virtual Compton scattering and the vector meson electroproduction processes. Indeed, in the proton rest frame, both can be viewed as follows: a photon dissociates into a  $q\bar{q}$  pair, which interacts with gluon content of the proton and then is projected onto the final state. The hard dynamics in both cases are the same, only difference lurking in the final state projection.

#### 2.1 Modeling virtual photoabsorption in QCD

The quantity which is measured in deep inelastic lepton production is the total cross section of photoabsorption  $\sigma_{\gamma^* p \rightarrow X}$  summed over all hadronic final states  $X$ , where  $\gamma = T, L$  are helicities of (T) transverse and (L) longitudinal virtual photons. One usually starts with the imaginary part of the amplitude  $A_{\gamma^* p \rightarrow p}$  of forward Compton scattering  $\gamma^* p \rightarrow p$ , which by optical theorem gives the total cross section of photoabsorption of virtual photons

$$\sigma_T^p(x_{bj}; Q^2) = \frac{1}{(W^2 + Q^2 - m_p^2)^2 + 4Q^2 m_p^2} \text{Im } A_{\gamma^* p \rightarrow p}^T; \quad (2.1)$$

$$\sigma_L^p(x_{bj}; Q^2) = \frac{1}{(W^2 + Q^2 - m_p^2)^2 + 4Q^2 m_p^2} \text{Im } A_{\gamma^* p \rightarrow p}^L; \quad (2.2)$$

where  $W$  is the total energy in the p.c.m.s.,  $m_p$  is the proton mass,  $Q^2$  is the virtuality of the photon and  $x_{bj} = Q^2/(Q^2 + W^2)$  is the Bjorken variable. Hereafter we will suppress the subscript  $bj$  and use  $x$ .

Figure 2.1: The pQCD modeling of DIS in terms of multiproduction of parton final states.

$$\int_{-\infty}^{\infty} M_x f dx = \int_{-\infty}^{\infty} M_n f^n \frac{dx}{x} d^2 \sim_i; \quad (2.3)$$

$$0 \leq \frac{\lambda_i^2}{4W^2} = \frac{Q^2(1-x)}{4x} : \quad (2.4)$$

$$\begin{array}{ccccccc} 1 & \times_1 & \times_2 \cdots & \times_{n-1} & \times_n & \times & ; \\ 0 & \sim_1^2 & \sim_2^2 \cdots & \sim_{n-1}^2 & \mathbb{K}^2 & \mathbb{Q}^2 & ; \end{array} \quad (25)$$

Hereafter we focus on how lifting the restrictions on the transverse phase space changes our understanding of the gluon structure function of the nucleon at very small  $x$ , that is, very large  $\frac{1}{x}$ . In this kinematical region the gluon density  $g(x; Q^2)$  is much higher than the density of charged partons  $q(x; Q^2); \bar{q}(x; Q^2)$ . As Fadin, Kuraev and Lipatov [19] have shown, to the leading  $\log \frac{1}{x}$  ( $LL\frac{1}{x}$ ) approximation the dominant contribution to photoabsorption comes in



this regime from multigluonnal states of g.2.1; alternatively, to the  $LL_x^{-1}$  splitting of gluons into gluons dominates the splitting of gluons into qq pairs. As a matter of fact, for the purposes of the present analysis we do not need the full BFKL dynamics, in the  $k_t$ -factorization only the qq loop is treated explicitly to the  $LL_x^{-1}$  approximation. In this regime the Compton scattering can be viewed as an interaction of the nucleon with the lightcone qq Fock states of the photon via the exchange by gluons, g.2.2, and the Compton scattering amplitude takes the form

$$A = \int \gamma^* \gamma; q; q \text{ helicity}; \text{ dependent lightcone wave function of the photon} \quad A_{qq} \quad (2.6)$$

Here  $\gamma^* \gamma; q; q \text{ helicity}; \text{ dependent lightcone wave function of the photon}$  and the QCD pomeron exchange qq proton scattering kernel  $A_{qq}$  does not depend on, and conserves exactly, the q;q helicities, summation over which is understood in (2.6).

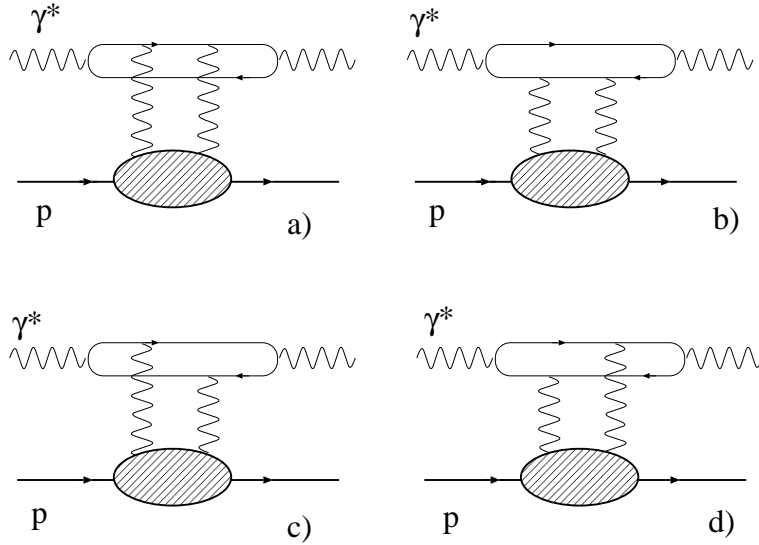


Figure 2.2: The  $k_t$ -factorization representation for DIS at small  $x$ .

The resummation of diagrams of g.2.1 defines the unintegrated gluon structure function of the target, which is represented in diagrams of g.2.2 as the dashed blob.

## 2.2 Details of calculation

Suppose that there were no interaction between the gluons exchanged in t-channel, so that the full calculation of the Compton scattering amplitude amounts only to picking up the Born diagrams. Consider one of such diagrams, i.e. Diagram in Fig.2.2, but without the dashed blob. A virtual photon turns into qq pair which interacts with a proton via two-gluon exchange. The general expression for this amplitude reads:

$$iA = \int \frac{d^4 k}{(2\pi)^4} \int \frac{d^4 l}{(2\pi)^4} u^0 (ig^0 t^B) i \frac{\not{p} \cdot \not{k} + m}{[p^2 - k^2 - m^2 + i\epsilon]} (ig^0 t^A) u$$

$$\left( -\frac{ig^0 A A^0}{2 + i\epsilon} \right) \left( -\frac{ig^0 B B^0}{2 + i\epsilon} \right) \frac{1}{f^2}$$

$$\frac{Sp \left( \frac{1}{\not{k}^2 - m^2 + i\epsilon} \not{\epsilon} i \not{k} \frac{1}{\not{q} + m} \right) \left( \frac{1}{\not{k}^2 - m^2 + i\epsilon} \not{\epsilon} i \not{k} + m \right) \left( \frac{1}{\not{k}^2 - m^2 + i\epsilon} \not{\epsilon} i \not{k} + m \right) \left( \frac{1}{\not{k}^2 - m^2 + i\epsilon} \not{\epsilon} i \not{k} + m \right)}{[(k^2 - m^2 + i\epsilon)^2][(k^2 - m^2 + i\epsilon)^2][(k^2 - m^2 + i\epsilon)^2]} \quad (2.7)$$

Let's first calculate the numerator.

Color factor

If we consider photon scattering off a single quark, we have

$$\frac{1}{N_c} Sp \left( \frac{1}{\not{k}^2 - m^2 + i\epsilon} \not{\epsilon} i \not{k} \frac{1}{\not{q} + m} \right) \left( \frac{1}{\not{k}^2 - m^2 + i\epsilon} \not{\epsilon} i \not{k} + m \right) \left( \frac{1}{\not{k}^2 - m^2 + i\epsilon} \not{\epsilon} i \not{k} + m \right) \left( \frac{1}{\not{k}^2 - m^2 + i\epsilon} \not{\epsilon} i \not{k} + m \right) = \frac{1}{N_c} \frac{1}{2} \frac{1}{2} \frac{1}{2} \frac{1}{2} = \frac{1}{2} \frac{1}{2N_c} (N_c^2 - 1) = \frac{1}{2} C_F = \frac{2}{3} \quad (2.8)$$

However, we should take into account that quarks are sitting inside a colorless proton, whose color structure is

$$color = \frac{1}{6} \epsilon^{abc} q^a q^b q^c \quad (2.9)$$

In this case there are two ways a pair of gluons can couple 3 quark lines. In the first way both gluons couple to the same quark. Since the quark momentum does not change after these two interactions, the nucleon stays in the same state:  $\langle N | j_i = 1 \rangle$ . In the second case, gluon legs are attached to different quark lines, so that extra momentum circulates between quarks, which gives rise to the factor  $\langle N | j_{exp}(i_1, i_2) | N \rangle$ , i.e. to the two-body form factor. Therefore, for the lower line instead of

$$\frac{1}{N_c} Sp \left( \frac{1}{\not{k}^2 - m^2 + i\epsilon} \not{\epsilon} i \not{k} \frac{1}{\not{q} + m} \right) \left( \frac{1}{\not{k}^2 - m^2 + i\epsilon} \not{\epsilon} i \not{k} + m \right) \left( \frac{1}{\not{k}^2 - m^2 + i\epsilon} \not{\epsilon} i \not{k} + m \right) \left( \frac{1}{\not{k}^2 - m^2 + i\epsilon} \not{\epsilon} i \not{k} + m \right) \quad (2.10)$$

one has

$$\begin{aligned} & \frac{1}{6} \epsilon^{abc} 3 \epsilon_{aa'bb'} t_{cc'}^A t_{c'c}^B + 6 \epsilon_{aa'bb'} t_{cc'}^A t_{c'c}^B \langle N | j_{exp}(i_1, i_2) | N \rangle \epsilon^{a'b'c'} \\ &= Sp \left( \frac{1}{\not{k}^2 - m^2 + i\epsilon} \not{\epsilon} i \not{k} \frac{1}{\not{q} + m} \right) \left( \frac{1}{\not{k}^2 - m^2 + i\epsilon} \not{\epsilon} i \not{k} + m \right) \left( \frac{1}{\not{k}^2 - m^2 + i\epsilon} \not{\epsilon} i \not{k} + m \right) \left( \frac{1}{\not{k}^2 - m^2 + i\epsilon} \not{\epsilon} i \not{k} + m \right) \\ &= \frac{1}{2} C_F (1 - \langle N | j_{exp}(i_1, i_2) | N \rangle) : \end{aligned} \quad (2.11)$$

Note also that a similar calculation for  $N_c$  number of colors would yield the same result. Thus, the overall color factor is

$$2V(i_1, i_2) = 2(1 - \langle N | j_{exp}(i_1, i_2) | N \rangle) : \quad (2.12)$$

As known, the highest powers contribution comes from so-called nonsense components of gluon propagator (density matrix) decomposition:

$$g_{\mu\nu} = \frac{2p^0 q^0}{s} + \frac{2p^0 q^0}{s} + g^2_{\mu\nu} + \frac{2p^0 q^0}{s} : \quad (2.13)$$

Therefore, the lower trace is calculated trivially

$$\frac{1}{2} Sp \left( \frac{1}{\not{k}^2 - m^2 + i\epsilon} \not{\epsilon} i \not{k} \frac{1}{\not{q} + m} \right) \left( \frac{1}{\not{k}^2 - m^2 + i\epsilon} \not{\epsilon} i \not{k} + m \right) \left( \frac{1}{\not{k}^2 - m^2 + i\epsilon} \not{\epsilon} i \not{k} + m \right) \left( \frac{1}{\not{k}^2 - m^2 + i\epsilon} \not{\epsilon} i \not{k} + m \right) = s^2 : \quad (2.14)$$

So, combining all factors, one has for numerator of Eq.(2.7)

$$\begin{aligned} & (4-s)^2 4 e_{em} e_f^2 \frac{4}{s^2} s^2 \text{Sp} \left( \hat{k} \not{q} + m \right) \not{e} (\hat{k} + m) \not{q}^0 (\hat{k} + \not{e} + m) \not{q}^0 (\hat{k} + m) \\ & = (4-s)^2 4 e_{em} e_f^2 8^{-2} 2s \Gamma(4) : \end{aligned} \quad (2.15)$$

Note that we factored out  $2s^2$  because it will appear later in all trace calculations. So, the resulting expression for amplitude (2.7) looks like

$$\begin{aligned} A = & (4-s)^2 4 e_{em} 16e_f^2 s^2 \int \frac{d^4 k}{(2)^4} \int \frac{d^4}{(2)^4} \frac{1}{[(\not{p} - \not{q} - m^2 + i)[\not{2} - \not{2} + i]]} \\ & \frac{\Gamma(4)}{[k^2 - m^2 + i][(k - \not{q})^2 - m^2 + i][(k - \not{q})^2 - m^2 + i]} \end{aligned} \quad (2.16)$$

One can now immediately write similar expressions for three other diagrams (Fig. 2.2 b,c,d). Indeed, they will differ from Eq.(2.16) only by the last line. Aside from different expressions for traces, the quark line propagator structures will read:

$$\begin{aligned} (b) & [k^2 - m^2 + i][(k - \not{q})^2 - m^2 + i][(k - \not{q})^2 - m^2 + i][(k - \not{q})^2 - m^2 + i] \\ (c) & [k^2 - m^2 + i][(k - \not{q})^2 - m^2 + i][(k - \not{q})^2 - m^2 + i][(k - \not{q})^2 - m^2 + i] \\ (d) & [k^2 - m^2 + i][(k - \not{q})^2 - m^2 + i][(k - \not{q})^2 - m^2 + i][(k - \not{q})^2 - m^2 + i] \end{aligned} \quad (2.17)$$

## 2.3 Denominator and trace evaluation

Now we turn to calculation of denominators. As usual, we implement Sudakov's decomposition and

$$\begin{aligned} k & = yp^0 + zq^0 + \tilde{k}; \\ & = p^0 + q^0 + \sim \\ q & = q^0 - xp^0; \end{aligned} \quad (2.18)$$

and make use of relation

$$d^4 k = \frac{1}{2} s dy dz d^2 \tilde{k} : \quad (2.19)$$

The complete analysis of denominator hierarchy and their integrals is performed in Appendix A. We show there that, for example, for diagram A, the imaginary part of the desired integral is equal to

$$\text{Im} \left( \int \frac{dy dz d^2 \tilde{k}}{\text{propagators}} \right) = \frac{4^{-2} 1}{s^3} \int_0^1 dz \frac{1}{z} \frac{1}{[k^2 - m^2 + z(1-z)Q^2]} \frac{1}{[\tilde{k}^2 + \tilde{k}^2]} : \quad (2.20)$$

The answers for the other three diagrams differ only by replacements  $\tilde{k} \rightarrow \tilde{k} + \sim$  in quark propagators whenever appropriate. The whole expression for the imaginary part of the amplitude is then

$$\text{Im} A = s \frac{32}{(2)^2} e_f^2 e_{em} \int dz d^2 \tilde{k} \int \frac{d^2 \tilde{V}(\tilde{k})}{(\tilde{k}^2 + \tilde{k}^2)^2}$$

$$\begin{aligned}
& \frac{1}{z} \frac{I^{(a)}}{[k^2 + m^2 + z(1-z)Q^2]^2} + \frac{z}{1-z} \frac{I^{(d)}}{[k^2 + m^2 + z(1-z)Q^2]^2} \\
& + \frac{I^{(b)} + I^{(c)}}{[(k + \tilde{m})^2 + m^2 + z(1-z)Q^2][k^2 + m^2 + z(1-z)Q^2]} \quad \text{::} \quad (2.21)
\end{aligned}$$

The short-hand notation  $\frac{2}{s}$  should be in fact understood as

$$s(\text{lower}) \quad s(\text{upper}) \quad s(\tilde{m}^2) \quad s(q^2) : \quad (2.22)$$

with

$$q^2 = \max[k^2 + m^2 + z(1-z)Q^2; \tilde{m}^2] : \quad (2.23)$$

Now we calculate the integrands  $I$  which enter Eq.(2.21). We will do this via light cone helicity amplitude technique. In the subsequent discussion we will use the following convention:

$$q^0 = q_+ n_+$$

i.e. the light cone direction  $+$  is taken along photon propagation.

A crucial point that justifies the usage of the helicity amplitude technique for all quarks lines inside the loop is that in the trace calculation all fermions can be treated as on-mass shell thanks to the presence of  $\hat{n}_+$  vertices. This property comes from the following arguments.

Note that every intermediate quark line in any diagram couples at least to one of the  $t$ -channel gluons. Algebraically, it means that every  $\hat{k} + m$  stands near the factor  $\hat{n}_+$ . Let us apply the Sudakov decomposition to the matrix:

$$\begin{aligned}
& \hat{k} + m = \hat{n}_+ n_+ + \hat{n}_- n_- + \tilde{m} ; \\
& \hat{n}_+ = \hat{n} = \frac{1}{2}(\gamma_0 + \gamma_3) ; \quad \hat{n}_- = \hat{n}_+ = \frac{1}{2}(\gamma_0 - \gamma_3) :
\end{aligned}$$

Now decompose the propagator numerator of the constituent, to which this  $\hat{n}_+$  leg couples:

$$\hat{k} + m = k_+ + k_- + \tilde{k} + m \quad (2.24)$$

and rewrite it using notation of (4.9), (4.11) as

$$\hat{k} + m = k_+ + k_- + \tilde{k} + m + (k_- - k_+) = \hat{k} + m + \frac{k_-^2 - m^2}{2k_+} : \quad (2.25)$$

In other words, we expressed the virtual quark propagator as the sum of on-shell quark propagator and an additional "instantaneous interaction" term. However, since  $\hat{n}_+$  is inserted between two  $(\hat{k} + m)$  factors, this item does not work due to identity  $\hat{n}_+ \hat{n}_+ = 0$ . The net result is that wherever  $\hat{n}_+$  appears, both constituents can be treated on-mass shell in the trace calculation, which completes the proof.

Having established that the fermion lines in the trace calculation can indeed be taken as if the quarks were real, we can now decompose the numerator of each of the quark lines as

$$\hat{k} + m = \hat{k} + m = \sum_u u \bar{u} ; \quad (2.26)$$

where spinors  $u$  are for an on-mass shell fermion.

In the case of antiquark line the above derived property is valid as well. The only thing to remember here is that antiquark propagates upstream the fermion arrow, so that

$$(\hat{k}) + m = \gamma^X \gamma^v \gamma^v ; \quad (2.27)$$

i.e. each antiquark propagator gives rise to factor  $-1$ .

The derivation is given in Appendix B in full detail and yields

$$\begin{aligned} \text{Im } A^T = & s \frac{32}{(2)^2} \gamma^X \gamma^i e_i^2 \gamma^{\text{em}} \int_0^1 dz \int_0^1 d^2 \tilde{k} \frac{d^2 \tilde{V}(\tilde{k})}{(\tilde{k}^2 + m^2)^2} \\ & \frac{1}{m^2} \frac{1}{(\tilde{k} + \tilde{z})^2 + m^2 + z(1-z)Q^2} \frac{1}{\tilde{k}^2 + m^2 + z(1-z)Q^2} \quad (2.28) \\ & + [z^2 + (1-z)^2]^4 \frac{\tilde{k} + \tilde{z}}{(\tilde{k} + \tilde{z})^2 + m^2 + z(1-z)Q^2} \frac{\tilde{k}}{\tilde{k}^2 + m^2 + z(1-z)Q^2} \end{aligned}$$

$$\begin{aligned} \text{Im } A^L = & s \frac{32}{(2)^2} \gamma^X \gamma^i e_i^2 \gamma^{\text{em}} \int_0^1 dz \int_0^1 d^2 \tilde{k} \frac{d^2 \tilde{V}(\tilde{k})}{(\tilde{k}^2 + m^2)^2} \\ & \frac{1}{4z^2(1-z)^2 Q^2} \frac{1}{(\tilde{k} + \tilde{z})^2 + m^2 + z(1-z)Q^2} \frac{1}{\tilde{k}^2 + m^2 + z(1-z)Q^2} \quad (2.29) \end{aligned}$$

## 2.4 Gluon density

It is obvious that Eqs.(2.28) and (2.29) are not directly related to the real experimental situation, for up to now we assumed that the two exchanged gluons do not interact. Such interaction will definitely change the properties of the entire t-channel exchange, and in fact, as predicted by the BFKL equation, the resultant Pomeron has rather little in common with the initial two perturbative gluons.

Since the BFKL evolution necessarily involves soft gluons (see below more on soft-to-hard disson), it does not allow for accurate perturbative calculations. It must be understood however that although we do not know what happens "inside the Pomeron" on the way from proton to the quark-antiquark pair, we nevertheless know  $|$  and the knowledge is based on the leading order BFKL analysis  $|$  that eventually the qq pair will interact with nothing else but two gluons. We underline that this conclusion does not require the gluons to be hard, but rather it relies on the fact that higher Fock states of the t-channel can be, to the leading  $\log \frac{1}{x}$  approximation, absorbed in the two gluon state [20].

Thus, the only thing we need to know is the momentum distribution of the uppermost gluons, or, to put it exactly, the probability distribution to find a gluon with given lightcone momentum fraction  $x_g$  and the transverse momentum  $\tilde{k}$ .

$$dn_g = F(\tilde{k}; x_g) \frac{d\tilde{k}^2}{\tilde{k}^2} \frac{dx_g}{x_g} : \quad (2.30)$$

This distribution is called the unintegrated (or differential) gluon structure function, DGSF, or simply the unintegrated gluon density.

Since the differential gluon density is uncalculable with pQCD, a reasonable way to proceed in our computation of the Compton scattering amplitude further consists in finding out the correspondence  $V(\vec{k}) \leftrightarrow F(\vec{k}; x_g)$ . Namely, we will calculate the unintegrated gluon density at the Born level  $F_{\text{Born}}$  in terms of  $V(\vec{k})$ , and then postulate that the BFKL dynamics amounts to replacement  $F_{\text{Born}} \rightarrow F$ . This procedure will give us a unique prescription how to correctly incorporate the unintegrated gluon density into the  $k_t$ -factorization calculations.

In order to provide a gentle introduction into the concept of the unintegrated parton densities, we start with famous Fermi-W eizsacker-W illiams approximation in QED. We will find the expression for the unintegrated photon densities in the case of a single charged particle and charge neutral positronium and then translate the results to the case of color forces.

### 2.4.1 Differential density of gauge bosons: the QED primer

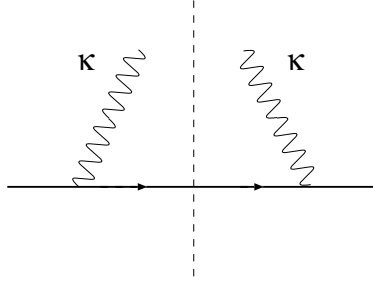


Figure 2.3: The Fermi-W eizsacker-W illiams diagram for calculation of the flux of equivalent photons

For the pedagogical introduction we recall the celebrated Fermi-W eizsacker-W illiams approximation in QED, which is the well known precursor of the parton model (for the review see [21]). Here high energy reactions in the Coulomb field of a charged particle are treated as collisions with equivalent transversely polarized photons – partons of the charged particle, Fig.2.3. The familiar flux of moving equivalent transverse soft photons carrying a lightcone fraction  $x \ll 1$  of the momentum of a relativistic particle, let it be the electron, reads

$$dn_e = \frac{e^2}{(2\pi)^2} \frac{d^2\vec{k}_\perp}{k_\perp^2} \frac{dx}{x} = \frac{e^2}{(2\pi)^2} \frac{d^2\vec{k}_\perp}{k_\perp^2} \frac{dx}{x}; \quad (2.31)$$

Here  $\vec{k}_\perp$  is photon transverse momentum and  $k_z = m_e x$  is the photon longitudinal momentum in the electron Breit frame. The origin of  $k_\perp^2$  in the numerator is in the current conservation, i.e. gauge invariance. Then the unintegrated photon structure function of the electron is by definition

$$F_2(x; k_\perp^2) = \frac{\partial G}{\partial \log k_\perp^2} = x \frac{dn_e}{dx d \log k_\perp^2} = \frac{e^2}{(2\pi)^2} \frac{k_\perp^2}{k_\perp^2 + m_e^2 x^2}; \quad (2.32)$$

### 2.4.2 Differential density of photons in a positronium

If the relativistic particle is a positronium, Fig.2.4, destructive interference of electromagnetic fields of the electron and positron must be taken into account. Specifically, for soft photons with the wavelength  $\lambda = \frac{1}{k_\perp} \gg a_p$ , where  $a_p$  is the positronium Bohr radius, the electromagnetic

elds of an electron and positron cancel each other and the flux of photons vanishes, whereas for  $a_p$  the flux of photons will be twice that for a single electron. The above properties are quantified by the formula

$$F^P(\mathbf{x}; \sim^2) = N_c \frac{e_m}{\sim^2 + \frac{1}{2}} V(\sim); \quad (2.33)$$

where factor  $N_c = 2$  is a number of charged particles in the positronium and corresponds to the Feynman diagrams of Fig. 2.4a, 2.4b. The vertex function  $V(\sim)$  is expressed in terms of the two-body form factor of the positronium,

$$V(\sim) = 1 - F_2(\sim; \sim) = 1 - \langle \mathbf{p} | j \exp(i\mathbf{r} \cdot \mathbf{r}_1) | \mathbf{p} \rangle; \quad (2.34)$$

where  $\mathbf{r} - \mathbf{r}_1$  is the spatial separation of  $e^+$  and  $e^-$  in the positronium. The two-body form factor  $F_2(\sim; \sim)$  describes the destructive interference of electromagnetic elds of the electron and positron and corresponds to the Feynman diagrams of Fig. 2.4c, 2.4d. It vanishes for large enough  $\sim > a_p^{-1}$ , leaving us with  $V(\sim) = 1$ , whereas for soft gluons one has

$$V(\sim) / \sim^2 a_p^2 \quad (2.35)$$

One can say that the law (2.35) is driven by electromagnetic gauge invariance, which guarantees that long wave photons decouple from the charge neutral system.

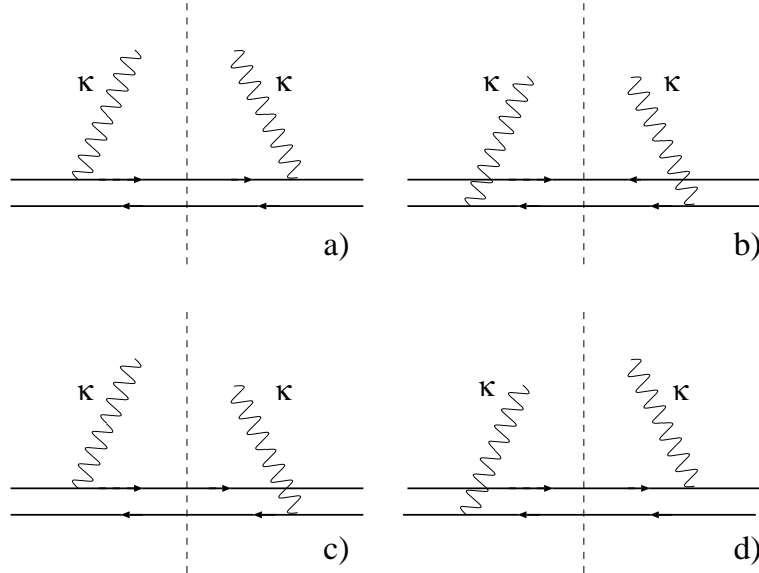


Figure 2.4: The Fermi-Weizsacker-Williams diagrams for calculation of the flux of equivalent photons in positronium.

Finally, recall that the derivation of the differential flux of transverse polarized photons would equally hold if the photons were massive vector bosons interacting with the conserved current, the only change being in the propagator. For instance, for the charge neutral source one finds

$$F_V^P(\mathbf{x}_V; \sim^2) = N_c \frac{e_m}{\sim^2 + m_V^2} V(\sim); \quad (2.36)$$

Recall that the massive vector fields are Yukawa-Dbye screened with the screening radius

$$R_c = \frac{1}{m_V} : \quad (2.37)$$

To the lowest order in QED perturbation theory the two exchanged photons in Eqs 2.3, 2.4 do not interact and we shall often refer to (2.36) as the Born approximation for the differential vector boson structure function. One can regard (2.36) as a minimal model for soft  $\sim$  behavior of differential structure function for Yukawa-Dbye screened vector bosons.

### 2.4.3 Differential gluon density in a proton

The expression for the Born level unintegrated gluon density in color neutral proton can be obtained immediately by generalization of (2.33) and (2.36). The only thing one has to do is an accurate color algebra, which leads to

$$F_g^{(B \text{ orn})} = C_F N_c \frac{s(\sim^2)}{V(\sim)} : \quad (2.38)$$

Therefore, a prescription how to include unintegrated gluon density is as follows:

$$C_F N_c \frac{s(\sim^2)}{V(\sim)} V(\sim) = F_g^{(B \text{ orn})} \rightarrow F : \quad (2.39)$$

Note that in this prescription one of the two strong coupling constants in (2.21) (the lower one) is absorbed into the definition of  $F$ .

## 2.5 Final expressions

With all pieces brought together, the answer for the total photoabsorption cross section reads

$$\begin{aligned} T(x; Q^2) = & \frac{e_m}{i} \sum_i e_i^2 \int_0^1 dz \int_0^1 d^2 \tilde{k} \frac{d^2 \sim}{\sim^4} s(q^2) \\ & F(x; \sim^2) m_i^2 \frac{z}{0} + [z^2 + (1 - z)^2] \frac{1}{1} ; \end{aligned} \quad (2.40)$$

$$L(x; Q^2) = \frac{e_m}{i} \sum_i e_i^2 \int_0^1 dz \int_0^1 d^2 \tilde{k} \frac{d^2 \sim}{\sim^4} s(q^2) F(x; \sim^2) 4Q^2 z^2 (1 - z)^2 \frac{z}{0} ; \quad (2.41)$$

where

$$\frac{z}{0} = \frac{1}{k^2 + m^2} - \frac{1}{(k - \sim f + m^2)} ; \quad \frac{z}{1} = \frac{k}{k^2 + m^2} - \frac{k - \sim}{(k - \sim f + m^2)} : \quad (2.42)$$

Here

$$m^2 = z(1 - z)Q^2 + m_f^2 ; \quad (2.43)$$

and the density of gluons enters at

$$x_g = \frac{Q^2 + M_t^2}{W^2 + Q^2} = x \left[ 1 + \frac{M_t^2}{Q^2} \right] : \quad (2.44)$$



Here  $M_t$  is the transverse mass of the produced qq pair in the photon-gluon fusion  $g \rightarrow qq$ :

$$M_t^2 = \frac{m_f^2 + k^2}{1 - z} + \frac{m_f^2 + (k - \tilde{z})^2}{z} : \quad (2.45)$$

No restrictions on the transverse momentum in the qq loop,  $k$ , and gluon momentum,  $\tilde{z}$ , are imposed in the above representations. The above used BFKL scheme defines DGSF uniquely in terms of physical observables.

We note that equations obtained are for forward diagonal Compton scattering, but similar representation in terms of the unintegrated gluons structure function holds also for the off-forward Compton scattering at finite momentum transfer, for off-diagonal Compton scattering when the virtualities of the initial and final state photons are different,  $Q_f^2 \neq Q_i^2$ , including the timelike photons and vector mesons,  $Q_f^2 = m_V^2$ , in the final state.

The photoabsorption cross sections define the dimensionless structure functions

$$F_{T,L}(x;Q^2) = \frac{Q^2}{4} \frac{1}{s} \sigma_{T,L} \quad (2.46)$$

and  $F_2 = F_T + F_L$ , which admit the familiar pQCD parton model interpretation

$$F_T(x;Q^2) = \sum_{f=u,d,s,c,b;\dots} e_f^2 [q_f(x;Q^2) + \bar{q}_f(x;Q^2)] ; \quad (2.47)$$

where  $q_f(x;Q^2); \bar{q}_f(x;Q^2)$  are the integrated densities of quarks and antiquarks carrying the fraction  $x$  of the lightcone momentum of the target and transverse momenta  $\perp Q$ .

## 2.6 The virtual Compton amplitude in the impact parameter space

A deep further insight into the Compton amplitude | and into the diffractive processes in general | can be gained by switching to the impact parameter (the transverse coordinate) representation. We will see that the answer will allow for a simple probabilistic form

$$A = \int dz \int d^2r (r) j(z;r) f : \quad (2.48)$$

The quantity  $(r)$  has the meaning of the dipole cross section, while the  $(z;r)$  represents the photon wave function.

In order to switch to the impact parameter space, we perform the 2-dimensional Fourier transform. We use the following equalities:

$$\begin{aligned} \frac{1}{k^2 + m^2} &= \frac{1}{2} \int_0^1 dz \int d^2r e^{ikr} f_0(r; z) = \int_0^1 dz \int d^2r e^{ikr} f_0(r) = \int_0^1 dz \int d^2r \frac{e^{ikr}}{k^2 + m^2} = K_0(r); \\ \frac{k}{k^2 + m^2} &= \frac{1}{2} \int_0^1 dz \int d^2r e^{ikr} \tilde{f}_1(r; z) = \int_0^1 dz \int d^2r e^{ikr} \tilde{f}_1(r) = \int_0^1 dz \int d^2r \frac{\partial}{\partial r} \frac{e^{ikr}}{k^2 + m^2} \\ &= \int_0^1 dz \int d^2r \frac{\partial}{\partial r} K_0(r) = i \frac{\partial}{\partial r} K_1(r) : \end{aligned} \quad (2.49)$$

This leads to representation

$$\begin{aligned} 0 &= \frac{1}{2} \int_0^Z d^2 \mathbf{r} e^{i\mathbf{k}\cdot\mathbf{r}} K_0(|\mathbf{r}|) e^{i\mathbf{r}\cdot\mathbf{r}}; \\ \sim_1 &= \frac{1}{2} \int_0^Z d^2 \mathbf{r} e^{i\mathbf{k}\cdot\mathbf{r}} \left( i\mathbf{r} \right) \frac{\mathbf{r}}{r} K_1(|\mathbf{r}|) e^{i\mathbf{r}\cdot\mathbf{r}}; \end{aligned} \quad (2.50)$$

Let us now take an approximation that there is no other  $\mathbf{k}$  dependence in the photoabsorption cross section. Then one will immediately have

$$\begin{aligned} \int_0^Z d^2 \mathbf{k} \sigma_{00} &= \int_0^Z d^2 \mathbf{k} \frac{1}{4} \int_0^Z d^2 \mathbf{r}_1 d^2 \mathbf{r}_2 e^{i\mathbf{k}\cdot\mathbf{r}_1 - i\mathbf{k}\cdot\mathbf{r}_2} K_0(|\mathbf{r}_1|) K_0(|\mathbf{r}_2|) e^{i\mathbf{r}_1\cdot\mathbf{r}_1} e^{i\mathbf{r}_2\cdot\mathbf{r}_2} \\ &= \int_0^Z d^2 \mathbf{r} K_0^2(|\mathbf{r}|) 2[1 - \cos(\mathbf{r}\cdot\mathbf{r})]; \end{aligned} \quad (2.51)$$

Substituting these expressions into photoproduction cross sections, one gets

$$\begin{aligned} T(\mathbf{x}; Q^2) &= \frac{em}{2} \int_0^Z e_i^2 \int_0^Z dz \int_0^Z d^2 \mathbf{r} m_i^2 K_0^2(|\mathbf{r}|) + [z^2 + (1-z)^2] m_i^2 K_1^2(|\mathbf{r}|) \\ &\quad \int_0^Z \frac{d^2 \mathbf{r}}{r^4} s F(\mathbf{x}_g; \mathbf{r}^2) 2[1 - \cos(\mathbf{r}\cdot\mathbf{r})]; \\ L(\mathbf{x}; Q^2) &= \frac{em}{2} \int_0^Z e_i^2 \int_0^Z dz \int_0^Z d^2 \mathbf{r} 4Q^2 z^2 (1-z)^2 K_0^2(|\mathbf{r}|) \\ &\quad \int_0^Z \frac{d^2 \mathbf{r}}{r^4} s F(\mathbf{x}_g; \mathbf{r}^2) 2[1 - \cos(\mathbf{r}\cdot\mathbf{r})]; \end{aligned} \quad (2.52)$$

### 2.6.1 Dipole cross section

The above results can put into the form (2.48) by breaking Eqs. (2.52) into some positively defined cross section and the square of the photo wave function. This is done in an unambiguous way by defining the dipole cross section.

Let us first consider the total quark-proton cross section

$$\sigma_{qp} = \frac{2}{3} \int_0^Z \frac{d^2 \mathbf{r}}{r^4} s (\mathbf{r}^2) F(\mathbf{x}; \mathbf{r}^2); \quad (2.53)$$

Note that this expression does not depend on the quark transverse momentum  $\mathbf{k}$ . This means that precisely this cross section corresponds not only to the plane wave, but also to any transverse wave packet. In particular, a localized state in the impact parameter space (that is, a quark with a fixed separation  $\sim_{qp}$  from the proton) would be described by the same formula.

Given this cross section, we can now ask for interaction of color dipole with the proton. In this each extra gluon that is attached to the antiquark rather than to the quark gives rise of extra phase factor  $\exp(-i\mathbf{r}\cdot\mathbf{r})$  as well as extra minus sign. These factors for the four diagrams will then sum up to produce

$$1 - e^{i\mathbf{r}\cdot\mathbf{r}} - e^{-i\mathbf{r}\cdot\mathbf{r}} + 1 = 2[1 - \cos(\mathbf{r}\cdot\mathbf{r})];$$

The result for the dipole cross section is then

$$\begin{aligned} \sigma_{dip}(\mathbf{r}) &= \frac{2}{3} \int_0^Z \frac{d^2 \mathbf{r}}{r^4} s \max(\mathbf{r}^2; \frac{A}{r^2}) F(\mathbf{x}; \mathbf{r}^2) 2[1 - \cos(\mathbf{r}\cdot\mathbf{r})] \\ &= \frac{4}{3} \int_0^Z \frac{d^2 \mathbf{r}}{r^4} s \max(\mathbf{r}^2; \frac{A}{r^2}) F(\mathbf{x}; \mathbf{r}^2) [1 - J_0(r)] \end{aligned} \quad (2.54)$$

Note that in contrast to (2.53) the argument of  $\sigma_s$  contains now the effect of a possible screening from the complementary charge. Indeed, even when  $\alpha_s^2$  is small, the strong coupling constant does not boost up, for such a boost requires the presence of soft gluon vertex correction loops, which are strongly suppressed by the color anti-charge of the antiquark.

Having defined the dipole color cross section, we can now return to the photoabsorption cross section and cast it into form

$$\begin{aligned} \sigma_T &= \int_0^1 dz \int d^2x \, \sigma_{\text{dip}}(x) \, \text{Tr} \, j^\dagger j(z; x); \quad \sigma_L = \int_0^1 dz \int d^2x \, \sigma_{\text{dip}}(x) \, \text{Tr} \, j^\dagger j(z; x); \\ \text{Tr} \, j^\dagger(z; x) j &= \frac{3}{2} \frac{e_{\text{em}}^2}{2} \sum_i e_i^2 \left[ m_i^2 K_0^2(r) + [z^2 + (1-z)^2] m_i^2 K_1^2(r) \right]; \\ \text{Tr} \, j^\dagger(z; x) j &= \frac{3}{2} \frac{e_{\text{em}}^2}{2} \sum_i e_i^2 4Q^2 z^2 (1-z)^2 K_0^2(r); \end{aligned} \quad (2.55)$$

Note that this representation literally represents the probabilistic form (2.6) of the forward scattering amplitude.

## Chapter 3

### DGLAP vs. $k_t$ factorization

The calculation of the forward Compton scattering amplitude conducted in the previous chapter within the framework of the  $k_t$ -factorization approach can be used now to investigate the major similarities and the gross differences in comparison with the widely used DGLAP approach to the computation of high energy reactions.

It turns out that in the double logarithmic regime — that is, when both  $\log \frac{1}{x}$  and  $\log Q^2$  are large, we might expect that both approaches are applicable and their predictions should asymptotically converge. We are now going to demonstrate that it is indeed the case, and during this analysis we will also show what sort of phase space restrictions DGLAP approach contains and what it leads to.

#### 3.1 How DGLAP and $k_t$ factorization approaches meet at high $Q^2$

Recall the familiar DGLAP equation [18] for scaling violations at small  $x$ ,

$$\frac{dF_2(x; Q^2)}{d \log Q^2} = \sum_f e_f^2 \frac{s(Q^2)}{2} \int_x^1 \frac{dy}{y} [Y^2 + (1-Y)^2] G\left(\frac{x}{y}; Q^2\right) - \frac{s(Q^2)}{3} G(2x; Q^2) \sum_f e_f^2; \quad (3.1)$$

where for the sake of simplicity we consider only light flavours. Upon integration we find

$$F_2(x; Q^2) = \sum_f e_f^2 \int_x^1 \frac{d\bar{Q}^2}{\bar{Q}^2} \frac{s(\bar{Q}^2)}{3} G(2x; \bar{Q}^2); \quad (3.2)$$

with  $\bar{Q}^2$  being the proper cut-off. In order to see the correspondence between the  $k_t$ -factorization and DGLAP factorization it is instructive to follow the derivation of (3.2) from the  $\tilde{\gamma}$ -representation.

First, separate the  $\tilde{\gamma}^2$ -integration into the DGLAP part of the gluon phase space  $\tilde{\gamma}^2 < \bar{Q}^2 = k^2 + m^2$  and beyond-DGLAP region  $\tilde{\gamma}^2 > \bar{Q}^2$ . One readily finds

$$\begin{aligned} \int_0^1 \frac{k^2}{k^2 + m^2} \frac{k^2}{(k^2 + m^2)^2} d\tilde{\gamma}^2 &= \int_0^{\bar{Q}^2} \frac{k^2}{(k^2 + m^2)^2} d\tilde{\gamma}^2 + \int_{\bar{Q}^2}^1 \frac{k^2}{(k^2 + m^2)^2} d\tilde{\gamma}^2 \\ &= \frac{1}{\bar{Q}^2} \left[ \frac{2z^2(1-z)^2 Q^4}{\bar{Q}^8} - \frac{2z(1-z)Q^2}{\bar{Q}^6} + \frac{1}{\bar{Q}^4} \right] \tilde{\gamma}^2 \quad \text{if } \tilde{\gamma}^2 < \bar{Q}^2 \\ &= \frac{1}{\bar{Q}^2} \left[ \frac{z(1-z)Q^2}{\bar{Q}^4} \right]; \quad \text{if } \tilde{\gamma}^2 > \bar{Q}^2 \end{aligned} \quad (3.3)$$

Consider first the contribution from the DGLAP part of the phase space  $\sim^2 < \bar{Q}^2$ . Notice that because of the factor  $\sim^2$  in (3.3), the straightforward  $\sim^2$  integration of the DGLAP component yields  $G(x_g; \bar{Q}^2)$  and  $\bar{Q}^2$  is precisely the pQCD hard scale for the gluonic transverse momentum scale:

$$\begin{aligned} & \int_0^{\bar{Q}^2} \frac{d\sim^2}{\sim^4} s(q^2) F(x_g; \sim^2) \otimes \frac{\bar{k}}{\bar{k}^2 + \sim^2} \frac{\bar{k} \sim}{(\bar{k} \sim + \sim^2)} A \\ &= \frac{2z^2 (1-z)^2 Q^4}{\bar{Q}^8} - \frac{2z (1-z) Q^2}{\bar{Q}^6} + \frac{1}{\bar{Q}^4} s(\bar{Q}^2) G(x_g; \bar{Q}^2) \end{aligned} \quad (3.4)$$

The contribution from the beyond-DGLAP region of the phase space can be evaluated in terms of  $F(x_g; \bar{Q}^2)$  and the rescaling factor  $C_2$ :

$$\begin{aligned} & \int_0^{\bar{Q}^2} \frac{d\sim^2}{\sim^4} s(q^2) F(x_g; \sim^2) \frac{1}{\bar{Q}^2} \frac{z (1-z) Q^2}{\bar{Q}^4} = \frac{1}{\bar{Q}^4} \frac{z (1-z) Q^2}{\bar{Q}^6} s(\bar{Q}^2) F(x_g; \bar{Q}^2) I(x_g; \bar{Q}^2) \\ &= \frac{2z^2 (1-z)^2 Q^4}{\bar{Q}^8} - \frac{2z (1-z) Q^2}{\bar{Q}^6} + \frac{1}{\bar{Q}^4} s(\bar{Q}^2) F(x_g; \bar{Q}^2) \log C_2(x_g; \bar{Q}^2; z) \end{aligned} \quad (3.5)$$

The latter form of (3.5) allows for convenient combination (3.4) and (3.5) rescaling the hard scale in the GSF

$$G(x_g; \bar{Q}^2) + F(x_g; \bar{Q}^2) \log C_2(x_g; \bar{Q}^2; z) = G(x_g; C_2(x_g; \bar{Q}^2; z) \bar{Q}^2) : \quad (3.6)$$

Here the exact value of  $I(x_g; \bar{Q}^2)$  depends on the rate of the  $\sim^2$ -rise of  $F(x_g; \sim^2)$ . At small  $x_g$  and small to moderate  $\bar{Q}^2$  one finds  $I(x_g; \bar{Q}^2)$  substantially larger than 1 and  $C_2(x_g; \bar{Q}^2; z) \approx 1$ , see more discussion below in section 9.

Now change from  $d\bar{k}^2$  integration to  $d\bar{Q}^2$  and again split the  $z, Q^2$  integration into the DGLAP part of the phase space  $\bar{Q}^2 \leq \frac{1}{4} Q^2$ , where either  $z < \frac{\bar{Q}^2}{Q^2}$  or  $1 - z < \frac{\bar{Q}^2}{Q^2}$ , and the beyond-DGLAP region  $\bar{Q}^2 > \frac{1}{4} Q^2$ , where  $0 < z < 1$ . As a result one finds

$$\begin{aligned} & \int_0^{\bar{Q}^2} dz [z^2 + (1-z)^2] \frac{2z^2 (1-z)^2 Q^4}{\bar{Q}^8} - \frac{2z (1-z) Q^2}{\bar{Q}^6} + \frac{1}{\bar{Q}^4} \\ & \approx \frac{4}{3\bar{Q}^2 Q^2}; \quad \text{if } \bar{Q}^2 \leq \frac{1}{4} Q^2 \\ & = \frac{2A_2 \bar{Q}^4}{Q^8} - 2A_1 \frac{Q^2}{\bar{Q}^6} + A_0 \frac{1}{\bar{Q}^4}; \quad \text{if } \bar{Q}^2 > \frac{1}{4} Q^2 \end{aligned} \quad (3.7)$$

where

$$A_m = \int_0^1 dz [z^2 + (1-z)^2] z^m (1-z)^m \quad (3.8)$$

Let  $\bar{C}_2$  be  $C_2(x_g; \bar{Q}^2; z)$  at a mean point. Notice also that  $M_t^2 \ll Q^2$ , so that  $x_g \approx 2x$ . Then the contribution from the DGLAP phase space of  $\bar{Q}^2$  can be cast in precisely the form (3.2)

$$F_2(x; Q^2)_{\text{DGLAP}} = e_f^2 \int_0^{\bar{C}_2 Q^2} \frac{d\bar{Q}^2}{\bar{Q}^2} \frac{s(\bar{Q}^2)}{3} G(2x; \bar{Q}^2) : \quad (3.9)$$

The beyond-DGLAP region of the phase space gives the extra contribution of the form

$$F_2(x;Q^2)_{\text{non-DGLAP}} = \sum_f e_f^2 \frac{s(Q^2)}{3} \int_{Q^2}^{\sqrt{s}} \frac{d\bar{Q}^2}{\bar{Q}^2} \frac{Q^2}{\bar{Q}^2} G(2x;\bar{Q}^2) + \sum_f e_f^2 \frac{s(Q^2)}{3} G(2x;Q^2) : \quad (3.10)$$

Eqs.(3.9) and (3.10) immediately reveal the phenomenological consequences of lifting the DGLAP restrictions in the transverse momenta integration. Indeed, the DGLAP approach respects the following strict inequalities

$$\sim^2 \quad \bar{k}^2 \quad \text{and} \quad \bar{k}^2 \quad Q^2 : \quad (3.11)$$

As we just saw, removing the first limitation effectively shifted the upper limit in the  $\bar{Q}^2$  integral to  $\frac{\sqrt{s}}{2} Q^2 \notin Q^2$ , while lifting the second constraint led to an additional, purely non-DGLAP contribution. Although both of these corrections lack one leading  $\log Q^2$  factor they are numerically substantial.

The above analysis suggests that the DGLAP and  $k_t$ -factorization schemes converge logarithmically at large  $Q^2$ . However, in order to reproduce the result (3.9) and (3.10) for the full phase space by the conventional DGLAP contribution (3.2) from the restricted phase space (2.5) one has to ask for DGLAP gluon density  $G_{\text{pt}}(x;Q^2)$  larger than the integrated GSF in the  $k_t$ -factorization scheme and the difference may be quite substantial in the domain of strong scaling violations.

## 3.2 The different evolution paths: soft-to-hard diffusion and vice versa

The above discussion of the contributions to the total cross section from the DGLAP and non-DGLAP parts of the phase space can conveniently be cast in the form of the Huygens principle. To the standard DGLAP leading  $\log Q^2$  (LL $Q^2$ ) approximation one only considers the contribution from the restricted part of the available transverse phase space (2.5). The familiar Huygens principle for the homogeneous DGLAP LL $Q^2$  evaluation of parton densities in the  $x$ - $Q^2$  plane is illustrated in Fig. 3.1a: one starts with the boundary condition  $p(x;Q_0^2)$  as a function of  $x$  at fixed  $Q_0^2$ , the evolution paths  $(z;Q^2)$  for the calculation of  $p(x;Q^2)$  shown in Fig. 3.1a are confined to a rectangle  $x \leq z \leq 1; Q_0^2 \leq Q^2 \leq Q^2$ , the evolution is unidirectional in the sense that there is no feedback on the  $x$ -dependence of  $p(x;Q_1^2)$  from the  $x$ -dependence of  $p(x;Q_2^2)$  at  $Q_2^2 \leq Q_1^2$ . In Fig. 3.1a we show some examples of evolution paths which are kinematically allowed but neglected in the DGLAP approximation. Starting with about at or slowly rising  $G(x;Q_0^2)$ , one finds that the larger  $Q^2$ , the steeper the small- $x$  rise of  $G(x;Q^2)$ .

At  $x \ll 1$  the DGLAP contribution from the restricted transverse phase space (2.5) no longer dominates the multiparton production cross sections, the restriction (2.5) must be lifted and the contribution to the cross section from small- $x$  and large- $x$   $Q^2$  can no longer be neglected. The Huygens principle for the homogeneous BFKL evolution is illustrated in Fig. 3.1b: one starts with the boundary condition  $F(x_0;Q^2)$  as a function of  $Q^2$  at fixed  $x_0 \ll 1$ , the evolution paths  $(z;Q^2)$  for the calculation of  $p(x;Q^2)$  are confined to a stripe  $x \leq z \leq x$ ,

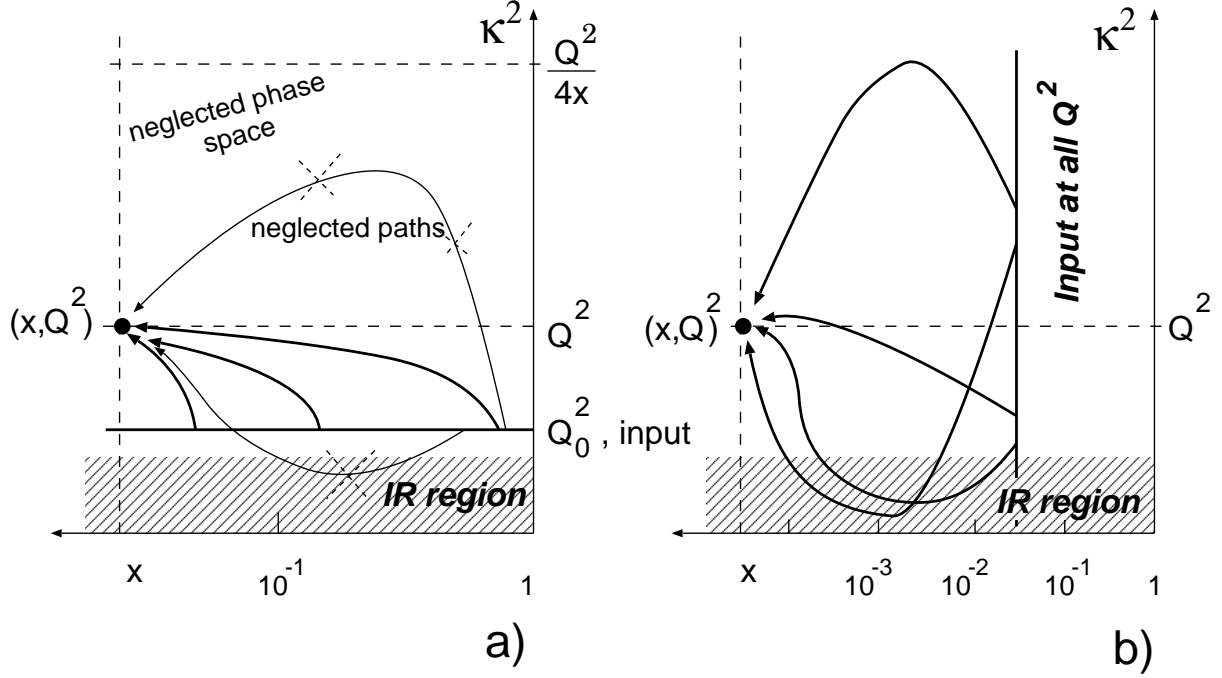


Figure 3.1: The Huygens principle for  $Q^2; x$  evolution of DIS structure functions with (a) DGLAP restricted transverse phase space and (b) for the BFKL  $x$  evolution without restrictions on the transverse phase space and hard-to-soft & soft-to-hard diffusion.

in contrast to the unidirectional DGLAP evolution one can say that under BFKL evolution the small- $x$  behaviour of  $p(x; Q^2)$  at large  $Q^2$  is fed partly by the  $x$ -dependence of soft  $p(x; Q^2)$  at larger  $x$  and vice versa. The most dramatic consequence of this soft-to-hard and hard-to-soft diffusion, which can not be eliminated, is that at very small  $x$  the  $x$ -dependence of the gluon structure in the soft and hard regions will eventually be the same. The rate of such a hard-to-soft diffusion is evidently sensitive to the infrared regularization of pQCD, the model estimates show that in the HERA range of  $x$  it is very slow [22, 23].

## Part II

Derivation of vector meson production  
amplitudes



## Chapter 4

# Description of a vector meson

In this chapter we first introduce the vector meson light cone wave function (LCWF) and show how it emerges in diagrammatic calculations. Then, describing S and D wave type vector particles, we give at once expressions for S and D wave vector meson spinorial structures, which we then prove by computing the normalization condition for LCWF. Finally, we also calculate  $V \rightarrow e^+e^-$  decay constants to be used afterwards.

### 4.1 Bound states in QFT

While describing particle motion in non-relativistic Quantum Mechanics, one usually deals with a configuration space particle wave function, which is a good description because the number of particles is conserved. So, when one has a system of particles and shows that the wave function corresponding to their relative motion decreases at large relative distances at least exponentially, one can speak of a bound state.

In Quantum Field Theory (QFT) this approach needs an update, since the field function becomes an operator in Fock space. Besides, since a bound state always implies the presence of interaction, the projection of a physical bound state onto the Fock space of free, non-interacting, plane-wave state vectors has a rather complicated structure:

$$|\psi_{\text{phys}}\rangle = c_0 |qq\rangle + c_1 |q\bar{q}g\rangle + c_2 |q\bar{q}gg\rangle + c_3 |q\bar{q}ggg\rangle + \dots \quad (4.1)$$

We emphasize that in this decomposition quarks and gluons are assumed free, i.e. on mass shell. Coefficients  $c_i$  can be called 'wave functions' of the given projection of a physical vector meson, with  $|c_i|^2$  being the probability of finding a vector meson in a given state.

The exact treatment of any reaction involving the vector meson must account for all terms in the above expansion. Demonstration of a method that would account for all these terms is however still an unresolved task, and currently one is bound to the term-by-term analysis of the vector meson reactions.

Given a large number of papers devoted to the high-energy reactions involving vector mesons, and in particular, the process of diffractive vector meson production in DIS, one might expect that the lowest Fock state in the above decomposition has been already thoroughly studied. It turns out however that it is not so, for in all early calculations the importance of the spin-angular coupling inside the vector meson and dramatic effects it entails was heavily overlooked.

In this Chapter we close this gap. We construct a full and exact theory of the vector meson structure, provided the vector meson Fock space is saturated only to the lowest qq state. Being only an approximation, this approach still is of vital importance to the whole field, for it results in a complete, self-consistent and self-contained spin-angular description of the vector meson. To our best knowledge, our work represents the only satisfactory theory of spin structure of the vector meson.

## 4.2 LCWF and vertex factor

Let us now outline how a wave function of a bound state appears in the diagrammatic language.

In the non-relativistic quantum mechanics, the two-particle bound state problem can be immediately reformulated as a problem for one particle of reduced mass  $\mu$ , moving in the external potential. This reformulation allows one to split the wave function into two factors: the wave function of the motion of the composite particle as a whole and the wave function corresponding to the internal motion of constituents. The former part factors out trivially, while the latter wave function obeys the following Schrodinger equation

$$\left[ \frac{p^2}{2\mu} + V(r) \right] \psi(r) = E \psi(r) : \quad (4.2)$$

Since the wave function  $\psi(r)$  and the interaction operator  $V(r)$  exhibit good infinity behavior, one can rewrite this equation in the momentum representation

$$\begin{aligned} \frac{p^2}{2\mu} \psi(p) + \frac{1}{(2\pi)^3} \int d^3k V(k) \psi(p-k) &= E \psi(p) ; \\ \frac{p^2}{m} \psi(p) &= \frac{1}{(2\pi)^3} \int d^3k V(k) \psi(p-k) : \end{aligned} \quad (4.3)$$

In this notation, this equation can be viewed as a homogeneous non-relativistic Bethe-Salpeter equation for the wave function  $\psi(p)$  that describes the relative motion of constituents inside a composite particle.

Let us now introduce

$$\psi(p) = \frac{p^2}{m} \psi(p) \quad (4.4)$$

Then Eq.(4.3) can be rewritten as

$$\psi(p) = \frac{1}{(2\pi)^3} \int d^3k V(k) \frac{1}{\frac{(p-k)^2}{m} - E} \psi(p-k) \quad (4.5)$$

This equation has an absolutely straightforward diagrammatic interpretation (Fig.4.1). One sees that  $\psi(p)$  stands for bound-state ! constituents transition vertex, with  $p$  being the relative momentum of the constituents, factor  $1 = [\frac{(p-k)^2}{m} - E]$  describes propagation of qq pair and  $V(k)$  stands for the interaction between constituents. Of course, the kinetic energy  $p^2 = 2\mu E$ , the total energy, which is in fact negative, so no pole arises in the propagator.

In the relativistic case, i.e. in QFT, it is not clear a priori whether the whole picture that involves somehow defined wave function and representation of the vector meson as free

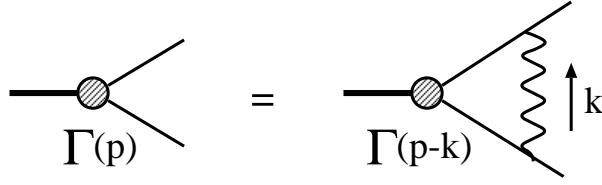


Figure 4.1: The diagrammatic interpretation of the integral equation for vertex function  $\Gamma(p)$  ( $p$  is the relative constituents momentum).

non-interacting constituents would work at all. So, in our approach we will be aiming at introducing an appropriately defined wave function and demonstrating that hard processes involving vector mesons can be expressed in terms of expectation values of qq amplitudes between wave functions, i.e. we intend to treat a hard process in a probabilistic, quantum mechanics-like manner.

In the following we will show that this program succeeds. Namely, we will introduce the radial wave function of the qq state of a vector meson as

$$(q) = \frac{(q)}{M^2 - m_V^2} \quad (4.6)$$

(the angular dependence of the wave function will be treated separately, see Sect.4.4) Here  $(q)$  is the vertex factor,  $M^2$  is the eigenvalue of the relativistic kinetic operator of the on mass shell qq state and  $m_V^2$  is eigenvalue of the total relativistic Hamiltonian, which is of course equal to the mass of the vector meson squared. Then, during an accurate and honest analysis of a hard process Feynman diagrams, we will always make sure that wave function (4.6) automatically appears in calculations and the rest looks the same as if both fermions were on mass shell. If we see that fermion virtualities modify the results, or if different Fock states mix during hard interactions of the vector meson, it would signal the invalidity of the free particle parton language and consequently the breakdown of the whole approach. This restriction must always be taken into account when obtaining and interpreting the parton model-based results.

### 4.3 Light cone formalism

The term "light cone approach" to high energy process calculations can have different meanings. Some prefer to re-formulate the whole QFT within light cone dynamics, introduce light cone quantization and derive light cone Feynman rules (on Light Cone Field Theory see [24, 25]). However, one should keep in mind that even within the usual QFT the light cone formalism can be freely used as a means to greatly simplify intermediate calculations. This is exactly the way we will use it.

It was noted long ago [26] that the calculation of a high energy collision is simplified if one decomposes all momenta in terms of light cone  $n_+$ ;  $n_-$  and transversal components, which we will always mark with the vector sign over a letter (so called Sudakov's decomposition):

$$\begin{aligned} n_+ &= \frac{1}{\sqrt{2}}(1;0;1); \quad n_- = \frac{1}{\sqrt{2}}(1;0;-1); \quad (n_+ n_-) = 1; \quad (n_+ n_+) = (n_- n_-) = 0 \\ p &= p_+ n_+ + p_- n_- + \vec{p}_\perp; \quad p^2 = 2p_+ p_- - \vec{p}_\perp^2 \end{aligned} \quad (4.7)$$

Indeed, imagine two high energy particles colliding with momenta  $p$  and  $q$  respectively and equal masses  $m$ . Then one can choose such a frame of reference that in the Sudakov's decomposition

$$\begin{aligned} p &= p_+ n_+ + p_- n_- + \mathbf{p}_\perp; \\ q &= q_+ n_+ + q_- n_- + \mathbf{q}_\perp \end{aligned}$$

quantities  $p_-$  and  $q_-$  are large  $p_-; q_- \gg m^2$  while  $p_+ = (\mathbf{p}_\perp^2 + m^2)/(2p_-)$  and  $q_+ = (\mathbf{q}_\perp^2 + m^2)/(2q_-)$  are small. The total energy squared of these two particles will be defined as

$$s = 2q_- p_- : \quad (4.8)$$

Note that our definition of  $s$  is somewhat different from the more familiar one  $(p+q)^2$  by terms  $\sim m^2; \mathbf{p}_\perp^2$ . However, it is not of any importance for us, since in the course of all calculations we will keep track only of the highest power  $s$  contributions, i.e. everything will be calculated in the leading power  $s$  approximation.

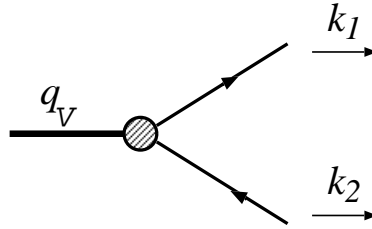


Figure 4.2: Kinematics of  $V \rightarrow qq$  vertex on the light cone. Vector meson momentum  $q_V$  is taken incoming, constituents momenta are outgoing.

Let us now go further and examine the kinematics of a typical  $qqV$  vertex (Fig.4.2). The Sudakov's decomposition of all momenta reads:

$$\begin{aligned} q_V &= q_{V+} n_+ + q_{V-} n_-; \\ k_1 &= k_{1+} n_+ + k_{1-} n_- + \mathbf{k}_\perp = z q_{V+} n_+ + y q_{V-} n_- + \mathbf{k}_\perp; \\ k_2 &= k_{2+} n_+ + k_{2-} n_- - \mathbf{k}_\perp = (1-z) q_{V+} n_+ + (1-y) q_{V-} n_- - \mathbf{k}_\perp \end{aligned} \quad (4.9)$$

so that

$$q_V^2 = 2q_{V+} q_{V-} = m_V^2; \quad k_1 + k_2 = q_V; \quad k_i^2 \ll m^2; \quad (4.10)$$

i.e. quarks can be on mass shell. Now let us introduce momenta  $k_i$ , which would correspond to on mass shell fermions. The only component in  $k_i$  subject to modification is  $k_{i-}$  component, or absolutely equivalently, the energy. Large  $k_{i+}$  components are insensitive to (reasonable) quark virtuality variations. So, to obtain the on mass shell momenta, one has to replace

$$k_{i-} = \frac{k_{i\perp}^2 + \mathbf{k}_\perp^2}{2k_{i+}} \rightarrow k_{i-} = \frac{m^2 + \mathbf{k}_\perp^2}{2k_{i+}} : \quad (4.11)$$

Then the 4-vector

$$q = k_1 + k_2 \quad (4.12)$$

squared is equal to

$$M^2 = q^2 = 2q_+ q_- = 2q_+ (-k_1 + k_2) = \frac{k^2 + m^2}{z(1-z)} : \quad (4.13)$$

And again we emphasize that the Feynman invariant mass (i.e. the total 4-momentum squared) of the virtual quark-antiquark pair is  $m_V^2$ . The quantity  $M^2$  is the invariant mass of the free, non-interacting qq state (see 4.6). However, it is precisely  $M$ , not  $m_V$  that will govern the hard interaction of qq pair with gluons.

Finally, it is useful to introduce the relative momentum of free qq system :

$$2p = (k_1 - k_2) : \quad (4.14)$$

Then, trivial algebra leads to

$$M^2 = 4m^2 + 4p^2 ; \quad p^2 = \vec{p}^2 ; \quad (pq) = 0 ; \quad (4.15)$$

where  $p$  is the 3-dimensional relative momentum in the qq pair rest frame of reference. Its components are

$$p = (p; p_z) ; \quad p = k ; \quad p_z = \frac{1}{2}(2z - 1)M : \quad (4.16)$$

## 4.4 Spin structure of a vector particle

Let us start with a well known example of a deuteron, which is a non-relativistic analogy of a vector meson: they are both vector particles built up of two fermions. To have the correct P-parity, proton and neutron must sit in the spin-triplet state, thus leaving us with two possible values of their angular momenta:  $L = 0$  and  $2$ .

In the conventional non-relativistic language one describes the spin-angular coupling by the Clebsch-Gordan technique. The non-relativistic Feynman diagram calculations can be best performed in an alternative approach. Here a deuteron, being a vector particle, is described by a 3 dimensional polarization vector  $V$ . So, while calculating high energy processes involving  $d \rightarrow pn$  transitions, one can use the following spin structure of deuteron-nucleon-nucleon vertex:

$$\begin{matrix} + \\ n \end{matrix} \quad p \quad V \quad (4.17)$$

Since both nucleons can be treated on mass shell, only two terms enter  $\Gamma_i$ , which can be written as:

$$\begin{matrix} + \\ n \end{matrix} \quad u(p) \quad \vec{\sigma}^i + w(p) (3p^i p^j - \delta^{ij} p^2) \quad \vec{\sigma}^j \quad p \quad \vec{V} \quad (4.18)$$

Here  $\vec{\sigma}^i$  are Pauli matrices and  $p$  is the relative proton-neutron momentum. One immediately recognizes here spin structures corresponding to pn pair sitting in S and D waves respectively. In particular, squaring the above expression gives

$$\begin{aligned} (V V) & \text{ for } \mathcal{S}^2 \\ 3(p V)(p V) - (V V)p^2 & \text{ for SD interference} \\ 3p^2(p V)(p V) + (V V)p^4 & \text{ for } \mathcal{D}^2 \end{aligned} \quad (4.19)$$

Now, let us go relativistic and turn to vector mesons. The polarization state of a vector particle is described by a four-vector  $V$ . Therefore, a general form of  $qqV$  vertex has the form

$$u^0 u V(p);$$

where  $(p)$  is the familiar vertex factor. Up to now, it has been customary in literature to choose the simplest form of the spinorial structure :

$$u^0 u V(p) : \quad (4.20)$$

However, one must admit that (4.20) is simply an analogy of  $qq$  vertex and does not reflect the true internal structure of a vector meson. It is known [27] that the correct spinorial structure corresponding to pure the S wave  $qq$  state reads

$$S = \frac{2p}{M + 2m} = g \frac{2p \cdot p}{m(M + 2m)} S : \quad (4.21)$$

It is implied here that spinorial structures are inserted between on mass shell spinors in accordance with our principal guideline (see discussion in Sect.4.2).

Once S wave spinorial structure is established, the expression for D wave can be obtained by contracting S wave with the symmetric traceless tensor of rank two  $3p_i p_j - \frac{1}{3} p^2 g_{ij}$ , rewritten in the Lorenz notation. To do so, one should replace

$$p_i \rightarrow p; \quad g_{ij} \rightarrow g + \frac{q \cdot q}{M^2}$$

(in the  $qq$  pair rest frame of reference  $q = (M; 0; 0; 0)$ ). However, since  $q$  inserted between on mass shell spinors gives zero due to the Ward identity, one obtains the required tensor in the form  $3p \cdot p + g \cdot p^2$ . Its contraction with  $S$  yields

$$D = (3p \cdot p + g \cdot p^2) S = p^2 + (M + m)p = p^2 g + \frac{M + m}{m} p \cdot p D : \quad (4.22)$$

We will prove below that structures (4.21), (4.22) after being squared indeed perfectly reproduce (4.19), i.e. they indeed correspond to pure S and D waves.

The quantities  $S$  and  $D$  used in (4.21), (4.22) have the meaning of S=D wave projectors, which will be used in all subsequent calculations. Namely, all calculations will be at first performed for the naive  $qqV$  vertex (4.20) and then we will apply the projector technique to obtain expressions for S and D wave states.

## 4.5 Vector meson LCWF normalization

Before tackling the diffractive vector meson production process, we first should have a prescription of normalization of the vector meson wave function.

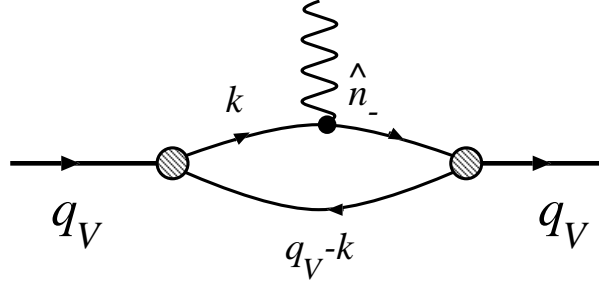


Figure 4.3: Diagram used for normalizing the vector meson LCWF. The amplitude of this diagram is set equal to  $2q_V$ .

#### 4.5.1 Naive qqV vertex

A natural way to normalize the wave function of a composite system is to put the amplitude given by this diagram in Fig.4.3 equal to  $2q_V$ . Here extra leg carries zero momentum but couples to the fermion line as  $\hat{n}$ . Note that for a charged composite particle (a deuteron) this is precisely setting the electric form factor equal to unity in the soft photon limit.

As described above, we first treat qqV vertex as  $u^0 u^0(p)$ . In this case the general expression for this amplitude is

$$A = \frac{(1)}{(2)^4} N_c \int d^4k \frac{\text{Spfi} \hat{V}_1 \hat{k} (\not{q} + m) \hat{V}_2 \hat{k} (+m) i \hat{n} \hat{k} (+m) g}{[k^2 - m^2 + i\epsilon] [k^2 - m^2 + i\epsilon] [(k - q)^2 - m^2 + i\epsilon]} \\ = \frac{N_c}{(2)^4} \int d^4k \frac{j^2 \text{Spfi} \hat{V}_1 \hat{k} (\not{q} + m) \hat{V}_2 \hat{k} (+m) i \hat{n} \hat{k} (+m) g}{[k^2 - m^2 + i\epsilon] [(k - q)^2 - m^2 + i\epsilon]}; \quad (4.23)$$

where  $N_c = 3$  is a trivial color factor originating from the quark loop. We deliberately recognized  $V_1$  and  $V_2$  as distinct entities just to make sure later that such a loop is indeed diagonal in polarization states.

The first step is to rewrite this expression in terms of Sudakov's variables. As usual, one implements decomposition

$$k = zq_V + n_+ + yq_V - n_- + \tilde{k}; \quad q_V^2 = 2q_V + q_V = m_V^2$$

and transform

$$d^4k = \frac{1}{2} m_V^2 d^2\tilde{k} dy dz;$$

Now we note that vertex functions do not depend on  $y$  (and neither does the trace, as will be shown later), so we can immediately perform the integrations over  $y$  by means of Cauchy theorem. Indeed, since the integral

$$\int_{-1}^1 dy \frac{1}{[yzm_V^2 - \tilde{k}^2 + m^2 + i\epsilon] [(1-y)(1-z)m_V^2 - \tilde{k}^2 + m^2 + i\epsilon]}; \quad (4.24)$$

is convergent and has good infinity behavior, one can close the integration contour in the most convenient way. To do so, one should analyze the position of all poles on the complex  $y$  plane:

$$y_{1,2} = \frac{\tilde{k}^2 + m^2}{zm_V^2} \pm \frac{i}{zm_V^2}; \quad y_3 = 1 - \frac{\tilde{k}^2 + m^2}{(1-z)m_V^2} + \frac{i}{(1-z)m_V^2};$$

One sees that if  $z < 0$  or  $z > 1$ , all poles lie on the same side of the real axis in the complex  $y$  plane, which leads to zero contribution. The contribution that survives comes from region  $0 < z < 1$ , which has in fact a simple physical meaning: all constituents must move in the same direction. In this region, we close the integration contour through the upper half-plane and take a residue at  $y = y_3$ . Physically, it corresponds to putting the antiquark on mass shell. After this procedure, one gets for (4.24):

$$\begin{aligned} & \frac{2-i}{(1-z)m_V^2} \frac{1}{[ym_V^2 - k^2 + m^2] + i\epsilon} \Big|_{y=y_3} = \frac{2-i}{(1-z)m_V^2} \frac{(1-z)^2}{[k^2 + m^2 - z(1-z)m_V^2]^2} \\ & = \frac{2-i}{m_V^2} \frac{1}{z^2(1-z)} \frac{1}{M^2 - m_V^2} : \end{aligned}$$

One immediately recognizes here the same two-particle propagator as in (4.6). Therefore, the equation for the amplitude reads

$$A = i \frac{N_c}{(2\pi)^3} \int^z d^2k \frac{dz}{z^2(1-z)} j^2 j \frac{1}{2} \text{Spf} \dots : \quad (4.25)$$

We now turn to the trace calculations. As we found during the calculation of the forward Compton scattering amplitude, all the fermions can be treated in the trace calculations as if they were on mass shell. We will use this property in all subsequent calculations.

The easiest way to calculate the traces in our case is to do it covariantly, without involving further the Sudakov technique. Since quarks in numerator can be treated on mass shell, we first note that

$$(\hat{k} + m) \hat{n} (\hat{k} + m) = 2(k \cdot n) (\hat{k} + m)$$

so that

$$\frac{1}{2} \text{Spf} \dots = \text{tr} \hat{V}_1 (\hat{k} - \hat{q} + m) \hat{V}_2 (\hat{k} + m) g = \text{tr} \hat{V}_1 \hat{V}_2 (M^2 - m^2) + 4(V_1 p)(V_2 p) ;$$

where  $p$  is the relative quark-antiquark momentum [see (4.15)]. Note that in the antiquark propagator we replaced  $\hat{k} - \hat{q} \rightarrow \hat{k} - \hat{q}$ , since the antiquark is now put on mass shell. Besides, we explicitly used here gauge condition  $(qV) = 0$ , which means that polarization vectors must be written for on mass shell  $q\bar{q}$  pair, not the vector meson, | another important consequence of our approach. Substituting this into (4.25), one gets

$$1 = \frac{N_c}{(2\pi)^3} \int^z d^2k \frac{dz}{z(1-z)} j^2 j^h [M^2(V_1 V_2) - 4(V_1 p)(V_2 p)] : \quad (4.26)$$

A prominent feature of this equation is the orthogonality of  $V_L$  and  $V_T$  polarization states | the necessary condition for any normalization prescription.

The next step is to realize that the integral can be cast in the form of  $d^3p$  integration by means of

$$\frac{dz}{z(1-z)} d^2k = \frac{4}{M} dp_z d^2p = \frac{4}{M} d^3p :$$

Thus, the final expression for normalization condition is

$$1 = \frac{N_c}{(2\pi)^3} \int^z d^3p \frac{4}{M} j^2 j^h [M^2(V_1 V_2) - 4(V_1 p)(V_2 p)] : \quad (4.27)$$

We see that the expression being integrated is explicitly spherically non-symmetric, which is a manifestation of a certain D-wave admixture. Thus we now apply projector technique to obtain results for S and D-wave states.



#### 4.5.2 Normalization for S wave vector meson

The correct expressions for pure S/D type vertices can be readily obtained with the aid of projector technique. Namely, to obtain an expression for S wave, replace

$$V \rightarrow V_S : \quad (4.28)$$

Such a replacement for  $V_1$  leads to

$$M^2 (V_1 V_2) - 4 (V_1 p) (V_2 p) = M^2 (V_1 V_2) - \frac{4M}{M + 2m} (V_1 p) (V_2 p)$$

Then, one applies the same replacement to  $V_2$  to obtain

$$M^2 (V_1 V_2) - \frac{4M}{M + 2m} (V_1 p) (V_2 p) = M^2 (V_1 V_2) :$$

Therefore, the answer for S wave states reads

$$1 = \frac{N_c}{(2\pi)^3} \int d^3p \, 4M \, j^S(p^2) f \quad (4.29)$$

which is manifestly spherically symmetric.

#### 4.5.3 Normalization for D wave vector meson

Results for D wave states are derived in the same way. The replacements  $V \rightarrow V_D$  lead to

$$M^2 p^4 (V_1 V_2) + 3M^2 p^2 (V_1 p) (V_2 p) : \quad (4.30)$$

After angular averaging

$$\langle p_i p_j \rangle = \frac{1}{3} p^2 \delta_{ij}$$

one gets the normalization formula for D wave state:

$$1 = \frac{N_c}{(2\pi)^3} \int d^3p \, 8M \, p^4 j^D(p^2) f \quad (4.31)$$

Several remarks are in order. First, S wave  $\rightarrow$  D wave transitions are forbidden. Indeed, such an amplitude will be proportional to

$$M^2 [p^2 (V_1 V_2) + 3 (V_1 p) (V_2 p)] : \quad (4.32)$$

which vanishes after angular integration. Then, we emphasize that the structure of results (4.29), (4.30), (4.32) is absolutely identical to Eq.(4.19). This fact can be viewed as the proof that spinorial structures (4.21), (4.22) indeed correspond to pure S and D wave states.

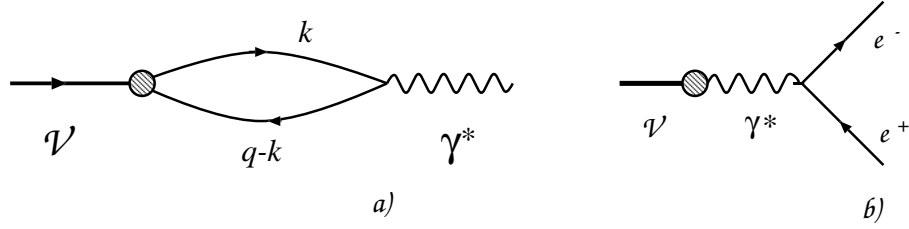


Figure 4.4: Normalizing LCWF to  $(V \rightarrow e^+ e^-)$  decay width: (a) the diagram for  $V \rightarrow \gamma^*$  transition, (b) the diagram for  $V \rightarrow e^+ e^-$  decay.

## 4.6 Decay constant

An additional normalization condition consists in relating the vector meson wave function to the experimentally measurable physical quantity  $\Gamma(V \rightarrow e^+ e^-)$  decay width (Fig.4.4). The loop at Fig.4.4a describes transition  $V \rightarrow \gamma^*$  and enters the amplitude of the decay  $V \rightarrow e^+ e^-$  (Fig.4.4b). Let us define the decay constant via relation

$$A = i e_0 j^\mu \epsilon_\mu = i f_V g_V \frac{p}{4} V : \quad (4.33)$$

So defined  $f_V$  has dimension  $\dim[f_V] = m^{-1}$ . The quantity  $g_V$  reflects the flavor content of a vector meson (in the previous calculations it simply gave unity) and is equal to

$$g_V = \frac{1}{\sqrt{2}}; \frac{1}{\sqrt{3}}; \frac{1}{\sqrt{2}}; \frac{1}{\sqrt{3}} \quad (4.34)$$

for  $\pi; \rho; \omega; \eta$  mesons correspondingly.

Knowing that such a loop does not mix polarization states, we can multiply both sides of eq.(4.33) by  $V$  and get the expression

$$i f_V = \frac{(1)}{(2)^4} N_c \int d^4 k \frac{\text{Sp} \{ i \hat{V} \frac{\hat{k} (+m)}{(k^2 - m^2 + i)} \hat{V} \frac{\hat{k} (-m)}{(k^2 - m^2 + i)} \}}{(k^2 - m^2 + i)} : \quad (4.35)$$

Calculations similar to the above normalization condition derivation yield (for the naive type of vertex)

$$f_V = \frac{N_c}{(2)^3} \int \frac{dz}{z(1-z)} d^3 k_V [M^2(VV) - 4(Vp)(Vp)] : \quad (4.36)$$

Applying now the projector technique, one gets in the case of S states (after proper angular averaging)

$$f^{(S)} = \frac{N_c}{(2)^3} \int d^3 p \frac{8}{3} (M + m) \quad (4.37)$$

and in the case of D wave states

$$f^{(D)} = \frac{N_c}{(2)^3} \int d^3 p \frac{32}{3} \frac{p^4}{M + 2m} : \quad (4.38)$$

Finally, one can write down the expression for the decay width in terms of  $f_V$  :

$$\Gamma(V \rightarrow e^+ e^-) = \frac{1}{32\pi^2 m_V^2} \frac{m_V}{2} 4 \mathcal{A}^2 = \frac{4}{3m_V^3} \frac{f_V^2}{4} : \quad (4.39)$$

This formula can be used to extract the numerical value of  $f_V$  from experimental data.

## 4.7 Ansatz for LCWF

Later on, we will be presenting numerical analyses of vector meson production cross sections, for which we will need some wave function Ansatz. Here we describe two forms of the wave function that will be exploited there. By no means should they be expected to accurately represent the true radial wave functions in a vector meson. Our Ansätze are pure guesses, based on non-relativistic quantum mechanical experience, of how the wave function might look like. Undoubtedly, such an approach involved a certain degree of ambiguity to the numerical results, and in our subsequent analysis we will study this ambiguity in detail.

### 4.7.1 Suppressed Coulomb wave functions

A first guess for the vector meson wave function, especially in the case of heavy non-relativistic meson, would be a Coulomb-like form, similar to wave function of a positronium :

$$\psi(p) \propto \frac{1}{(1 + p^2 a^2)^2} ; \quad (4.40)$$

where  $a$  is a typical size of the meson.

However, such a hard wave function will not fit our course of calculations, since the expression for the decay constant will be ultra-violet divergent. Furthermore, as we will see later, this hard wave function will lead to the vector meson production amplitudes saturated not at the scale  $p^2 < 1/a^2$ , but will extend to  $1/a^2 < p^2 < Q^2$ .

Thus, it appears that the hard wave function Ansatz leads to complications, which do not seem to be resolvable within the lowest Fock state only. Therefore, starting from now, we will limit ourselves to the soft wave function Ansatz only, "soft wave function" meaning that all integrals of physically relevant amplitudes involving the wave function will be saturated by  $p^2 < 1/a^2$ .

If we still prefer to have a Coulomb-like wave function, we can consider its slightly regularized form, which we will call the "suppressed Coulomb" wave function. Besides, in order to be able to conduct simple estimates, we will take as simple form as possible. So, in this ansatz the normalized wave functions read

$$\begin{aligned} \psi_{1S}(p^2) &= \sqrt{\frac{C_1}{M}} \frac{1}{(1 + a_1^2 p^2)^2} ; \\ \psi_{2S}(p^2) &= \sqrt{\frac{C_2}{M}} \frac{(1 - \text{node}) a_2^2 p^2}{(1 + a_2^2 p^2)^3} ; \\ \psi_D(p^2) &= \sqrt{\frac{C_D}{M}} \frac{1}{(1 + a_D^2 p^2)^4} : \end{aligned} \quad (4.41)$$

with normalization constants to be determined from Eqs.(4.29) and (4.31). Here parameters  $a_i$  are connected to the size of a bound system: in the coordinate representation  $\psi_i / \exp(-r/a_i)$ . For strict Coulomb functions one would have  $a_D = 3a_2 = 2 = 3a_1 = R_{\text{Bohr}}$ , where  $R_{\text{Bohr}}$  is the Bohr radius. However, this relation should be treated with care in the case of  $q\bar{q}$  quarkonia, where the quark-antiquark potential is quite complicated and therefore  $a_i$  should rather be considered as free parameters. Value of  $n_{\text{node}}$  pinpoints the position of the node in the 2S radial wave function. For the pure Coulombic system  $n_{\text{node}} = 1$ , but in our case the exact value of  $n_{\text{node}}$  should be obtained from the requirement of the orthogonality between 1S and 2S states with  $a_1$  and  $a_2$  fixed from other requirements.

#### 4.7.2 Oscillator type LCWF

By oscillator-type wave function we mean

$$\psi(p) \propto \exp\left(-\frac{p^2 a^2}{2}\right);$$

with  $a$  again being a typical size of the wave function. This wave function Ansatz corresponds to the case of a strong confinement. Although the approximately quadratic potential that leads to such an abrupt decrease at  $p^2 > 1/a^2$  is not exactly what is suspected about the color-singlet static quark-antiquark potential (in the quenched approximation), these wave function still possess the main confinement-like properties.

In this ansatz one has

$$\begin{aligned} \psi_{1S} &= c_1 \exp\left(-\frac{p^2 a_1^2}{2}\right); \\ \psi_{2S} &= c_2 \exp\left(-\frac{p^2 a_2^2}{2}\right) \exp\left(-\frac{p^2 a_2^2}{2}\right); \\ \psi_D &= c_D \exp\left(-\frac{p^2 a_D^2}{2}\right); \end{aligned} \quad (4.42)$$

Note again that for purely oscillator potential one also has relation  $a_D = a_2 = a_1$ , which might not hold in our case, since the oscillator type potential is also a crude approximation of the true quark-antiquark interaction. The position of node  $n_{\text{node}}$  would be equal to 3/2 for pure oscillator model, but again in our case its value can turn out different.

# Chapter 5

## Vector meson production amplitudes

### 5.1 Preliminary notes

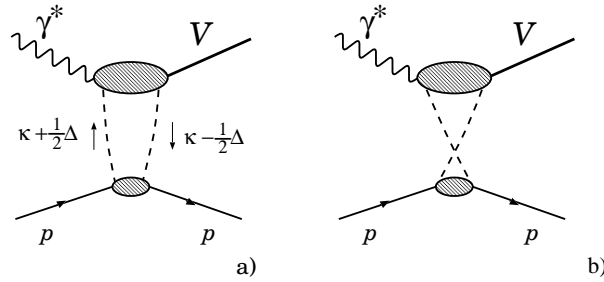


Figure 5.1: The QCD inspired diagrams for  $\gamma^* p \rightarrow V p$  process with two gluon t-channel. Only Diagram (a) does contribute to the imaginary part of amplitudes.

Having set up the notation and defined and described a vector meson by itself, we are now ready to evaluate the full set of amplitudes of its off-forward virtual diffractive photoproduction.

In the pQCD motivated approach to this process the pomeron exchange is viewed as a two-gluon exchange as it is shown in Fig. 5.1a. Using the scalarization procedure, we will split the diagram into 2 pieces and will treat each of them separately. The upper blob describes the pomeron-assisted transition of the virtual photon into a vector meson. In the perturbative QCD approach, which is legitimate here due to the presence of the relevant hard scale  $\bar{Q}^2 = m_q^2 + z(1-z)Q^2$ , the quark antiquark pair of the virtual photon interacts with two hard gluons and then fuses to produce a vector meson. This interaction is described by four diagrams given in Fig. 5.2, with all possible two-gluon attachments to qq pair taken into account. All of them are equally important and needed for maintaining gauge invariance and color transparency. The latter property means that in the case of very soft gluons the upper blob must yield zero, for the qq pair is colorless.

The lower part of the general diagram Fig. 5.1a is of course not computable in pQCD. The physically meaningful procedure is to relate it to the experimentally measurable gluon density. To do so, we will first calculate this lower blob in the Born approximation and then give a prescription how to introduce the unintegrated gluon density. In the course of this procedure,

we will neglect in the intermediate calculations proton off-forwardness and take it into account only at the very end, as a certain factor to the unintegrated gluon density.

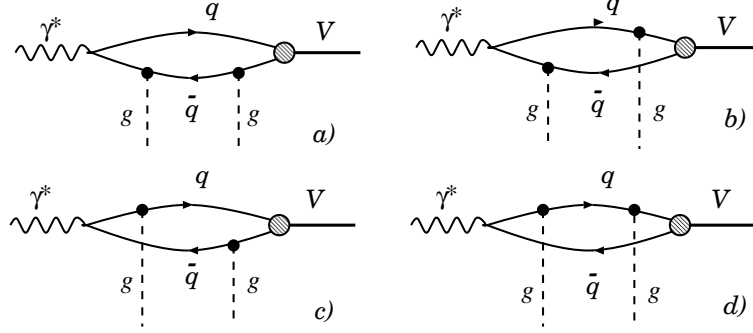


Figure 5.2: The content of the upper blob in Fig 5.1a in the pQCD approach. The true vector meson internal structure is approximated by qq Fock state.

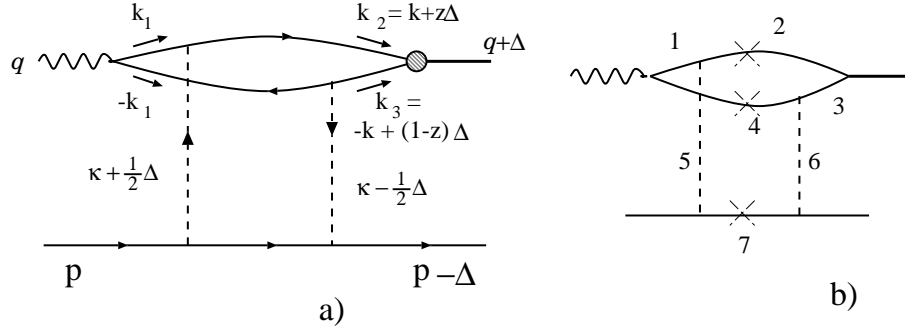


Figure 5.3: (a): A particularly useful convention of the loop momenta (only transverse components of quark momenta are shown). (b): the propagator notation used while calculating denominators. The crosses denote on-shell particles.

## 5.2 Notation and helicity amplitudes

In our calculation we will use the following Sudakov's decomposition (see also Fig 5.3a)

$$\begin{aligned}
 k &= y p^0 + z q^0 + \tilde{k} ; \\
 &= p^0 + q^0 + \sim ; \\
 &= p^0 + q^0 + \sim
 \end{aligned}
 \tag{5.1}$$

Here  $k$  and  $\tilde{k}$  are momenta that circulate in the quark and gluon loops respectively;  $\sim$  is the momentum transfer. Vectors  $p^0$  and  $q^0$  denote the light-cone momenta: they are related to the proton and virtual photon momenta as

$$p = p^0 + \frac{m_p^2}{s} q^0; \quad q = q^0 - x p^0; \quad q^2 = p^2 = 0; \quad x = \frac{Q^2}{s} \ll 1; \quad s = 2(p^0 q^0); \tag{5.2}$$

As it was mentioned in the Introduction, the condition  $x \ll 1$  is necessary to speak about diffractive processes. The longitudinal momentum transfer can be readily found from kinematics (see Fig.5.1). To the higher powers terms it reads

$$\begin{aligned} m_p^2 = p^2 = (p^0)^2 &= m_p^2 - 2(p^0) + \tilde{p}^2; \quad = \frac{\tilde{p}^2}{s}; \\ m_v^2 = (q^0)^2 &= Q^2 + 2(q^0) + \tilde{q}^2; \quad = x + \frac{m_v^2 + \tilde{q}^2}{s}; \end{aligned} \quad (5.3)$$

The **nal** vector meson momentum reads:

$$q_v = q^0 + \frac{m_v^2 + \tilde{q}^2}{s} p^0 + \tilde{q} : \quad (5.4)$$

Finally, throughout the text transverse momenta will be marked by the vector sign as  $\vec{k}$  and 3D vectors will be written in bold.

There are several possible helicity amplitudes in the transition  $! V_v$ . First of all, both photon and vector meson can be transversely polarized. The polarization vectors are

$$e_T = e; \quad V_T = \vec{V} + \frac{2(\tilde{V})}{s} (p^0 - q^0) : \quad (5.5)$$

Note that we took into account the fact that the vector meson momentum has finite transverse component  $\tilde{q}$ . Then, the virtual photon can have the scalar polarization (which is often called longitudinal; we will use both terms) with polarization vector

$$e_0 = \frac{1}{Q} (q^0 + x p^0) : \quad (5.6)$$

Finally, the longitudinal polarization state of a vector meson is described by

$$V_L = \frac{1}{M} @ q^0 + \frac{\tilde{q}^2}{s} M^2 p^0 + \tilde{q} : \quad (5.7)$$

Note that, as we already mentioned, in the self-consistent approach we must take the running polarization vector for the longitudinal polarization state. It depends on  $M$ , not  $m_v$ , which reflects the fact that in our approach we first calculate the production of an on-shell  $q\bar{q}$  pair with (whose dynamics is governed by  $M$ ) and then projects it onto the physical vector meson. We stress that this projection will automatically arise in the course of usual Feynman diagram evaluation.

Thus, there are 5 different amplitudes:

$$\begin{aligned} L ! L \\ T ! T ( = v ) \\ T ! L \\ L ! T \\ T ! T ( = v ) \end{aligned} \quad (5.8)$$

The first two are helicity conserving amplitudes. They are dominant and almost insensitive to the momentum transfer  $\tilde{t}$ . The next two are single helicity flipping amplitudes. They are unavoidably proportional to  $\tilde{t}$  in the combination  $(\epsilon \tilde{\gamma})$  or  $(\nabla \tilde{\gamma})$  and would be vanishing for the strictly forward scattering. Finally, the last amplitude corresponds to the double helicity flip and will be proportional to  $(\epsilon \tilde{\gamma})(\nabla \tilde{\gamma})$ .

## 5.3 General amplitude

We will take diagr.(c) at Fig 5.2 (it is shown in Fig 5.3) as a generic diagram and perform a thorough analysis for it. It turns out that the other diagrams are calculated in the same fashion.

The general expression for the amplitude given by diagr.(c) reads:

$$iA = \int \frac{d^4 k}{(2\pi)^4} \int \frac{d^4 p}{(2\pi)^4} u_p^0 (\gamma^0 t^B)^i \frac{\hat{p} \cdot \hat{1} + m_p}{(p^2 - m_p^2 + i0)} (\gamma^0 t^A)^0 u_p^0$$

$$\left( \frac{-i}{2} \frac{g^{AA^0}}{2 + i} \right) \left( \frac{-i}{2} \frac{g^{BB^0}}{2 + i} \right) V_C$$

$$\frac{\text{Sp} \left[ \epsilon \epsilon^i \hat{k}_4 + m \right] (\gamma^0 t^B)^i (\hat{k}_3 + m) i \hat{V}^i (\hat{k}_2 + m) (\gamma^0 t^A)^i (\hat{k}_1 + m)^0}{[k_1^2 - m^2 + i0][k_2^2 - m^2 + i0][k_3^2 - m^2 + i0][k_4^2 - m^2 + i0]} \quad (5.9)$$

Here  $\alpha_V$  is the same as in (4.34) and  $\hat{V}$  is the familiar qq! V vertex function. Note that we introduced 'gluon mass' in gluon propagators to account for confinement at a phenomenological level.

Let's first calculate the numerator.

## 5.4 Color factor

If we consider strictly forward gluon scattering off a single quark, we have

$$\frac{1}{N_c} \text{Sp} t^B t^A g^{AA^0} g^{BB^0} \text{Sp} t^B t^A g = \frac{1}{N_c} \frac{1}{2} \text{Tr} t^A t^A = \frac{1}{N_c} \frac{N_c^2 - 1}{2} = \frac{1}{2} C_F = \frac{2}{3} \quad (5.10)$$

However, we should take into account that quarks are sitting inside a colorless proton, whose color structure is

$$\text{color} = \frac{1}{\sqrt{6}} \epsilon^{abc} q^a q^b q^c \quad (5.11)$$

In this case there are two ways a pair of gluons can couple 3 quark lines (see Fig 5.4). In the first way both gluons couple to the same quark. Since the quark momentum does not change after these two interactions, the nucleon stays in the same state:  $\langle N | N \rangle = 1$ . In the second case gluon legs are attached to different quark lines, so that extra momentum circulates between quarks, which gives rise to the factor  $\langle N | \exp(i \mathbf{r}_1 \cdot \mathbf{p} - i \mathbf{r}_2 \cdot \mathbf{p}) | N \rangle$ , i.e. to the two-body form factor. Therefore, for the lower line instead of

$$\frac{1}{N_c} \text{Sp} t^B t^A g = \frac{1}{N_c} \frac{1}{2} \text{Tr} t^A t^A \quad (5.12)$$



one has

$$\begin{aligned}
& \frac{1}{6} \text{abc} \ 3 \ t_{aa^0 bb^0}^A t_{cc^0}^B + 6 \ t_{aa^0}^A t_{bb^0}^B \text{hN jexp}(i \ r_1 \ - \ i \ r_2) \text{N i} \ a^0 b^0 c^0 \\
&= \text{Spft}^A t^B g \ - \ \text{Spft}^A t^B g \text{hN jexp}(i \ r_1 \ - \ i \ r_2) \text{N i} \\
&= \frac{1}{2} \ t_{AB} (1 \ - \ \text{hN jexp}(i \ r_1 \ - \ i \ r_2) \text{N i}) :
\end{aligned} \tag{5.13}$$

Note also that a similar calculation for  $N_c$  number of colors would yield the same result. Thus, the overall color factor is

$$\frac{1}{2} C_F N_c V( ) = 2V( ) \ - \ \frac{1}{2} C_F N_c (1 \ - \ \text{hN jexp}(i \ r_1 \ - \ i \ r_2) \text{N i}) : \tag{5.14}$$

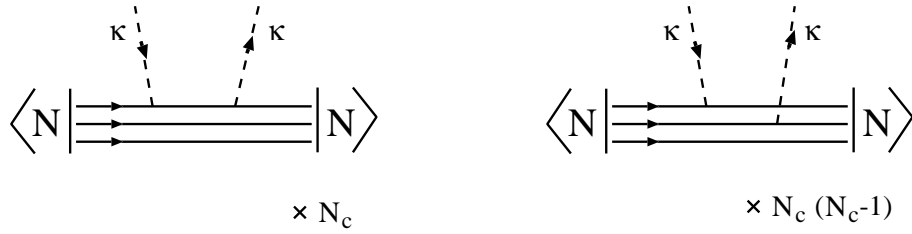


Figure 5.4: The ways two glons can couple a colorless nucleon.

## 5.5 Scalarization of upper and lower parts

As known, the highest power  $s$  contribution comes from so-called nonsense components of gluon propagator (density matrix) decomposition:

$$g_{\mu\nu} = \frac{2p^0 q^0}{s} + \frac{2p^0 q^0}{s} + g^2_{\mu\nu} \ - \ \frac{2p^0 q^0}{s} : \tag{5.15}$$

The lower (proton) line gives then

$$u^0(p) \ \hat{q}^0 \ (\hat{k}_1 + m_p) q^0 \ u(p) \tag{5.16}$$

To the highest power  $s$  order, it can be rewritten as

$$u_p^0 \hat{q}^0 \hat{q}^0 u_p \text{forward} = \frac{1}{2} \text{Sp} \hat{p}^0 \hat{q}^0 \hat{q}^0 g = s^2 : \tag{5.17}$$

As we mentioned, the effect of off-forwardness (skewedness) will be taken into account later. So, combining all factors, one has for numerator of Eq.(5.9)

$$\begin{aligned}
& (4 \ s)^2 \ P \ \frac{1}{4 \ \text{em}} \ C_V \ \frac{1}{2} C_F N_c V( ) \ \frac{4}{s^2} s^2 \ \text{Sp}^n (\hat{k}_4 + m) q^0 (\hat{k}_3 + m) \hat{V} \ (\hat{k}_2 + m) q^0 (\hat{k}_1 + m) \\
&= (4 \ s)^2 \ P \ \frac{1}{4 \ \text{em}} \ C_V \ \frac{1}{2} C_F N_c V( ) \ \frac{4}{s^2} s^2 \ \text{Tr} ( \hat{1} \ - \ V ) :
\end{aligned} \tag{5.18}$$

Note that we factored out  $2s^2$  from the trace because it will appear later in all trace calculations. So, the resulting expression for amplitude (5.9) looks like

$$A = \frac{1}{4} \frac{1}{\epsilon_m} 4C_F N_c s^2 \alpha_V \int \frac{d^4 k}{(2\pi)^4} \int \frac{d^4}{(2\pi)^4} \frac{(4-s)^2 V(\dots)}{(p_1)^2 (m_p^2 + i) [\frac{1}{2}^2 + i] [\frac{2}{2}^2 + i]} \frac{I^{(c)}(\dots V)}{[k_1^2 + m^2 + i] [k_2^2 + m^2 + i] [k_3^2 + m^2 + i] [k_4^2 + m^2 + i]} \quad (5.19)$$

One can now immediately write similar expressions for the other three diagrams (Fig. 5.2 a,b,d). Indeed, they will differ from Eq.(5.19) only by the last line: they will have different expressions for traces and propagator structures (i.e. the exact values for  $k_i$ ).

## 5.6 Denominator evaluation

Now we turn to the calculation of denominators. As usual, we implement Sudakov's decomposition (5.1) and make use of relation

$$d^4 k = \frac{1}{2} s dy dz d^2 \tilde{k} :$$

The physical picture of the way we will do the resulting integrals is the following. We are interested only in the imaginary part of these diagrams. In fact, it can be shown that at the level of accuracy used here the diagram in Fig. 5.1a gives rise only to the imaginary part of the amplitude. The real part is given by Fig. 5.1b and can be readily found from analyticity (so that here is no need for additional calculations), however it turns out small due to smallness of pomeron intercept, so we will neglect it in our subsequent calculations.

The imaginary part is computed by setting three particles in the s-channel cut on mass shell (this is illustrated in Fig. 5.3b). One way to do so is to apply Cutkosky rule to modify our expression. Another, more straightforward and 'honest' way is to calculate three of the integrals (namely, over  $\tilde{k}$ ;  $y$ ) via residues. That's what we are going to do.

The details of this calculations are given in Appendix A. Here we cite the result:

$$\begin{aligned} & \int dy dz d^2 \tilde{k} \frac{1}{[all propagators]} \\ &= \frac{i}{s} \frac{2-i}{s} \int \frac{dz}{z(1-z)} V(z; \tilde{k}^2) \frac{1}{[k_1^2 + m^2 + z(1-z)Q^2]} \frac{1}{(\tilde{k}^2 + \frac{1}{2})^2} \end{aligned} \quad (5.20)$$

Here  $k_1$  is the transverse momentum flowing through photon vertex along the fermion line. Particularly, for diagr.(c) it is equal to  $k_1 = \tilde{k} - (1-z)\tilde{k} \sim \tilde{k}_2$  (with the specific quark loop momentum choice given at Fig.(5.3a)).

Thus, the amplitude for diagr.(c) has the form

$$A = \frac{1}{4} \frac{1}{\epsilon_m} 4C_F N_c s^2 \alpha_V \frac{1}{2} s \frac{1}{2} s \frac{i}{s} \frac{2-i}{s} \frac{1}{(2\pi)^8} \int \frac{dz}{z(1-z)} d^2 \tilde{k} V(z; \tilde{k}^2) \int \frac{d^2 \tilde{k} V(\dots)}{(\tilde{k}^2 + \frac{1}{2})^2} (4-s)^2 \frac{I^{(c)}}{[k_1^2 + m^2 + z(1-z)Q^2]} : \quad (5.21)$$

After bringing all coefficients together, one gets

$$A^{(a)} = \frac{C_F N_c G_V^2}{64 \pi^5} \int_0^1 \frac{dz}{z(1-z)} d^2 \tilde{k}_\perp V(z; \tilde{k}^2) \frac{d^2 \tilde{V}(\tilde{q})}{(\tilde{q}^2 + \tilde{q}_\perp^2)^2} (4 - s)^2 \frac{I^{(c)}}{\tilde{k}_1^2 + m^2 + z(1-z)Q^2} : \quad (5.22)$$

The other diagrams are calculated in the same way. The most important difference is that for each diagram we will have a propagator  $1/[\tilde{k}_1^2 + m^2 + z(1-z)Q^2]$  with its own definition of  $\tilde{k}_1$ , the transverse momentum in photon vertex:

$$\begin{aligned} \text{diagram 1a: } \tilde{k}_{1a} &= \tilde{k} - (1-z)\tilde{\gamma} = \tilde{x} - \frac{1}{2}\tilde{\gamma} \\ \text{diagram b: } \tilde{k}_{1b} &= \tilde{k} - (1-z)\tilde{\gamma} + \tilde{\gamma} + \frac{1}{2}\tilde{\gamma} = \tilde{x} + \tilde{\gamma} \\ \text{diagram c: } \tilde{k}_{1c} &= \tilde{k} - (1-z)\tilde{\gamma} - \tilde{\gamma} + \frac{1}{2}\tilde{\gamma} = \tilde{x} - \tilde{\gamma} \\ \text{diagram d: } \tilde{k}_{1d} &= \tilde{k} + z\tilde{\gamma} = \tilde{x} + \frac{1}{2}\tilde{\gamma} \end{aligned} \quad (5.23)$$

Here  $\tilde{x} = \tilde{k} - (1-2z)\tilde{\gamma} = 2$ . Thus, the whole expression for the imaginary part of the amplitude is

$$A = \frac{C_F N_c G_V^2}{64 \pi^5} \int_0^1 \frac{dz}{z(1-z)} d^2 \tilde{k}_\perp V(z; \tilde{k}^2) \frac{d^2 \tilde{V}(\tilde{q})}{(\tilde{q}^2 + \tilde{q}_\perp^2)^2} (4 - s)^2 \left[ \frac{1}{z} \frac{I^{(a)}}{\tilde{k}_{1a}^2 + m^2 + z(1-z)Q^2} + \frac{I^{(b)}}{\tilde{k}_{1b}^2 + m^2 + z(1-z)Q^2} + \frac{I^{(c)}}{\tilde{k}_{1c}^2 + m^2 + z(1-z)Q^2} + \frac{z}{1-z} \frac{I^{(d)}}{\tilde{k}_{1d}^2 + m^2 + z(1-z)Q^2} \right] : \quad (5.24)$$

## 5.7 0<sup>+</sup>-forward gluon density

In Sect. 2.4 we discussed the forward unintegrated gluon density  $F(x_g; \tilde{\gamma})$  and developed a prescription (see Eq.(2.39)) how to introduce it into the  $k_t$ -factorization calculations. Being devised for forward scattering processes only, this gluon density bears a clear probabilistic sense, which is in fact reflected in the word 'density'.

In the present case of vector meson production, the initial and final states are kinematically distinct, therefore the forward unintegrated gluon density in its pure form is not the relevant quantity; instead, 0<sup>+</sup>-forward (or skewed) gluon structure function [28]

$$F(x_1; x_2; \tilde{\gamma}; \tilde{\gamma}) \quad (5.25)$$

should be used. It depends on the lightcone momenta  $x_1$  and  $x_2$  carried by the first and the second gluon, on the transverse momentum  $\tilde{\gamma}$  inside the gluon loop, and on the total transverse momentum transfer  $\tilde{\gamma}$ . At  $x_1 = x_2$  and  $\tilde{\gamma} = 0$ , the forward gluon structure function is recovered, which means that even the strictly forward vector meson production should be described by 0<sup>+</sup>-forward gluon structure function.

The experimental determination of the  $\phi$ -forward gluon density might be in principle possible from accurate measurements of the  $\phi$ -forward virtual Compton scattering process, but the lack of such measurements makes this analysis not feasible in the nearest future. Thus, the original idea to involve in the vector meson calculations as little ambiguity as possible by determining the gluon content of the proton from other reactions does not work. One might of course expect that replacement

$$F(x_1; x_2; \tilde{\gamma}; \tilde{\gamma}) \rightarrow F\left(\frac{x_1 + x_2}{2}; \tilde{\gamma}\right) \quad (5.26)$$

should be quite legitimate in kinematical regimes when  $x_1 \approx x_2$ ,  $\tilde{\gamma} \approx \tilde{\gamma}$ . However, such a regime takes place only in the photoproduction of light mesons and is severely violated as we go to higher  $Q^2$  or higher  $m_V$ , therefore such a replacement would be a poor option for the most of the case we study.

There is however way around, which allows us to reduce the unknown  $\phi$ -forward gluon distributions to the forward ones. As shown in [29], if the energy behavior of the gluon densities is describable by a simple Regge-type behavior

$$F \sim \frac{1}{x} \quad (5.27)$$

then in the case  $x_1 \approx x_2$  the  $\phi$ -forward unintegrated gluon structure functions can be related to the forward unintegrated gluon density according to

$$F(x_1; x_2; 0; \tilde{\gamma}; \tilde{\gamma}; 0) = R_g F(x; \tilde{\gamma}); \quad R_g = \frac{2^{2+\gamma} (\gamma + \frac{5}{2})}{\gamma + 4} : \quad (5.28)$$

Bearing this exact result in mind, one can hope that a similar relation will hold for gluon densities with a somewhat more complicated energy behavior, if the effective exponent is calculated in the vicinity of the kinematical point  $x_1; \tilde{\gamma}$ .

Note that for the purposes of approximate numerical calculation correspondence (5.28) can be further simplified. Introduce an argument shift  $c(\gamma)$  such that

$$F(x_1; 0; \tilde{\gamma}; 0) / \frac{2^{2+\gamma} (\gamma + \frac{5}{2})}{\gamma + 4} \frac{1}{x_1} = \frac{1}{c(\gamma) x_1} \quad (5.29)$$

holds for all  $x_1$ . Simple arithmetics shows that  $c(\gamma)$  changes from 0.435 at  $\gamma = 0$  to 0.4 at  $\gamma = 1$ . Given this very flat dependence, we can approximate  $c(\gamma)$  by a constant value 0.41 so that

$$F(x_g; 0; \tilde{\gamma}; 0) = F(0.41 x_g; \tilde{\gamma}) : \quad (5.30)$$

This form will be used in our numerical calculations.

The effect of non-zero  $\tilde{\gamma}$  comes both from the Pomeron-exchange and from the proton in part factor. Since Pomeron singularity moves in complex  $j$  plane as  $j = \tilde{\gamma}^2$  changes, the value of the effective Pomeron intercept will be affected by  $\tilde{\gamma}^2$ , a customary representation of this effect (in the linear Regge trajectory approximation) being

$$\alpha_P(\tilde{\gamma}^2) = \alpha_P(0) + \beta_P \tilde{\gamma}^2 : \quad (5.31)$$

Although in our case the effective intercept of the gluon density is not an input number, but is generated dynamically, we still account for the above effect by multiplying the gluon density by factor

$$\exp^{h_p} \sim^2 \log(x_0=x) ; \quad (5.32)$$

with  $x_0 = 0.03$  and trajectory slope  $b_p$  being different for hard ( $x_p^{\text{hard}} = 0.07$ ) and soft ( $x_p^{\text{soft}} = 0.15$ ) parts of the gluon density. Since the resulting contribution to the slope increases with energy growth, this effect is called the diffractive cone shrinkage.

The second and the most significant effect of non-zero  $\tilde{t}$  comes from the proton impact factor. Effectively, it amounts to introduction of a proton form factor  $F(\tilde{t})$ , which would be equal to 1 at  $\tilde{t} = 0$  and would start significantly decreasing when  $\tilde{t}$  grows larger than a certain scale  $1 = \frac{2}{p}$ . In our numerical calculations we used the dipole form factor

$$F(\tilde{t}) = \frac{1}{1 + \tilde{t}^2 = \frac{2}{p}} \quad (5.33)$$

with  $\frac{2}{p} = 1 \text{ GeV}^2$ .

## 5.8 Final results for the naive vertex

Now, with the off-forward gluon structure function properly defined, the only thing left to be computed is integrands  $I^i(\tilde{t} \neq V)$ . For convenience, their calculation is also given in Appendix B. It turns out that the results can be written in the same way for all four diagrams via  $K_1$  given by (5.23), i.e. all quantities:

$$\frac{1}{z} I^{(a)} ; \quad I^{(b)} ; \quad I^{(c)} ; \quad \frac{z}{1-z} I^{(d)}$$

can be written in a similar way:

$$\begin{aligned} T &= T^h (eV)(m^2 + KK_1) + (V\bar{K})(eK_1)(1-2z)^2 (K)(V\bar{K}_1) \\ L &= L^h 4z^2(1-z)^2 QM \\ T &= L^h 2z(1-z)M (K_1)(1-2z) \\ L &= T^h 2z(1-z)Q(1-2z)(\bar{K}) \end{aligned}$$

Therefore, we can cast amplitude (5.24) in a compact form with aid of functions  $\tilde{t}_1$  and  $\tilde{t}_2$ :

$$\tilde{t}_2 = \frac{1}{(x + \tilde{t})^2 + \bar{Q}^2} - \frac{1}{(x - \tilde{t})^2 + \bar{Q}^2} + \frac{1}{(x + \tilde{t}=2)^2 + \bar{Q}^2} + \frac{1}{(x - \tilde{t}=2)^2 + \bar{Q}^2} \quad (5.34)$$

and

$$\tilde{t}_1 = \frac{x + \tilde{t}}{(x + \tilde{t})^2 + \bar{Q}^2} - \frac{x - \tilde{t}}{(x - \tilde{t})^2 + \bar{Q}^2} + \frac{x + \tilde{t}=2}{(x + \tilde{t}=2)^2 + \bar{Q}^2} + \frac{x - \tilde{t}=2}{(x - \tilde{t}=2)^2 + \bar{Q}^2} \quad (5.35)$$

With these functions, for the naive qqV vertex the whole expression in square brackets in (5.24) with sign minus (which we denote here as  $I_{-V}$ ) has the form :

$$\begin{aligned} I_{LL} &= 4QM^2(1-z)^2; \\ I_{TT} &= (eV)[m^2 + (K_1)] + (1-2z)^2(KV)(e_1) - (K)(V_1); \\ I_{TL} &= 2Mz(1-z)(1-2z)(e_1); \\ I_{LT} &= 2Qz(1-z)(1-2z)(K)_2; \end{aligned} \quad (5.36)$$

Replacing  $V(\cdot)$  by the unintegrated gluon density according to (2.39) and using approximation for the on-forward gluon density (5.30), we obtain the final expressions for a general amplitude of reaction  $\pi^+ \rightarrow V_{-V}$  in the naive vertex:

$$A(x; Q^2; \gamma) = i s \frac{C_V}{4} \frac{p}{4} \frac{1}{z} \int_0^1 \frac{dz}{z(1-z)} d^2K(z; K) \frac{d^2\gamma}{\gamma^4} s F(x; \gamma; \gamma) I(-V);$$

(5.37)

## 5.9 Final results for S and D wave amplitudes

Now we can use projector technique to obtain results for S/D wave states.

$$\begin{aligned} V \rightarrow V S; S &= g \left( \frac{2p \cdot p}{m(M+2m)} \right) I^S = I + \frac{2(V \cdot p)}{m(M+2m)} p; \\ V \rightarrow V D; D &= p^2 g + \frac{(M+m)p \cdot p}{m} I^D = I p^2 + \frac{(M+m)(V \cdot p)}{m} p; \end{aligned} \quad (5.38)$$

Note that  $(V \cdot p)$  is 3D scalar product. While contracting, we encounter terms proportional to  $p$  which should be understood as

$$p = I_{V_T} fV \rightarrow pg + I_{V_L} f1 \quad V_z \rightarrow p_z \quad \frac{1}{2}(2z-1)Mg; \quad (5.39)$$

The result of this substitution reads:

for  $e_T$ :

$$\begin{aligned} I_{T \rightarrow T} fV \rightarrow pg + I_{T \rightarrow L} f1 \quad V_z \rightarrow p_z \quad \frac{1}{2}(2z-1)Mg \\ = m^2 (eK)_2 (e_1)(1-2z)^2 \end{aligned} \quad (5.40)$$

for  $e_0$ :

$$\begin{aligned} I_{L \rightarrow T} fV \rightarrow pg + I_{L \rightarrow L} f1 \quad V_z \rightarrow p_z \quad \frac{1}{2}(2z-1)Mg \\ = 2Qz(1-z)(2z-1)m^2_2 \end{aligned} \quad (5.41)$$

So, the resulting integrands for S wave type mesons are

$$\begin{aligned}
I_{L!L}^S &= 4QMz^2(1-z)^2 \left[ 1 + \frac{(1-2z)^2}{4z(1-z)} \frac{2m}{M+2m} \right] ; \\
I_{T!T}^S &= (\mathbf{e}\mathbf{V}) \cdot \mathbf{p}^2 \left[ m^2 + (\mathbf{k}\tilde{\mathbf{V}}_1) \right] + (1-2z)^2 (\mathbf{k}\mathbf{V}) \cdot (\mathbf{e}\tilde{\mathbf{V}}_1) \frac{M}{M+2m} \\
&\quad (\mathbf{e}\mathbf{k}) \cdot (\mathbf{V}\tilde{\mathbf{V}}_1) + \frac{2m}{M+2m} (\mathbf{k}\mathbf{e}) \cdot (\mathbf{k}\mathbf{V}) ; \\
I_{T!L}^S &= 2Mz(1-z)(1-2z) (\mathbf{e}\tilde{\mathbf{V}}_1) \cdot \mathbf{k} + \frac{(1-2z)^2}{4z(1-z)} \frac{2m}{M+2m} \frac{M-m}{M+2m} (1-2z) (\mathbf{e}\mathbf{k}) ; \\
I_{L!T}^S &= 2Qz(1-z)(1-2z) \mathbf{V} \cdot (\mathbf{k}) \frac{M}{M+2m} ; \tag{5.42}
\end{aligned}$$

and for D wave type mesons are

$$\begin{aligned}
I_{L!L}^D &= QMz(1-z) \mathbf{k}^2 \frac{4m}{M} p_z^2 ; \\
I_{T!T}^D &= (\mathbf{e}\mathbf{V}) \cdot \mathbf{p}^2 \left[ m^2 + (\mathbf{k}\tilde{\mathbf{V}}_1) \right] + (1-2z)^2 (\mathbf{p}^2 + m^2 + Mm) (\mathbf{k}\mathbf{V}) \cdot (\mathbf{e}\tilde{\mathbf{V}}_1) \\
&\quad p^2 (\mathbf{e}\mathbf{k}) \cdot (\mathbf{V}\tilde{\mathbf{V}}_1) - m(M+m) (\mathbf{k}\mathbf{e}) \cdot (\mathbf{k}\mathbf{V}) ; \\
I_{T!L}^D &= \frac{1}{2}M(1-2z) (\mathbf{e}\tilde{\mathbf{V}}_1) \cdot \mathbf{k}^2 \frac{4m}{M} p_z^2 + m(M+m) (\mathbf{e}\mathbf{k}) ; \\
I_{L!T}^D &= 2Qz(1-z)(1-2z) \mathbf{V} \cdot (\mathbf{k}) (p^2 + m^2 + Mm) ; \tag{5.43}
\end{aligned}$$

Equations (5.42), (5.43) together with expression (5.37) constitute the ultimate sets of all helicity amplitudes. They give explicit answers for the vector meson production amplitudes within leading-log-approximation.

## Chapter 6

# Analysis for heavy quarkonia

The general answers (5.42), (5.43) are of course incomprehensible at a quick glance. Therefore, a further analysis is needed to grasp the most vivid features of the results and to disentangle s-channel helicity conserving and double helicity flip amplitudes.

Since in the heavy vector mesons quarks can be treated non-relativistically, further simplifications in analytical formulas (5.42), (5.43) are possible due to the presence of an additional small parameter  $p^2/m^2$ .

In what follows we will first perform the twist expansion and then relate simplified amplitudes to the decay constants (4.37), (4.38). We will then analyze twist hierarchy of the amplitudes and compare results for S vs. D wave states. Though we perform this analysis for heavy mesons, we wish to stress that all qualitative features (S vs. D difference,  $Q^2$  dependence etc.) will hold for light quarkonia as well.

### 6.1 Twist expansion

Here we are going to expand the amplitudes (or to be more exact, the quantities  $\tilde{\gamma}_1$  and  $\tilde{\gamma}_2$  (5.34), (5.35)) in inverse powers of the hard scale  $\overline{Q}^2$  and then perform azimuthal angular averaging over  $\phi$ .

Expanding  $\tilde{\gamma}_2$  in twists in the main logarithmic region

$$\tilde{\gamma}_2; \sim^2; \tilde{\mathbf{k}}^2 \sim^2 \overline{Q}^2; \quad (6.1)$$

one observes that twist{1 terms cancel, so one has to retain twist{2 and twist{3 terms proportional  $\sim^2$ :

$$\tilde{\gamma}_2 = \frac{2\sim^2}{\overline{Q}^4} - \frac{8\sim^2 \mathbf{x}^2}{\overline{Q}^6} \quad (6.2)$$

The analogous decomposition for  $\tilde{\gamma}_1$  reads

$$\tilde{\gamma}_1 = \frac{4\sim^2}{\overline{Q}^4} - \frac{12\sim^2 \mathbf{x}^2}{\overline{Q}^6} - \frac{\sim^2 (\mathbf{x} \cdot \sim)}{\overline{Q}^4} \quad (6.3)$$

Note that the last term does not contain  $\sim^2$ . However, one must track it because it will be important in double helicity flip amplitudes.



## 6.2 Twist expansion for S wave type mesons

With the aid of this decomposition one obtains:

for amplitude  $L \rightarrow L$

$$I_{L \rightarrow L}^S = 4QMz(1-z)^2 \frac{2\tilde{z}^2}{Q^4} \left( 1 + \frac{(1-2z)^2}{4z(1-z)M+2m} \frac{2m}{M+2m} \right); \quad (6.4)$$

for amplitude  $T \rightarrow T$

$$I_{T \rightarrow T}^S = (e\tilde{V})^2 m^2 \frac{2\tilde{z}^2}{Q^4} + \frac{4\tilde{z}^2}{Q^2} K^2 + \frac{2m}{M+2m} \frac{1}{2} K^2 (e\tilde{V})^2 \frac{2\tilde{z}^2}{Q^4} \\ + (1-2z)^2 \frac{M}{M+2m} \frac{1}{4} K^2 (e\tilde{V})^2 \frac{2\tilde{z}^2}{Q^4} - \frac{K^2}{2Q^4} (e\tilde{V})^2 (\tilde{V} \cdot \tilde{V}) \left( 1 + \frac{6\tilde{z}^2(1-2z)^2}{Q^2} \right)^3 \quad (6.5)$$

This amplitude is naturally split into s-channel helicity conserving and double helicity flip parts

$$I_{T \rightarrow T}^S (\lambda = \lambda') = (e\tilde{V})^2 \frac{2\tilde{z}^2}{Q^4} m^2 + 2K^2(z^2 + (1-z)^2) + \frac{m}{M+2m} K^2 (1-2(1-2z)^2) \\ I_{T \rightarrow T}^S (\lambda = -\lambda') = 4z(1-z) (e\tilde{V})^2 (\tilde{V} \cdot \tilde{V}) \frac{K^2}{2Q^4} \left( 1 + \frac{6\tilde{z}^2(1-2z)^2}{Q^2} \right) + \frac{(1-2z)^2}{4z(1-z)M+2m} \frac{2m}{M+2m} \quad (6.6)$$

Finally, single spin flip amplitudes are

$$I_{L \rightarrow L}^S = 2Mz(1-z) (1-2z)^2 \frac{2\tilde{z}^2}{Q^4} (e\tilde{V})^2 \left( 1 + \frac{(1-2z)^2}{4z(1-z)M+2m} \frac{2m}{M+2m} \right); \\ I_{L \rightarrow T}^S = 2Qz(1-z) (1-2z)^2 \frac{2\tilde{z}^2}{Q^4} (\tilde{V} \cdot \tilde{V}) \frac{2K^2}{Q^2} \frac{M}{M+2m}; \quad (6.7)$$

## 6.3 Twist expansion for D {type vector mesons

Here we will need to track higher twist terms. It will turn out later that leading contributions vanish, so twist 3 terms will be crucial for our results.

For amplitude  $L \rightarrow L$  one has

$$I_{L \rightarrow L}^D = QMz(1-z) K^2 \left( \frac{4m}{M} p_z^2 \frac{2\tilde{z}^2}{Q^4} \otimes 1 + \frac{4K^2}{Q^2} A \right); \quad (6.8)$$

For  $T \rightarrow T$  amplitude, one obtains

$$I_{T \rightarrow T}^D = (e\tilde{V})^2 p^2 4m^2 \frac{2\tilde{z}^2}{Q^4} \otimes 1 + \frac{4K^2}{Q^2} A + \frac{2\tilde{z}^2}{Q^4} 2K^2 5 \\ + 4z(1-z) p_z^2 + (1-2z)^2 m(M+m) \left( \frac{2\tilde{z}^2}{Q^4} K^2 (e\tilde{V})^2 \frac{K^2}{2Q^4} (e\tilde{V})^2 (\tilde{V} \cdot \tilde{V}) \right) \left( 1 + \frac{6\tilde{z}^2(1-2z)^2}{Q^2} \right)^9; \\ m(M+m) \frac{1}{2} K^2 (e\tilde{V})^2 \frac{2\tilde{z}^2}{Q^4} \otimes 1 + \frac{4K^2}{Q^2} A \quad (6.9)$$

Note that we kept track of all terms  $\propto p^4$ . Again, one can separate out s-channel helicity conserving and double helicity flip parts:

$$\begin{aligned}
I_{T \rightarrow T}^D(\lambda = \lambda_V) &= (\vec{e} \cdot \vec{\nabla}) \frac{\tilde{p}^2}{Q^4} (2p^2 - m^2 + 2K^2 - 4\frac{m^2}{Q^2} - m(M + m)K^2) \frac{1}{Q^2} A \\
&\quad + K^2 - K^2 - \frac{4m}{M} p_z^2 \\
I_{T \rightarrow T}^D(\lambda = -\lambda_V) &= K^2 - \frac{4m}{M} p_z^2 - (\vec{e} \cdot \vec{\nabla}) \frac{K^2}{2Q^4} \left( 1 + \frac{6\tilde{p}^2(1 - 2z)^2}{Q^2} \right)
\end{aligned} \tag{6.10}$$

Finally, single helicity flipping amplitudes are

$$\begin{aligned}
I_{T \rightarrow L}^D &= \frac{1}{2} M (1 - 2z)^4 \frac{2(1 - 2z)(\vec{e} \cdot \vec{\nabla}) \tilde{p}^2}{Q^4} K^2 - \frac{4m}{M} p_z^2 + m(M + m) \frac{4\tilde{p}^2 K^2}{Q^6} (1 - 2z)(\vec{e} \cdot \vec{\nabla})^3 \\
&= \frac{\tilde{p}^2}{Q^4} (1 - 2z)^2 M (\vec{e} \cdot \vec{\nabla})^4 K^2 - \frac{4m}{M} p_z^2 - m(M + m) \frac{2K^2}{Q^2}^3; \\
I_{L \rightarrow T}^D &= 8Qz(1 - z)(1 - 2z)(p^2 + m^2 + mM) \frac{\tilde{p}^2}{Q^6} K^2 (\vec{\nabla} \cdot \vec{\nabla}) :
\end{aligned} \tag{6.11}$$

## 6.4 Final results for S wave mesons

In order to grasp the major features of various S and D wave amplitudes, further simplifications can be achieved if one neglects spherically non-symmetric arguments of  $\vec{s}$  and gluon density. First we rewrite general expression (5.37) in the more convenient form

$$A(\vec{x}; Q^2; \vec{\gamma}) = i s \frac{\alpha_V \frac{p}{4} \frac{\vec{\gamma}}{em}}{4^2} d^3 p \frac{4}{M} (p^2)^{\frac{z}{4}} \frac{d^2 \vec{\gamma}}{4} {}_S F_1(\vec{\gamma} | V) : \tag{6.12}$$

In this expression everything except for integrands  $I(\vec{\gamma} | V)$  is spherically symmetric, thus making it possible to perform angular averaging over  $\vec{p}$  in these integrands.

### 6.4.1 S wave: $\vec{p}$ averaging

Here all the calculations are rather straightforward. In the non-relativistic case one can everywhere put  $z = 1/2$ ;  $M = 2m = m_V$ . The resultant integrands are:

$$\begin{aligned}
I^S(L \rightarrow L) &= \frac{8QM}{(Q^2 + M^2)^2} \sim^2 \\
I^S(T \rightarrow T; \rightarrow v) &= \frac{8M^2}{(Q^2 + M^2)^2} \sim^2 \\
I^S(T \rightarrow T; \rightarrow v) &= \frac{16(e\gamma)(\nabla \gamma)}{3(Q^2 + M^2)^2} \sim^2 + \frac{96}{5M^2(Q^2 + M^2)} \sim^2 p^2 \\
I^S(T \rightarrow L) &= \frac{64}{3} \frac{M(e\gamma)}{(Q^2 + M^2)^2} \frac{p^2}{M^2} \sim^2 \\
I^S(L \rightarrow T) &= \frac{512}{15} \frac{Q(\nabla \gamma)}{(Q^2 + M^2)^2} \frac{p^4}{M^2(Q^2 + M^2)} \sim^2
\end{aligned} \tag{6.13}$$

Note several things: since the accurate 1S wave differs from the naive spinorial structure only by relativistic corrections, one would obtain the same results in the case of naive  $qqV$  vertex. The only difference would be only extra factor 2 for the  $L \rightarrow T$  amplitude (which is higher-twist amplitude, anyway).

Thus the only thing left is  $p$  integration. Note that these amplitudes are naturally expressed in terms of decay constants. Indeed, in the extremely non-relativistic case expression (4.37) turns into

$$f^{(S)} = \frac{3m_V}{2^3} \int d^3p \psi_s(\mathbf{p}) \int d^3p \psi_s(\mathbf{p}) = \frac{2^3}{3m_V} f^{(S)} \tag{6.14}$$

#### 6.4.2 S wave: answers for $L \rightarrow L$ up to differential cross section

Here we would like to digress and for the sake of logical completeness show how one obtains the final result for the differential cross section with the example of  $L \rightarrow L$  amplitude. If needed, the same can be done for the other amplitudes, so we will do it just once.

One has:

$$\begin{aligned}
&\int d^3p \psi_s(\mathbf{p}) \frac{4}{m_V} \frac{8QM_V}{(Q^2 + m_V^2)^2} \int d^3\bar{Q} \frac{d^2 \partial G(\mathbf{x}; \bar{Q}^2)}{\partial \log \bar{Q}^2} \psi_s(\bar{Q}^2) \exp\left(-\frac{1}{2}B_{3P} \bar{Q}^2\right) \\
&= \frac{32Q}{(Q^2 + m_V^2)^2} G(\mathbf{x}; \bar{Q}_0^2) \psi_s(\bar{Q}_0^2) \exp\left(-\frac{1}{2}B_{3P} \bar{Q}_0^2\right) \int d^3p \psi_s(\mathbf{p}) \\
&= \frac{32Q}{(Q^2 + m_V^2)^2} \exp\left(-\frac{1}{2}B_{3P} \bar{Q}_0^2\right) G(\mathbf{x}; \bar{Q}_0^2) \psi_s(\bar{Q}_0^2) \frac{2^3}{3m_V} f_V
\end{aligned}$$

With this result, (6.12) becomes

$$\begin{aligned}
A &= i s \frac{f_V g_V}{4^2} \frac{p}{4} \frac{64}{3} \frac{Q}{m_V} \frac{G_s}{(Q^2 + m_V^2)^2} \\
&= i s \frac{16}{3} \frac{Q}{m_V} \frac{p}{4} \frac{G_s \exp\left(-\frac{1}{2}B_{3P} \bar{Q}_0^2\right)}{(Q^2 + m_V^2)^2}
\end{aligned}$$

The expression for the differential cross section reads ( $t \sim^2$ ):

$$\begin{aligned} \frac{d}{dt} &= \frac{1}{16 s^2} \mathcal{A}^2 \\ &= \frac{16^3 Q^2}{9 m_V^2} (\alpha_V)^2 4_{em} \frac{G^2 s^2 \exp(-B_{3P} t)}{(Q^2 + m_V^2)^4} : \end{aligned}$$

Finally, one can express this cross section through  $(V \rightarrow e^+ e^-)$  (see (4.39)):

$$\frac{d}{dt} = \frac{16^3}{3_{em}} Q^2 m_V (V \rightarrow e^+ e^-) \frac{G^2 s^2 \exp(-B_{3P} t)}{(Q^2 + m_V^2)^4} :$$

(6.15)

### 6.4.3 S wave: the other amplitudes

$T \rightarrow T; =_V$

. In the non-relativistic case, this amplitude is readily obtained from the above formulas after  $Q \rightarrow m_V$  replacement in the numerator of the amplitude (see (6.13)). This means in particular that in this limit

$$R^{(S)} = \frac{A_{LL}^2}{A_{TT}} = \frac{Q^2}{m_V^2} : \quad (6.16)$$

$T \rightarrow T; =_V$

. This amplitude is very interesting because of the competition of two very different terms | soft and hard scale contribution. Indeed, integration over gluon loop gives

$$A \sim \frac{G(x; Q^2)}{2} + \frac{96}{5} \frac{G(x; Q^2) p^2}{M^2 (Q^2 + M^2)} \quad (6.17)$$

We see that the soft contribution turns out to be of leading twist, while the pQCD contribution is of higher twist. This observation was first made in [6] for the naive type of  $qqV$  vertex; here we see that it also holds for accurate S and D wave vector mesons.

$T \rightarrow L$  and  $L \rightarrow T$

. In the case of heavy quarkonia these single spin ip amplitudes have suppressing non-relativistic factors. Besides, the amplitude  $L \rightarrow T$  is of twist 3, which is another source of suppression. Their ratios to  $A(T \rightarrow T) = A(T \rightarrow T; =_V)$  read

$$\frac{A(T \rightarrow L)}{A(T \rightarrow T)} = \frac{8 \langle e \rangle}{3 m_V} w; \quad \frac{A(L \rightarrow T)}{A(T \rightarrow T)} = \frac{64 Q \langle \nabla \rangle}{15 Q^2 + m_V^2} w : \quad (6.18)$$

The model dependent quantities  $w_2$  and  $w_4$  are defined via

$$w_2 = \frac{1}{m_V^2} \frac{\int_R d^3 p p^2 s}{\int d^3 p s}; \quad w_4 = \frac{1}{m_V^4} \frac{\int_R d^3 p p^4 s}{\int d^3 p s} : \quad (6.19)$$

Within the oscillator ansatz (4.42) their values are

$$w_2 = \frac{3}{2} \frac{1}{(m_V R)^2}; \quad w_4 = \frac{15}{4} \frac{1}{(m_V R)^4} : \quad (6.20)$$

## 6.5 Final results for D wave

This case is much more tricky. It turns out that the leading terms in integrands  $I^{(D)}$ , proportional to  $m^2 p^2$  cancel out after angular averaging, so that many new terms, including higher twist terms come into play. This cancellation is in fact quite understandable. Indeed, in the very beginning we showed that vertex  $u^0 u$  contains both S and D waves, with D wave probability being suppressed for heavy quarks due to non-relativistic motion. This means in particular that the photon couples to  $q\bar{q}$  pairs sitting either in S or D wave state. However, at the other end of the quark loop we have a vector meson in pure D wave state. Therefore, the largest terms in  $\langle h_{S+D} \rangle \langle V_D \rangle$  cancel out due to S/D orthogonality.

### 6.5.1 D wave: $p$ averaging for $L=1$ amplitude

If we limited ourselves only to the leading  $p^2=m^2$  terms, we would get

$$\int d\Omega_p \left( \mathbf{k}^2 - \frac{4m}{M} p_z^2 \right) = 4 \left( \frac{2}{3} p^2 - 2 \frac{1}{3} p^2 \right) = 0;$$

which is the manifestation of S/D orthogonality. Thus, we see that  $p^2=m^2$  terms vanish after angular averaging. Therefore, one has to be extremely careful now and must take into account all possible sources of  $p^4=m^4$  terms. To do so, one has to perform the following averaging

$$\int d\Omega_p \left( 1 - \frac{z}{Q^4} \right) \left( \mathbf{k}^2 - \frac{4m}{M} p_z^2 \right) = \int d\Omega_p \left( 1 - \frac{4\mathbf{k}^2}{Q^2} \right) \quad (6.21)$$

Before performing the averaging, let us generate a list of useful formulas:

$$\begin{aligned} \int d\Omega_p \mathbf{k}^2 &= \frac{2}{3} p^2 & \int d\Omega_p p_z^2 &= \frac{1}{3} p^2 \\ \int d\Omega_p \mathbf{k}^2 \mathbf{k}^2 &= \frac{8}{15} p^4 & \int d\Omega_p \mathbf{k}^2 p_z^2 &= \frac{2}{15} p^4 & \int d\Omega_p p_z^2 p_z^2 &= \frac{3}{15} p^4 \end{aligned} \quad (6.22)$$

Finally, remember that  $p_z^2 = \frac{1}{4} (1 - 2z) M^2$ .

One has to perform the following averaging

$$\int d\Omega_p \left( 1 - \frac{z}{Q^4} \right) \left( \mathbf{k}^2 - \frac{4m}{M} p_z^2 \right) = \int d\Omega_p \left( 1 - \frac{4\mathbf{k}^2}{Q^2} \right) \quad (6.23)$$

Note that all factors should be carefully examined; all four do contribute to the final answer. Decomposing  $\overline{Q}^2$  as

$$\overline{Q}^2 = m^2 + z(1-z)Q^2 = m^2 + \frac{1}{4}Q^2 - \frac{1}{4}(1-2z)^2Q^2 = \overline{Q}_0^2 - \frac{p_z^2}{M^2}Q^2; \quad (6.24)$$

with  $\overline{Q}_0^2 = m^2 + Q^2/4$ , one gets

$$\frac{1}{\overline{Q}^4} = \frac{1}{\overline{Q}_0^4} \left( 1 + 2 \frac{p_z^2}{M^2} \frac{Q^2}{\overline{Q}_0^2} \right) : \quad (6.25)$$

So, omitting  $\overline{Q}_0^4$ , one has

$$1 + \frac{4p_z^2}{M^2} + 1 + 2\frac{p_z^2 Q^2}{M^2 \overline{Q}_0^2} + k^2 \frac{4m}{M} p_z^2 \approx 1 + \frac{4k^2}{\overline{Q}_0^2} A \quad (6.26)$$

With the aid of (6.12), one obtains

$$\begin{aligned} & k^2 \frac{4m}{M} p_z^2 + \frac{4}{M^2} k^2 p_z^2 + 2p_z^2 + 2\frac{Q^2}{M^2 \overline{Q}_0^2} k^2 p_z^2 + 2p_z^2 + \frac{4}{\overline{Q}_0^2} k^2 k^2 + 2p_z^2 \\ = & \frac{2}{3} p^2 + \frac{4m}{3M} p^2 + \frac{4}{M^2} p^4 + \frac{2}{15} + \frac{6}{15} + 2\frac{Q^2}{M^2 \overline{Q}_0^2} p^4 + \frac{2}{15} + \frac{6}{15} + \frac{4}{\overline{Q}_0^2} p^4 + \frac{8}{15} + \frac{4}{15} \\ = & \frac{2}{3} p^2 \frac{4p^2}{M + 2m} + \frac{16p^4}{15M^2} + \frac{8Q^2 p^4}{15M^2 \overline{Q}_0^2} + \frac{16p^4}{15\overline{Q}_0^2} \\ = & \frac{4p^4}{3M^2} \left( 1 + \frac{4}{5} + \frac{8}{5} \frac{Q^2}{Q^2 + M^2} + \frac{16}{5} \frac{M^2}{Q^2 + M^2} \right) \\ = & \frac{4p^4}{15M^2} \left( 1 + \frac{8}{5} \frac{M^2}{Q^2 + M^2} \right) \end{aligned} \quad (6.27)$$

One can now again express the integral over quark loop through the decay constant (see (4.38)):

$$\int d^3p p^4 \langle D \rangle f^{(D)} = \frac{3m_V}{2} : \quad (6.28)$$

to give

$$\frac{64}{15} \frac{Q^4}{m_V} \frac{G}{m_V} \frac{\exp(\frac{1}{2} B_{3P} \sim 2)}{(Q^2 + m_V^2)^2} \langle D \rangle = 1 + 8 \frac{m_V^2}{Q^2 + m_V^2} : \quad (6.29)$$

Comparison with  $L \rightarrow L$  amplitude reveals that

$$\boxed{\frac{A_{LL}^D}{A_{LL}^S} = \frac{1}{5} \left( 1 + 8 \frac{m_V^2}{Q^2 + m_V^2} \right) \frac{f^{(D)}}{f^{(S)}} :} \quad (6.30)$$

### 6.5.2 D wave: the other amplitudes

For the helicity conserving amplitude one has to repeat the same averaging procedure. The calculation proceeds as follows:

$$\begin{aligned} & 1 + 2\frac{p_z^2 Q^2}{M^2 \overline{Q}_0^2} + 2p^2 + m^2 + 2k^2 + 4k^2 \frac{m^2}{Q^2} + m(M + m) k^2 \approx 1 + \frac{4k^2}{\overline{Q}_0^2} A + k^2 k^2 + \frac{4m}{M} p_z^2 \\ = & 2m^2 p^2 + \frac{2}{3} m(M + m) p^2 + 2\frac{p_z^2 Q^2}{M^2 \overline{Q}_0^2} + \frac{1}{2} M^2 + \frac{1}{3} + 3M^2 \frac{2}{15} + \frac{8}{3} p^4 + \frac{8}{15} p^4 + \frac{m^2}{\overline{Q}_0^2} p^4 + \frac{16}{15} \\ = & \frac{2}{3} p^4 + \frac{8}{15} p^4 + \frac{8}{3} p^4 + \frac{16}{15} \frac{M^2}{M^2 + Q^2} p^4 + \frac{8}{15} \frac{Q^2}{M^2 + Q^2} p^4 \\ = & 2p^4 \left( 1 + \frac{4}{15} \frac{M^2}{M^2 + Q^2} \right) : \end{aligned} \quad (6.31)$$

The result can be written as

$$\frac{A_{LL}^D}{A_{TT}^D} = \frac{1}{15} \frac{1 - \frac{8m_V^2}{Q^2 + m_V^2}}{1 + \frac{4}{15} \frac{m_V^2}{Q^2 + m_V^2}} : \quad (6.32)$$

In the case of double helicity flip amplitude we again have contributions from soft and hard scales with the same hierarchy of twists. Namely,

$$A \sim \frac{G(x; Q^2)}{2} - \frac{96}{7} \frac{G(x; Q^2) p^2}{M^2 (Q^2 + M^2)} \quad (6.33)$$

so we again see the soft domination in the double helicity flip amplitude.

In the case of single spin flip amplitudes, no dangerous cancellations among leading terms arise. Before giving a list of amplitudes, we wish to emphasize that in the case of D wave mesons there is no non-relativistic suppressing factors like  $w_2$  and  $w_4$  defined in (6.19). This means that for moderate momentum transfers helicity non-conserving amplitudes are absolutely important for that case of D wave mesons.

## 6.6 S wave vs. D wave comparison

We would like to present our final results in the form which stresses the remarkable differences between S wave and D wave amplitudes. Below we give a table of the ratios

$$_{ij} = \frac{A^D(i \rightarrow j) f^{(S)}}{A^S(i \rightarrow j) f^{(D)}} \quad (6.34)$$

for helicity conserving and single spin flipping amplitudes. Double spin flip amplitudes are not given due to the presence of incalculable non-perturbative contributions.

$$\begin{aligned} \frac{A_{LL}^D}{A_{LL}^S} &= \frac{1}{5} \frac{1 - \frac{8m_V^2}{Q^2 + m_V^2}}{1 - \frac{8m_V^2}{Q^2 + m_V^2}} \\ \frac{A_{TT}^D}{A_{TT}^S} &= \frac{3}{5} \frac{1 + \frac{4}{15} \frac{m_V^2}{Q^2 + m_V^2}}{1 + \frac{4}{15} \frac{m_V^2}{Q^2 + m_V^2}} \\ \frac{A_{TL}^D}{A_{TL}^S} &= \frac{3}{5} \frac{1}{w_2} \frac{1 + 3 \frac{m_V^2}{Q^2 + m_V^2}}{1 + 3 \frac{m_V^2}{Q^2 + m_V^2}} \\ \frac{A_{LT}^D}{A_{LT}^S} &= \frac{9}{8} \frac{1}{w_4} \end{aligned} \quad (6.35)$$

Thus, we note several things. First, the abnormally large higher twist contributions to D wave amplitudes are seen here as terms  $\sim m_V^2/(Q^2 + m_V^2)$ . They even force the opposite sign of  $L \rightarrow L$  amplitude in the moderate  $Q^2$  domain. Second, we see highly non-trivial and even non-monotonous  $Q^2$  dependence of  $(A_{LL}/A_{TT})^2$  ratio, which will lead to the presence of a dip in experimentally measured  $\sigma_L = \sigma_T$  for D wave meson production. Finally, we must stress that in the case of D wave mesons there is no non-relativistic suppression for single spin flip amplitudes as it was in S wave mesons. This leads us to a conclusion that s-channel helicity is strongly violated in the case of D wave meson production.

P art III

N um erical analysis



## Chapter 7

# Determination of the unintegrated gluon structure function of the proton: DGLAP 2000 analysis

The familiar objects from Gribov-Lipatov-Dekshitzer-Altarelli-Parisi (DGLAP) evolution description of deep inelastic scattering (DIS) are quark, antiquark and gluon distribution functions  $q_i(x;Q^2); \bar{q}_i(x;Q^2); g(x;Q^2)$  (hereafter  $x;Q^2$  are the standard DIS variables). At small  $x$  they describe the integral flux of partons with the lightcone momentum  $x$  in units of the target momentum and transverse momentum squared  $Q^2$  and form the basis of the highly sophisticated description of hard scattering processes in terms of collinear partons [18]. On the other hand, at very small  $x$  the object of the Balitskii-Fadin-Kuraev-Lipatov evolution equation is the differential gluon structure function (DGSF) of the target [19, 30]

$$F(x;Q^2) = \frac{\partial G(x;Q^2)}{\partial \log Q^2} \quad (7.1)$$

with  $G(x;Q^2) = xg(x;Q^2)$  (evidently the related unintegrated distributions can be defined also for charged partons). For instance, it is precisely DGSF of the target proton that emerges in the familiar color dipole picture of inclusive DIS at small  $x$  [31, 32, 33] and diffractive DIS into dijets [34]. Another familiar example is the QCD calculation of helicity amplitudes of diffractive DIS into continuum [35, 36] and production of vector mesons [37, 38]. DGSF's are custom-tailored for QCD treatment of hard processes, when one needs to keep track of the transverse momentum of gluons neglected in the standard collinear approximation [39, 40, 41, 42].

In the past two decades DGLAP phenomenology of DIS has become a big industry and several groups — notably GRV [43], CTEQ [44] & MRS [45] and some other [46] — keep continuously incorporating new experimental data and providing the high energy community with updates of the parton distribution functions supplemented with the interpolation routines facilitating practical applications. On the other hand, there are several pertinent issues — the onset of the purely perturbative QCD treatment of DIS and the impact of soft mechanisms of photoabsorption on the proton structure function in the region of large  $Q^2$  being top ones on the list — which can not be answered within the DGLAP approach itself because DGLAP evolution is obviously hampered at moderate to small  $Q^2$ . The related issue is to what extent the soft mechanisms of photoabsorption can bias the  $Q^2$  dependence of the proton structure

function and, consequently, determination of the gluon density from scaling violations. We recall here the recent dispute [47] on the applicability of the DGLAP analysis at  $Q^2 < 2\{4 \text{ GeV}^2$  triggered by the so-called Caldwell's plot [48]. Arguably the  $\sim$ -factorization formalism of DGSF, in which the interesting observables are expanded in interactions of gluons of transverse momentum  $\sim$  changing from soft to hard is better suited to look into the issue of soft-hard interface. Last but not least, neglecting the transverse momentum  $\sim$  of gluons is a questionable approximation in evaluation of production cross sections of jets or hadrons with large transverse momentum. It is distressing, then, that convenient, ready-to-use, parameterizations of DGSF are not yet available in the literature.

Here we perform a simple phenomenological determination of the DGSF at small  $x$  based on the 1978 Baltskii-Lipatov (BL) scheme [30], in which the DGSF is directly related to the physical observable — the proton structure function  $F_{2p}(x; Q^2)$ . In early 90's the BL scheme has been extended to other observables and dubbed  $\sim$ -factorization [49]; it is also closely related to the color dipole factorization in the color dipole BFKL approach [31, 32, 33]. Our interest is in producing the ready-to-use Ansatz for  $F(x; \sim^2)$ , so that we take advantage of large body of the early work on color dipole BFKL factorization [32, 50, 51] and follow a very pragmatic strategy first applied in [35, 36]: (i) for hard gluons with large  $\sim$  we make as much use as possible of the existing DGLAP parameterizations of  $G(x; \sim^2)$ , (ii) for the extrapolation of hard gluon densities to small  $\sim^2$  we use an Ansatz [34] which correctly describes the color gauge invariance constraints on radiation of soft gluons by colour singlet targets, (iii) as suggested by color dipole phenomenology, we supplement the density of gluons with small  $\sim^2$  by nonperturbative soft component, (iv) as suggested by the soft-hard duality inherent to the BFKL evolution, we allow for propagation of the predominantly hard-interaction driven small- $x$  rise of DGSF into the soft region invoking plausible soft-to-hard interpolations. The last two components of DGSF are parameterized following the modern wisdom on the infrared freezing of the QCD coupling and short propagation radius of perturbative gluons. Having specified the infrared regularization, we can apply the resulting  $F(x; \sim^2)$  to evaluation of the photoabsorption cross section in the whole range of small to large  $Q^2$ .

## 7.1 The Ansatz for differential gluon structure function

The major insight into parameterization of DGSF comes from early experience with color dipole phenomenology of small- $x$  DIS. In color dipole approach, which is closely related to  $\sim$ -factorization, the principal quantity is the total cross section of interaction of the qq color dipole  $r$  with the proton target [32, 52, 53]

$$\sigma(x; r) = \frac{r^2}{3} \int_0^1 \frac{d\sim^2}{\sim^2} \frac{4 [1 - J_0(\sqrt{r^2 \sim^2})]}{(r^2 \sim^2)} s \max f_{\sim^2}; \frac{A}{r^2} g F(x; \sim^2); \quad (7.2)$$

which for very small color dipoles can be approximated by

$$\sigma(x; r) = \frac{r^2}{3} s \frac{A}{r^2} G(x; \frac{A}{r^2}); \quad (7.3)$$

where  $A \approx 10$  comes from properties of the Bessel function  $J_0(z)$ . The phenomenological properties of the dipole cross section are well understood, for extraction of  $\sigma(x; r)$  from the

experimental data see [20, 54]. The known dipole size dependence of  $(x;r)$  serves as a constrain on the possible  $\sim^2$ -dependence of  $F(x;\sim^2)$ .

As we argued in section 3.2, DGLAP's are likely to overestimate  $F_{\text{hard}}(x;\sim^2)$  at moderate  $\sim^2$ . Still, approximation (7.3) does a good job when the hardness  $A=r^2$  is very large, and at large  $Q^2$  we can arguably approximate the DGSF by the direct differentiation of available ts (GRV, CTEQ, MRST, ...) to the integrated gluon structure function  $G_{\text{pt}}(x;Q^2)$ :

$$F_{\text{pt}}(x;\sim^2) = \frac{\partial G_{\text{pt}}(x;\sim^2)}{\partial \log \sim^2} \quad (7.4)$$

Hereafter the subscript pt serves as a reminder that these gluon distributions were obtained from the pQCD evolution analyses of the proton structure function and cross sections of related hard processes.

The available DGLAP's are only applicable at  $\sim^2 \gg Q_c^2$ , see table 1 for the values of  $Q_c^2$ , in the extrapolation to soft region  $\sim^2 \ll Q_c^2$  we are bound to educated guess. To this end recall that perturbative gluons are confined and do not propagate to large distances; recent ts [55] to the lattice QCD data suggest Yukawa-Debye screening of perturbative color elds with propagation/screening radius  $R_c \approx 0.27\text{fm}$ . Incidentally, precisely this value of  $R_c$  for Yukawa screened colour elds has been used since 1994 in the very successful color dipole phenomenology of small- $x$  DIS [50, 51]. Furthermore, important nding of [51] is a good quantitative description of the rising component of the proton structure function starting with the Yukawa-screened perturbative two-gluon exchange as a boundary condition for the color dipole BFKL evolution.

The above suggests that  $\sim^2$  dependence of perturbative hard  $F_{\text{hard}}(x;\sim^2)$  in the soft region  $\sim^2 \ll Q_c^2$  is similar to the Yukawa-screened flux of photons in the positron, cf. eq. (2.33), with  $\alpha_{\text{em}}$  replaced by the running strong coupling of quarks  $C_F \alpha_s(\sim^2)$  and with factor  $N_c$  instead of 2 leptons in the positronium, for the early discussion see [34],

$$F_{\text{pt}}^{(\text{B})}(\sim^2) = C_F N_c \frac{\alpha_s(\sim^2)}{\sim^2 + \frac{1}{R_c^2}} V_N(\sim); \quad (7.5)$$

Here  $\frac{1}{R_c} = 0.75\text{ GeV}$  is the inverse Yukawa screening radius and must not be interpreted as a gluon mass; more sophisticated forms of screening can well be considered. Following [50, 51, 56, 22] we impose also the infrared freezing of strong coupling:  $\alpha_s(\sim^2) \approx 0.32$ ; recently the concept of freezing coupling has become very popular, for the review see [57].

The vertex function  $V_N(\sim)$  describes the decoupling of soft gluons,  $\sim \frac{1}{R_p}$ , from color neutral proton and has the same structure as in eq. (2.34). In the nonrelativistic oscillator model for the nucleon one can relate the two-quark form factor of the nucleon to the single-quark form factor,

$$F_2(\sim; \sim) = F_1 \frac{2N_c}{N_c - 1} \sim^2 : \quad (7.6)$$

To the extent that  $R_c^2 \gg R_p^2$  the detailed functional form of  $F_2(\sim; \sim)$  is not crucial, the simple relation (7.6) will be used also for a more realistic dipole approximation

$$F_1(\sim^2) = \frac{1}{(1 + \frac{\sim^2}{\Lambda^2})^2} : \quad (7.7)$$

The gluon probed radius of the proton and the charge radius of the proton can be somewhat different and  $\sim 1$  GeV must be regarded as a free parameter. Anticipating the forthcoming discussion of the diffractive slope in vector meson production we put  $\mu = 1$  GeV.

As discussed above, the hard-to-soft diffusion makes the DGSF rising at small- $x$  even in the soft region. We model this hard-to-soft diffusion by matching the  $\sim^2$  dependence (7.5) to the DGLAP  $\alpha_s F_{pt}(x; Q_c^2)$  at the soft-hard interface  $Q_c^2$  and assigning to  $F_{hard}(x; \sim^2)$  in the region of  $\sim^2 < Q_c^2$  the  $\sim^2$  dependence of the Born term (7.5) and the  $x$ -dependence as shown by the DGLAP  $\alpha_s F_{pt}(x; Q_c^2)$ , i.e.,

$$F_{hard}(x; \sim^2) = F_{pt}^{(B)}(\sim^2) \frac{F_{pt}(x; Q_c^2)}{F_{pt}^{(B)}(Q_c^2)} (Q_c^2 - \sim^2) + F_{pt}(x; \sim^2) (\sim^2 - Q_c^2); \quad (7.8)$$

Because the accepted propagation radius  $R_c \sim 0.3$  fm for perturbative gluons is short compared to a typical range of strong interaction, the dipole cross section (7.2) evaluated with the DGSF (7.8) would miss an interaction strength in the soft region, for large color dipoles. In Ref.[50, 51] this missing strength for large dipoles has been modeled by the non-perturbative, soft mechanism with energy-independent dipole cross section, whose specific form [50, 38] has been driven by early analysis [56] of the nonperturbative two-gluon exchange and tested against the diffractive vector meson production data [38]. More recently several closely related models for  $\sigma_{soft}(r)$  have appeared in the literature, see for instance models for dipole-dipole scattering via polarization of non-perturbative QCD vacuum [58] and the model of soft-hard two-component pomeron [59]. In the spirit of eq. (7.4) one can parameterize interaction of large color dipoles in terms of the genuinely soft, nonperturbative component of DGSF. The principal point about this non-perturbative component of DGSF is that it must not be subjected to pQCD evolution. Thus the arguments about the hard-to-soft diffusion driven rise of perturbative DGSF even at small- $\sim^2$  do not apply to the non-perturbative DGSF and we take it energy-independent,

$$F_{soft}^{(B)}(x; \sim^2) = a_{soft} C_F N_c \frac{s(\sim^2)}{\sim^2 + \frac{s}{s_{soft}}} \frac{\sim^2}{\sim^2 + \frac{s}{s_{soft}}} V_N(\sim); \quad (7.9)$$

where  $\frac{s}{s_{soft}} < \frac{s}{s_{pt}}$ . Furthermore, it is natural that the soft component of DGSF decreases in the perturbative domain of  $\sim^2 > \frac{s}{s_{pt}}$  faster than the perturbative Born term (7.5), which is achieved by the extrapolation of the form suggested in [35, 36]

$$F(x; \sim^2) = F_{soft}^{(B)}(x; \sim^2) \frac{\frac{s}{s}}{\sim^2 + \frac{s}{s}} + F_{hard}(x; \sim^2) \frac{\sim^2}{\sim^2 + \frac{s}{h}}; \quad (7.10)$$

with  $\frac{s}{s_{pt}} < \frac{s}{s}$ .

The above described Ansatz for DGSF must be regarded as a poor man's approximation. The separation of small- $\sim^2$  DGSF into the genuine nonperturbative component and small- $\sim^2$  tail of the hard perturbative DGSF is not unique. Specifically, we attributed to the latter the same small- $x$  rise as in the DGLAP  $\alpha_s$  at  $Q_c^2$ , though one can not exclude that the hard DGSF has a small- $x$ -independent component. The issues of soft-hard separation and whether the non-perturbative component of DGSF enters different observables in a universal manner must be addressed in dynamical models for infrared regularization of perturbative QCD and non-perturbative QCD vacuum and only can be answered confronting such models to the

experiment. We recall that in the conventional DGLAP analysis the effect of soft gluons is reabsorbed into the input gluon distributions.

The  $\sim$ -factorization formulas (2.40) and (2.41) correspond to the full-phase space extension of the LO DGLAP approach at small  $x$ . For this reason our Ansatz for  $F_{\text{hard}}(x; Q^2)$  will be based on LO DGLAP fits to the gluon structure function of the proton  $G_{\text{pt}}(x; Q^2)$ . We consider the GRV98LO [43], CTEQ4L, version 4.6 [44] and MRS LO 1998 [45] parameterizations. We take the liberty of referring to our Ansatz for DGSF based on those LO DGLAP input as D-GRV, D-CTEQ and D-MRS parameterizations, respectively.

Our formulas (2.40), (2.41) describe the sea component of the proton structure function. Arguably these  $LL_{\frac{1}{x}}$  formulas are applicable at  $x < x_0 = 10^{-3} - 10^{-1}$ . At large  $Q^2$  the experimentally attainable values of  $x$  are not so small. In order to give a crude idea on finite-energy effects at moderately small  $x$ , we stretch our fits to  $x > x_0$  multiplying the above Ansatz for DGSF by the purely phenomenological factor  $(1 - x)^5$  motivated by the familiar large- $x$  behaviour of DGLAP parameterizations of the gluon structure function of the proton. We also add to the sea components (2.40), (2.41) the contribution from DIS on valence quarks borrowing the parameterizations from the respective GRV, CTEQ and MRS fits. The latter are only available for  $Q^2 > Q_c^2$ . At  $x < 10^{-2}$  this valence contribution is small and fades away rapidly with decreasing  $x$ , for instance see [51].

## 7.2 The parameters of DGSF for different DGLAP inputs

Our goal is a determination of small- $x$  DGSF in the whole range of  $\sim^2$  by adjusting the relevant parameters to the experimental data on small- $x$   $F_{2p}(x; Q^2)$  in the whole available region of  $Q^2$  as well as the real photoabsorption cross section. The theoretical calculation of these observables is based on Eqs. (2.40), (2.41), (7.10).

The parameters which we did not try adjusting but borrowed from early work in the color dipole picture are  $R_c = 0.27 \text{ fm}$ , i.e.,  $\mu_{\text{pt}} = 0.75 \text{ GeV}$  and the frozen value of the LO QCD coupling with  $\alpha_{\text{QCD}} = 0.2 \text{ GeV}$ :

$$s(Q^2) = m \ln \frac{8}{\frac{4}{0 \log \frac{Q^2}{Q_{\text{CD}}}}} \geq \quad (7.11)$$

We recall that the GRV, MRS and CTEQ fits to GSF start the DGLAP evolution at quite a different soft-to-hard interface  $Q_c^2$  and diverge quite a lot, especially at moderate and small  $\sim^2$ . The value of  $Q_c^2$  is borrowed from these fits and is not a free parameter.

The adjustable parameters are  $\alpha_{\text{soft}}$ ,  $a_{\text{soft}}$ ,  $m_{u,d}$ ,  $\sim_s^2$  and  $\sim_h^2$  (for the heavier quark masses we take  $m_s = m_{u,d} + 0.15 \text{ GeV}$  and  $m_c = 1.5 \text{ GeV}$ ). The both  $m_{u,d}$  and  $\alpha_{\text{soft}}$  have clear physical meaning and we have certain insight into their variation range from the early work on color dipole phenomenology of DIS. The rôle of these parameters is as follows. The quark mass  $m_{u,d}$  defines the transverse size of the  $q\bar{q} = u\bar{u}; d\bar{d}$  Fock state of the real photon, whose natural scale is the size of the  $\pi$ -meson. Evidently, roughly equal values of  $F_{2p}(x; Q^2)$  can be obtained for somewhat smaller  $F(x; Q^2)$  at the expense of taking smaller  $m_{u,d}$ , i.e. larger size of the photon, and vice versa. Therefore, though the quark mass does not explicitly enter the

parameterization for  $F(x; \sim^2)$ , the preferred value of  $m_{\text{u,d}}$  could have been correlated with the DGLAP input. We find that it is sufficient to take the universal  $m_{\text{u,d}} = 0.22 \text{ GeV}$ .

The  $\mu_{\text{soft}}^2$  defines the soft scale in which the non-perturbative glue is connected, and controls the  $x$ -dependence of, and in conjunction with  $a_{\text{soft}}$  sets the scale for, the dipole cross section for large size qq dipoles in the photon. We find that it is sufficient to take the universal  $a_{\text{soft}} = 2$  and  $\mu_{\text{s}}^2 = 3 \text{ GeV}^2$  for the parameter of suppression of the hard tail of non-perturbative soft glue.

The magnitude of the dipole cross section at large and moderately small dipole size depends also on the soft-to-hard interpolation of DGSF, which is sensitive to DGLAP inputs for perturbative component  $G_{\text{pt}}(x; Q^2)$ . This difference of DGLAP inputs can be corrected for by adjusting  $\mu_{\text{soft}}^2$  and the hard-to-soft interface parameter  $\sim_h^2$ . The slight rise of  $\sim_h^2$  helps to suppress somewhat too strong  $x$ -dependence of the soft tail of the perturbative glue. The specific parameterizations for  $\sim_h^2$  depend on the DGLAP input and are presented in table 1. Only  $\sim_h^2$  and  $\mu_{\text{soft}}^2$  varied from one DGLAP input to another. The soft components of the D-GRV and D-CTEQ parameterizations turn out identical. The eye-balls are sufficient for the purposes of the present exploratory study. The parameters found are similar to those used in [35, 36] where the focus has been on the description of diffractive DIS.

Table 1. The parameters of differential gluon structure function for different DGLAP inputs.

	D-GRV	D-MRS	D-CTEQ
LO DGLAP input	GRV98LO [43]	MRS-LO-1998 [45]	CTEQ4L (v4.6) [44]
$Q_c^2, \text{ GeV}^2$	0.895	1.37	3.26
$\mu_h^2, \text{ GeV}^2$	$1 + 0.0018 \log^4 \frac{1}{x}^{1=2}$	$1 + 0.038 \log^2 \frac{1}{x}^{1=2}$	$1 + 0.047 \log^2 \frac{1}{x}^{1=2}$
$\mu_{\text{soft}}, \text{ GeV}$	0.1	0.07	0.1

One minor problem encountered in numerical differentiation of all three parameterizations for  $G_{\text{pt}}(x; Q^2)$  was the seesaw  $\sim^2$ -behavior of the resulting DGSF (7.4), which was an artifact of the grid interpolation routines. Although this seesaw behavior of DGSF would be smoothed out in integral observables like  $G(x; Q^2)$  or  $F_{2p}(x; Q^2)$ , we still preferred to remove the unphysical seesaw cusps and have smooth DGSF. This was achieved by calculating DGSF from (7.4) at the center of each interval of the  $Q^2$ -grid and further interpolating the results between these points. By integration of the so-smoothed  $F_{\text{pt}}(x; Q^2)$  one recovers the input  $G_{\text{pt}}(x; Q^2)$ . The values of  $Q_c^2$  cited in Table 1 corresponds to centers of the first bin of the corresponding  $Q^2$ -grid.

### 7.3 The description of the proton structure function $F_{2p}(x; Q^2)$

We focus on the sea dominated leading  $\log \frac{1}{x}$  region of  $x < 10^{-2}$ . The practical calculation of the proton structure function involves the two running arguments of DGSF:  $x_g$  and  $\sim^2$ . We recall that in the standard collinear DGLAP approximation one has  $\sim^2 = K^2 = Q^2$  and  $x_g = 2x$ , see eq. (3.1). Within the  $\sim$ -factorization one finds that the dominant contribution to  $F_{2p}(x; Q^2)$  comes from  $M_t^2 = Q^2$  with little contribution from  $M_t^2 > Q^2$ . Because at small  $x_g$  the  $x_g$  dependence of  $F(x_g; Q^2)$  is rather steep, we take into account the  $x_g = x$  relationship

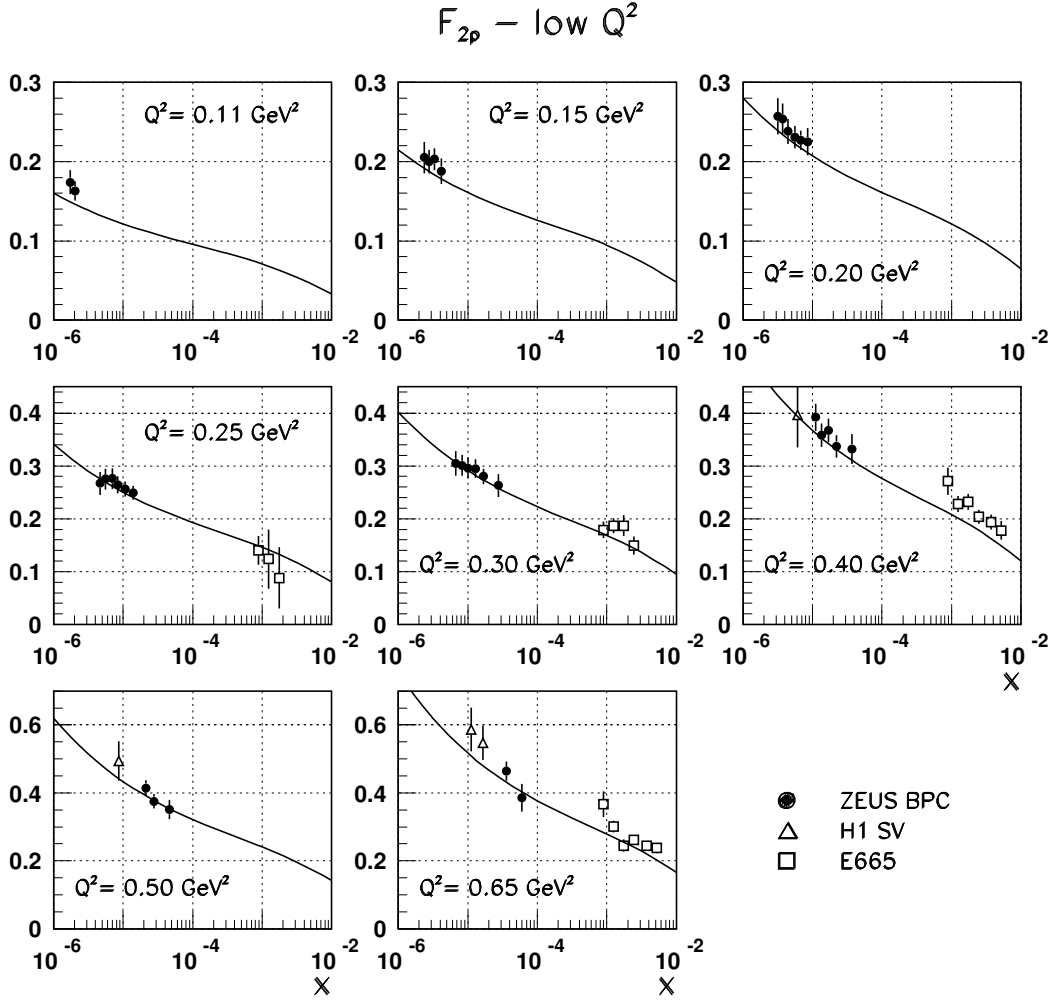


Figure 7.1: The  $\sim$ -factorization description of the experimental data on  $F_{2p}(x; Q^2)$  in the low  $Q^2$  region; black circles are ZEUS BPC data [62], open triangles denote H1 shifted vertex (SV) data [64], open squares are E665 data [65]. Solid line represents  $\sim$ -factorization results for the D-GRV parameterization of the differential gluon structure function  $F(x; \sim^2)$ .

(2.44). Anticipating the results on effective intercepts to be reported in section 7, we notice that for all practical purposes one can neglect the impact of  $\sim$  on the relationship (2.44), which simplifies greatly the numerical analysis. Indeed, the  $x_g$  dependence of  $F(x_g; \sim^2)$  is important only at large  $\sim^2$ , which contribute to  $F_{2p}(x; Q^2)$  only at large  $Q^2$ ; but the larger  $Q^2$ , the better holds the DGLAP ordering  $\sim^2 \sim k^2; Q^2$ . Although at small to moderate  $Q^2$  the DGLAP ordering breaks down, the  $x_g$  dependence of  $F(x_g; \sim^2)$  is weak here.

Obviously, achieving a good agreement from small to moderate to large  $Q^2$  is a highly non-trivial task, because strong modification of the soft contribution to  $F(x; \sim^2)$  unavoidably echos

## $F_{2p}$ – moderate and high $Q^2$

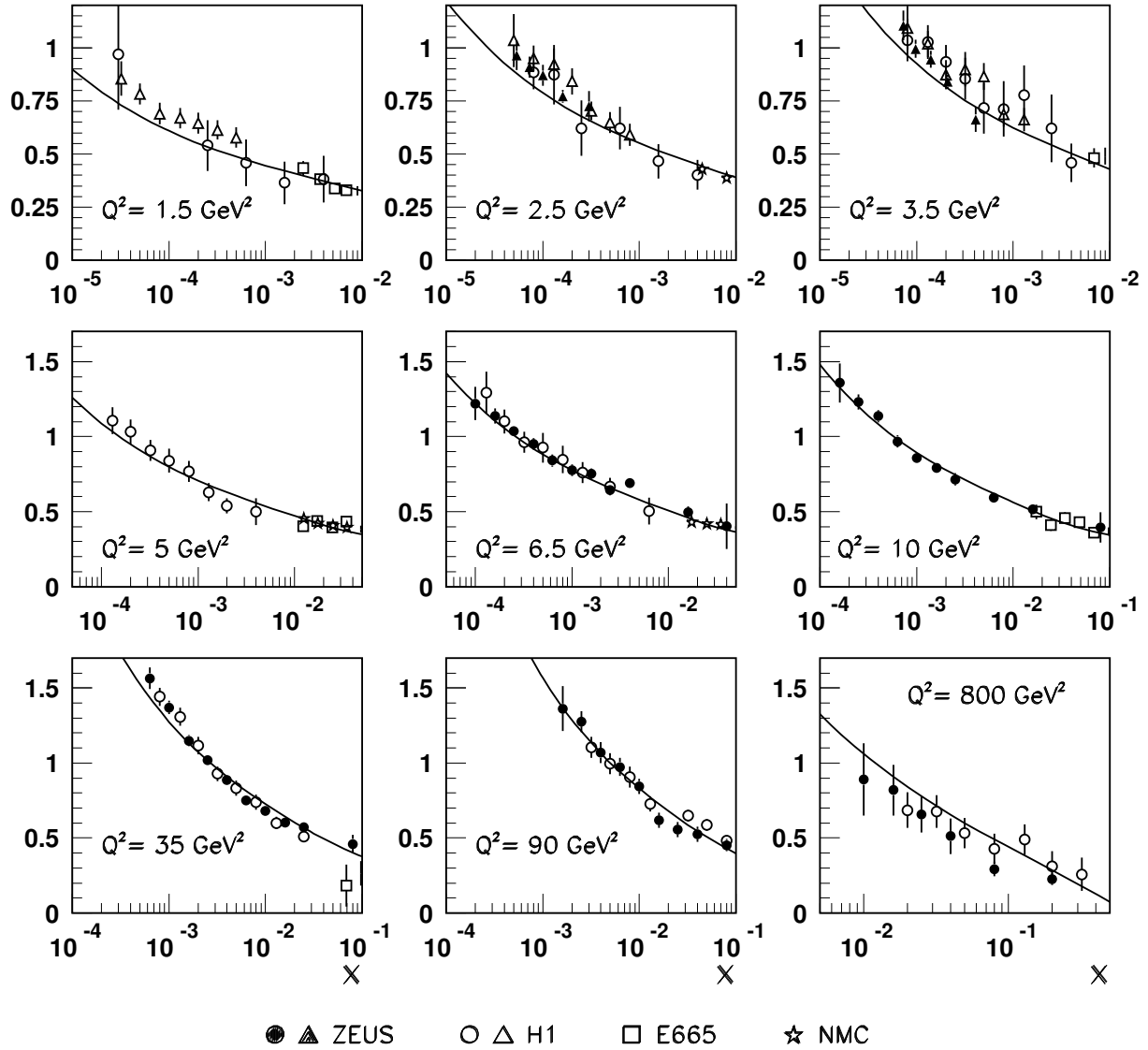


Figure 7.2: The  $\sim$ -factorization description of the experimental data on  $F_{2p}(x; Q^2)$  in the moderate and high  $Q^2$  region; black circles and triangles are ZEUS data [60], [61], open circles and triangles show H1 data [63], [64], open squares are E665 data [65], stars refer to NMC results [66]. Solid line represents  $\sim$ -factorization results for the D-GRV parameterization of the differential gluon structure function  $F(x; \sim^2)$ .

in the integrated gluon SF throughout the whole range of  $Q^2$  and shall affect the calculated structure function from small to moderate to large  $Q^2$ .

The quality of achieved description of the experimental data on the small- $x$  proton structure function is illustrated by figs. 7.1, 7.2. The data shown include recent HERA data (ZEUS [60], ZEUS shifted vertex [61], ZEUS BPC [62], H1 [63], H1 shifted vertex [64]), FNAL E665 experiment [65] and CERN NMC experiment [66]. When plotting the E665 and NMC data, we took the liberty of shifting the data points from the reported values of  $Q^2$  to the closest  $Q^2$



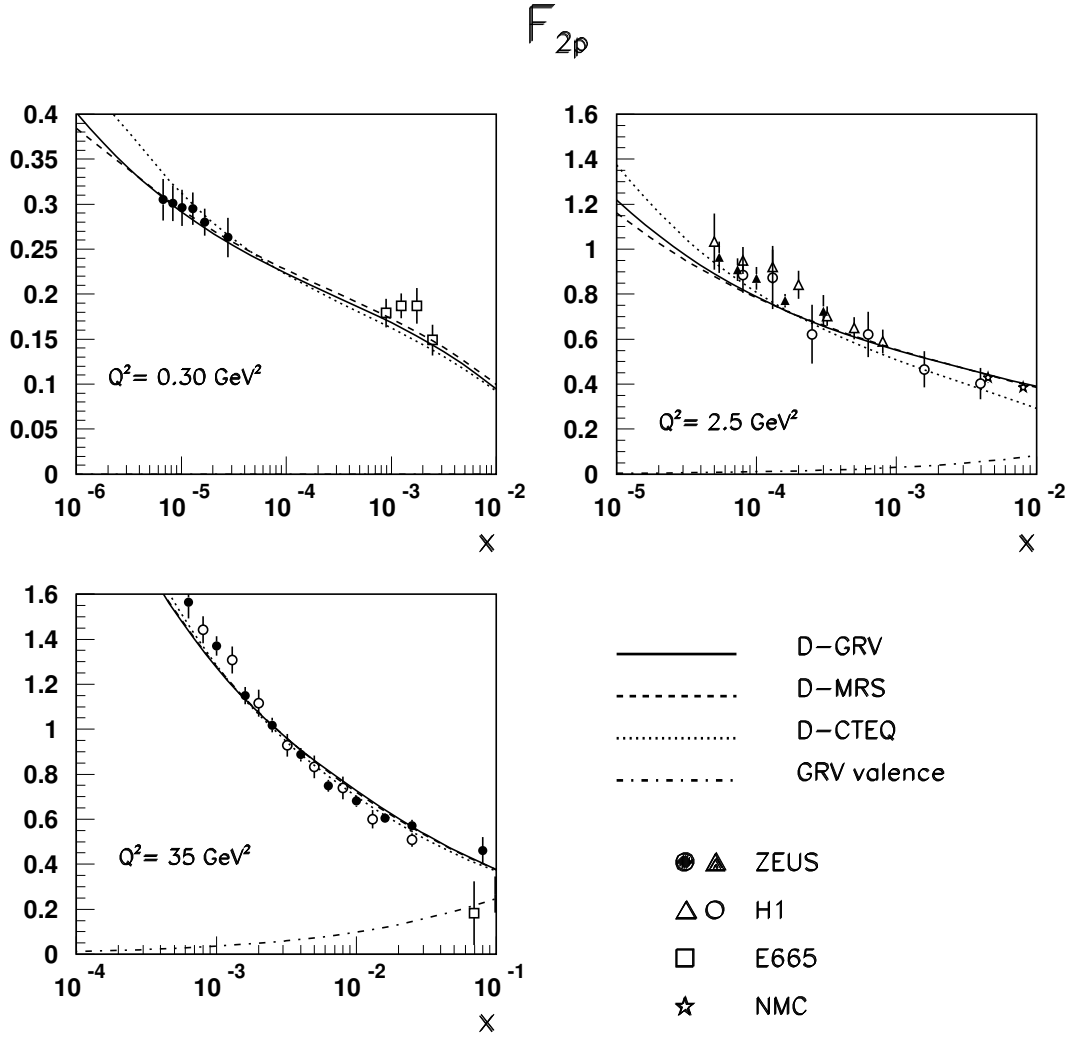


Figure 7.3: A comparison of the  $\sim$ -factorization description of the experimental data on  $F_{2p}(x; Q^2)$  for several values of  $Q^2$  with the D-GRV, D-CTEQ and D-MRS parameterizations of the differential gluon structure function  $F(x; \sim^2)$ . The contribution to  $F_{2p}(x; Q^2)$  from DIS on valence quarks is shown separately for larger  $Q^2$ .

boxes for which the HERA data were available. For  $Q^2 < Q_c^2 = 0.9 \text{ GeV}^2$  the parameterizations for valence distributions are not available and our curves show only the sea component of  $F_{2p}(x; Q^2)$ , at larger  $Q^2$  the valence component is included.

At  $x < 10^{-2}$  the accuracy of our D-GRV description of the proton structure function is commensurate to that of the accuracy of standard LO GRV's. In order not to cram the figures with nearly overlapping curves, we show the results for D-GRV parameterization. The situation with D-CTEQ and D-MRS is very similar, which is seen in Fig. 7.3, where we show on a larger scale simultaneously the results based on the D-GRV, D-CTEQ and D-MRS DGLAP's for several selected values of  $Q^2$ . Here at large  $Q^2$  we show separately the contribution from valence quarks. The difference between the results for  $F_{2p}(x; Q^2)$  for different DGLAP inputs is marginal for all practical purposes, see also a comparison of the results for  $F_p$  for different DGLAP inputs in Fig. 7.4.

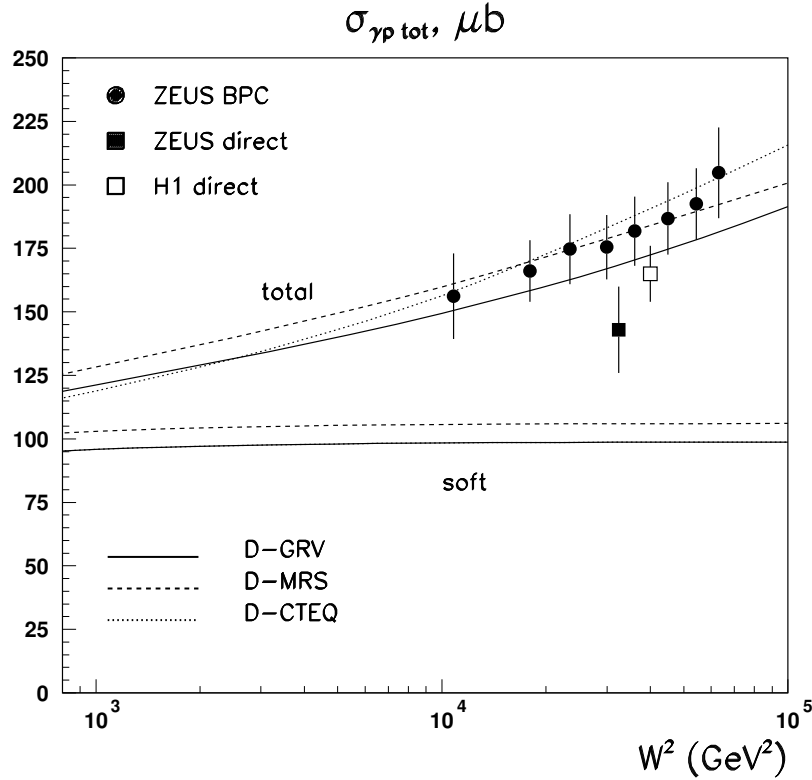


Figure 7.4: A comparison of the  $\sim$ -factorization description of the experimental data on real photoabsorption cross section based on the D-GRV, D-CTEQ and D-MRS parameterizations of the differential gluon structure function  $F(x; \sim^2)$ . The squares show the experimental data from 1992-93 direct measurements, the bullets are the results of extrapolation of virtual photoabsorption to  $Q^2 = 0$  ([62] and references therein). The soft component of photoabsorption cross section is shown separately.

## 7.4 Real photoabsorption cross section $\sigma^P$

In the limiting case of  $Q^2 = 0$  the relevant observable is the real photoabsorption cross section  $\sigma^P$ . Although the Bjorken variable is meaningless at very small  $Q^2$ , the gluon variable  $x_g$  remains well defined at  $Q^2 = 0$ , see eq. (2.44). In Fig. 7.4 we present our results alongside the results of the direct measurements of  $\sigma^P$  and the results of extrapolation of virtual photoabsorption cross sections to  $Q^2 = 0$ , for the summary of the experimental data see [62]. The soft contribution to the cross section is shown separately. We recall that our parameterizations for  $F(x; \sim^2)$  give identical soft cross sections for the GRV and CTEQ inputs (see table 1). The barely visible decrease of  $\sigma_{\text{soft}}^P$  towards small  $W$  is a manifestation of  $1/(1-x)^5$  large- $x$  behaviour of gluon densities. The extension to lower energies requires introduction of the secondary reggeon exchanges which goes beyond the subject of this study.

We emphasize that we reproduce well the observed magnitude and pattern of the energy dependence of  $\sigma^P$  in an approach with manifestly energy-independent soft contribution to

the total cross section. In this scenario the energy dependence of  $\sigma^p$  is entirely due to the  $x_g$ -dependent hard component  $F_{\text{hard}}(x_g; Q^2)$  and as such this rise of the total cross section for soft reaction can be regarded as driven entirely by very substantial hard-to-soft diffusion. Such a scenario has repeatedly been discussed earlier [50, 51, 67]. Time and time again we shall see similar effects of hard-to-soft diffusion and vice versa. Notice that hard-to-soft diffusion is a straightforward consequence of full phase space calculation of partonic cross sections and we do not see any possibility for decoupling of hard gluon contribution from the total cross sections of any soft interaction, whose generic example is the real photoabsorption.

## Chapter 8

# Properties of differential gluon structure function

### 8.1 D G SF in the momentum space

#### 8.1.1 Soft/hard decomposition of D G SF

Now we focus on the  $x$  and  $\sim^2$  behavior of the so-determined D G SF starting for the reference with the D-GRV parameterization. The same pattern holds for D G SF based on CTEQ and MRSDGLAP inputs, see below. In Figs. 8.1 and 8.2 we plot the differential gluon density  $F(x_g; Q^2)$ , while in Fig. 8.3 we show the integrated gluon density

$$G_D(x; Q^2) = \int_0^{Q^2} \frac{d\sim^2}{\sim^2} F(x; \sim^2) : \quad (8.1)$$

Here the subscript D is a reminder that the integrated  $G_D(x; Q^2)$  is derived from D G SF. As such, it must not be confused with the DGLAP parameterizations  $G_{pt}(x; Q^2)$  supplied with the subscript pt.

Figs. 8.1 and 8.2 illustrate the interplay at various  $x$  of the nonperturbative soft component of D G SF and perturbative hard contribution supplemented with the above described continuation into  $\sim^2 = Q_c^2$ . The soft and hard contributions are shown by dashed and dotted lines respectively; their sum is given by solid line.

Apart from the large- $x$  suppression factor  $(1-x)^5$  our non-perturbative soft component does not depend on  $x$ . At not so small  $x = 10^{-2}$  it dominates the soft region of  $\sim^2 < 1-2 \text{ GeV}^2$ , the hard component takes over at higher  $\sim^2$ . The soft-hard crossover point is close to  $\sim_{pt}^2$ , but because of the hard-to-soft diffusion it moves with decreasing  $x$  to a gradually smaller  $\sim^2$ .

In this determination of D G SF we focus on the ready-to-use parameterizations, the dynamical evolution properties of the so-found D G SF will be addressed elsewhere. In what concerns the relationship between D G SF and the observable proton structure function, the early work by Kwiecinski et al. [68] is close in spirit to ours, the difference being in a treatment of the nonperturbative soft component and subjecting D G SF to unified BFKL/DGLAP evolution. In Fig. 8.2 we present D G SF read off the plots in [68]; the agreement with our results is good, which indicates a consistency of our purely phenomenological parameterizations of D G SF with general expectations from the BFKL dynamics.

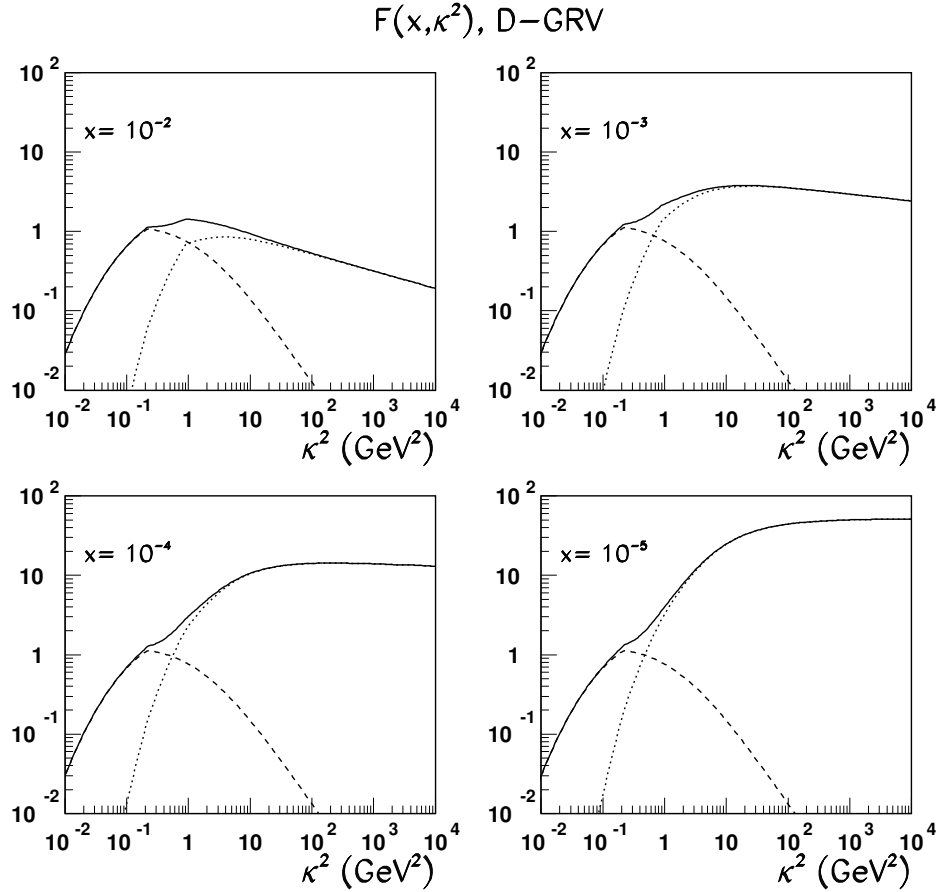


Figure 8.1: D-GRV differential gluon structure function  $F(x; \kappa^2)$  as a function of  $\kappa^2$  at several values of  $x$ . Dashed and dotted lines represent the soft and hard components; the total unintegrated gluon density is shown by the solid line

### 8.1.2 Soft/hard decomposition of the integrated gluon structure function

The rôle of the soft component is further illustrated by Fig. 8.3, where we show the integrated gluon density (8.1) and its soft and hard components  $G_{\text{soft}}(x; Q^2)$  and  $G_{\text{hard}}(x; Q^2)$ , respectively. The soft contribution  $G_{\text{soft}}(x; Q^2)$  is a dominant feature of the integrated gluon density  $G_D(x; Q^2)$  for  $Q^2 < 1 \text{ GeV}^2$ . It builds up rapidly with  $Q^2$  and receives the major contribution from the region  $\kappa^2 \approx 0.3 - 0.5 \text{ GeV}^2$ . Our Ansatz for  $F_{\text{soft}}(x; \kappa^2)$  is such that it starts decreasing already at  $\kappa^2 \approx 0.2 \text{ GeV}^2$  and vanishes rapidly beyond  $\kappa^2 > \kappa_{\text{soft}}^2$ , see gs. 10, 11. Still the residual rise of the soft gluon density beyond  $Q^2 \approx 0.5 \text{ GeV}^2$  is substantial:  $G_{\text{soft}}(x; Q^2)$  rises by about the factor two before it attains at large  $Q^2$ . We emphasize that  $G_{\text{soft}}(Q^2)$  being finite at large  $Q^2$  is quite natural | a decrease of  $G_{\text{soft}}(Q^2)$  at large  $Q^2$  only is possible if  $F_{\text{soft}}(Q^2)$  becomes negative valued at large  $Q^2$ , which does not seem to be a viable

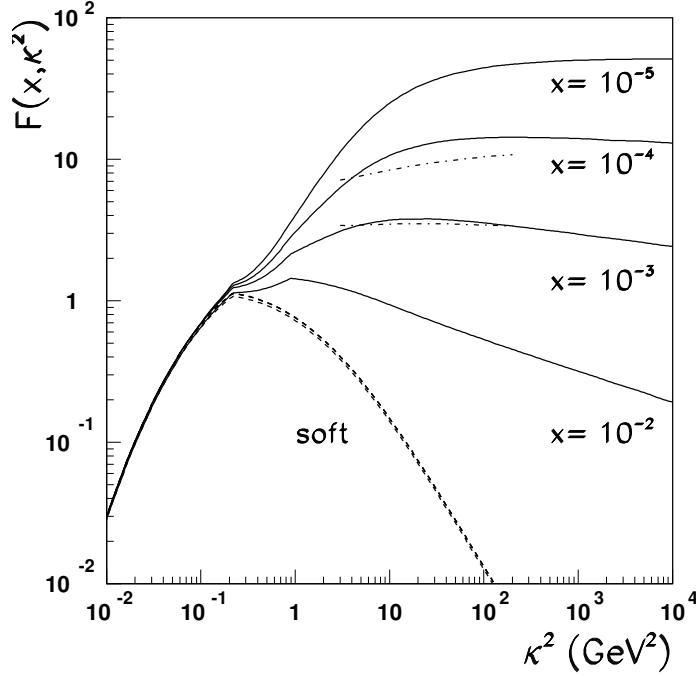


Figure 8.2: The same as in Fig. 8.1 but overlaid onto one graph for illustration of the  $x$ -dependence of  $F(x; \kappa^2)$ . The dashed lines shows the soft component  $F_{\text{soft}}(x; \kappa^2)$  and its slight variation with  $x$  due to the finite- $x$  factor  $(1-x)^5$ . The dot-dashed curves show the Kwiecinski et al. [68] results for DGSF from a  $\sim$ -factorization phenomenology of  $F_{2p}(x; Q^2)$  based on the solution of the unified BFKL/DGLAP equation.

option.

At moderately small  $x = 10^{-2}$  the scaling violations are still weak and the soft contribution  $G_{\text{soft}}(x; Q^2)$  remains a substantial part, about one half, of integrated GSF  $G_D(x; Q^2)$  at all  $Q^2$ . At very small  $x < 10^{-3}$  the scaling violations in the gluon structure function are strong and  $G_{\text{hard}}(x; Q^2) \gg G_{\text{soft}}(x; Q^2)$  starting from  $Q^2 \approx 1-2 \text{ GeV}^2$ .

### 8.1.3 Soft/hard decomposition of the proton structure function $F_2(x; Q^2)$

Eqs. (2.40), (2.41) define the soft/hard decomposition of the proton structure function. In Fig. 8.4 we show  $F_{2p}^{\text{hard}}(x; Q^2)$  and  $F_{2p}^{\text{soft}}(x; Q^2)$  as a function of  $Q^2$  for two representative values of  $x$ . Notice how significance of soft component as a function of  $Q^2$  rises from fully differential  $F(x; Q^2)$  to integrated  $G_D(x; Q^2)$  to doubly integrated  $F_{2p}^{\text{soft}}(x; Q^2)$ . At a moderately small  $x \approx 10^{-3}$ , the soft contribution is a dominant part of  $F_{2p}(x; Q^2)$ , although the rapidly rising hard component  $F_{2p}^{\text{hard}}(x; Q^2)$  gradually takes over at smaller  $x$ .

Notice that not only does  $F_{2p}^{\text{soft}}(x; Q^2)$  not vanish at large  $Q^2$ , but also it rises slowly with

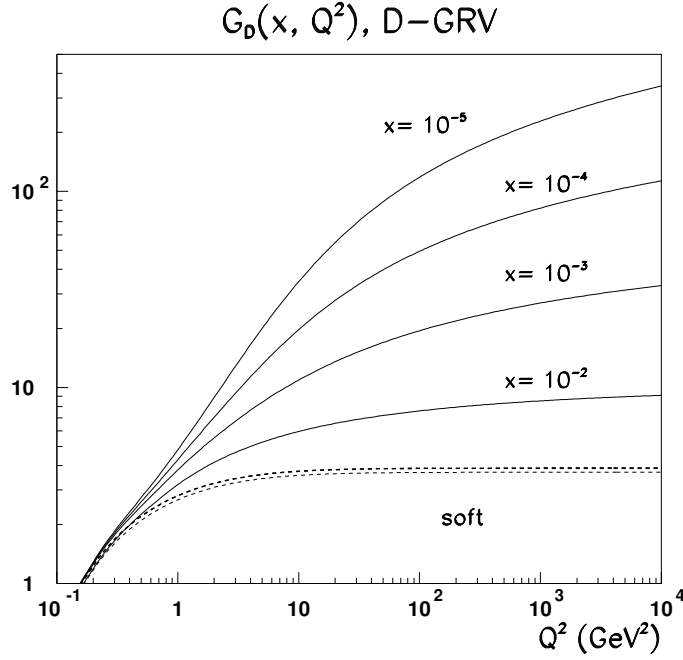


Figure 8.3: The same as Fig. 8.1 but for integrated gluon structure function  $G_D(x; Q^2)$  as given by the D-GRV parameterization of the differential gluon structure function  $F(x; \sim^2)$ , for the discussion see Section 6.2.

$Q^2$  as

$$F_{2p}^{\text{soft}}(x; Q^2) \propto e_f^2 \frac{4G_{\text{soft}}(Q^2)}{3_0} \log \frac{1}{s(Q^2)} : \quad (8.2)$$

Again, the decrease of  $F_{2p}^{\text{soft}}(x; Q^2)$  with  $Q^2$  would only be possible at the expense of unphysical negative valued  $G_{\text{soft}}(Q^2)$  at large  $Q^2$ .

## 8.2 D G SF in the x-space: effective intercepts and hard-to-soft diffusion

It is instructive to look at the change of the x-dependence from the differential gluon structure function  $F(x; \sim^2)$  to integrated gluon structure function  $G_D(x; Q^2)$  and further to proton structure function  $F_{2p}(x; Q^2)$ . It is customary to parameterize the x dependence of various structure functions by the effective intercept. For instance, the effective intercept  $\alpha_{\text{eff}}$  for differential gluon structure function is defined by the parameterization

$$F(x; \sim^2) / \frac{1}{x} \propto x^{\alpha_{\text{eff}}(\sim^2)} : \quad (8.3)$$

One can define the related intercepts  $\alpha_{\text{hard}}$  for the hard component  $F_{\text{hard}}(x; \sim^2)$ . Notice, that in our Ansatz  $\alpha_{\text{soft}} = 0$ .

### $F_{2p}$ , D-GRV

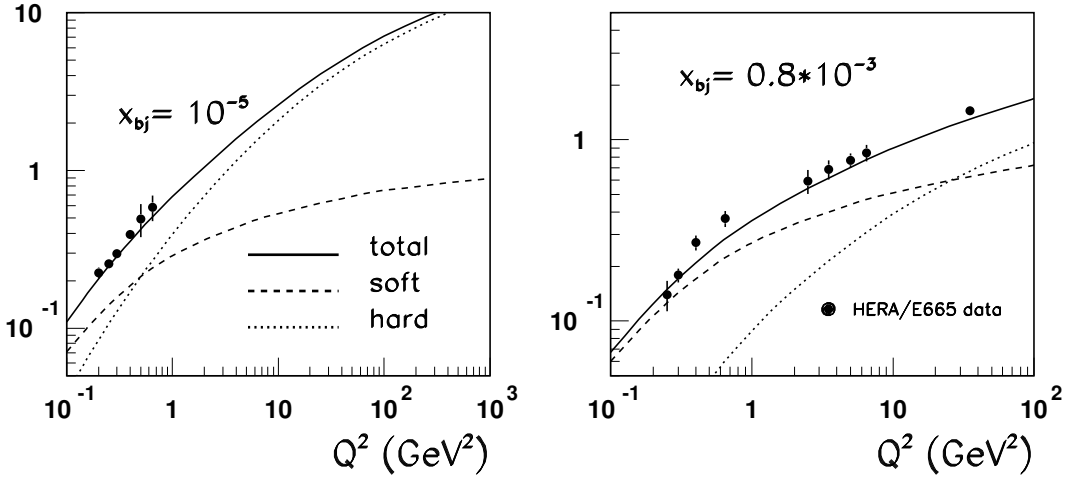


Figure 8.4: The soft-hard decomposition of  $\sim$ -factorization results for the proton structure function  $F_{2p}(x; Q^2)$  evaluated with the D-GRV parameterization of the differential gluon structure function  $F(x; \sim^2)$ .

The power law (8.3) is only a crude approximation to the actual  $x$  dependence of DGSF and the effective intercept  $\alpha_{eff}$  will evidently depend on the range of fitted  $x$ . To be more definitive, for the purposes of the present discussion we define the effective intercept as

$$\alpha_{eff}(\sim^2) = \frac{\log[F(x_2; \sim^2) - F(x_1; \sim^2)]}{\log(x_1/x_2)} \quad (8.4)$$

taking  $x_2 = 10^{-5}$  and  $x_1 = 10^{-3}$ . The effective intercept  $\alpha_{hard}(\sim^2)$  is defined by (8.4) in terms of  $F_{hard}(x; \sim^2)$ .

One can define the related intercepts  $\alpha_{eff}; \alpha_{hard}$  for the integrated gluon structure function  $G_D(x; Q^2)$ :

$$G_D(x; Q^2) / \frac{1}{x^{\alpha_{eff}(Q^2)}} : \quad (8.5)$$

In the case of  $F_{2p}(x; Q^2)$  we define the intercept  $\alpha(Q^2)$  in terms of the variable  $\bar{x}$  defined as

$$\bar{x} = \frac{Q^2 + M_V^2}{W^2 + Q^2} x_g ; \quad (8.6)$$

where  $M_V$  is the mass of the ground state vector meson in the considered flavor channel. Such a replacement allows one to treat on equal footing  $Q^2 < 1 \text{ GeV}^2$ , where the formally defined Bjorken variable  $x$  can no longer be interpreted as a lightcone momentum carried by charged partons. For the purposes of the direct comparison with  $\alpha(Q^2); \alpha_{hard}(Q^2)$  and in order to avoid



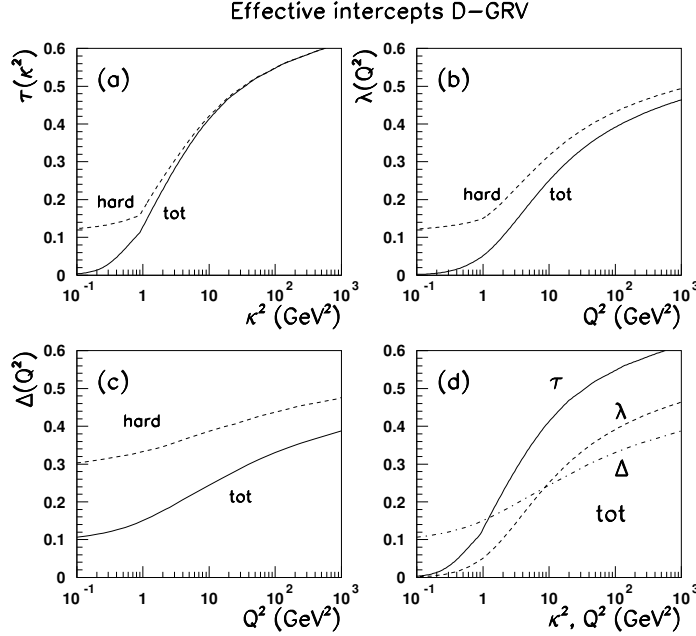


Figure 8.5: Effective intercepts for total, and hard components of, (a) the differential gluon structure function  $F(x; Q^2)$ ; (b) integrated gluon structure function  $G_D(x; Q^2)$  and (c) proton structure function  $F_{2p}(x; Q^2)$  evaluated with the D-GRV parameterization of the differential gluon structure function  $F(x; Q^2)$ . In the box (d) we compare the effective intercepts  $\tau_{\text{eff}}(Q^2)$ ;  $\lambda_{\text{eff}}(Q^2)$  and  $\Delta_{\text{eff}}(Q^2)$  for  $F(x; Q^2)$ ,  $G_D(x; Q^2)$  and  $F_{2p}(x; Q^2)$ , respectively.

biases caused by the valence structure function, here we focus on intercepts  $\tau_{\text{eff}}$ ;  $\lambda_{\text{eff}}$  for the sea component of the proton structure function  $F_{2p}^{\text{sea}}(x; Q^2)$ :

$$F_{2p}^{\text{sea}}(x; Q^2) / \frac{1}{x} \tau_{\text{eff}}(Q^2) : \quad (8.7)$$

The results for the effective intercepts are shown in Figs. 8.5, 8.6 and 8.7.

In our simplified hard-to-soft extrapolation of  $F_{\text{hard}}(x; Q^2)$  we attribute to  $F_{\text{hard}}(x; Q^2)$  at  $Q^2 = Q_c^2$  the same  $x$ -dependence as at  $Q^2 = Q_c^2$  modulo slight modifications for the  $x$ -dependence of  $\sim x_h^2$ . This gives the cusp in  $\tau_{\text{hard}}(Q^2)$  at  $Q^2 = Q_c^2$ , i.e., the first derivative of  $\tau_{\text{hard}}(Q^2)$  is discontinuous at  $Q^2 = Q_c^2$ .

A comparison of Fig. 8.2 with Fig. 8.3 and further with Fig. 8.4 shows clearly that only in DGSF  $F(x; Q^2)$  the effect of the soft component is concentrated at small  $Q^2$ . In integrated  $G_D(x; Q^2)$  and especially in the proton structure function  $F_{2p}(x; Q^2)$  the impact of the soft component extends to much larger  $Q^2$ . The larger the soft contribution, the stronger is the reduction of  $\tau_{\text{eff}}$  from  $\tau_{\text{hard}}$  and so forth, the pattern which is evident from Fig. 8.5a to 8.5b to 8.5c, see also Figs. 8.6 and 8.7.

The change of effective intercepts from differential  $F(x; Q^2)$  to integrated  $G_D(x; Q^2)$  is straightforward, the principal effect is that  $\tau_{\text{hard}}(Q^2) < \tau_{\text{hard}}(Q^2)$  and  $\tau_{\text{eff}}(Q^2) < \tau_{\text{eff}}(Q^2)$  which reflects the growing importance of soft component in  $G_D(x; Q^2)$ . The change of effective

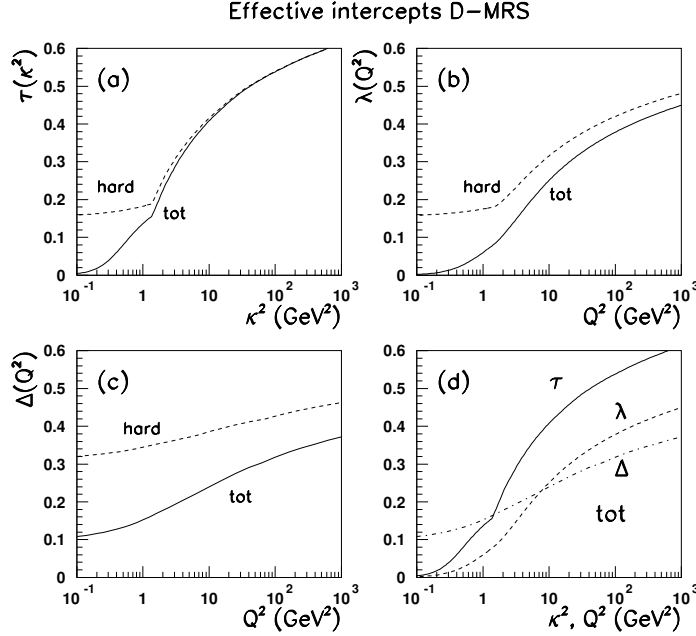


Figure 8.6: Effective intercepts for total, and hard components of, (a) the differential gluon structure function  $F(x; Q^2)$ ; (b) integrated gluon structure function  $G_D(x; Q^2)$  and (c) proton structure function  $F_{2p}(x; Q^2)$  evaluated with the D-MRS parameterization of the differential gluon structure function  $F(x; \tilde{s}^2)$ . In the box (d) we compare the effective intercepts  $\tau_{\text{eff}}(Q^2)$ ;  $\lambda_{\text{eff}}(Q^2)$  and  $\Delta_{\text{eff}}(Q^2)$  for  $F(x; Q^2)$ ,  $G_D(x; Q^2)$  and  $F_{2p}(x; Q^2)$ , respectively.

intercepts from  $F(x; Q^2)$  and  $G_D(x; Q^2)$  to  $F_{2p}(x; Q^2)$  is less trivial and exhibits two dramatic consequences of the hard-to-soft and soft-to-hard diffusion. If the standard DGLAP contribution (3.2) were all, then the change from the intercept  $\tau(Q^2)$  for integrated gluon density to the intercept  $\Delta(Q^2)$  for the proton structure function  $F_{2p}(x; Q^2)$  would be similar to the change from  $\tau(Q^2)$  to  $\lambda(Q^2)$ , i.e., the effective intercept  $\tau_{\text{eff}}(Q^2)$  would have been close to zero for  $Q^2 < 1 \text{ GeV}^2$ . However, by virtue of the hard-to-soft diffusion phenomenon inherent to the  $\tilde{s}$ -factorization,  $F_{2p}(x; Q^2)$  receives a contribution from gluons with  $\tilde{s}^2 > Q^2$ , which enhances substantially  $\lambda_{\text{hard}}(Q^2)$  and  $\Delta_{\text{eff}}(Q^2)$ . The net result is that at small to moderately large  $Q^2$  we find  $\lambda_{\text{hard}}(Q^2) > \tau_{\text{hard}}(Q^2)$  and  $\Delta_{\text{eff}}(Q^2) > \tau_{\text{eff}}(Q^2)$ . As we emphasized above in sections 5.3, the rise of real photoabsorption cross section is precisely of the same origin.

The second effect is a dramatic attenuating of effective hard intercept,  $\lambda_{\text{hard}}(Q^2)$ , over the whole range of  $Q^2$ . For all three DGLAP inputs  $\lambda_{\text{hard}}(Q^2)$  attenuates at approximately the same hard  $\tau_{\text{hard}} \approx 0.4$ .

The whole set of figs. 8.5{8.7 also shows that the systematics of intercepts in the hard region of  $Q^2 > Q_c^2$  is nearly identical for all the three DGLAP inputs. In the soft region we have a slight inequality  $\lambda_{\text{hard}}(\tilde{s}^2)_{\text{MRS}} > \lambda_{\text{hard}}(\tilde{s}^2)_{\text{GRV}}$ , which can be readily attributed to a slight inequality  $Q_c^2(\text{MRS}) > Q_c^2(\text{GRV})$ . In the case of CTEQ4L (v.4.6) input the value of  $Q_c^2(\text{CTEQ})$  is substantially larger than  $Q_c^2(\text{MRS}); Q_c^2(\text{GRV})$ . In the range  $Q_c^2(\text{MRS}); Q_c^2(\text{GRV}) < \tilde{s}^2 < Q_c^2(\text{CTEQ})$  the effective intercept  $\lambda_{\text{hard}}(\tilde{s}^2)$  rises steeply with

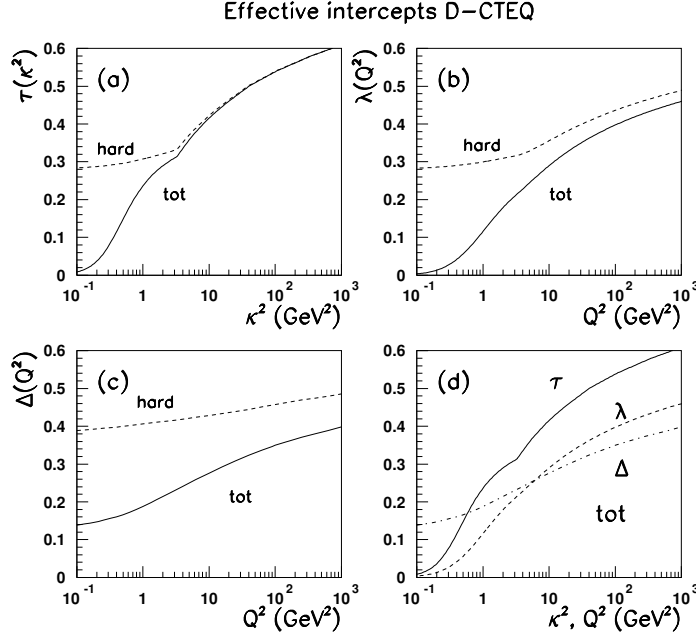


Figure 8.7: Effective intercepts for total, and hard components of, (a) the differential gluon structure function  $F(x; Q^2)$ ; (b) integrated gluon structure function  $G_D(x; Q^2)$  and (c) proton structure function  $F_{2p}(x; Q^2)$  evaluated with the D-CTEQ parameterization of the differential gluon structure function  $F(x; \tilde{Q}^2)$ . In the box (d) we compare the effective intercepts  $\tau_{\text{eff}}(Q^2)$ ;  $\lambda_{\text{eff}}(Q^2)$  and  $\Delta_{\text{eff}}(Q^2)$  for  $F(x; Q^2)$ ,  $G_D(x; Q^2)$  and  $F_{2p}(x; Q^2)$ , respectively.

$\tilde{Q}^2$ . This explains a why in the soft region  $\tau_{\text{hard}}(\tilde{Q}^2)_{\text{D-TEQ}}$  is significantly larger than for the D-GRV and D-MRS parameterizations. The difference among intercepts for the three parameterizations decreases gradually from differential  $F(x; \tilde{Q}^2)$  to integrated  $G_D(x; Q^2)$  gluon density to the proton structure function  $F_{2p}(x; Q^2)$ .

Finally, in Fig. 8.8 we compare our results for  $\tau_{\text{eff}}(Q^2)$  with the recent experimental data from ZEUS collaboration [61]. Since in the experimental fit the range of  $x = [x_{\text{max}}; x_{\text{min}}]$  varies from point to point, we mimicked the experimental procedure in our evaluation of  $\tau_{\text{eff}}$  from eq. (8.11) by taking  $\bar{x}_2 = x_{\text{max}}$  and  $\bar{x}_1 = x_{\text{min}}$ . This explains the somewhat irregular  $Q^2$  dependence. The experimental data include both sea and valence components. At  $Q^2 > Q_c^2(\text{GRV}) = 0.9 \text{ GeV}^2$  we included the valence component of the structure function taking the GRV98LO parameterization. For CTEQ4L (v4.6) and MRS-LO-1998 the values of  $Q_c^2$  are substantially larger. However, the valence component is a small correction and we took a liberty of extracting the valence contribution  $F_{2p}^{\text{val}}(x; Q^2)$  from GRV fits for  $Q_c^2(\text{GRV}) < Q^2 < Q_c^2(\text{MRS}); Q_c^2(\text{CTEQ})$ . The overall agreement with experiment is good. Difference among the three parameterization is marginal and can of course be traced back to figs. 8.5{8.7.

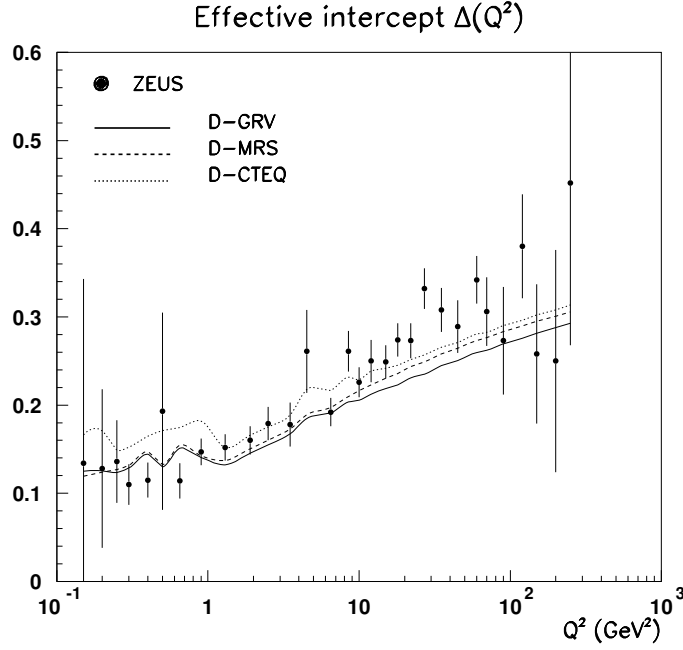


Figure 8.8: Effective intercepts  $\Delta(Q^2)$  of the proton structure function  $F_{2p}(x;Q^2)$  in the HERA domain evaluated for the D-GRV, D-MRS and D-CTEQ parameterizations for the differential gluon structure function  $F(x;\sim^2)$ ; the experimental data points are from ZEUS [61]

### 8.3 How the gluon densities of $\sim$ -factorization differ from DGLAP gluon densities

It is instructive also to compare our results for integrated GSF (8.1) with the conventional DGLAP  $\int G_{pt}(x;Q^2)$ . In Fig. 8.9 we present such a comparison between our integrated D-GRV distribution (the solid curves) and the GRV98LO distribution (the dashed curves). As was anticipated in section 3.2, at very large  $Q^2$  the two gluon distributions converge. We also anticipated that at small  $x$  and moderate  $Q^2$  the DGLAP gluon structure functions  $G_{pt}(x;Q^2)$  are substantially larger than the result of integration of DGSF, see eq. (8.1). At  $x = 10^{-5}$  they differ by as much as the factor two-three over a broad range of  $Q^2 < 100 \text{ GeV}^2$ . The difference between integrated DGSF and the DGLAP  $\int$  decreases gradually at large  $x$ , and is only marginal at  $x = 10^{-2}$ .

Recall the substantial divergence of the GRV, MRS and CTEQ gluons structure functions of DGLAP approximation  $G_{pt}(x;Q^2)$  at small and moderate  $Q^2$ . Contrary to that, the  $\sim$ -factorization D-GRV, D-CTEQ and D-MRS gluon structure functions  $G_D(x;Q^2)$  are nearly identical. We demonstrate this property in Fig. 8.10 where we show integrated  $G_D(x;Q^2)$  and their DGLAP counterparts  $G_{pt}(x;Q^2)$  for the three parameterizations at two typical values of  $x$ . Because of an essentially unified treatment of the region of  $\sim^2 \sim Q_c^2$  and strong constraint on DGSF in this region from the experimental data at small  $Q^2$ , such a convergence of D-GRV, D-CTEQ and D-MRS DGSFs is not unexpected.

One can also compare the effective intercepts for our integrated GSF  $G_D(x;Q^2)$  with

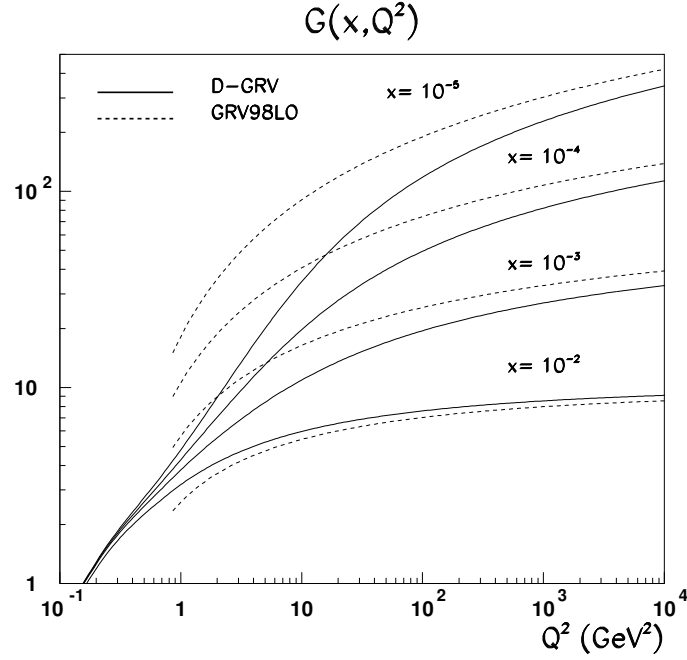


Figure 8.9: Comparison of our results for integrated gluon density  $G_D(x; Q^2)$  evaluated with the D-GRV parameterization of the differential gluon structure function  $F(x; Q^2)$  with the GRV98LO DGLAP input parameterization  $G_{pt}(x; Q^2)$ .

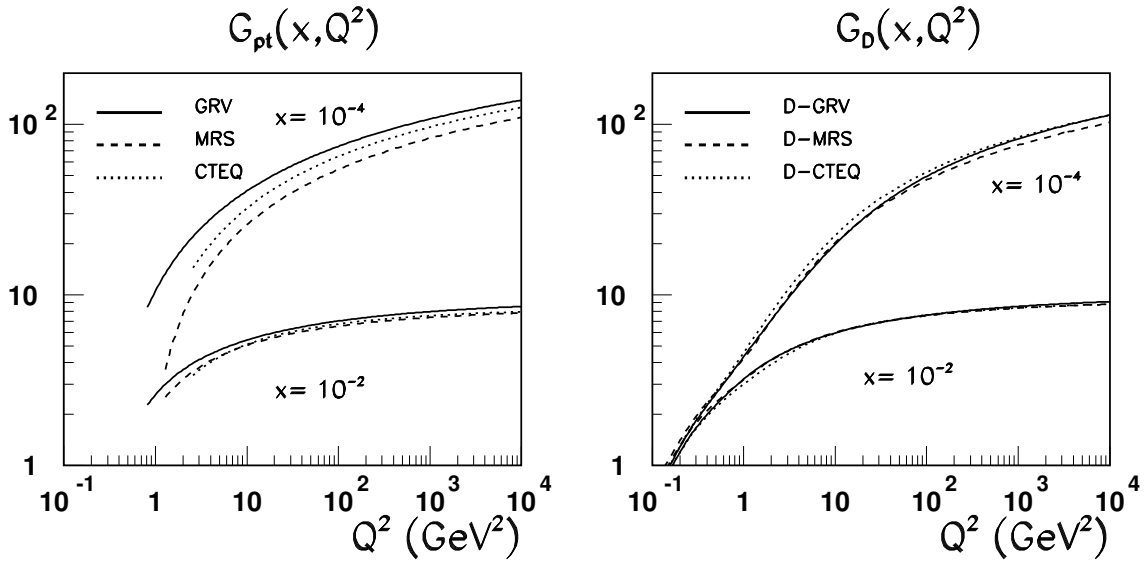


Figure 8.10: A comparison of the divergence of GRV98LO, CTEQ4L (v.4.6) and MRS-LO-1998 gluon structure functions  $G_{pt}(x; Q^2)$  in the left box with the divergence of our integrated gluon structure functions  $G_D(x; Q^2)$  evaluated for the D-GRV, D-CTEQ and D-MRS parameterizations for differential gluon structure function  $F(x; Q^2)$  at two typical values of  $x$ .

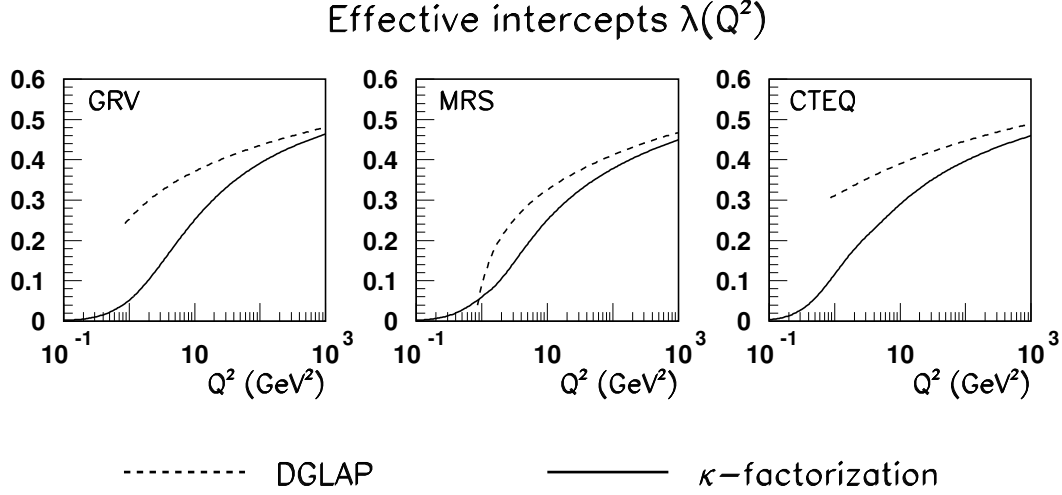


Figure 8.11: A comparison of the intercept  $\lambda_{\text{eff}}^{(\text{pt})}(Q^2)$  of the  $x$ -dependence of the GRV 98L0, CTEQ 4L (v.4.6) and MRS-L0-1998 gluon structure functions  $G_{\text{pt}}(x; Q^2)$  with their counterpart  $\lambda_{\text{eff}}(Q^2)$  for integrated  $G_D(x; Q^2)$  evaluated with D-GRV, D-CTEQ and D-MRS parameterizations for differential gluon structure function  $F(x; Q^2)$ .

those obtained from DGLAP gluon distributions  $G_{\text{pt}}(x; Q^2)$ . Fig.8.11 shows large scattering of  $\lambda_{\text{eff}}^{(\text{pt})}(Q^2)$  from one DGLAP input to another. At the same time, this divergence of different DGLAP input parameterizations is washed out to a large extent in the  $\kappa$ -factorization description of physical observables (see also (8.8)).

## 8.4 How different observables probe the DGSF

The issue we address in this section is how different observables map the  $\sim^2$  dependence of  $F(x; \sim^2)$ . We expand on the qualitative discussion in section 3.2 and corroborate it with numerical analysis following the discussion in [52]. We start with the two closely related quantities — longitudinal structure function  $F_L(x; Q^2)$  and scaling violations  $\partial F_2(x; Q^2)/\partial \log Q^2$  — and proceed to  $F_{2p}(x; Q^2)$  and the charm structure function of the proton  $F_{2p}^{\text{cc}}(x; Q^2)$ . This mapping is best studied if in (2.40) and (2.41) we integrate first over  $k$  and  $z$ . In order to focus on the  $\sim^2$  dependence we prefer presenting different observables in terms of  $F(2x; \sim^2)$  and  $G_D(2x; \sim^2)$

$$F_L(x; Q^2) = \frac{s(Q^2)x}{3} e_f^2 \int_{\sim^2}^Z \frac{d\sim^2}{\sim^2} \lambda_L^{(\text{ff})}(Q^2; \sim^2) F(2x; \sim^2); \quad (8.8)$$

$$\frac{\partial F_2(x; Q^2)}{\partial \log Q^2} = \frac{s(Q^2)x}{3} e_f^2 \int_{\sim^2}^Z \frac{d\sim^2}{\sim^2} \lambda_2^{(\text{ff})}(Q^2; \sim^2) F(2x; \sim^2); \quad (8.9)$$

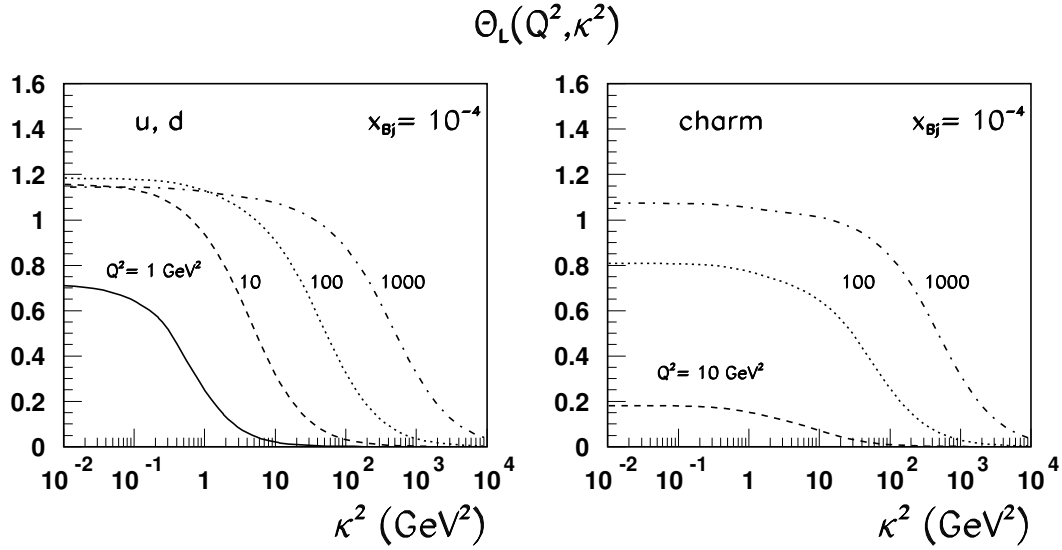


Figure 8.12: The weight function  $\Theta_L$  for mapping of the differential gluon structure function  $F(x; \kappa^2)$  as a function of  $\kappa^2$  for several values of  $Q^2$ . We show separately the results for light flavours,  $u; d$ , and charm.

In the numerical calculation of  $F_L(x; Q^2)$  starting from eq. (2.41) we have  $x_g$  and  $\kappa^2$  as the two running arguments of  $F(x_g; \kappa^2)$ . As discussed above, the mean value of  $x_g$  is close to  $2x$ , but the exact relationship depends on  $\kappa^2$ . The  $\kappa; z$  integration amounts to averaging of  $F(x_g; \kappa^2)$  over certain range of  $x_g$ . The result of this averaging is for the most part controlled by the effective intercept  $\gamma_{eff}(\kappa^2)$ :

$$\langle F(x_g; \kappa^2) \rangle = \int_{x_g}^{2x} F(2x; \kappa^2) \frac{2x}{x_g} \gamma_{eff}(\kappa^2) d\kappa = r(\kappa^2) F(2x; \kappa^2); \quad (8.10)$$

Because the derivative of  $\gamma_{eff}(\kappa^2)$  changes rapidly around  $\kappa^2 = Q_c^2$ , the rescaling factor  $r(\kappa^2)$  also has a rapid variation of the derivative at  $\kappa^2 = Q_c^2$ , which in the due turn generates the rapid change of derivatives of  $\frac{d}{d\kappa^2} \frac{\partial}{\partial \log \kappa^2} F_L^{(ff)}(Q^2; \kappa^2)$  around  $\kappa^2 = Q_c^2$ . As far as the mapping of differential  $F(2x; \kappa^2)$  is concerned, this is an entirely marginal effect. However, if we look at the mapping of integrated gluon structure function  $G_D(x; Q^2)$ , which is derived from (8.8), (8.9) by integration by parts:

$$F_L(x; Q^2) = \frac{s(Q^2)x}{3} \int_{\kappa^2}^Z e_f^2 \frac{d\kappa^2}{\kappa^2} \frac{\partial}{\partial \log \kappa^2} F_L^{(ff)}(Q^2; \kappa^2) G_D(2x; \kappa^2); \quad (8.11)$$

$$\frac{\partial F_2(x; Q^2)}{\partial \log Q^2} = \frac{s(Q^2)x}{3} \int_{\kappa^2}^Z e_f^2 \frac{d\kappa^2}{\kappa^2} \frac{\partial}{\partial \log \kappa^2} F_2^{(ff)}(Q^2; \kappa^2) G_D(2x; \kappa^2); \quad (8.12)$$

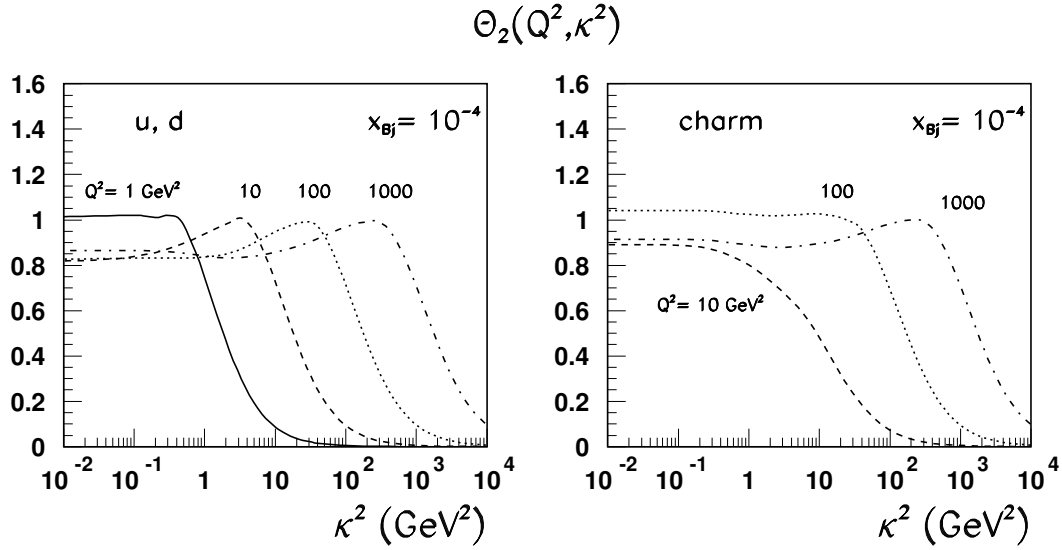


Figure 8.13: The weight function  $\Theta_2$  for mapping of the differential gluons structure function  $F_2(x; \kappa^2)$  as a function of  $\kappa^2$  for several values of  $Q^2$ . We show separately the results for light flavours,  $u; d$ , and charm.

then the weight functions  $\Theta_{2;L}^{(ff)}(Q^2; \kappa^2) = \Theta \log \kappa^2$  will exhibit a slightly irregular behaviour around  $\kappa^2 = Q_c^2$ . Evidently, such an irregularity appears in any region of fast variation of  $e_{ff}(\kappa^2)$ ; in our simplified model it is somewhat amplified by the cusp-like  $\kappa^2$  dependence of  $e_{ff}(\kappa^2)$ .

Finally, starting from (8.12) one obtains a useful representation for how the proton structure function  $F_{2p}(x; Q^2)$  maps the integrated gluon structure function:

$$\begin{aligned}
 F_{2p}(x; Q^2) &= \int_0^{Q^2} \frac{dq^2}{q^2} \frac{s(q^2)}{3} \times e_f^2 \int_{\kappa^2}^{\infty} \frac{d\kappa^2}{\kappa^2} \frac{\Theta_{2;L}^{(ff)}(q^2; \kappa^2)}{\Theta \log \kappa^2} G_D(2x; \kappa^2) \\
 &= \frac{1}{3} \times e_f^2 \int_{\kappa^2}^{\infty} \frac{d\kappa^2}{\kappa^2} W_2^{(ff)}(Q^2; \kappa^2) s(\kappa^2) G_D(2x; \kappa^2)
 \end{aligned} \quad (8.13)$$

In figs. 8.12 and 8.13 we show the weight functions  $\Theta_L$  and  $\Theta_2$ . Evidently, for light flavours and very large  $Q^2$  they can be approximated by step-functions

$$\Theta_{L;2}^{(ff)}(Q^2; \kappa^2) = (C_{L;2} Q^2 / \kappa^2); \quad (8.14)$$

where the scale factors  $C_L = \frac{1}{2}$  and  $C_2 = 2$  can be readily read from figures, for the related discussion see [52]. Note that the value  $C_2 = 2$  corresponds to  $C_2 = 8$  introduced in Section 3.2. Recall that the development of the plateau-like behaviour of  $\Theta_L$  and  $\Theta_2$  which extends to  $\kappa^2 = Q^2$  signals the onset of the leading  $\log Q^2$  approximation. For large  $Q^2$  in the approximation (8.14) the  $\kappa^2$  integration can be carried out explicitly and  $F_L(x; Q^2) / G_D(2x; C_L Q^2)$ . Similarly,  $\Theta F_2(x; Q^2) = \Theta \log Q^2 / G_D(2x; C_2 Q^2)$ , cf. eq. (3.6).



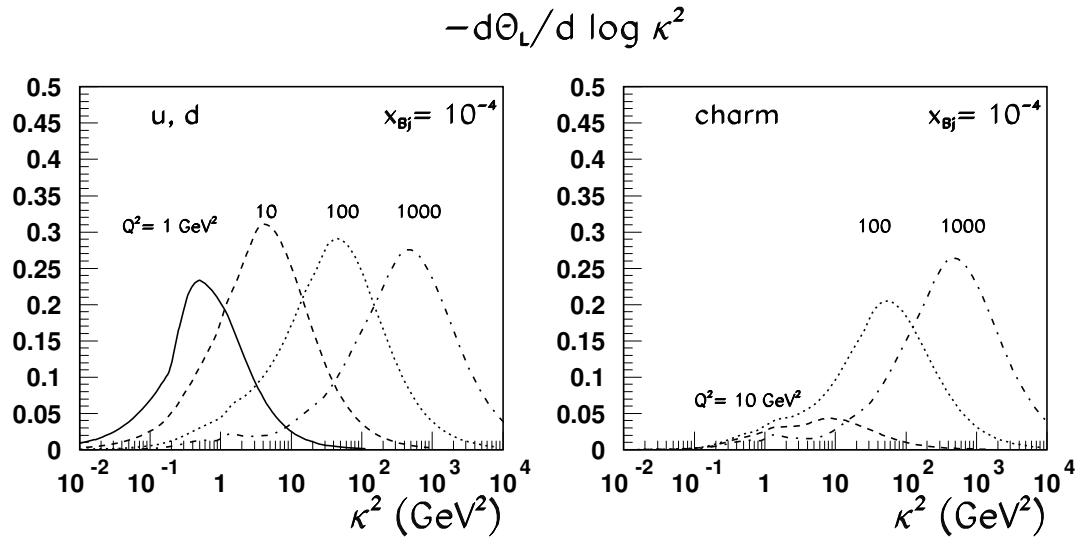


Figure 8.14: The same as Fig. 8.12 but for mapping of the integrated gluon structure function  $G_D(x; \sim^2)$  as a function of  $\sim^2$  for several values of  $Q^2$ . We show separately the results for light flavours and charm.

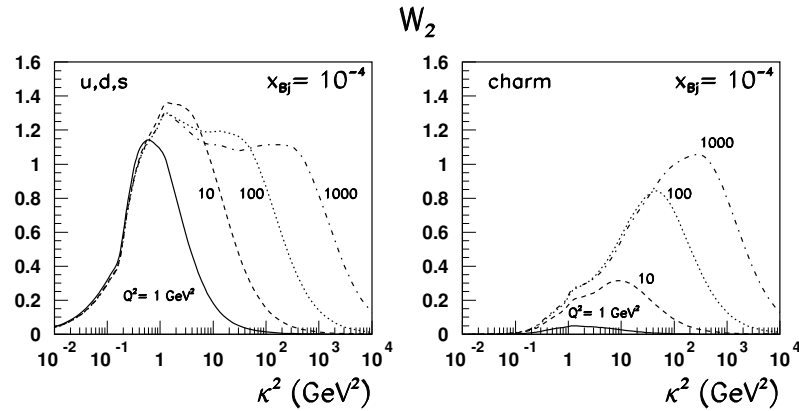


Figure 8.15: The weight function  $W_2$  for mapping of the integrated gluons structure function  $G_D(x; \sim^2)$  as a function of  $\sim^2$  for several values of  $Q^2$ . We show separately the results for light flavours and charm.

Still better idea on how  $F_L$  and scaling violations map the integrated GSF is given by gs. 8.14, 8.15, where we show results for  $\Theta^{(ff)}_L = \Theta \log \sim^2$  and  $W_2^{(ff)}$ . The first quantity is sharply peaked at  $\sim^2 = C_L Q^2$ . The second quantity visibly develops a plateau at large

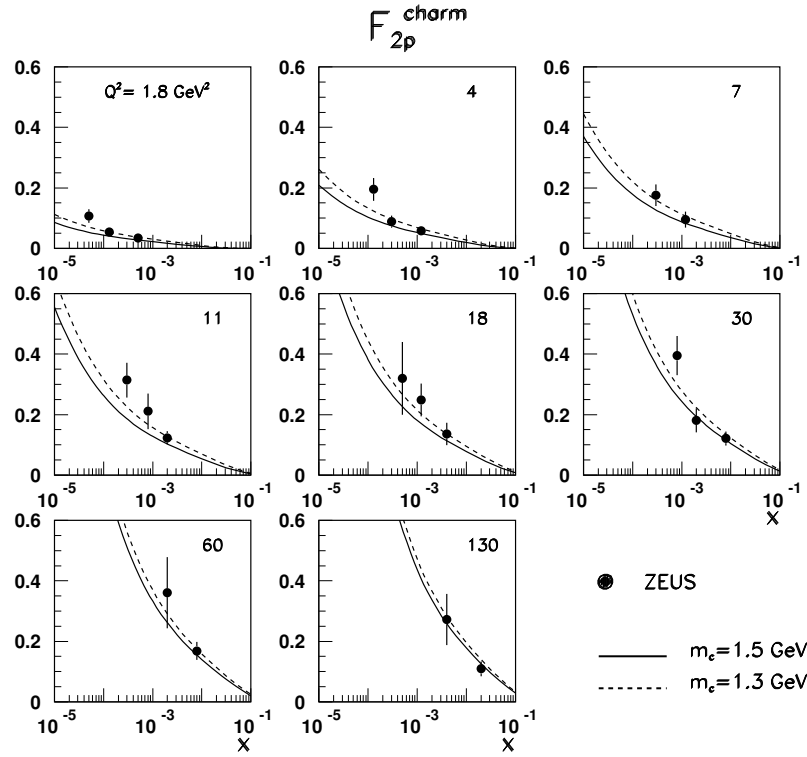


Figure 8.16: A comparison of the experimental data from ZEUS [69] on the charm structure function of the proton with  $\sim$ -factorization results for  $F_{2p}^{\infty}(x;Q^2)$  based on the D-GRV parameterization of the differential gluon structure function  $F(x;Q^2)$ .

$Q^2$ . As can be easily seen, scaling violations do receive a substantial contribution from the beyond-DGLAP region of  $\sim^2 > Q^2$ .

Because of the heavy mass, the case of the charm structure function  $F_{2p}^{\infty}(x;Q^2)$  is somewhat special. Figs. 8.14 and 8.15 show weak sensitivity of  $F_{2p}^{\infty}(x;Q^2)$  to the soft component of  $F(x;\sim^2)$ , which has an obvious origin: long-wavelength soft gluons with  $\sim < m_c$  decouple from the color neutral cc Fock state of the photon, which has a small transverse size  $< \frac{1}{m_c}$ . Our results for  $F_{2p}^{\infty}(x;Q^2)$  are shown in Fig. 8.16, the agreement with the recent precision experimental data from ZEUS [69] is good.

## Chapter 9

# Improved determination of the differential gluon in proton: DGD 2002 analysis

During the last two years new high-accuracy measurements of structure function  $F_{2p}$  in the expanded parameter space were presented by ZEUS [70], [71] and H1 [72]. In the light of our analysis, the most important improvement was further plunging into low- $x$  region (down to  $x = 6 \cdot 10^{-5}$ , [70]) and 2–3% accurate determination of  $F_{2p}$  in the small- $Q^2$  ( $0.25 \text{ GeV}^2 < Q^2 < 0.65 \text{ GeV}^2$ ) and relatively small- $x$  ( $10^{-5} < x < 10^{-3}$ ) region. Even a brief comparison of  $k_t$ -factorization predictions for  $F_{2p}$  in this region based on the differential gluon from the previous section showed a systematic several-sigma deviation from experimental points. The second problem with old differential gluon was that we did not quite match the experimentally measured exponent of  $F_{2p}$  rise towards high  $1/x$ . As our analysis showed (see Fig. 8.8), the predicted intercept was 1–2% lower at  $Q^2 > 10 \text{ GeV}^2$ .

Thus, not being able to claim that we reproduce with old differential gluon the  $F_{2p}$  data well enough, we re-extracted the differential gluon structure function. This time, the eye-balls were not acceptable, and therefore a  $\chi^2$ -minimization procedure was carried out. This communication presents the results of this reevaluation.

## 9.1 Fitting procedure and parameters of DGSF

Our goal is a determination of small- $x$  DGSF in the whole range of  $x$  by adjusting the relevant parameters to the experimental data on small- $x$   $F_{2p}(x; Q^2)$  in the whole available region of  $Q^2$ . The  $k_t$ -factorization predictions for  $F_{2p}$  were calculated at  $N = 191$  points in  $(x; Q^2)$  space and compared to the experimentally values measured at HERA. These points include all data available at the moment for low- $Q^2$  region ( $Q^2 < 1 \text{ GeV}^2$ ) as well as all data points for several higher values of  $Q^2$ , namely, at  $Q^2 = 1.5 \text{ } 2.5 \text{ } 2.7 \text{ } 3.5 \text{ } 4.5 \text{ } 5.0 \text{ } 6.5 \text{ } 10 \text{ } 35 \text{ GeV}^2$ . The  $\chi^2$  was calculated according to

$$\chi^2 = \sum_{i=1}^N \frac{(F_{2p}^{\text{theor}} - F_{2p}^{\text{exp}})^2}{\sigma_{\text{stat}}^2 + \sigma_{\text{syst}}^2} : \quad (9.1)$$

The parameters which we did not try adjusting but borrowed from early work in the color dipole picture are  $R_c = 0.27 \text{ fm}$ , i.e.,  $\mu_{\text{pt}} = 0.75 \text{ GeV}$  and the frozen value of the

LO QCD coupling with  $\alpha_{\text{QCD}} = 0.2 \text{ GeV}$  (7.11). Our previous analysis showed that the parametrizations D-GRV, D-MRS, and D-CTEQ (that is, DGSF based on GRV, MRS, and CTEQ sets to integrated gluons) run very close to one another throughout the whole  $x, \sim^2$  space. This can be verbalized as no matter from what particular DGLAP parametrization we start, we will arrive at virtually the same shape of the differential gluon structure function. To this end, we used only GRV98LO sets, since they are available for the widest range of  $x$  and  $Q^2$  values.

The adjustable parameters are  $\mu_{\text{soft}}, a_{\text{soft}}, m_{u,d}, \sim_s^2$  and  $\sim_h^2$  (for the heavier quark masses we take  $m_s = m_{u,d} + 0.15 \text{ GeV}$  and  $m_c = 1.5 \text{ GeV}$ ). The both  $m_{u,d}$  and  $\mu_{\text{soft}}$  have clear physical meaning and we have certain insight into their variation range from the early work on color dipole phenomenology of DIS. The role of these parameters is as follows. The quark mass  $m_{u,d}$  defines the transverse size of the  $q\bar{q} = u\bar{u}; d\bar{d}$  Fock state of the real photon, whose natural scale is the size of the  $\rho$ -meson. Evidently, roughly equal values of  $F_{2p}(x; Q^2)$  can be obtained for somewhat smaller  $F(x; Q^2)$  at the expense of taking smaller  $m_{u,d}$  and vice versa. Therefore, though the quark mass does not explicitly enter the parametrization for  $F(x; \sim^2)$ , the preferred value of  $m_{u,d}$  could have been correlated with the DGLAP input. We find that it is sufficient to take the universal  $m_{u,d} = 0.21 \text{ GeV}$ , which is slightly lower than  $0.22 \text{ GeV}$ , used before.

Parameter  $\mu_{\text{soft}}$  defines the soft scale in which the non-perturbative glue is connected, and controls the  $r$ -dependence of, and in conjunction with  $a_{\text{soft}}$  sets the scale for, the dipole cross section for large size  $q\bar{q}$  dipoles in the photon. We find that it is sufficient to take the universal  $\mu_{\text{soft}} = 0.1 \text{ GeV}$  and  $\sim_s^2 = 1 \text{ GeV}^2$ .

The magnitude of the dipole cross section at large and moderately small dipole size depends also on the soft-to-hard interpolation of DGSF, which is sensitive to DGLAP inputs for perturbative component  $G_{\text{pt}}(x; Q^2)$ . This difference of DGLAP inputs can be corrected for by adjusting the hard-to-soft interface parameter  $\sim_h^2$ . The slight rise of  $\sim_h^2$  helps to suppress somewhat too strong  $x$ -dependence of the soft tail of the perturbative glue. The specific parametrizations for  $\sim_h^2$  depend on the DGLAP input and are presented in Table 2. Only  $\sim_h^2$  and  $\mu_{\text{soft}}$  varied from one DGLAP input to another.

In order to be able to assess the uncertainty in determination of differential glue, we performed several  $\chi^2$  minimization procedures using slightly different sets of free parameters. The resulting parameters of the fits are shown in Table 2; below we comment on each fit in detail.

## Fit 1

When obtaining Fit 1, we adjusted values of  $a_{\text{soft}}$ , transition point  $Q_c^2$  in (7.8), functional form of  $\sim_h^2 = \sim_h^2(x)$ , which we took as a first order polynomial  $a + b \log(1/x)$ , and the power of the high- $x$  suppressing factor  $(1 - x)$ .

The resulting value of  $\chi^2$  turned out uncomfortably large 11. Numerically, such a strong suppression serves as a remedy against somewhat too slow  $x$  behavior of  $F_{2p}$  as we approach  $x \sim 10^2$  from the low- $x$  side. Although rather artificial, this suppressing factor does not invalidate our approach since the exact behavior of the glue in the limit  $x \rightarrow 1$  lies far beyond the scope of the present approach. Still, we would like to note the alarming tendency that even with this factor large part of the overall  $\chi^2$  comes precisely from the region we wanted to correct ( $10^{-3} < x < 10^{-2}$ ). This might be an indication that our understanding of this region

is far from perfect. More analysis is needed to settle up this issue.

### Fit 2

In Fit 2 we opened up another degree of freedom, namely, we allowed for shifting in the second argument of  $G(x; Q^2)$ . As early analyses showed, the best  $k_t$ -factorization vs. DGLAP correspondence would be

$$F(x; \tilde{Q}^2) \propto \frac{\partial G(x; Q^2)}{\partial \log Q^2} \Big|_{Q^2 = C \tilde{Q}^2} \quad (9.2)$$

The early analysis gave  $C = 2$ , but in our approach we treated  $C$  as free parameter.

We started from Fit 1 and let the  $\tilde{Q}^2$  slide to its minimum as we freed parameter  $C$ . We expected  $C > 1$  at minimum point. Indeed, our predictions with Fit 1 for high- $Q^2$  region suffered from too high values at high  $x$  and too low values at very small  $x$ . As early analysis indicated, when we shift the  $\tilde{Q}^2$  scale according to (9.2), we make the unintegrated gluon density increase at  $x < 10^{-3}$  and decrease at higher values of  $x$ . We expect this tendency to survive the multiple integration procedure and to echo in the proton structure  $F_{2p}$ .

The minimization procedure gave  $C = 1.1$  with slight adjustment of other parameters, see Table 1 for details.

### Fit 3

In the region of very hard gluons both Fit 1 and Fit 2 rely on the leading order DGLAP parametrizations of  $G(x; Q^2)$ . Although it is desirable that integrated gluon structure function  $G_D(x; Q^2)$  based on our parametrizations approaches in the double logarithmic limit the conventional gluon density obtained from DGLAP evolution, there is certainly no requirement that our fits be built on these DGLAP fits. One should only make sure that at  $\log(1-x) \rightarrow 1$  and  $\log(Q^2 = \frac{2}{Q_{CD}}) \rightarrow 1$  behavior of our fits is compatible with the corresponding behavior of the DGLAP fits.

The properties of the DGLAP-evolved gluon density in the limit is well understood. Since the anomalous dimension of gluons is higher than that of the sea quarks, the secondary gluons in this limit tend to be radiated off gluons as well. The evolution of the integrated gluon density  $G(x; Q^2) = xg(x; Q^2)$  separates out and is governed by

$$\frac{\partial G(x; Q^2)}{\partial \log Q^2} = \frac{s(Q^2)}{2} \int_x^1 dz G\left(\frac{x}{z}; Q^2\right) P_{GG}(z); \quad (9.3)$$

with splitting function

$$P_{GG}(z) = 2N_c \left[ z(1-z) + \frac{z}{(1-z)_+} + \frac{1}{z} \right] + \frac{11}{6} N_c (1-z); \quad (9.4)$$

The Regge-type behavior

$$G(x; Q^2) = f(Q^2) \frac{1}{x} \quad (9.5)$$

with constant  $f$  is compatible with the DGLAP equations and leads to

$$\frac{d \log f(Q^2)}{ds} = 4N_c \int_x^1 dz z \left[ z(1-z) + \frac{z}{(1-z)_+} + \frac{1}{z} \right] + (1-z) \frac{11}{12}$$

$$= 4N_c \left[ \frac{1}{+1} + \frac{1}{+2} + \frac{1}{+3} + \frac{11}{12} + C + \gamma_E \right] \quad (9.6)$$

Here

$$s = \log^4 \frac{\log^2 Q^2}{\log^2 Q_0^2} \quad (9.7)$$

and  $C$  and  $\gamma_E$  are the Euler constant and the digamma function respectively. One immediately gets the solution for the integrated gluon structure function

$$G(x; Q^2) / \log^2 \frac{Q^2}{Q_0^2} \sim \frac{1}{x} \quad ; \quad (9.8)$$

which leads to the differential glue of the form

$$F(x; \tilde{s}^2) / \log^2 \frac{\tilde{s}^2}{Q_0^2} \sim \frac{1}{x} \quad : \quad (9.9)$$

This analysis inspires us search for a parametrization of  $F_{pt}$  that would be power-like both in  $\log \tilde{s}^2 = \log^2 Q^2$  and  $\log(1-x)$  in the double logarithmic regime.

The functional form of  $F_{pt}$  Fit 3 is based on is

$$F_{pt}(x; \tilde{s}^2)_{Fit3} = 0.245 \log^2 \frac{\tilde{s}^2}{Q_0^2} \left( 1 - \frac{1}{x} \right)^{0.4} \quad (9.10)$$

Table 2. The parameters of DGD 2002 fits to differential gluon densities.

	Fit 1	Fit 2	Fit 3
hard input $\tilde{s}^2$ -shift	GRV 98LO	GRV 98LO	Eq.(9.10)
$Q_c^2, \text{GeV}^2$	1.45	1.45	1.4
$a_{\text{soft}}$	2.66	2.63	2.6
$a_h^2, \text{GeV}^2$	$0.4 + 0.245 \log \frac{1}{x}$	$0.38 + 0.245 \log \frac{1}{x}$	$0.31 \log \frac{1}{x}$
total $\chi^2$	257	245	226

## 9.2 The properties of the gluon structure function

In Fig. 9.1 we plotted the three fits to the differential gluon structure functions obtained above vs.  $\tilde{s}^2$  at several values of  $x$ . One observes here a number of interesting features. First, the three curves display rather similar behavior at very small  $x$ , but at  $x$  as high as  $10^{-2}$  the difference among them throughout the region  $\tilde{s}^2 > 1 \text{ GeV}^2$  is quite sizable. Still, all of these parametrizations of DGSF do provide a reasonably accurate description of  $F_{2p}$ . Thus, we conclude that modern experimental data on  $F_{2p}$  do not place severe restrictions on the shape of differential glue at not very small  $x$  (say,  $x > 10^{-3}$ ).

The second feature of the curves presented is their salient two-peak shape. The technical origin of this clear separation of the soft and hard exchange mechanisms is, of course, the

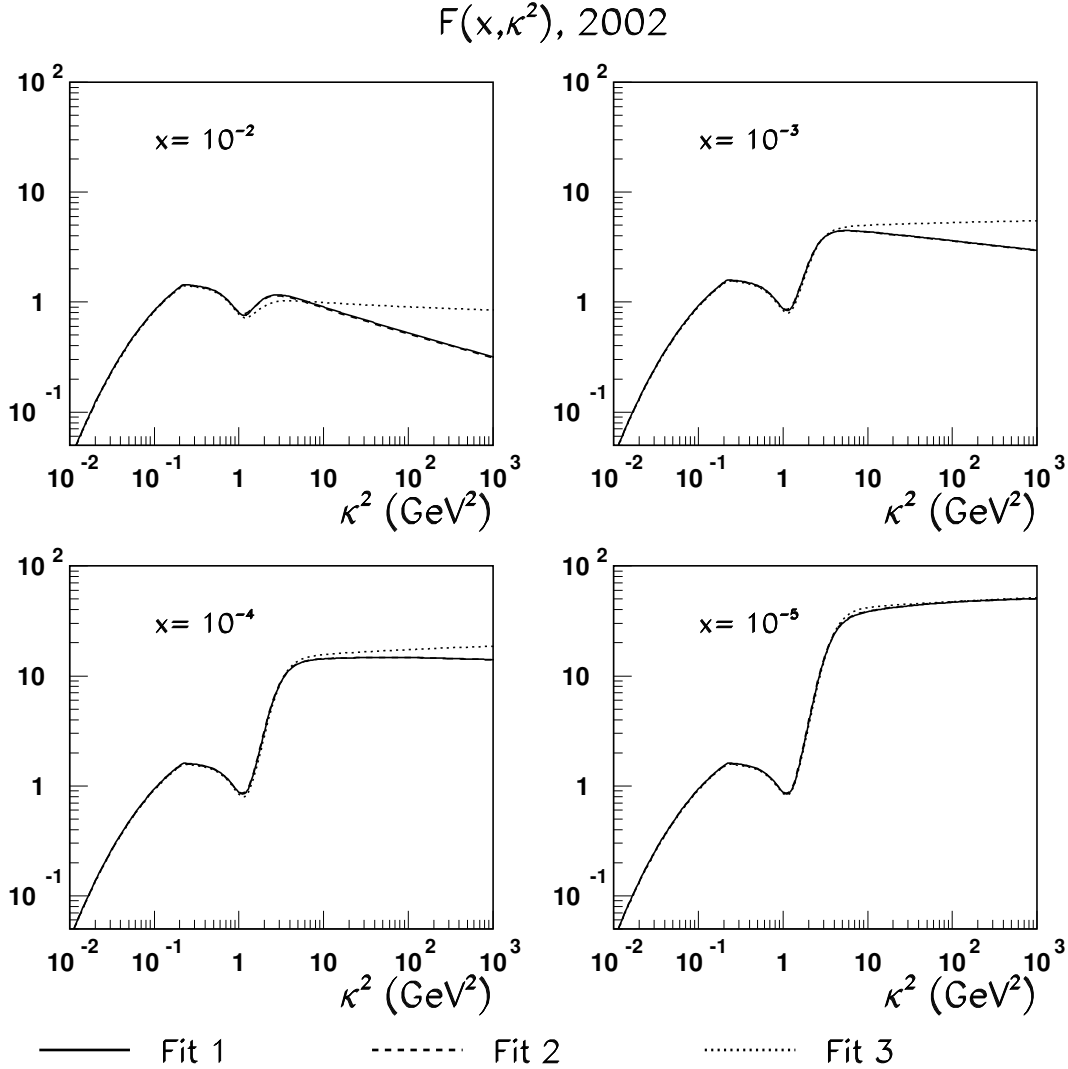


Figure 9.1: Differential gluon structure function as function of  $\kappa^2$ : DGD 2002 analysis

very abrupt extrapolation of soft gluons into hard region and vice versa, generated by high powers  $\sim \kappa^2$ . This might seem artificial, but as we described, such abrupt extrapolation seemed necessary in order to obtain the correct behavior of effective intercept of  $F_{2p}$  and therefore it was quite essential for getting better  $\sim \kappa^2$ . Thus, we inclined to think that such clear separation of the soft and hard mechanisms is indeed preferred by experiment.

The integrated gluon structure function is shown in Figs. 9.2. A similar observation, though in a subdued form, can be made. At  $x = 10^{-2} - 10^{-3}$  one can notice some departure among the curves, which die out as we shift towards lower and lower  $x$ . As we go to smaller  $x$ , we observe plateau around  $\sim \kappa^2 = 1 - 3 \text{ GeV}^2$ , which originates from the two-peak shape of  $F(x; \sim \kappa^2)$ , become more and more prominent.

Note also that at small  $x$  and very large  $Q^2$  all three  $G_D(x; Q^2)$  curves, including Fit 3

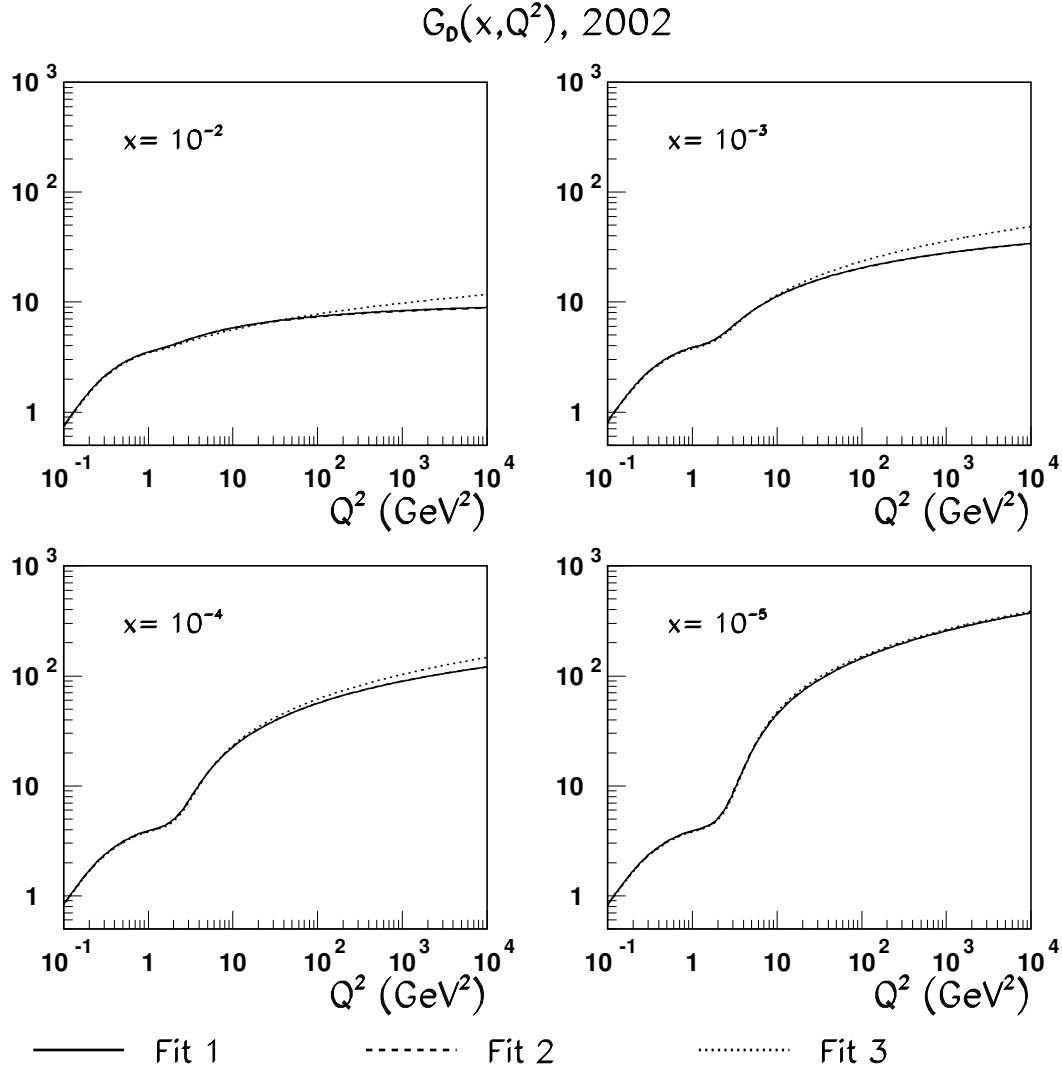


Figure 9.2: Integrated gluon structure function as function of  $Q^2$ : DGD 2002 analysis

with simple-formula parameterization of  $F_{\text{hard}}$ , approach each other.

## 9.3 The observables

### 9.3.1 Structure function $F_{2p}$ and its derivatives

Since the overall behavior of structure function  $F_{2p}(x; Q^2)$  was the quantity we tried to fit, one can expect a very good description of the data. Indeed, as Figs. 9.3 and 9.4 show, our calculations for  $F_{2p}$  based on all three DGSF fits go almost directly through the experimental points. This trend is somewhat spoiled beyond the region of fitting, namely, at  $x > 0.01$ , but still we do not run into any severe discrepancy even here. Note also that throughout the



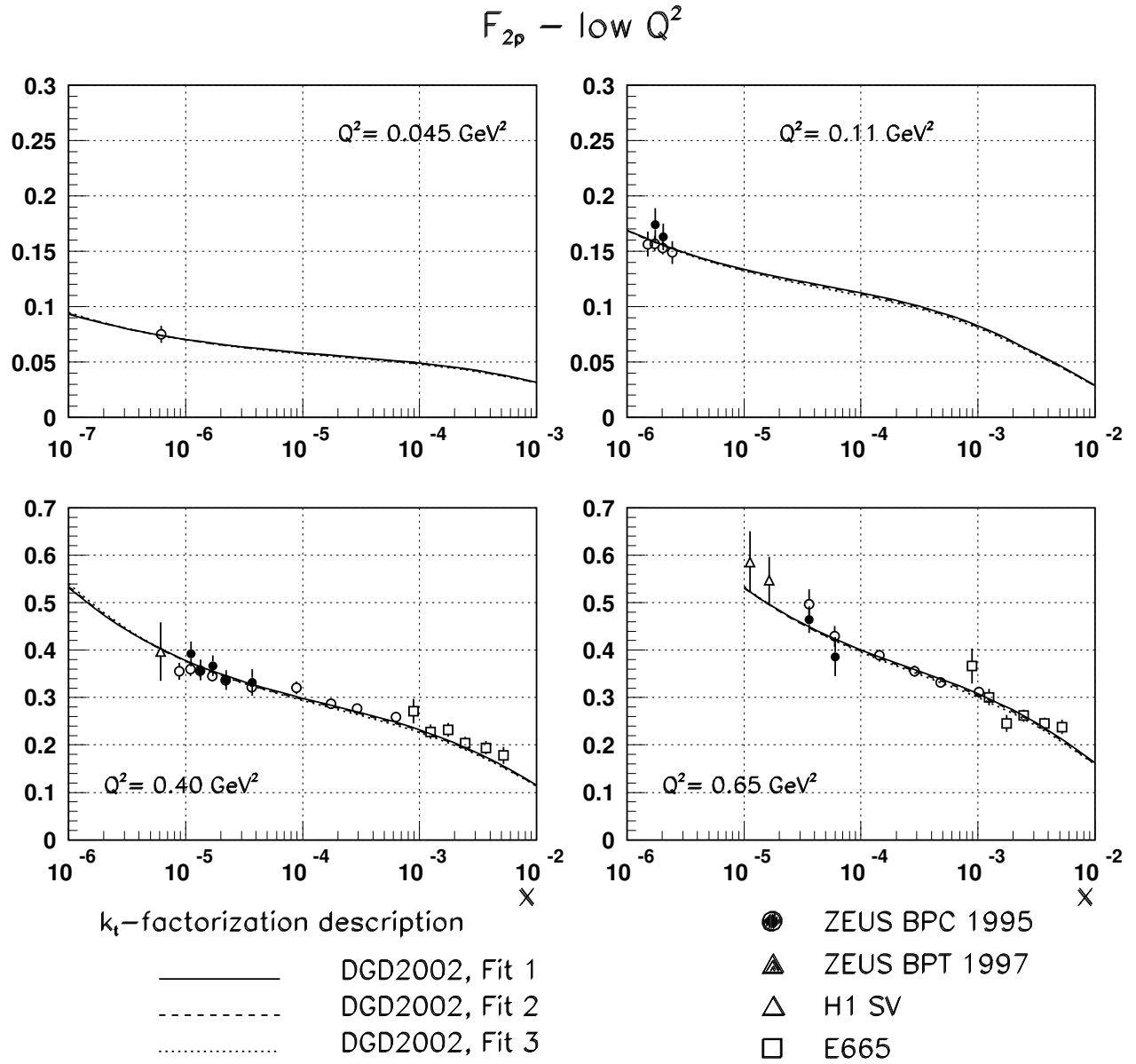


Figure 9.3: The  $k_t$ -factorization results for the structure function  $F_{2p}(x; Q^2)$  in the small  $Q^2$  region

# $F_{2p}$ – moderate and high $Q^2$

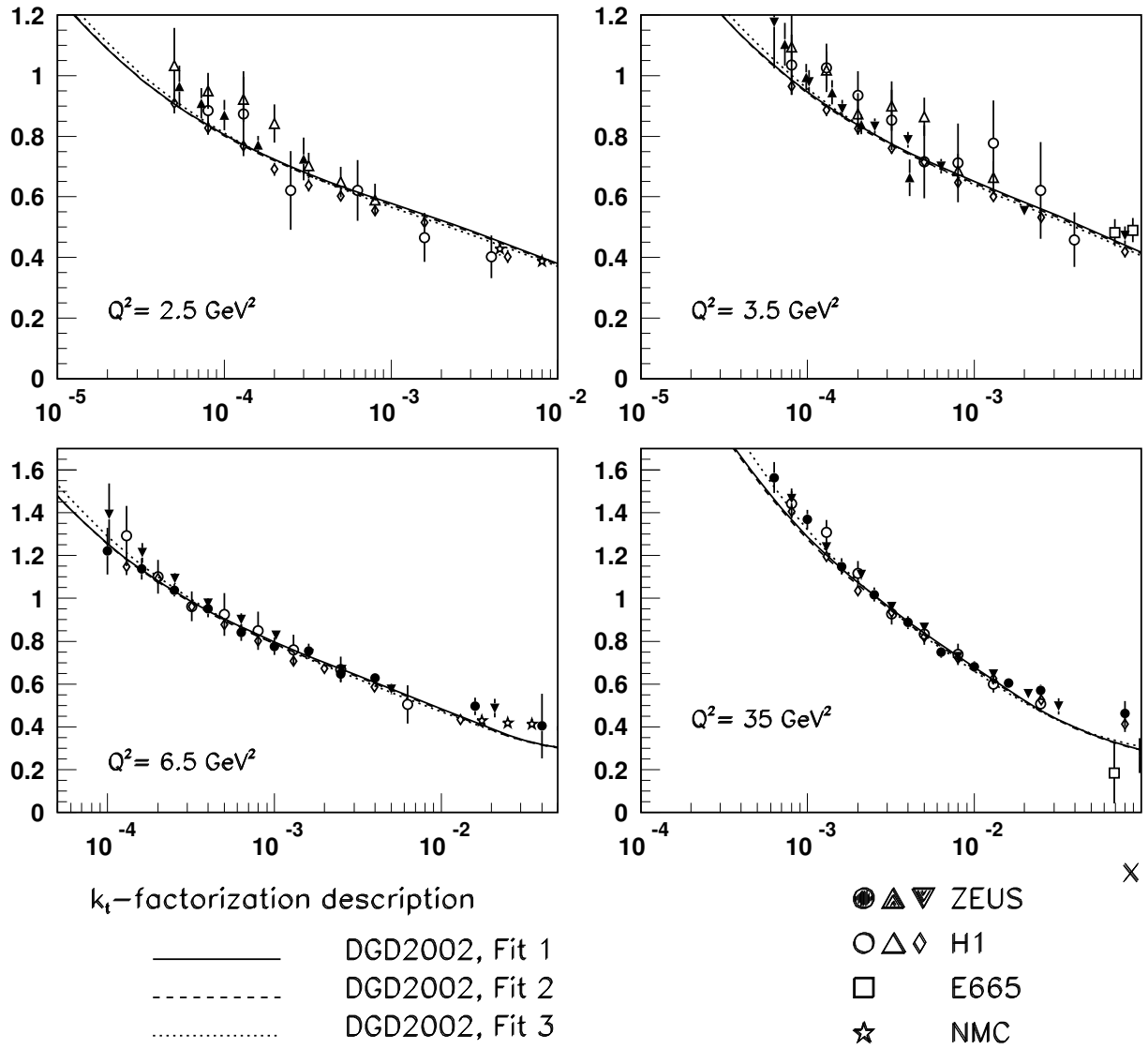


Figure 9.4: The  $k_t$ -factorization results for the structure function  $F_{2p}(x; Q^2)$  in the moderate and high  $Q^2$  region

ting region all three curves differ less than 5% .

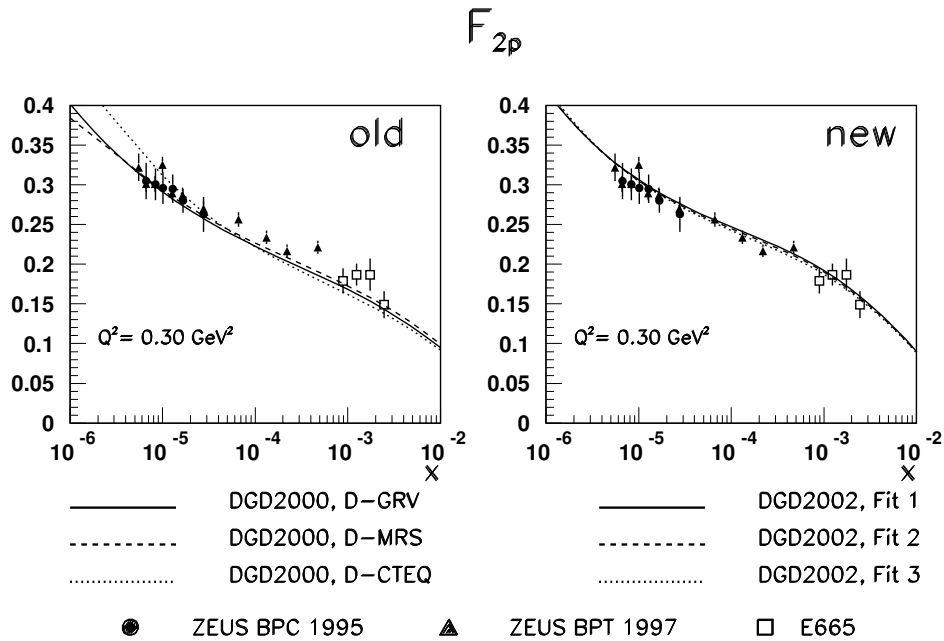


Figure 9.5: The improvement of the  $k_t$ -factorization predictions for the structure function  $F_{2p}$  based on DGD 2000 (left pane) and DGD 2002 (right pane) parametrizations of the differential gluon structure function

Fig. 9.5 illustrates the improvement in the description of the structure function  $F_{2p}$  by the  $k_t$ -factorization calculations as we switch from old DGD 2000 parametrizations of DGSF to the new DGD 2002 ts. The curves now go directly through very constraining new data points and therefore have less tendency to depart from each other outside the fitting range.

Fig. 9.6 shows the effective intercept of structure function  $F_{2p}$  in the moderate  $Q^2$  domain together with recent H1 data [73]. The intercepts were calculated according to

$$\alpha(Q^2) = \frac{\log[F_{2p}(x_1; Q^2) / F_{2p}(x_2; Q^2)]}{\log(x_2 / x_1)} : \quad (9.11)$$

For each differential gluon density we plotted here two curves: the upper one corresponds to the effective intercept taken between  $x_1 = 10^{-5}$  and  $x_2 = 10^{-4}$ , while the lower one is for  $x_1 = 10^{-4}$  and  $x_2 = 10^{-3}$ . Significant deviation between the two curves indicates the fact that the powerlike law

$$F_{2p}(x; Q^2) \sim \frac{1}{x} \alpha(Q^2) \quad (9.12)$$

is only a very crude approximation.

The agreement with the data is reasonable, especially when one takes into account that at lower  $Q^2$  one should compare the data with the upper curves and at higher  $Q^2$  the data

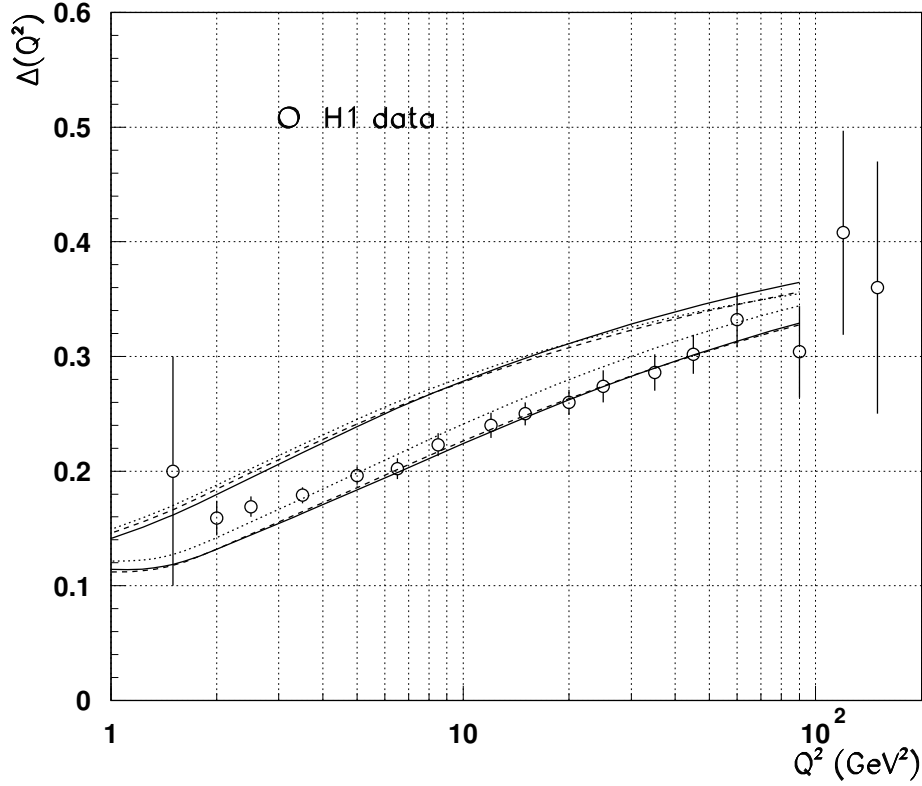


Figure 9.6: The  $k_t$ -factorization predictions for the effective intercepts of the structure function  $F_{2p}$  in the moderate  $Q^2$  region confronted with H1 data (solid circles)

should be compared with the lower curves. This is due to the experimental procedure used by H1 to determine the intercepts: at smaller  $Q^2$  the value of the intercept comes from data points in the range  $x \in (10^{-5}; 10^{-3})$ , while at higher  $Q^2$  only  $x \in 10^{-3} - 10^{-2}$  were available.

### 9.3.2 Structure function $F_L$

In 1999 H1 published improved data on determination of structure function  $F_L(x; Q^2)$ . We show them in Fig. 9.7 together with our predictions. The general agreement can be seen, however, since the data are not very constraining, little further information can be extracted from this plot.

### 9.3.3 Real photoabsorption cross section

Finally, in Fig. 9.8 we show experimental data for real photoabsorption cross section  $\sigma_p$  together with our predictions.

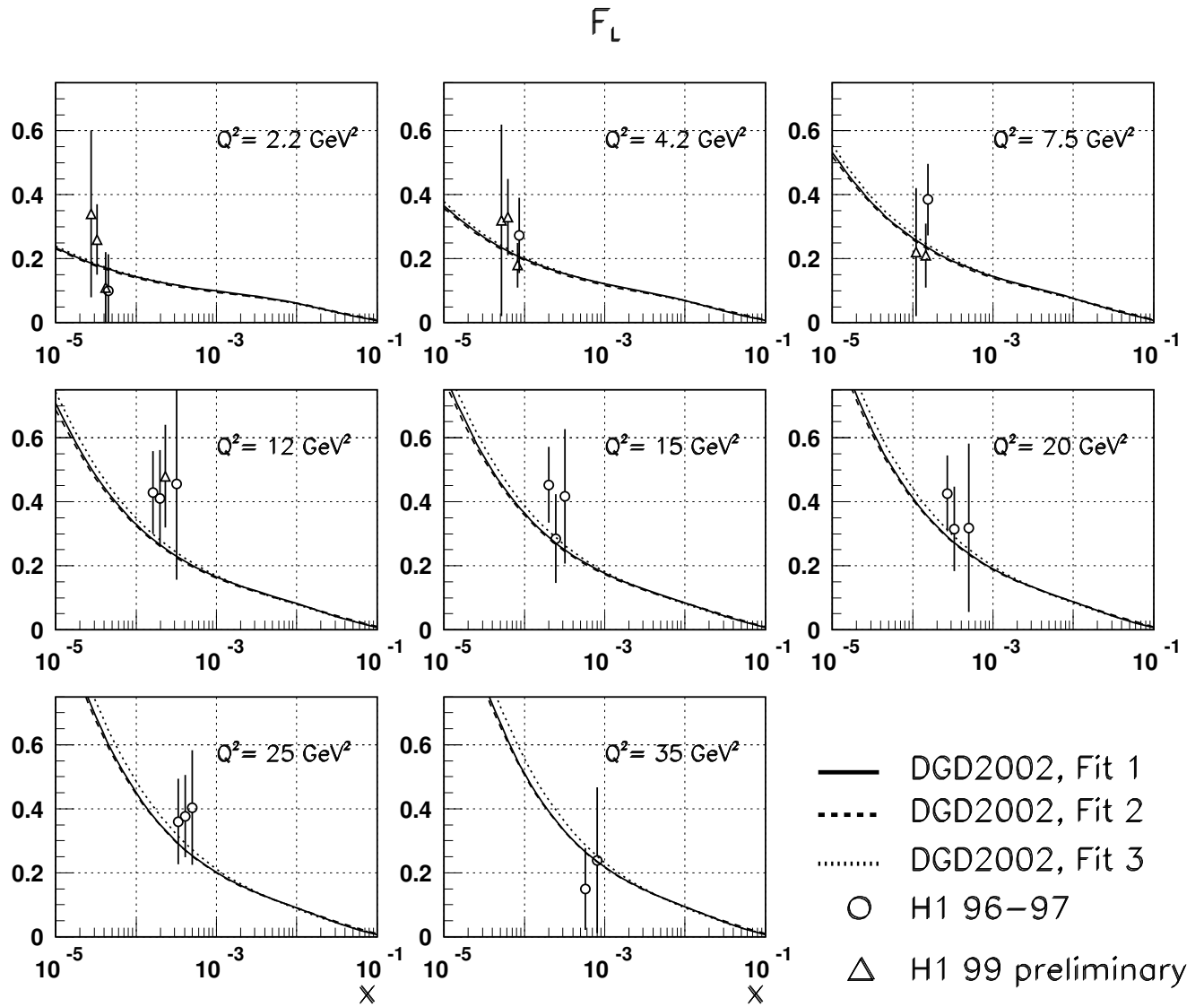


Figure 9.7: The longitudinal structure function  $F_L$  of the proton in the moderate  $Q^2$  region

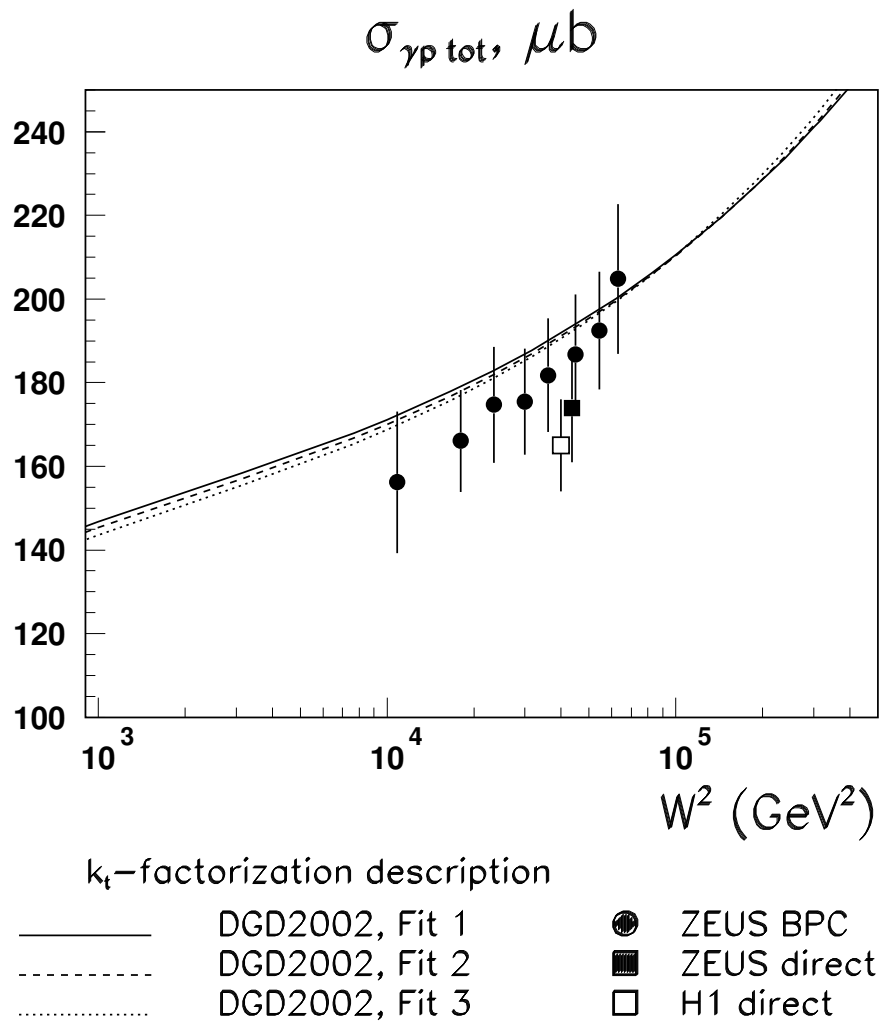


Figure 9.8: The predictions of the real photoabsorption cross section as function of total energy based on DGD2002 parametrization

# Chapter 10

## Numerical analysis of the vector meson production

### 10.1 1S states: a brief look

#### 10.1.1 Absolute values of cross sections and scaling phenomenon

An overview of the experimental results on vector meson production together with our predictions is given by Fig. (10.1). Here we plotted the experimentally measured values of meson cross sections for photoproduction (H1 [74] and ZEUS [75]) and electroproduction (H1 [76] and ZEUS [77]) cases, mesons electroproduction cross sections (H1 [78] and ZEUS [79], [80]),  $J=$  photoproduction (H1 [81]) and electroproduction cross sections (H1 [82] and ZEUS [77], [83]), and (1S) photoproduction cross sections (H1 [81] and ZEUS [84]). All experimental data points are either taken at  $W = 75$  GeV or are extrapolated to this energy. Whenever possible, we used the energy dependence measured experimentally in the corresponding papers. In the case of mesons photoproduction no reliable data on energy are available, and we used power law  $( ) / W$  with  $= 1.75$ , which comes from our calculations.

In the case of  $\rho$ ,  $J=$ , and mesons the cross sections were multiplied by appropriate favor factors in order to remove trivial sensitivity of the cross sections to the mean-square charge  $\langle e_q^2 \rangle$  of the quark content in a vector meson.

As suggested by the twist expansion analysis, the total production cross sections should exhibit an approximate scaling in variable  $\overline{Q}^2$ . Indeed, as Fig. (10.1) shows, the experimental data for various vector mesons do possess such a scaling property: data points for  $\rho$ ,  $J=$ , and  $J=$  taken at the same values of  $\overline{Q}^2$  almost coincide. It is worth noting that the scaling phenomenon takes place even at small  $\overline{Q}^2$ . Note that the  $k_t$ -factorization predictions also exhibit approximate scaling phenomenon.

#### 10.1.2 The energy and $t$ -dependence

The remarkable scaling in variable  $\overline{Q}^2$  is observed not only in the magnitude of the production cross sections, but also in the patterns of energy dependence and  $t$ -dependence.

The energy dependence of the vector meson production cross sections is compatible within

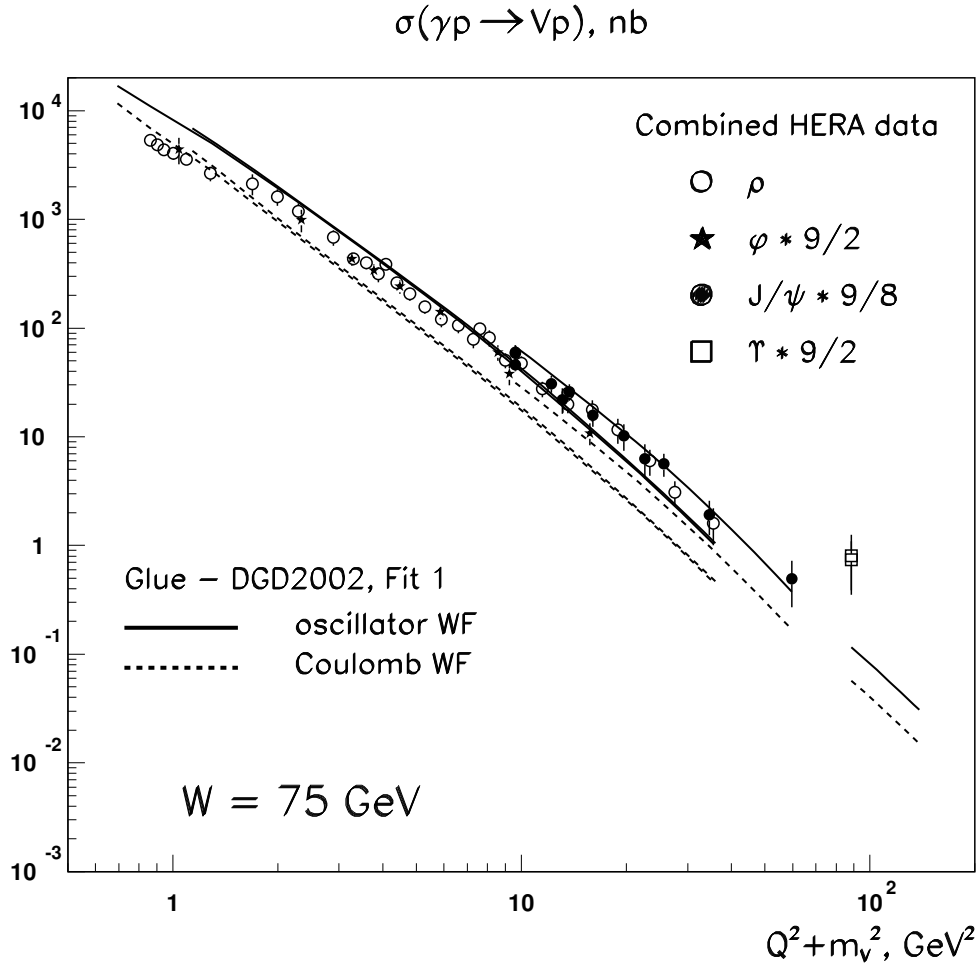


Figure 10.1: The total cross section of diffractive electroproduction of various vector mesons against scaling variable  $Q^2 + m_V^2$ . Results are scaled according to flavor content to equilibrate the electric charges of different flavours. The  $k_t$ -factorization predictions based on oscillator (solid lines) and suppressed Coulomb (dashed lines) are also shown. All calculations are performed for  $W = 75 \text{ GeV}$ ; the experimental points are either taken in this energy range or consistently extrapolated to this energy.

experimental errors with the power-like Regge-type growth:

$$\sigma / W ; \quad = 4[\alpha_P - 1] : \quad (10.1)$$

The latter equality reflects the assumption that the energy behavior comes from the gluon content of the proton, which is usually linked to the Pomeron intercept  $\alpha_P$  at  $t_j = 0$ .

The  $t$ -dependence of the differential cross section  $d\sigma/dt_j$  can be approximated at  $|t_j| < 0.5 \text{ GeV}^2$  by a simple exponential law

$$\frac{d\sigma}{dt_j} \sim e^{B t_j} : \quad (10.2)$$



The magnitude of the slope parameter  $B$  shows how "fragile" the proton and the produced meson are.

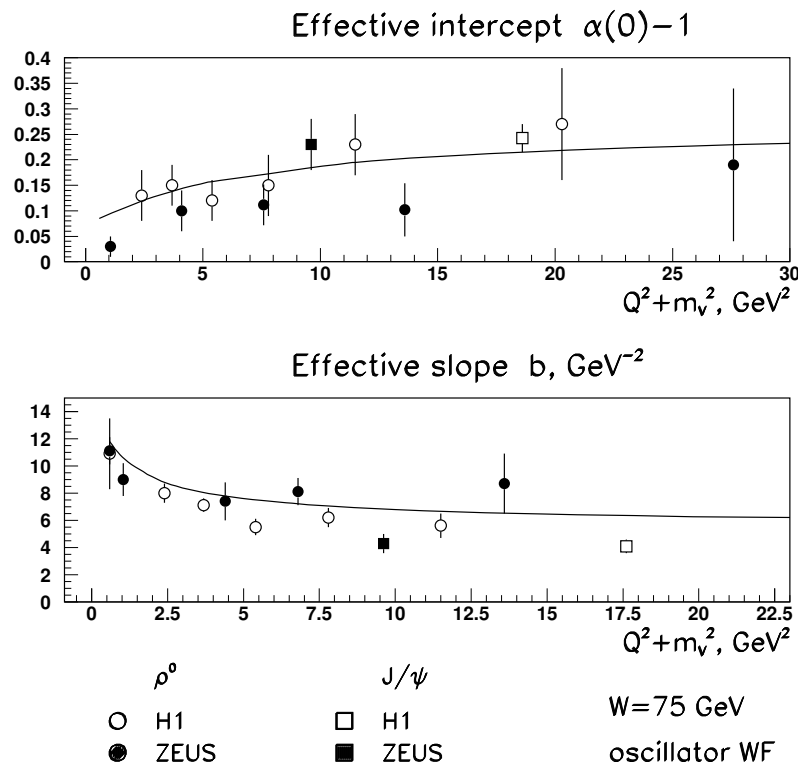


Figure 10.2: The effective intercepts (upper pane) and effective slopes (lower pane) of the vector meson production cross sections vs. scaling variable  $Q^2 + m_v^2$ . The data points represent meson and  $J/\psi$  meson results. The curves are the  $k_t$ -factorization calculations for the meson with the oscillator wave function.

Both quantities — the intercept and the slope — do exhibit  $Q^2$  dependence, but again via scaling variable  $\bar{Q}^2$ . Fig. 10.2 shows a plot from [16], where the  $k_t$ -factorization predictions for these quantities are compared with the experimental results then available. Although the agreement is not perfect, the tendency is caught by the  $k_t$ -factorization calculations. Below we will give more detailed investigation of both quantities.

### 10.1.3 The level of accuracy

Before proceeding further, we should have a clear idea of what level of accuracy one can expect from the  $k_t$ -factorization predictions.

There is a number of quantities that can be a source of uncertainty in the final answers. Below we discuss them.

## The gluon density

The gluon content of the proton is an intrinsically non-perturbative quantity, and therefore it is not calculable within the  $k_t$ -factorization approach. Our extensive analysis of the structure function  $F_{2p}$  lead us to an accurate determination of the differential gluon density  $F(x; \sim^2)$  in the proton. The  $k_t$ -factorization results for various physical observables based on distinct fits to  $F(x; \sim^2)$  differ from each other at the level of several percent.

As we discussed above, the vector meson production amplitudes are related not to the diagonal quantity  $F(x; \sim^2)$ , but to the off-diagonal (skewed) gluon distribution  $F(x_1; x_2; \sim; \sim)$ . The situation can be partially cured by linking the skewed gluon distribution to the diagonal one by means of Shuvaev formula (5.28) or its simplified version (5.30). Since such a linking is strictly valid only when  $x_1$  or  $x_2$  vanishes, and therefore it is a good approximation in the cases  $Q^2 \sim m_V^2$  and  $Q^2 \sim m_V^2$ .

If  $Q^2 \sim m_V^2$ , this linking becomes not well justified, and the whole procedure introduces an uncertainty. In order to test the magnitude of the uncertainty associated with the skewness of the gluon density, we performed an additional check, namely we calculated the meson cross sections at low  $Q^2$  using strictly forward and simplified off-forward (5.30) Ansätze for the gluon structure function. We found that at  $Q^2 = 0$  using forward instead of non-forward (the latter is default option for all calculations here) reduced the cross section by a factor of 1.07. Obviously, smallness of this factor originates from low average value of energy growth exponent.

Thus, the inaccuracy introduced at low  $Q^2$  by forward/off-forward Ansatz for gluon density is no more than 10%.

## The wave function

With the gluon density being brought under reasonable control, the only major uncalculable piece of the pie is vector meson wave function. As described above, we focus on the soft wave function, in particular, we used the oscillator and "suppressed Coulomb" wave function Ansätze. Being virtually the two limiting cases of how the radial part of the wave function can look like, they represent fairly well the region of uncertainty introduced by a specific choice of the wave function.

As can be seen from the above Figures, the calculations based on the oscillator wave function Ansatz are roughly twice higher than those obtained with the suppressed Coulomb W F.

## The width of vector meson

In our calculations we treated the produced vector mesons as particles with negligible width. This is not the case for the meson, whose width is about  $1/5$  of its mass. Usually, the incorporation of a finite width of a produced particle is conducted via effective 'smearing' of the results (which depend on the mass of the particle produced) over a certain mass interval. If the cross sections calculated for a given mass happen to have convex dependence on mass (which is precisely the case in the meson production), then such a smearing will lower the values of the cross sections. Thus, from a very general arguments we can expect such a smearing in our case as well. Roughly, it should amount to decreasing of the cross sections by factor of  $(1 + \frac{\Gamma}{m}) \sim 1.2$ .

A more accurate calculation of this effect is a non-trivial task. The problem is that in our treatment of the vector meson production we never refer to the vector meson mass. We deal only with the effective invariant mass of the qq pair. Therefore accurate calculation of the smearing effect requires solution of conceptually non-trivial problems.

The limits of  $k_t$ -factorization approach

Finally, the very approach we use has limited applicability domain. In particular, it would be fallacious to extend our calculations to high  $Q^2$  region. A rough criterion to border of the applicability domain can be given by  $Q_{max}^2 \sim W^2_{soft}$ , which is about  $50 \text{ GeV}^2$  for the HERA energy range. Above this values, the logarithms  $\log(Q^2 = s_{soft})$  will be more important than  $\log(1-x)$ , and one can expect that  $k_t$ -factorization will underestimate observed cross sections.

## 10.2 The meson production

In this section we provide a detailed description of the  $k_t$ -factorization predictions for the meson production. Note that throughout this chapter we treat the physical meson as pure 1S state. Whether this is indeed realized in Nature and what changes if S=D wave mixing occurs, will be discussed in Chapter 11.

Whenever experimental data available, we compare them with our results.

### 10.2.1 $Q^2$ dependence

The  $Q^2$ -dependence of the meson production cross section is shown in Fig. 10.3. One sees that as we slide to higher values of  $Q^2$ , the cross section drops sharply. Although for the major part of the  $Q^2$  region shown the experimental data points fall roughly between the oscillator and Coulomb wave function predictions, two separate places of discrepancy are easily visible.

Low  $Q^2$  region

The first problematic point is low- $Q^2$  region. As we come from moderate  $Q^2$  down to  $Q^2 = 1 \text{ GeV}^2$  and below, our predictions, if compared to the experimental points, tend to climb too high.

The first thought would be to suspect that our predictions rise too steeply as  $Q^2 \rightarrow 0$ . An accurate analysis shows, however, that this suspicion is off the point. In fact, the  $Q^2 \rightarrow 0$  behavior of our predictions is perfectly compatible with experimentally observed tendencies. This rather unexpected fact is illustrated by Figs.(10.4) and (10.5).

In Fig.(10.4) we zoom in on the region  $Q^2 < 1 \text{ GeV}^2$ , where the available experimental data include ZEUS 95 BPC [77], ZEUS 94 photoproduction [75] and H1 photoproduction [74] measurements. The  $k_t$ -factorization prediction based on the oscillator wave function (which seems to be a more reasonable choice for the mesons than the Coulomb W F) and on DGD 2002, Fit 3 are shown with solid line. The  $k_t$  predictions overshoot the data throughout the whole region shown here. However, when simply divided by 2, the predictions pass exactly through all the data points (dotted curve in Fig.(10.4)), including the photoproduction point.

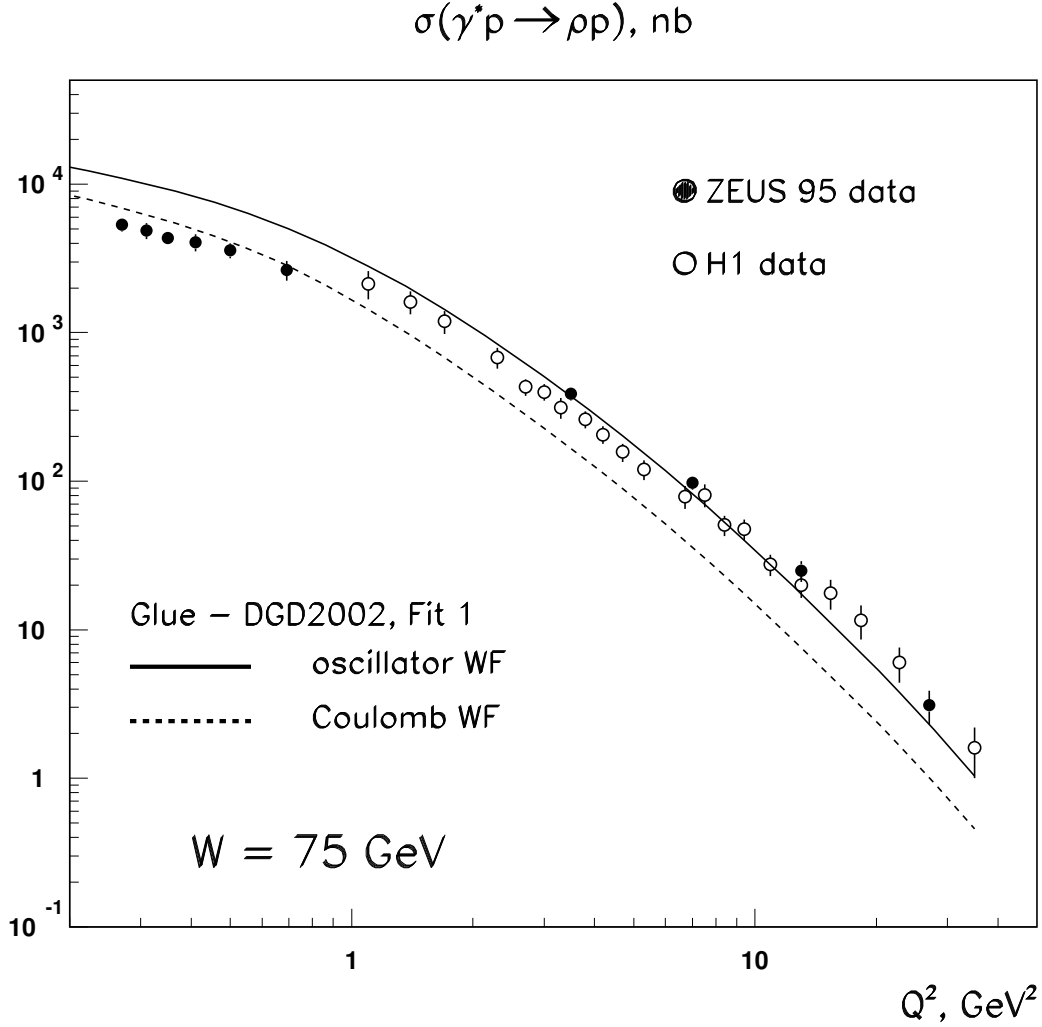


Figure 10.3: Total cross section of the diffractive meson production as a function of  $Q^2$ . The  $k_t$ -factorization predictions based on oscillator (solid lines) and suppressed Coulomb (dashed lines) are also shown. All calculation are performed for  $W = 75 \text{ GeV}$  using DGD 2002, Fit 1.

Alternatively, one can try parametrizing the cross sections at low  $Q^2$  by a simple formula:

$$\sigma(Q^2) \sim \frac{1 + R(Q^2)}{(Q^2 + m_{\text{eff}}^2)^n}; \quad R(Q^2) = \frac{L(Q^2)}{T(Q^2)}; \quad (10.3)$$

which is equivalent to

$$T(Q^2) \sim \frac{1}{(Q^2 + m_{\text{eff}}^2)^n}; \quad (10.4)$$

In order to find parameters  $m_{\text{eff}}^2$ ;  $n$  that reproduce the low- $Q^2$  behavior of our predictions, we

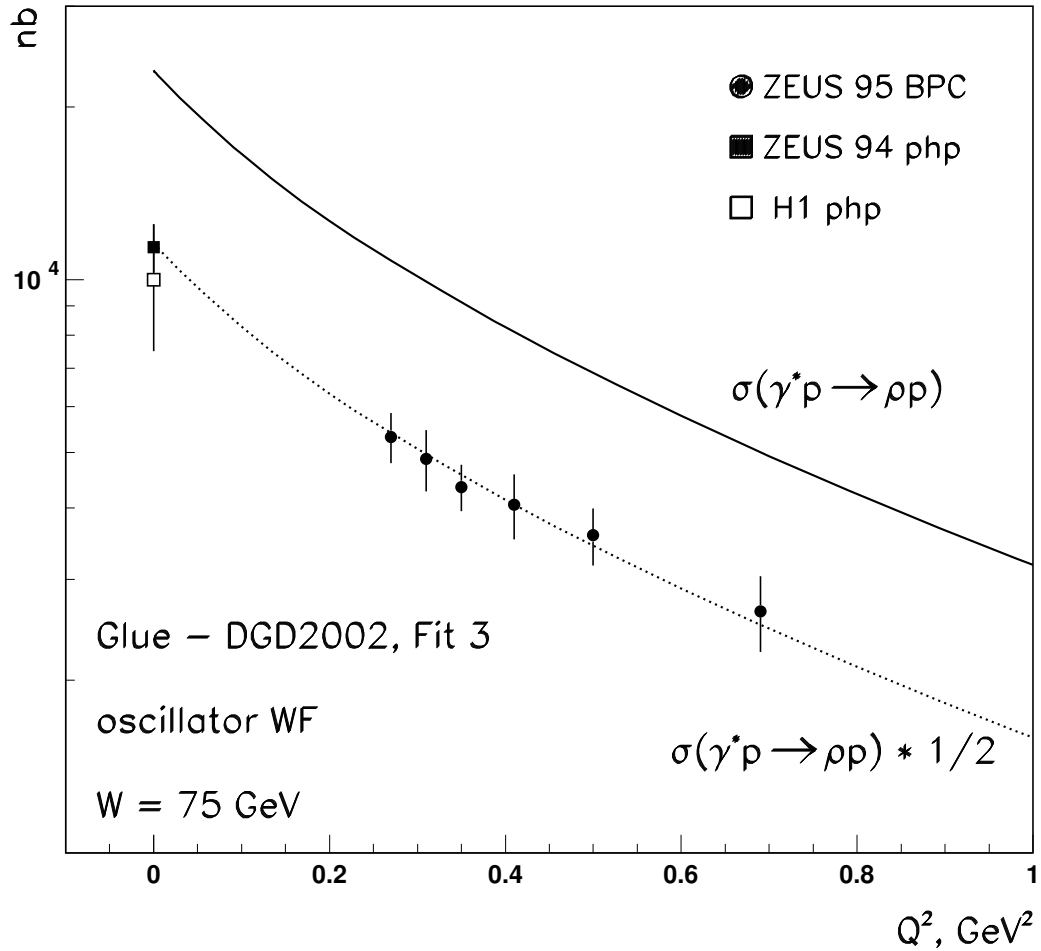


Figure 10.4: Total cross section of the diffractive meson production as a function of  $Q^2$  in the small- $Q^2$  region. The solid curve represents the  $k_t$ -factorization predictions; dashed line shows the same prediction divided by two.

plotted in Fig. (10.5) the quantity

$$R = \frac{\log[\sigma_T(Q^2 = 0) = \sigma_T(Q^2)]}{\log(1 + Q^2/m_{\text{eff}}^2)} \quad (10.5)$$

against  $1 + Q^2/m_{\text{eff}}^2$ . If Eq.(10.4) holds, this quantity should be equal to  $n$  for all values of  $Q^2$ . We see that when  $m_{\text{eff}}^2 \rightarrow 0.4 \text{ GeV}^2$ ,  $R$  has the most flat shape vs.  $Q^2$  and is  $\approx 2$ .

This result is in perfect agreement with low- $Q^2$  analysis of the ZEUS BPC data [77]: when

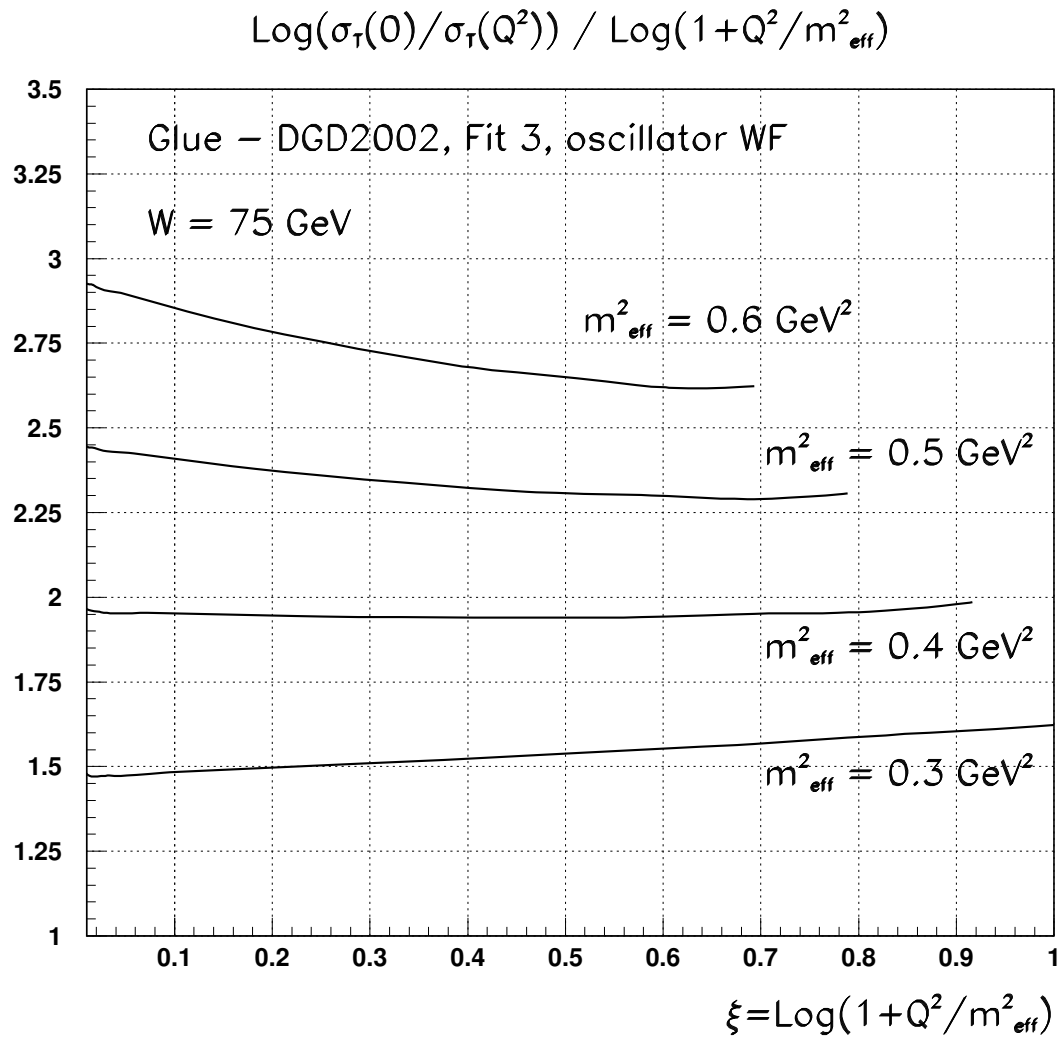


Figure 10.5: Effective  $Q^2 + m_{\text{eff}}^2$  exponent of the transverse meson production cross section in the low- $Q^2$  region as a function of  $\xi = 1 + Q^2/m_{\text{eff}}^2$  at various values of  $m_{\text{eff}}$

tted by the formula

$$(Q^2) / \frac{1 + R(Q^2)}{(Q^2 + m_{\text{eff}}^2(\text{exp}))^2}; \quad (10.6)$$

the data yield

$$m_{\text{eff}}(\text{exp}) = 0.66 \pm 0.11 \text{ GeV};$$

in perfect agreement with our  $m_{\text{eff}} = 0.6 \pm 0.65 \text{ GeV}$ . Note that although in our analysis power  $n$  was a free parameter, it turned out close to 2.

Three conclusions can be drawn from this analysis.

First, we showed that although there is a sizable (by factor of 2) departure between the magnitude of the experimentally measured cross sections and the  $k_t$  factorization predictions,

the shape of low- $Q^2$  behavior is perfectly reproduced by the calculations based on the oscillator wave function.

Second, this analysis proves that the value  $m_{\text{eff}} = 0.65 \text{ GeV}$  is dynamically generated. Indeed, the light quark mass used in our approach was predicted by the gluon structure function analysis at the level  $m_q = 0.21 \text{ GeV}$ . Still  $m_{\text{eff}}^2 > 4m_q^2$ , which means that approximately one half of  $m_{\text{eff}}^2$  comes from quark momentum. The exact proportion depends of course on the particular choice of the vector meson wave function. It is still to be investigated whether the oscillator wave function was an unexpectedly lucky guess, or whether the perfect reproduction of low- $Q^2$  behavior is accidental.

Third, the above means that the actual region where our predictions and the experimental data really mismatch is not the low- $Q^2$ , but rather moderate  $Q^2$  region ( $Q^2 \approx 1 \text{ GeV}^2$ ).

High  $Q^2$  region

The second region where our predictions tend to depart from the data is high- $Q^2$  region,  $Q^2 > 5 - 10 \text{ GeV}^2$ . If the cross section is (locally) fitted by the powerlike fall-off

$$\langle \sigma \rangle \sim \frac{1}{(Q^2 + m^2)^n}; \quad (10.7)$$

then this discrepancy can be expressed numerically in terms of effective  $Q^2$  exponent  $n$ . The experimental determination of this exponent resulted in the following values. The ZEUS 95 data [77] with  $Q^2 > 5 \text{ GeV}^2$  are consistent with fit (10.7) with energy independent  $n_{\text{exp}}$ , whose average value is found to be  $2.32 \pm 0.10$ . More copious H1 data sample [76] taken at  $W = 75 \text{ GeV}$  results in  $n_{\text{exp}} = 2.24 \pm 0.09$ , which is in agreement with ZEUS fit.

The  $k_t$  factorization predictions for this exponent is shown in Fig. (10.6). Here we plotted local analogue of the exponent  $n_{\text{exp}}$ , i.e. quantity

$$n_{Q^2} = \frac{q}{Q_1^2 Q_2^2} = \frac{\log[(Q_1^2) = (Q_2^2)]}{\log[(Q_2^2 + m^2) = (Q_1^2 + m^2)]}; \quad (10.8)$$

Again, if fit (10.7) holds,  $n$  should be independent of  $Q^2$ .

Graphs in Fig. 10.6 show that this is not the case. At intermediate  $Q^2$   $n$  starts already from about 2.5, then grows as  $Q^2$  increases, and at  $Q^2 > 20 \text{ GeV}^2$  it is even higher than 3.0.

Although being in contrast with fits to experimental data, such a  $Q^2$  growth of  $n(Q^2)$  is still firmly grounded theoretically. Qualitatively, this can be understood from the analysis of the leading  $\log Q^2$  result. At fixed  $W^2$  and high enough  $Q^2$ , the  $Q^2$  dependence of the cross section comes from

$$\langle \sigma \rangle \sim \frac{1 + R(Q^2)}{(Q^2 + m^2)^4} \sim G \cdot c \frac{Q^2}{W^2}; Q^2=4 \quad ; \quad (10.9)$$

where  $c = 0.41$  comes from the approximate representation of the off-forward gluon distribution (5.30). The  $Q^2$  dependence of slope  $B$  and of running coupling  $\alpha_s$  is inessential for our point.

The non-trivial  $Q^2$  behavior arises from the integrated gluon structure function. In Fig. 10.7, left pane, we show its  $Q^2$  behavior at  $W = 75 \text{ GeV}$ . The origin of the peaked shape is obvious: at moderate  $Q^2$  the integrated glue grows due to the sharp explicit  $Q^2$  dependence (that is,

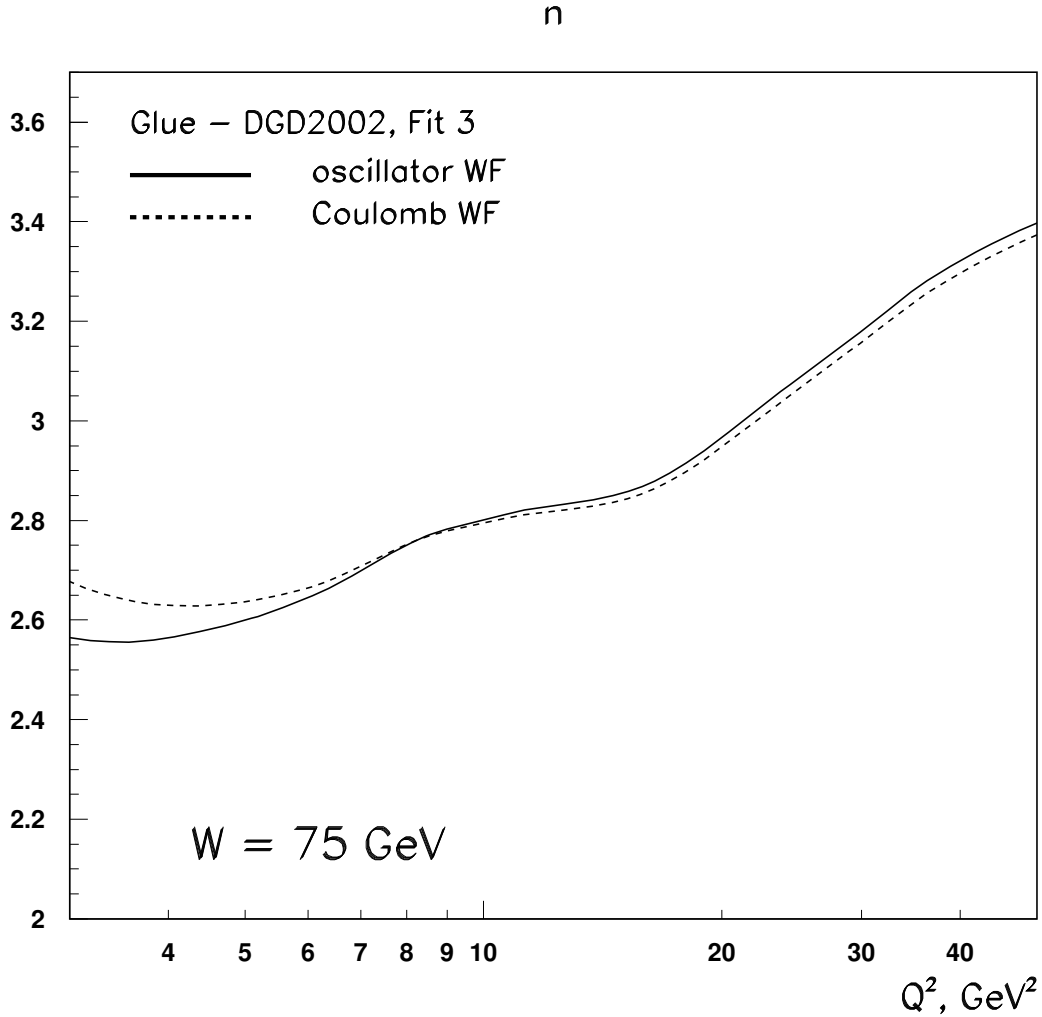


Figure 10.6: Effective  $Q^2 + m_{\text{eff}}^2$  exponent of the total meson production cross section in the high- $Q^2$  region as a function of  $Q^2$ . The solid and dashed curves represent calculations for oscillator and suppressed Coulomb wave functions respectively

due to large values of unintegrated gluon density  $F(x; \sim^2)$ , while for larger  $Q^2$  the effect of decreasing  $x_{\text{eff}}$  overpowers and leads to decreasing of  $G$  as  $Q^2$  grows further.

On the right pane of Fig. 10.7 we show the local  $Q^2$  exponent  $n_G$  of the gluon density (the gluon density contribution to the local  $Q^2$  exponent  $n$  is equal to  $2n_G$ )

$$n_G \quad Q^2 = \frac{1}{Q_1^2 Q_2^2} \frac{\log[G(Q_1^2)G(Q_2^2)]}{\log[(Q_2^2 + m^2)(Q_1^2 + m^2)]} : \quad (10.10)$$

One sees that at moderate  $Q^2$ , when  $G$  is still rising, it tamps the  $Q^2$  fall, but when  $Q^2 > 10 \text{ GeV}^2$ , gluon density starts decreasing on its own. This is precisely the reason why at higher



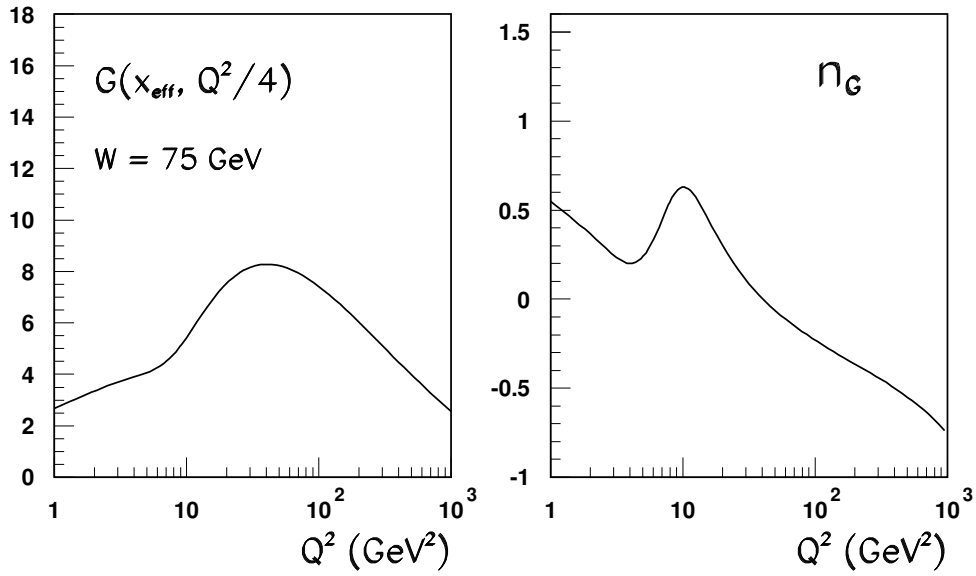


Figure 10.7: (Right pane) The  $Q^2$  behavior of the integrated gluon density  $G$  ( $0.41Q^2=W^2; Q^2=4$ ) at fixed value of  $W = 75$  GeV obtained by integration of the DGD 2002 Fit 1; (left pane) The effective  $Q^2$  exponent of this integrated gluon density

$Q^2$  the  $Q^2$  exponent  $n$  (Fig. 10.6) boosts up.

The arguments that justify such a behavior seem to be universal, and to this end, it is surprising why the experimental data do not possess such a behavior.

## 10.2.2 $\sigma_L$ and $\sigma_T$ decomposition

An important insight of the  $Q^2$  behavior of the meson production cross sections comes from the separate analysis of  $\sigma_L(Q^2)$  and  $\sigma_T(Q^2)$ , that is proportion of the meson production rates cause by transverse and longitudinal photons.

Fig. 10.8 represents the results for these cross sections within the  $k_t$ -factorization approach confronted with experimental data [85].

One sees that at high  $Q^2$  we do provide a reasonably good description of the  $\sigma_L$ , but our  $\sigma_T$  curves sink significantly deeper as  $Q^2$  grows. Thus, it is mostly a way too steep  $Q^2$ -behavior of  $\sigma_T$  that causes departure of our curves from the data.

If analyzed in terms of power-like fits

$$\sigma_T(Q^2) / (Q^2 + m^2)^{n_T}; \quad \sigma_L(Q^2) / (Q^2 + m^2)^{n_L}; \quad (10.11)$$

the experimental data yield [85]

$$n_T(\text{exp}) = 2.47 \pm 0.03; \quad (10.12)$$

We found no direct experimental results for  $n_L$ , but clearly it should be even less than  $n_T$ .

The  $k_t$ -factorization predictions for the local values of  $n_L$  and  $n_T$ , defined similarly to (10.8), are shown in Fig. 10.9. At higher  $Q^2$ ,  $n_L$  and  $n_T$  grow up to 3 and 4 respectively, the latter being in stark contrast to the data.

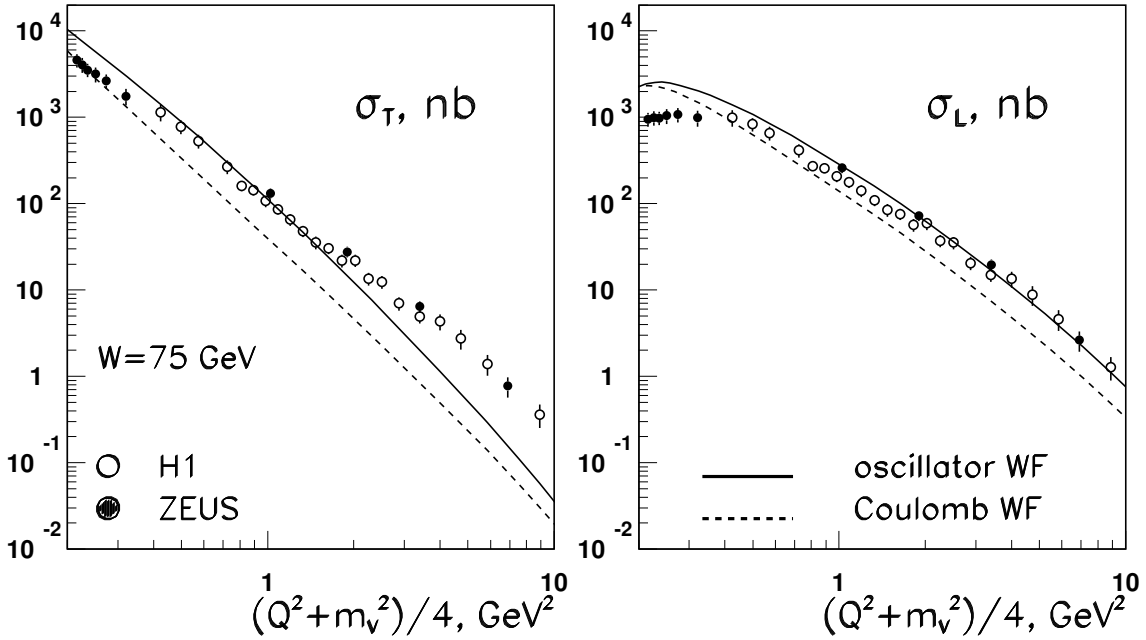


Figure 10.8: Experimental data on transverse  $\sigma_T$  and longitudinal  $\sigma_L$  cross sections of meson production compared with the  $k_t$ -factorization approach.

Fig. 10.10 depicts the ratio

$$R(Q^2) = \frac{\sigma_L(p) - \sigma_T(p)}{\sigma_T(p) + \sigma_L(p)}; \quad (10.13)$$

experimental points taken from [76]. The glaring disagreement at higher  $Q^2$  is, of course, caused by too much suppressed  $\sigma_T$  out calculations predict. Evidently, if we found a way to increase  $\sigma_T$ , the ratio  $R(Q^2)$  would be automatically cured.

### 10.2.3 Energy dependence

The growth of the vector meson production cross sections is a well-established fact. It is linked basically to the energy growth of the Pomeron exchange, and therefore fitting the cross sections to the energy power law

$$\sigma(W) \propto W^\alpha \quad (10.14)$$

seems a natural way to quantize the energy growth.

Fig. 10.11 shows the experimental data on  $\sigma$  from ZEUS [77] and H1 [76] together with the  $k_t$ -factorization predictions based on oscillator and Coulomb wave function. Since the true  $W$  dependence of the cross sections can deviate from simple power law (10.14), the exponent can depend on  $W$  as well. At lower  $Q^2$  the upper pair of curves corresponds to  $\sigma$  calculated between 50 and 75 GeV, while the upper pair corresponds to energy range between 110 and 150 GeV.

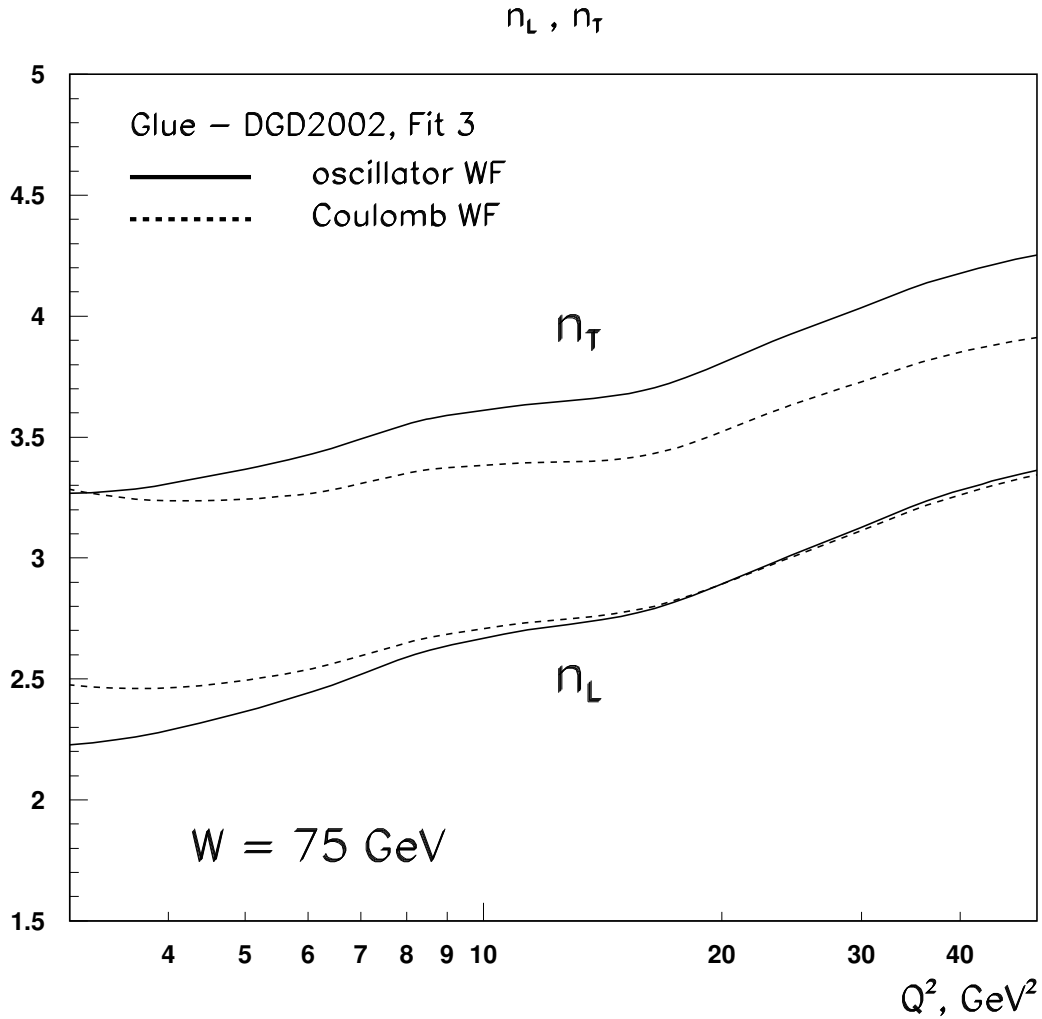


Figure 10.9: The effective  $Q^2$  exponents shown separately for  $n_L$  and  $n_T$  as functions of  $Q^2$ . Solid and dashed lines correspond to oscillator and suppressed Coulomb wave functions respectively

One sees that the agreement is rather good, although a tendency that our curves go slightly higher than the (ZEUS) data is noticeable. However due to still significant experimental errors, it is too early to draw any more definite conclusions.

#### 10.2.4 $t$ -dependence

The analysis of  $t$ -dependence of the differential cross sections within a perturbative framework has an ambiguous status. On the one side, if we deal with proton in final state, this dependence is governed largely by the intrinsically nonperturbative (multiparticle) form factor

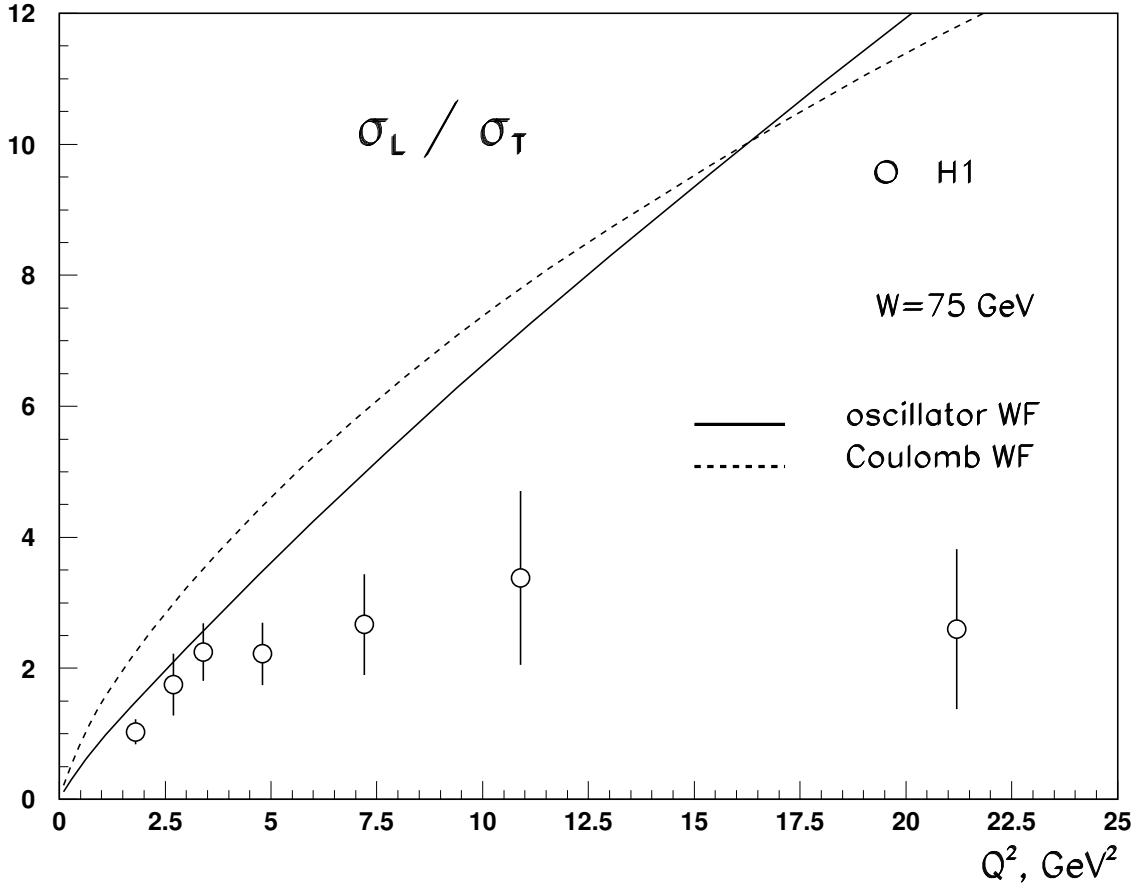


Figure 10.10: Ratio  $R = \sigma_L / \sigma_T$  as a function of  $Q^2$  for  $\rho$  meson as a function of  $Q^2$ . Solid and dashed lines correspond to oscillator and suppressed Coulomb wave functions respectively

of the proton. Therefore, in order to have a plausible  $t$ -dependence, we have to introduce a certain "educated guess". On the other hand, our gluon density analysis already uses this form factor, and therefore places some constraints on it. Finally, as the analysis suggests, the at low  $t$ , within diffraction cone, several other mechanisms modify the  $t$  dependence of the proton form factor. If one parametrizes the differential cross sections at low  $t$  ( $t < 0.5 \text{ GeV}^2$ ) by an exponential law with slope parameter  $b$ ,

$$\frac{d}{dt} \propto e^{bt}; \quad (10.15)$$

one finds that various sources of  $t$ -dependence can be treated in terms of contributions to the overall slope  $b$  approximately additively.

In principle, there can be three sources of the non-zero contributions to the slope: the proton transition, the  $\rho \rightarrow V$  transition, and the exchange (the Pomeron propagation):

$$b = b_{\rho \rightarrow V} + b_{\text{exch}} + b_{\text{Pom}}; \quad (10.16)$$

First term appears in our calculations explicitly as an effective slope of the energy- and  $\sim^2$ -

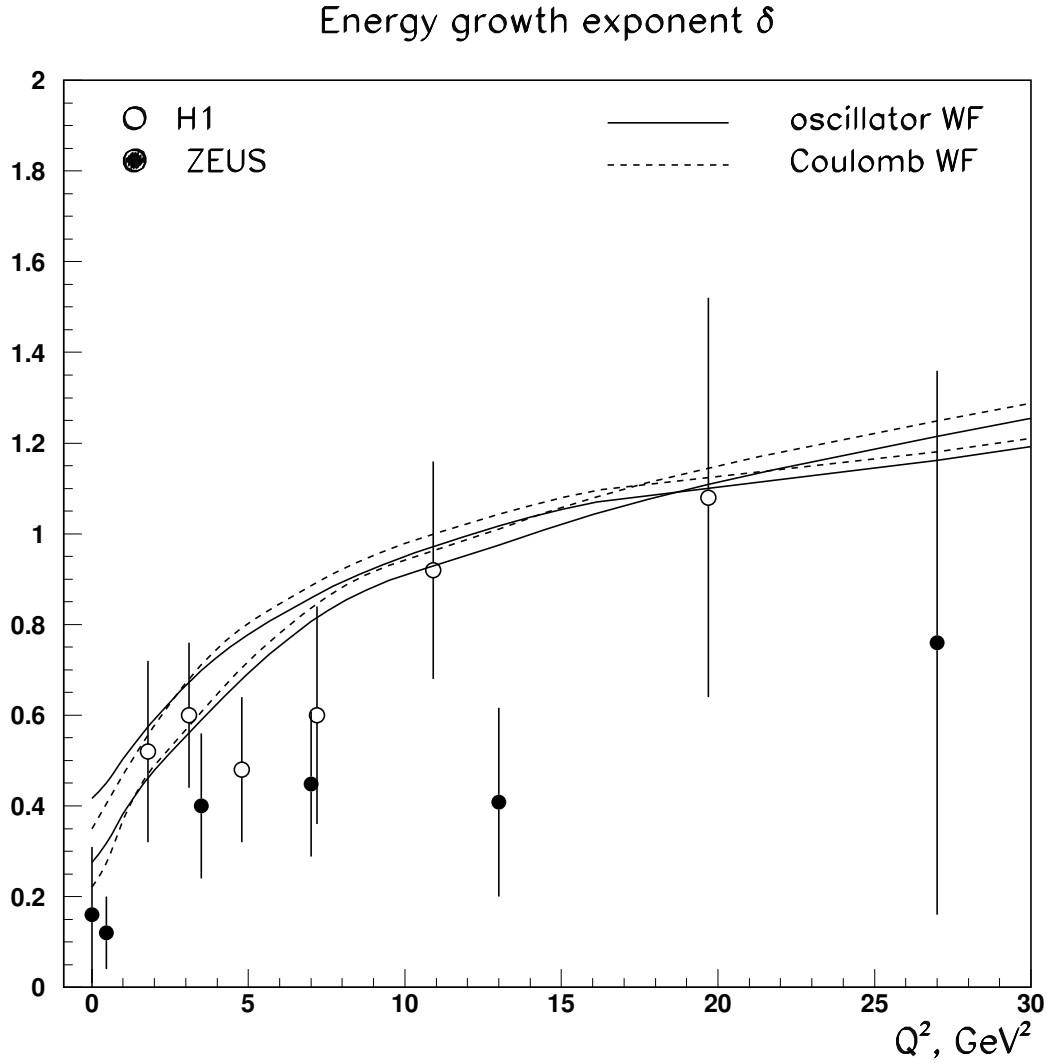


Figure 10.11: Effective exponents of energy growth for the meson production cross sections. Solid and dashed lines correspond to oscillator and suppressed Coulomb wave functions respectively. The upper pair of curves (at low  $Q^2$ ) corresponds to  $\delta$  calculated between 50 and 75 GeV, while the lower pair is the result for  $\delta$  calculated between 110 and 150 GeV.

independent dipole form factor

$$F(\sim^2) = \frac{1}{1 + \sim^2 = 2^2}; \quad \sim = 1 \text{ GeV}; \quad ! \quad b_{p!p} = 4 \text{ GeV}^2 : \quad (10.17)$$

The second term is also introduced explicitly. It is responsible for the shrinkage of the diffractive cone with energy growth. The third term appears from the accurate QCD treatment of the  $\pi^0 \rightarrow V$  transition. It possesses a characteristic  $1/(Q^2 + m_V^2)$  shape, which leads to the scaling phenomenon mentioned earlier.

Due to the above blend of non-calculable soft and perturbative hard contributions, the  $k_t$ -factorization approach should not be expected to yield first-principles predictions for the absolute value of the slope parameter. However, several kinematical dependencies observed in the experiment must be confronted with the predictions.

In principle, one can invoke several definitions of the effective slope parameter. However there is no significant difference among them. Below in Table 3 we compare results for three definitions of the effective slope:

$$b(\text{def.1}) = \frac{d \log(d = d_{Tj})}{d_{Tj}} \Big|_{Tj=0} ; \quad b(\text{def.2}) = \frac{1}{d_{Tj}} \frac{d}{d_{Tj}} \Big|_{Tj=0} ; \quad b(\text{def.3}) = \frac{1}{h_{Tj}} = \frac{R}{d_{Tj}} \frac{d}{d_{Tj}} ; \quad (10.18)$$

calculated at several  $Q^2$  points.

Table 3. Various possible definitions of the effective slope and their values obtained from  $k_t$ -factorization calculations at three characteristic values of  $Q^2$ .

$Q^2, \text{GeV}^2$	$b(\text{def.1})$	$b(\text{def.2})$	$b(\text{def.3})$
0	14.0	13.1	11.4
2.2	10.2	9.6	8.7
27	6.7	6.3	6.3

In Fig. 10.12 we present our results for the slope parameter of the meson production cross sections. The results for our calculations give somewhat too high values of the slope than the experimentally measured numbers (ZEUS [77] and H1 [76]), but nevertheless they exhibit the right  $Q^2$  dependence.

It is interesting to note that the slopes for  $L$  and  $T$  slightly differ, see Fig. 10.13. Note also that at small  $Q^2$  the calculations based on the Coulomb wave function give higher results for slopes.

Fig. 10.14 shows a typical pattern of the  $Tj$ -dependence of the differential cross sections in the region of small to moderate  $t$  ( $0 < Tj < 1.5 \text{ GeV}^2$ ). Oscillator wave function was used everywhere in this Figure. One sees that initially exponentially decreasing of the differential cross section flattens at higher  $Tj$  as the process leaves the diffractive peak.

### 10.2.5 Helicity amplitudes

Our analysis explicitly takes into account all possible helicity amplitudes  $(\lambda) \rightarrow V(\lambda_v)$ , with  $\lambda_v = 0; \pm 1$ . Since the Pomeron exchange does not distinguish left from right, only  $v$ -even independent helicity amplitudes survive.

Fig. 10.15 shows the absolute values of the  $v$ -even helicity amplitudes against the momentum transfer squared  $Tj$ . Within diffraction cone one sees the characteristic behavior of all the amplitudes. In the region of moderate  $Tj$  one can observe diffractive dips, whose location changes from one amplitude to the other. Certainly, since we did not focus on large  $t$ , we cannot be sure that the dips are located exactly where we predicted. Still this picture shows a general pattern of the  $t$ -behavior of the helicity amplitudes.

It is clear that the presence of helicity flip amplitudes leads to the breaking of the  $s$ -channel helicity conservation. It is therefore interesting to check what is the magnitude of the helicity flip amplitudes.

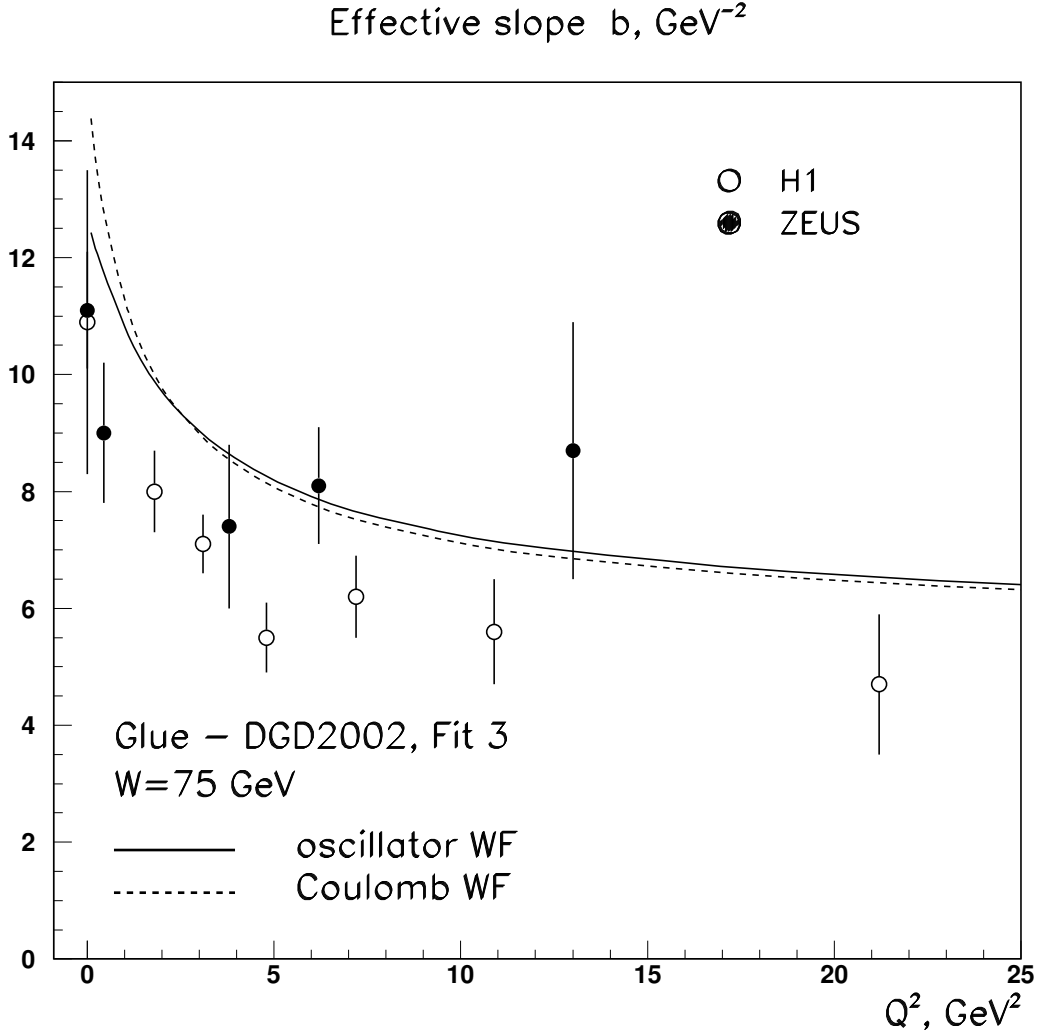


Figure 10.12: Effective slopes  $b$  of the meson differential cross sections within diffraction cone as functions of  $Q^2$ . Solid and dashed lines correspond to oscillator and suppressed Coulomb wave functions respectively.

Fig. 10.16 gives the answer to this question. Here we show ratios of the helicity  $\rho$  to helicity non- $\rho$  amplitudes

$$\frac{\mathcal{A}(\rho \rightarrow V_T)j}{\mathcal{A}(\rho \rightarrow V_T)j}, \quad \frac{\mathcal{A}(\rho \rightarrow V_L)j}{\mathcal{A}(\rho \rightarrow V_L)j}, \quad \frac{\mathcal{A}(\rho \rightarrow V_T)j}{\mathcal{A}(\rho \rightarrow V_L)j}, \quad (10.19)$$

and whenever possible compare  $k_t$ -factorization predictions to the available experimental data, taken from [85].

Finally, we made predictions to the full number of spin density matrix elements for the meson production and compared them with H1 [76] and ZEUS [86] data. Results are shown in Fig. 10.17.

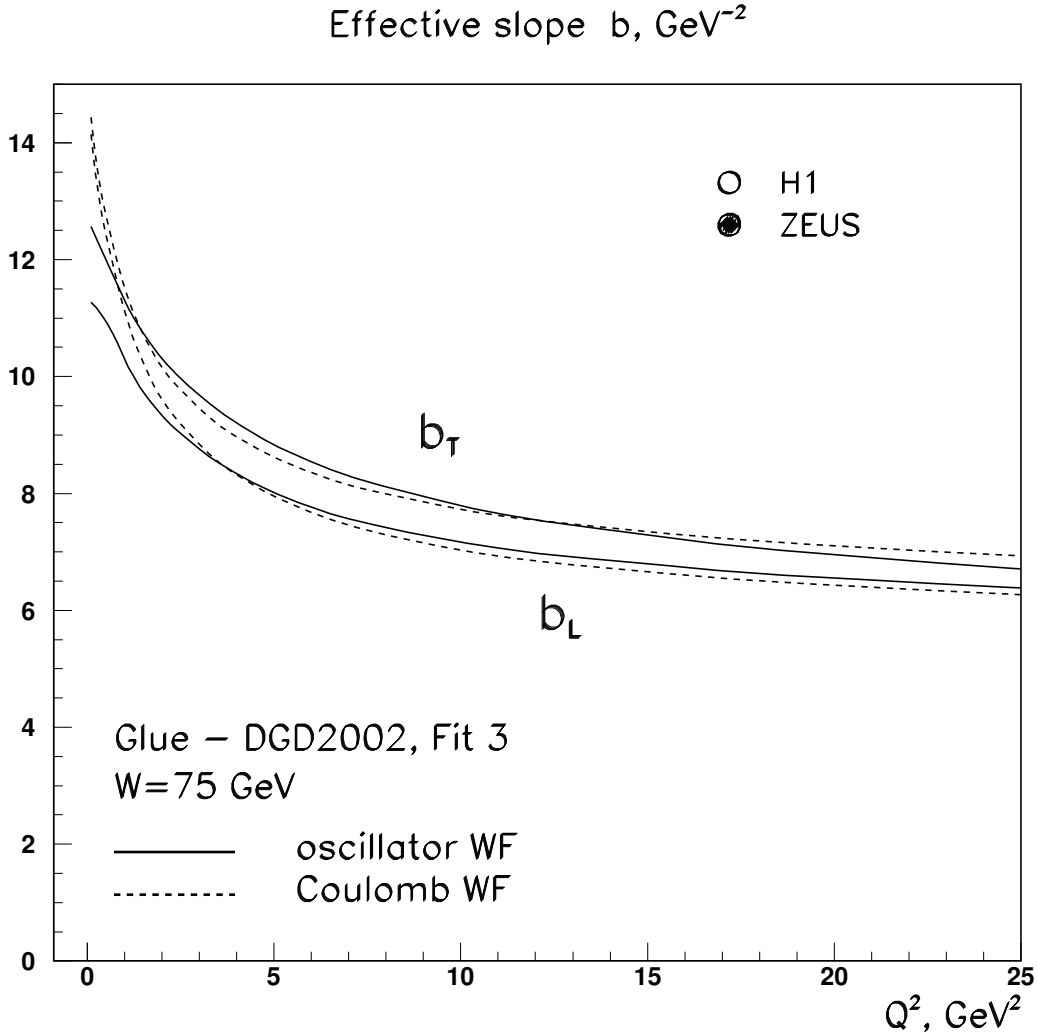


Figure 10.13: Effective slopes  $b_L$  and  $b_T$  of the meson longitudinal and transverse differential cross sections within di-raction cone as functions of  $Q^2$ . Solid and dashed lines correspond to oscillator and suppressed Coulomb wave functions respectively.

### 10.3 mesons

Production of mesons has much similarity with meson production. Therefore we will not provide as detailed discussion of the predictions as we did for meson, but will rather show our direct predictions for the quantities that have been measured experimentally for the mesons.

Fig. 10.18 shows the total cross sections of di-ractive meson production as a function of  $Q^2$  data taken from H1 [78] and ZEUS [79], [80]. Remembering the scaling phenomenon of the vector meson production cross sections, we should expect the picture similar to what happens



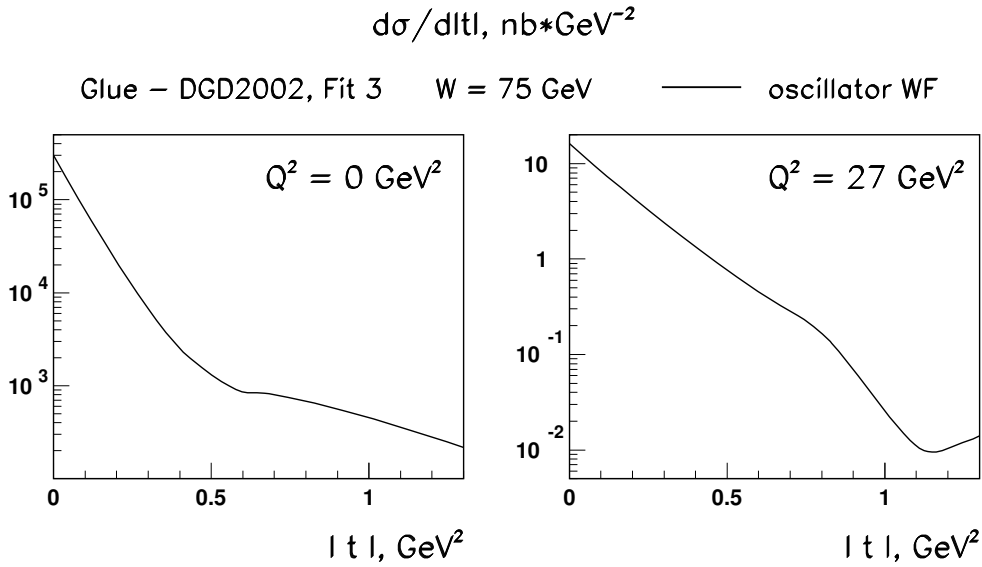


Figure 10.14: The transverse momentum squared dependence of the differential meson production cross sections at two characteristic values of  $Q^2$ .

in the meson case. Indeed, we see at this figure a reasonably good description of the data for moderate  $Q^2$  and a slight overshooting of our predictions as we shift towards small  $Q^2$ .

It is interesting to directly compare meson and meson production cross sections taken at equal  $Q^2$ . Fig. 10.19 shows our predictions for the ratio  $(\pi^+ \pi^-)/(\pi^+ \pi^-)$  together with experimental data. If the scaling phenomenon holds, at higher  $Q^2$  the ratio is expected to approach constant value of 2/9, a tendency to do so is indeed visible at the figure. However, at smaller  $Q^2$  the ratio goes down. This behavior should be expected, for at smaller  $Q^2$  the ratio can be approximated by

$$\frac{(\pi^+ \pi^-)}{(\pi^+ \pi^-)} \sim \frac{Q^2 + m_{\text{eff}}^2}{Q^2 + m_{\text{eff}}^2} \quad ; \quad (10.20)$$

with  $m_{\text{eff}} < m_{\text{eff}}$ .

One sees that our predictions for this ratio agree with the data very well. Moreover, note a remarkable coincidence of the results based on the oscillator and Coulomb wave functions. The reason for that is of course the fact that we study here not absolute values of cross sections, but their ratios. This removes a significant part of ambiguity present in this or that specific choice of the wave function and reveals the features of the  $k_t$  factorization approach in its pure form.

Finally, Fig. 10.20 shows the experimental results for the meson density matrix measurement, published by H1 [78]. Our predictions agree with the data well.

## 10.4 $J = 0$ and mesons

Fig. 10.21 shows the  $k_t$ -factorization predictions for the total cross sections of the  $J = 0$  meson electroproduction as a function of  $Q^2$  compared with available data from H1 [81], [82] and

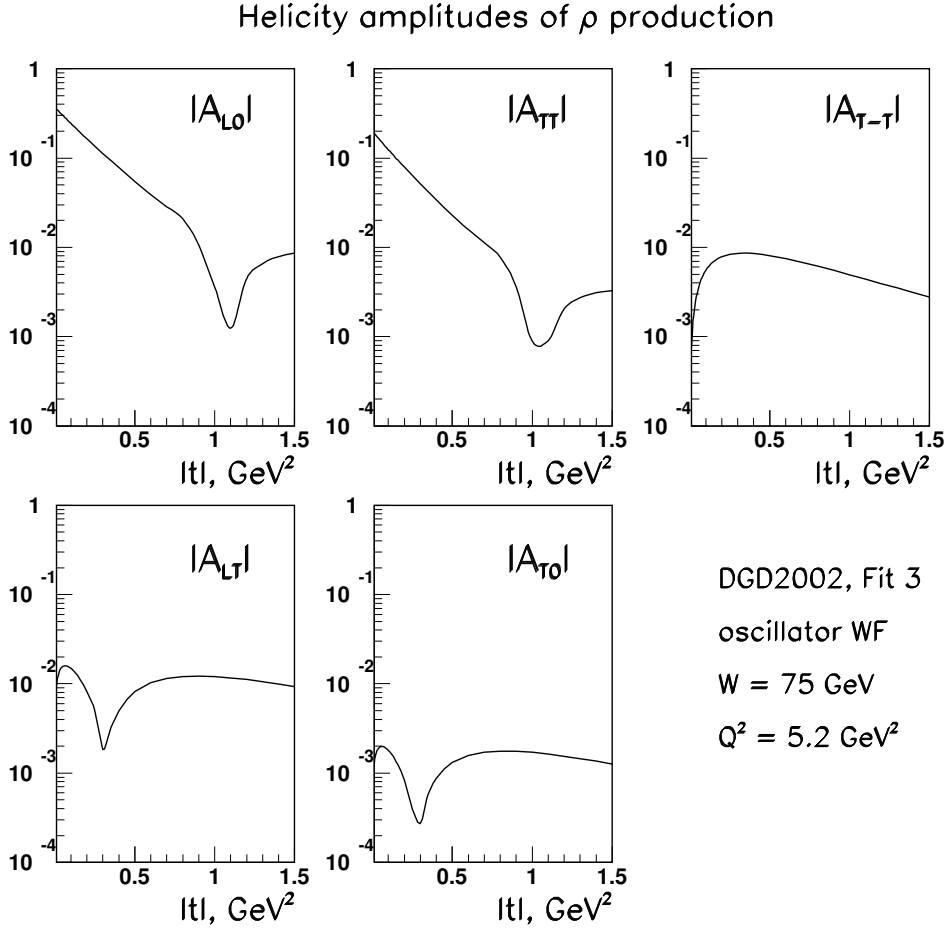


Figure 10.15: The transverse momentum squared dependence of the helicity amplitudes of meson production at  $Q^2 = 5.2 \text{ GeV}^2$ .

ZEUS [77], [83]. A reasonable agreement throughout the whole  $Q^2$  range is seen.

The photoproduction cross sections are shown at Fig. 10.22 versus total energy  $W$  of the  $p$  collision. One can see again that the  $k_t$ -factorization calculations give prediction with accuracy roughly of factor 2, uncertainty coming from the meson wave function. Still, the experimental data fit between the two curves.

Fig. 10.23 shows  $\sigma_L$  -  $\sigma_T$  decomposition of the  $J=1$  meson production cross sections, taken from [85]. An agreement at a similar level of accuracy is observed as well. The ratio  $R(Q^2) = \sigma_L/\sigma_T$  is shown at Fig. 10.24. The data are taken from ZEUS and H1.

The energy dependence of the (1s) meson photoproduction is shown at Fig. 10.25. One observes that the experimental points soar about 10 times higher than the both curves. The origin of this discrepancy is not clear. At the one hand, the  $k_t$  factorization predictions for the production cross sections follow the scaling behavior in Fig. 10.1, while the photoproduction data do not comply with this tendency. It should be noted also that a similar behavior is observed for other processes: that is, the production rates for  $\rho$  seem to

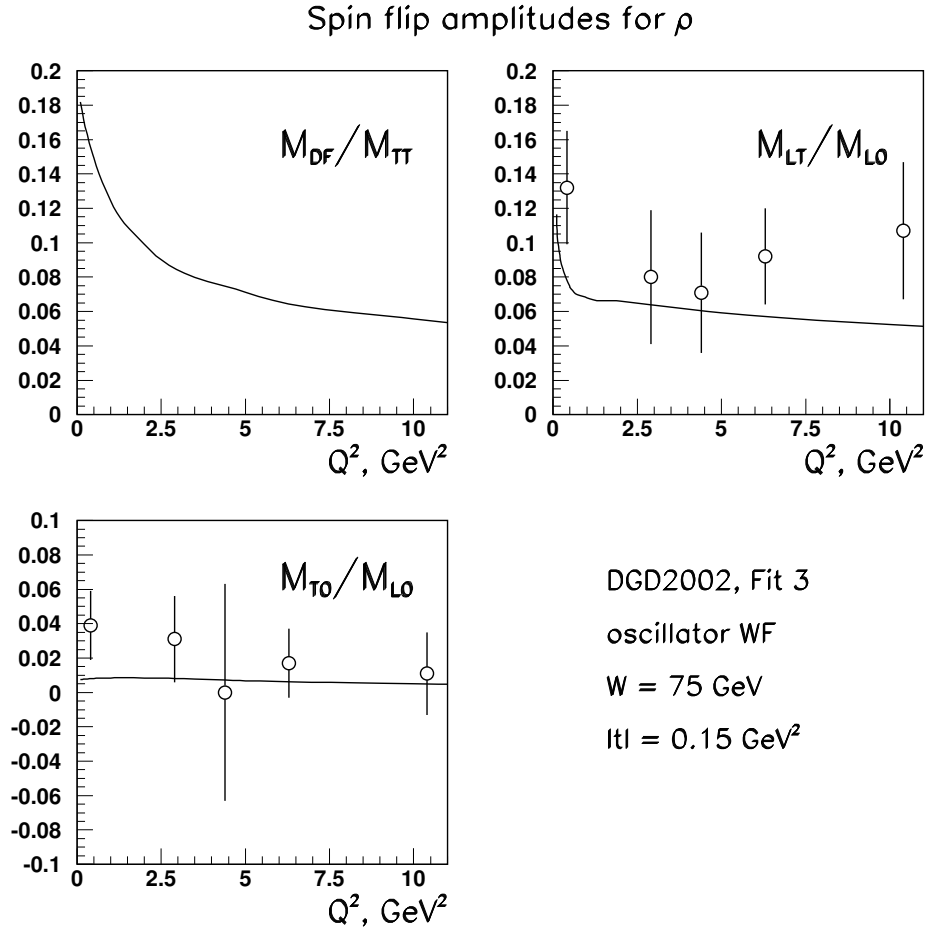


Figure 10.16: The  $Q^2$  dependence of the spin- flip to non-spin- flip amplitudes in the  $\rho$  meson production compared with combined HERA data.

be higher than expected.

## 10.5 Production of excited states

In this section we will give some of the most prominent features in the reaction of diffractive production of 2S and D-wave vector mesons.

In Fig. 10.26 we show the ratios of the excited-to-ground state production cross sections

$$r(2S=1S) = \frac{(\pi \int |V(2S)p|)}{(\pi \int |V(1S)p|)}; \quad r(D=1S) = \frac{(\pi \int |V(D)p|)}{(\pi \int |V(1S)p|)}; \quad (10.21)$$

for  $\rho$  system and for charmonium.

A brief look reveals that although the production rate both of 2S and of D-wave states are suppressed in respect to ground state, a radically different  $Q^2$  behavior of the suppress-

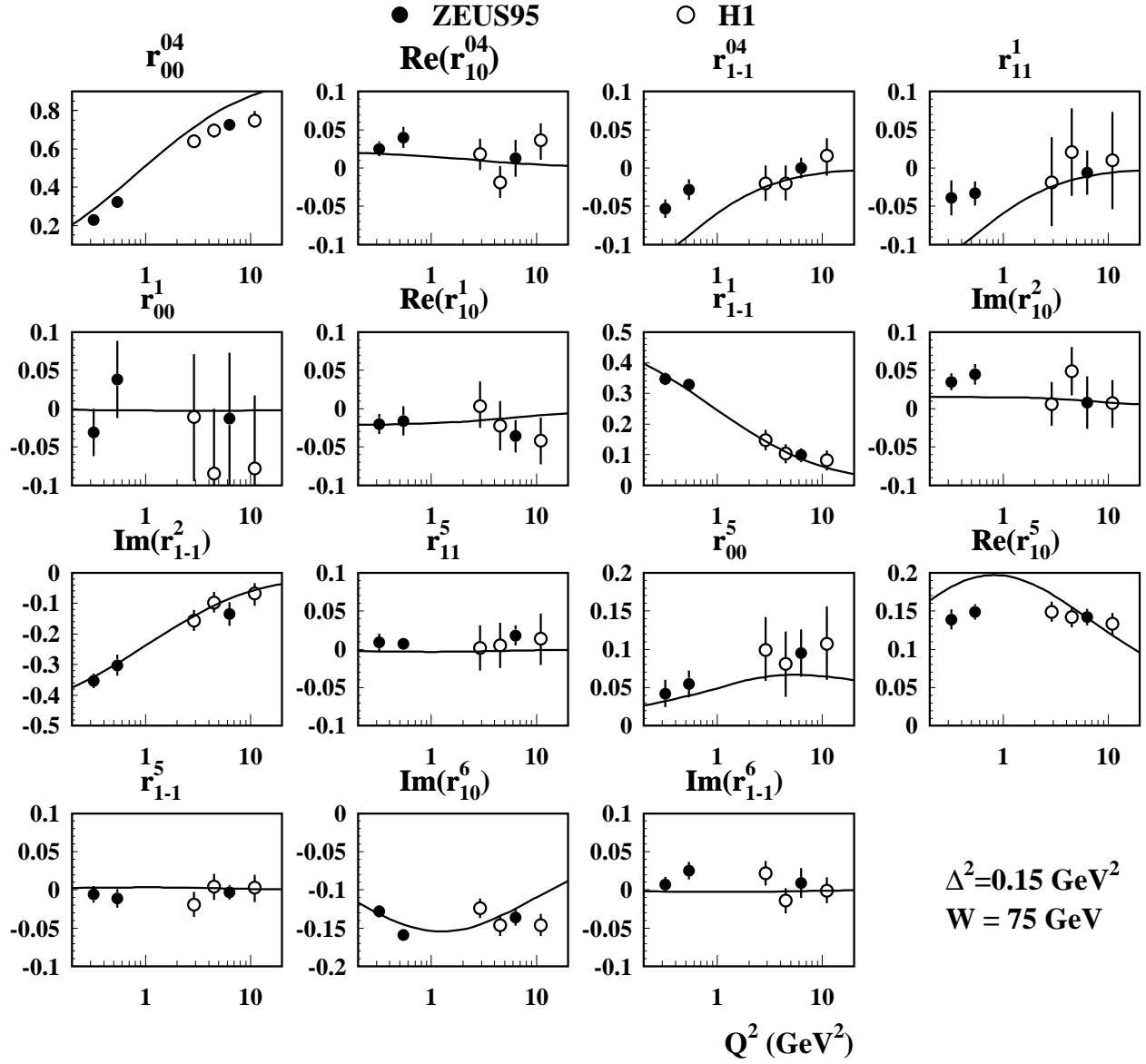


Figure 10.17: Experimental data on spin density matrix for the  $\pi^0$  meson production as function of  $Q^2$  compared with  $k_t$ -factorization predictions based on oscillator wave function.

ing factors  $r(2S=1S)$  and  $r(D=1S)$  is observed. This difference is due to distinct nature of suppression in these two cases.

The suppression for  $2S$  state production comes from much discussed node effect of  $2S$  state wave function. Indeed, if one looks at the  $2S$  production amplitude in the impact parameter space, then one product of two factors: the photon wave function multiplied by dipole cross section  $\sigma_{\text{dip}}$  and the radial wave function of the produced meson. At low  $Q^2$ ,  $\sigma_{\text{dip}}$  is a wide function, peaked at a hadronic scale, that is precisely where the node of the vector meson wave function is located. This results in significant cancellation between contributions

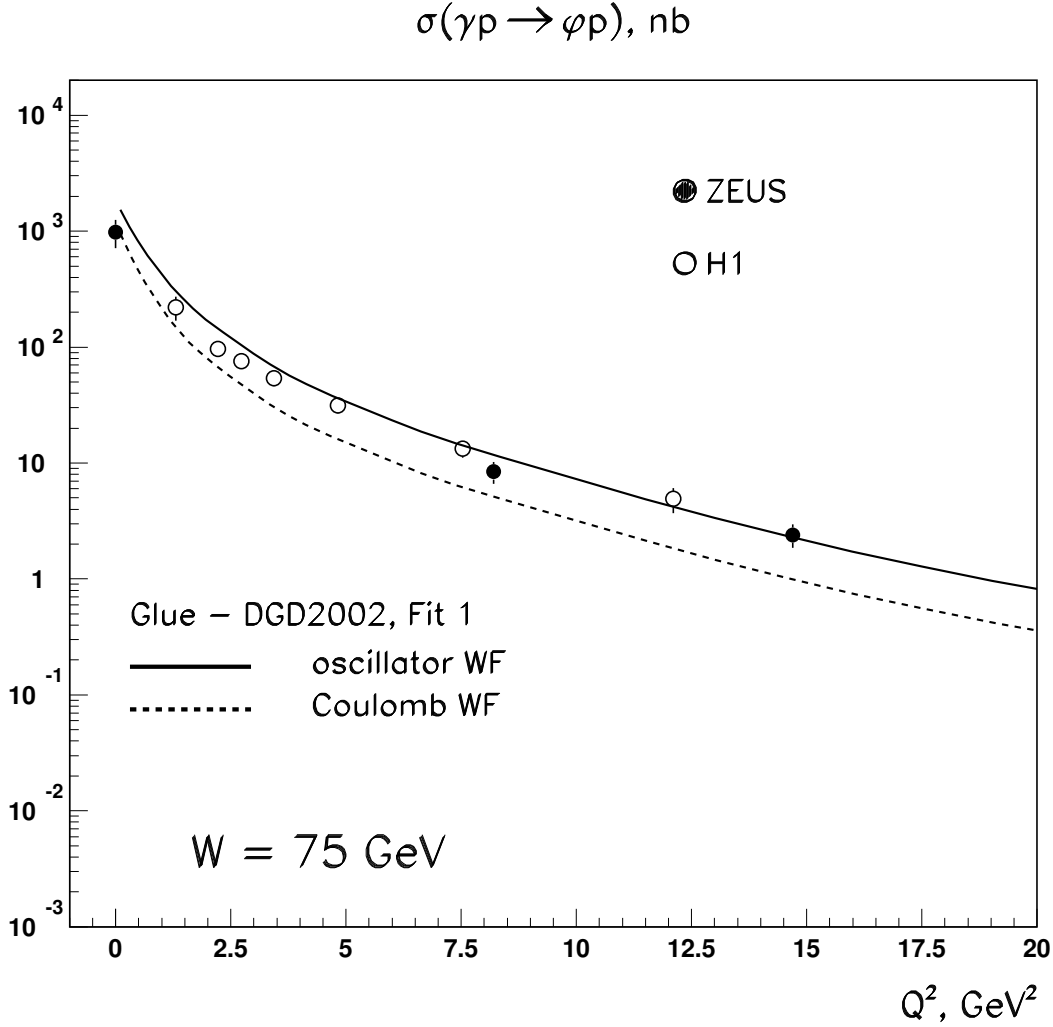


Figure 10.18: Total cross section of the diffractive meson production as a function of  $Q^2$ . The  $k_t$ -factorization predictions based on oscillator (solid lines) and suppressed Coulomb (dashed lines) are also shown. All calculation are performed for  $W = 75 \text{ GeV}$  using DGD 2002, Fit 1.

from impact parameter regions smaller and higher than the node position. At higher  $Q^2$ , the photon wave function shrinks, and the peak of  $\text{dip}$  shifts toward smaller  $r$ , that is away from the node. Thus, the effect of cancellation vanished.

As for the D wave meson suppression, it arises from the angular part of the integrals. In fact, if the initial photon were built only of the S wave  $q\bar{q}$  pair, then, due to orthogonality between pure S and D waves, there would be no D wave vector mesons at all. However, the spinorial structure of the photon coupling to the quark line does not correspond to the pure S wave, but contains an admixture of D wave as well. This D wave part leads to the D wave meson production, and since it is rather small, the cross sections turn out suppressed as well.

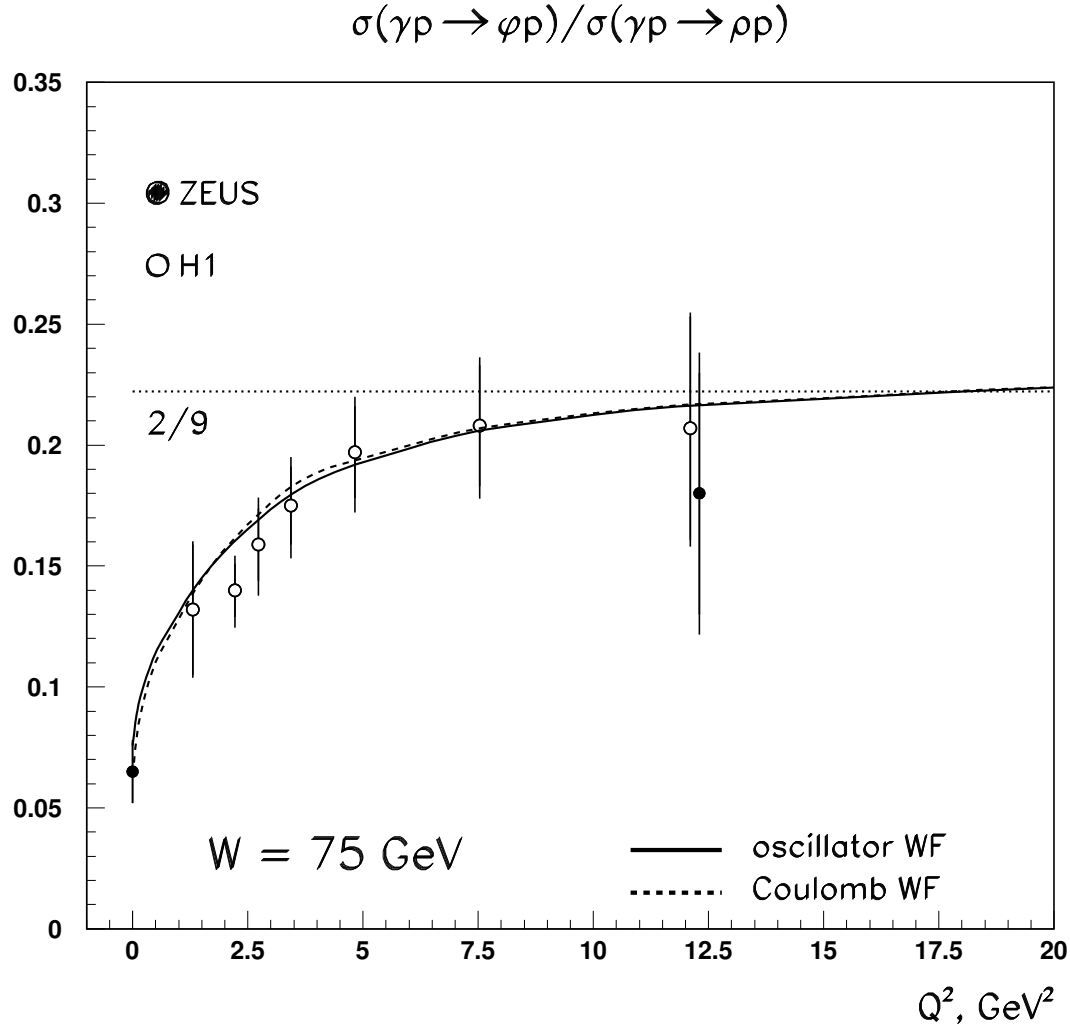


Figure 10.19: Ratio of  $\phi$  meson to  $\rho$  meson total production cross sections as function  $Q^2$ . Solid and dashed lines correspond to oscillator and suppressed Coulomb wave functions respectively.

The situation is basically the same both in the  $\psi$  system and in the charmonium. The major difference is the energy scale of the node effect suppression, which can be directly related to the mass of the corresponding meson.

In the case of charmonium the  $k_t$ -factorization predictions are compared with the available H1 data on  $(2s)$  production [87], [88]. A good agreement is seen.

As vividly illustrated by Fig. 10.26, a mere measurement of the production cross section for high-lying states in the  $\psi$  spectrum (such as  $\psi(1450)$  and  $\psi(1700)$ ) at high  $Q^2$  might be enough to get some insight into the spin-angular structure of these states. However, even more dramatic distinction between S and D wave states is offered by the  $R_V = \Gamma_L(V) / \Gamma_T(V)$  measurements.

## Spin density matrix for $\phi$ meson

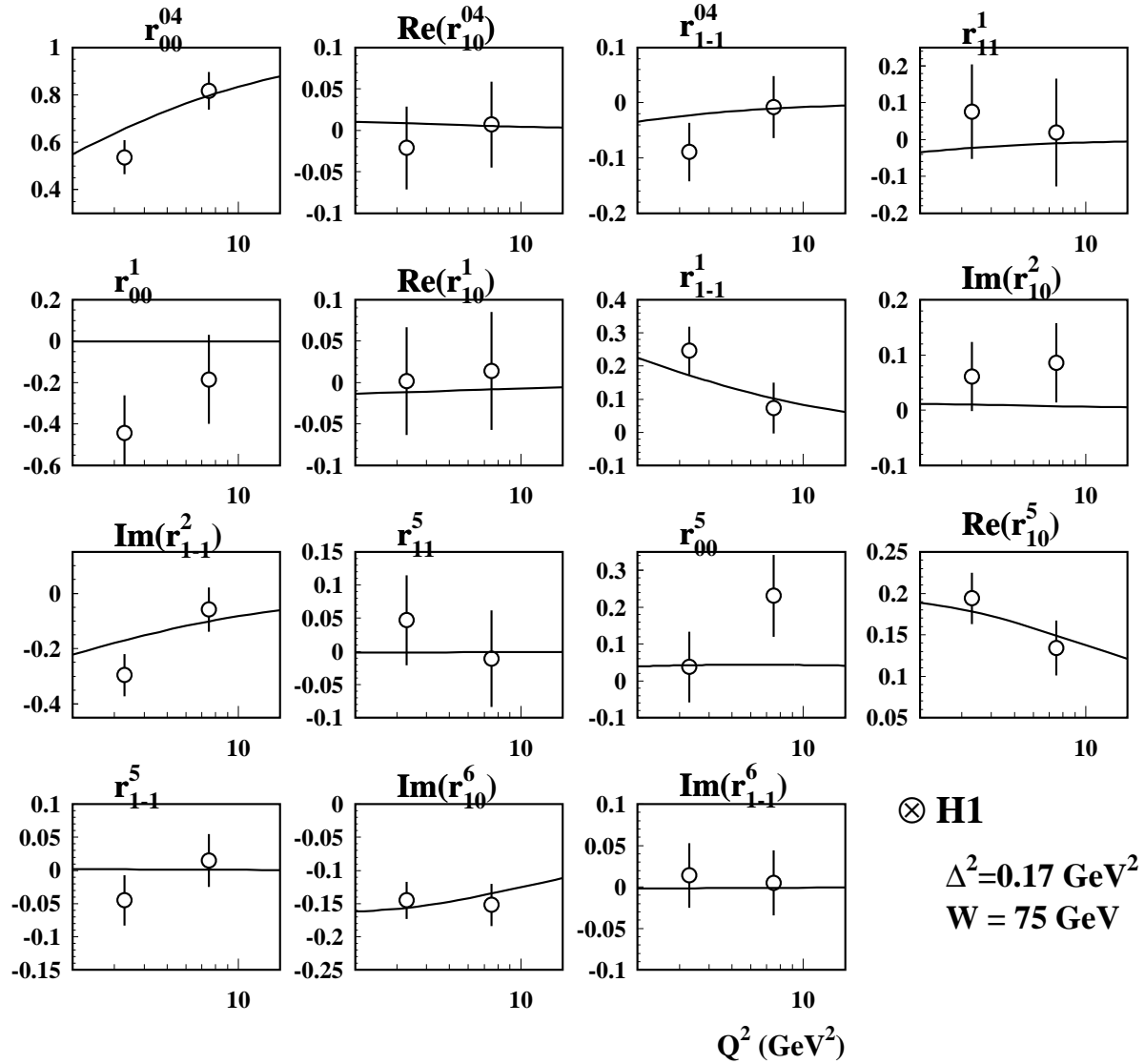


Figure 10.20: Experimental data on spin density matrix for the  $\phi$  meson production as function of  $Q^2$  compared with  $k_t$ -factorization predictions based on oscillator wave function.

Fig. 10.27 shows ratios  $R(1S)$ ,  $R(2S)$ , and  $R(D)$  for the  $\phi$  system. We see that at higher  $Q^2$  the following hierarchy takes place

$$R(1S) > R(2S) > R(D); \quad (10.22)$$

with about one order of magnitude difference between the 1S and D-wave states production rates. At smaller  $Q^2$ ,  $R(2S)$  exhibits very characteristic spectacular wiggles. Starting from zero at  $Q^2 = 0$ , it springs to a local maximum of  $\sim 0.7$  at  $Q^2 \approx 1 \text{ GeV}^2$ , then rapidly fall down, and then rises again. This behavior is the manifestation of the node effect as well. Indeed, since the structure of the transverse and longitudinal photons is not identical, the strongest cancellation takes places at different  $Q^2$  values in these two cases. In particular, the curve

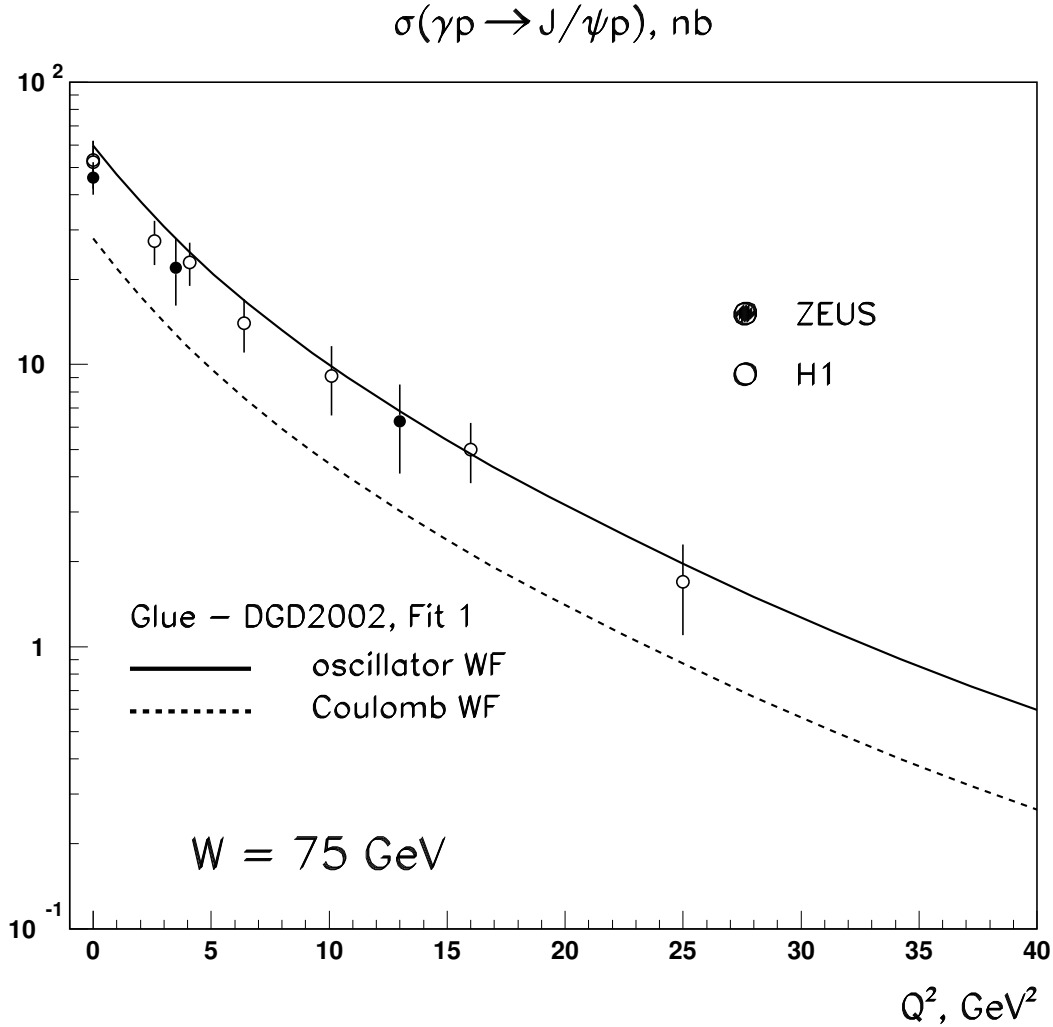


Figure 10.21: Total cross section of the diffractive  $J/\psi$  meson production as a function of  $Q^2$ . The  $k_t$ -factorization predictions based on oscillator (solid lines) and suppressed Coulomb (dashed lines) are also shown. All calculations are performed for  $W = 75 \text{ GeV}$  using DGD2002, Fit 1.

suggests that as start from  $Q^2 = 0$  and we slide along  $Q^2$  scale, the strongest cancellation occurs in  $T$  earlier than in  $L$ .

A word of caution should be said now. The exact position of the node in the  $2S$  state wave function cannot be predicted accurately and depends on the particular Ansatz for the wave function chosen. This means that the wiggly shape of  $R(2S)$  in Fig. 10.27 with the  $Q^2$  positions and the values of local extrema should not be regarded as an accurate prediction. In fact, one cannot even be sure that the non-monotonous  $Q^2$  behavior of  $R(2S)$  actually takes place. This curve simply illustrates what kind of effect can be expected. The specific



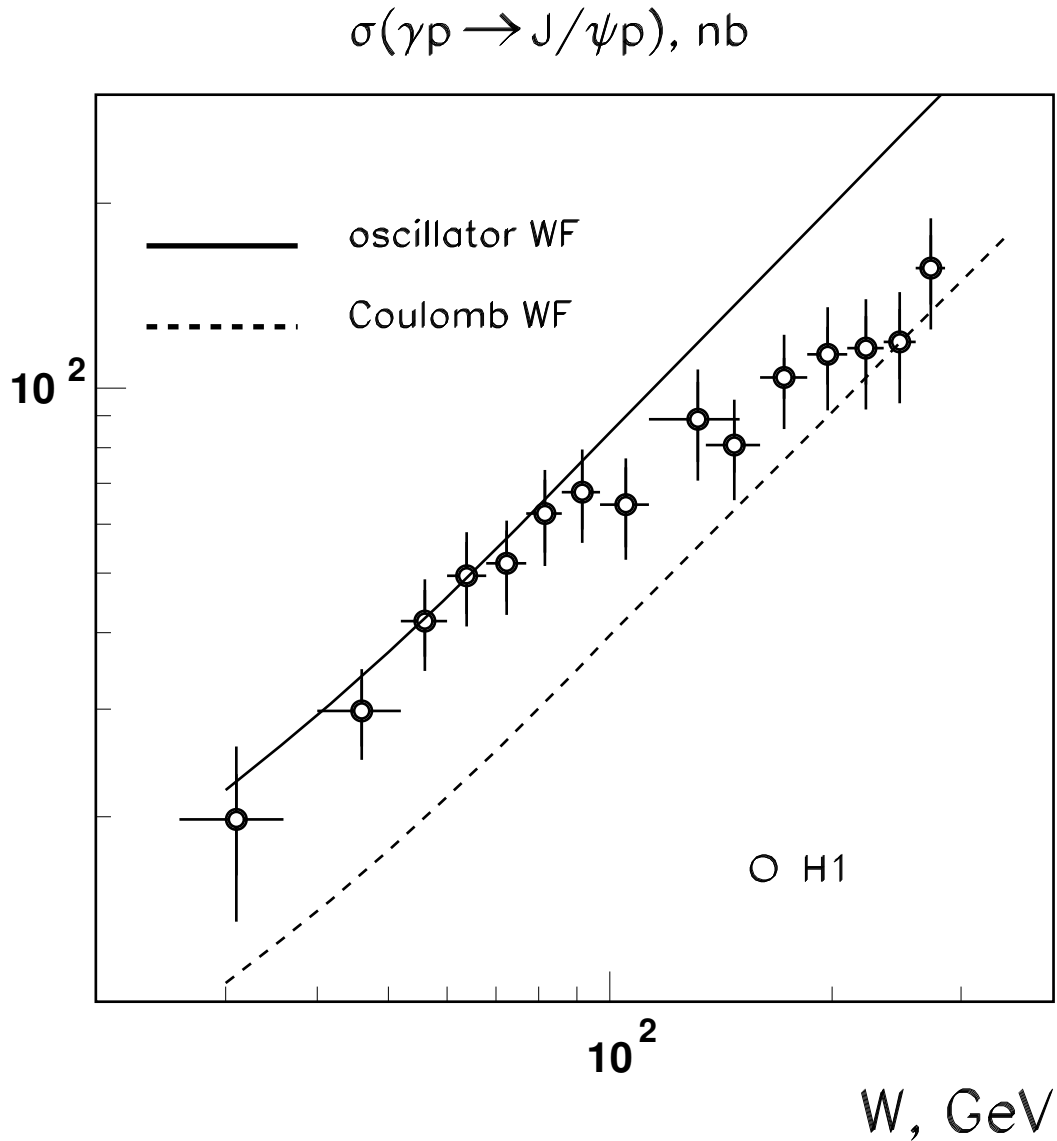


Figure 10.22: The energy dependence of the total  $J=1$  meson photoproduction cross section. The  $k_t$ -factorization predictions based on oscillator (solid lines) and suppressed Coulomb (dashed lines) are also shown. All calculations are performed for  $W = 75$  GeV using DGD 2002, Fit 1.

profile of this curve is not of course predictable, as long as we rely on simple vector meson wave functions.

An immediate conclusion from here is that we found an observable that is extremely sensitive to the minute details of the vector meson wave function — a powerful tool that would help distinguish among various models of the vector meson structure.

The  $t$ -dependence of the 2S state production also shows remarkable features originating from the node effect. Fig. 10.28 shows how the  $t$ -profile of the differential cross section changes over a narrow  $Q^2$  region. The strongest cancellation due to the node effect takes place at

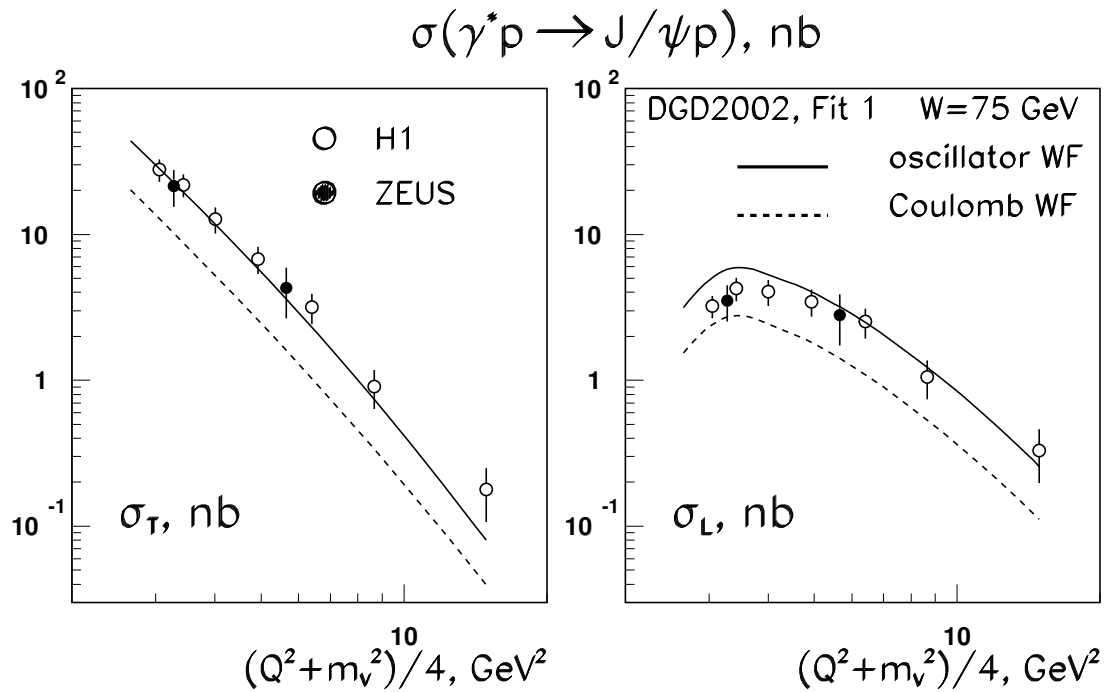


Figure 10.23: Decomposition of the  $J=0$  production cross sections in  $\sigma_L$  and  $\sigma_T$ .

$Q^2 = 0; j_z = 0$ . When we increase  $j_z$  or  $Q^2$ , the strength of the cancellation diminishes, and the differential cross section grows.

Finally, in Fig. 10.29 we show the spin-angular density matrix for the  $1S$ ,  $2S$ , and  $D$  states in the  $\gamma^*p$  system. A dramatic difference among the  $Q^2$  profiles both SCHC and SCHNC matrix elements is seen. Note that some of the matrix elements are even of opposite sign for  $S$  and  $D$  wave states.

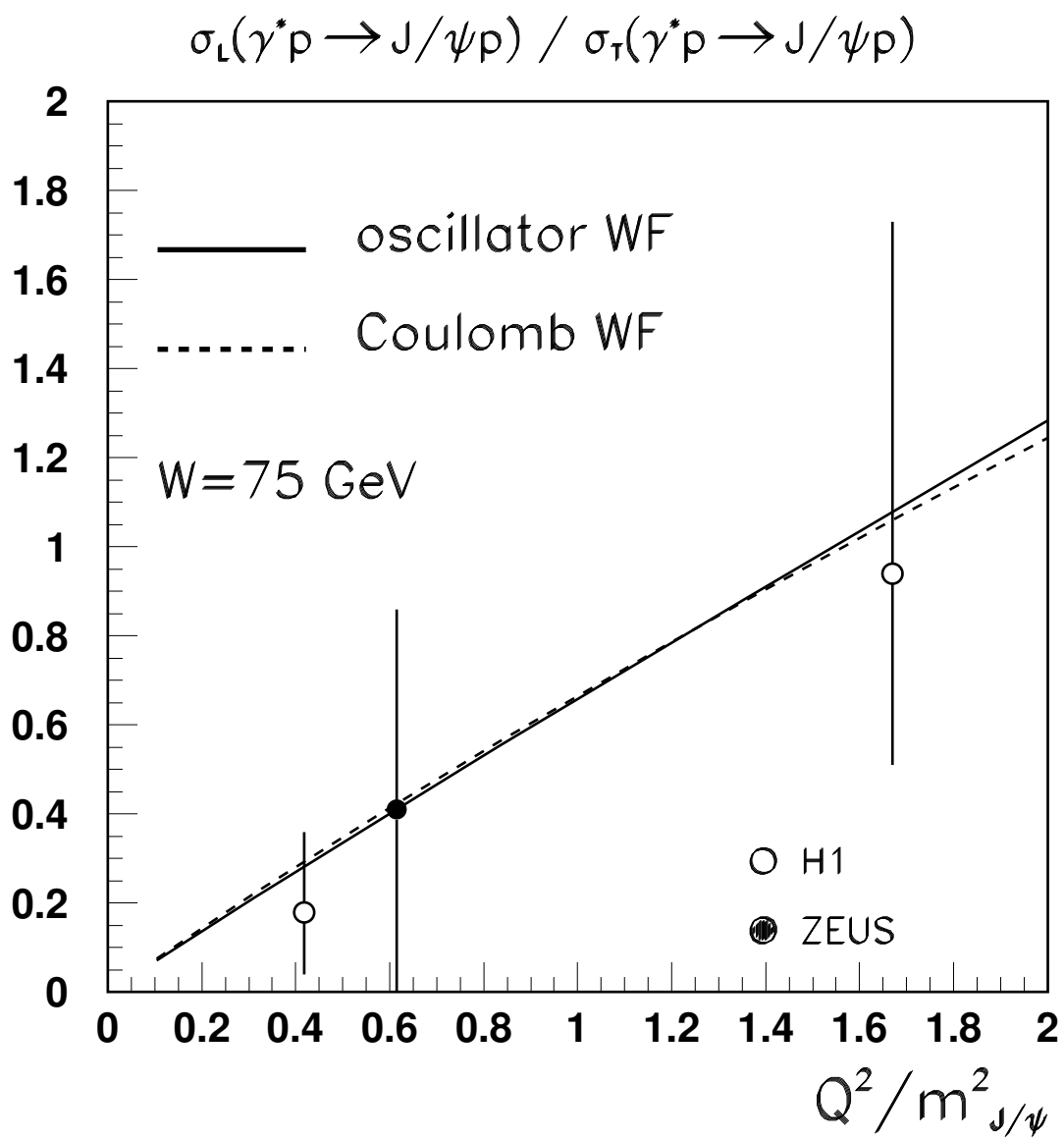


Figure 10.24: Ratio  $R = \sigma_L / \sigma_T$  as a function of  $Q^2$  for  $J/\psi$  meson as a function of  $Q^2$ . Solid and dashed lines correspond to oscillator and suppressed Coulomb wave functions respectively

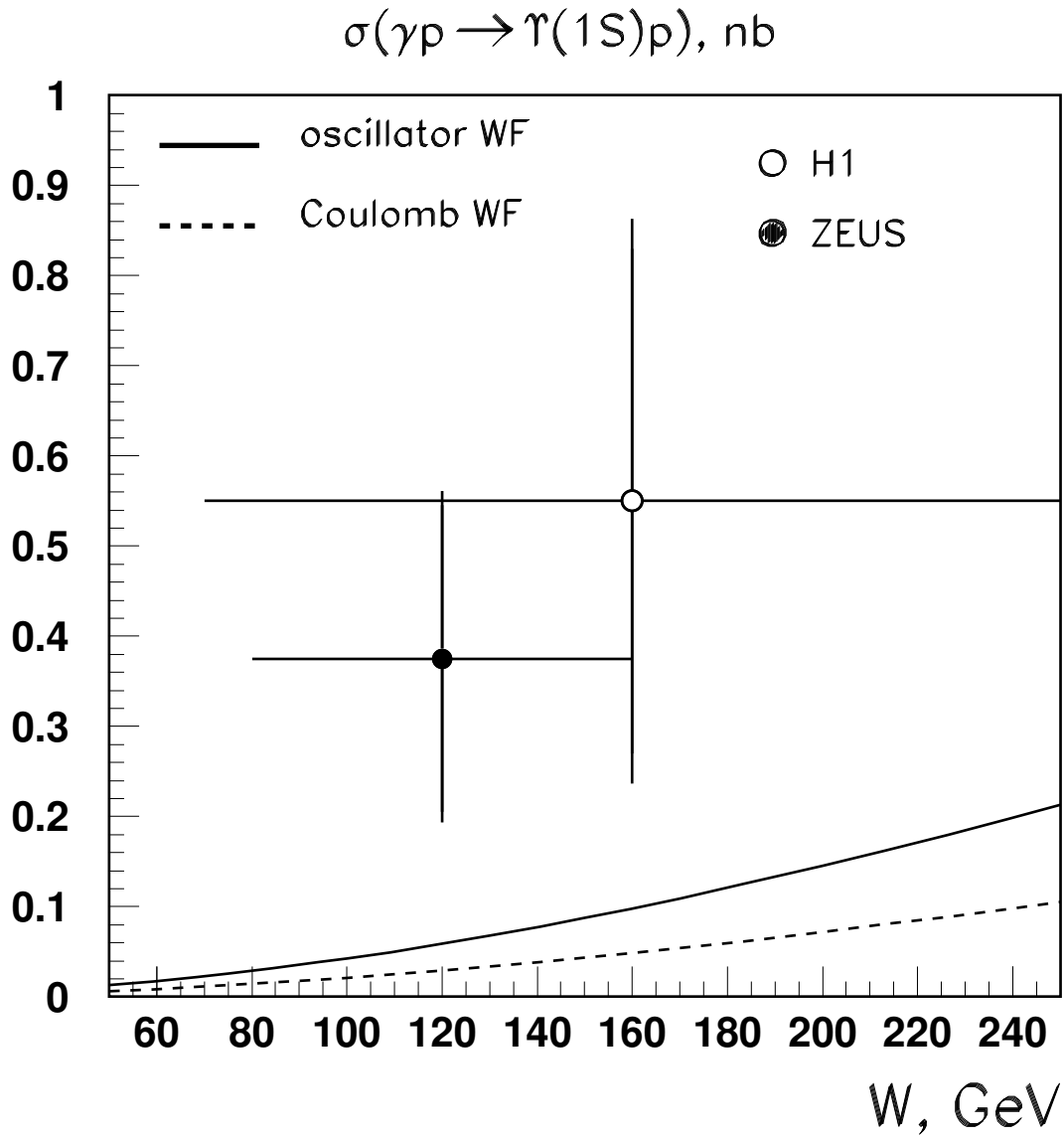


Figure 10.25: The energy dependence of the total  $(1S)$  meson photoproduction cross section. The  $k_t$ -factorization predictions based on oscillator (solid lines) and suppressed Coulomb (dashed lines) are also shown. All calculations are performed for  $W = 75 \text{ GeV}$  using DGD 2002, Fit 1.

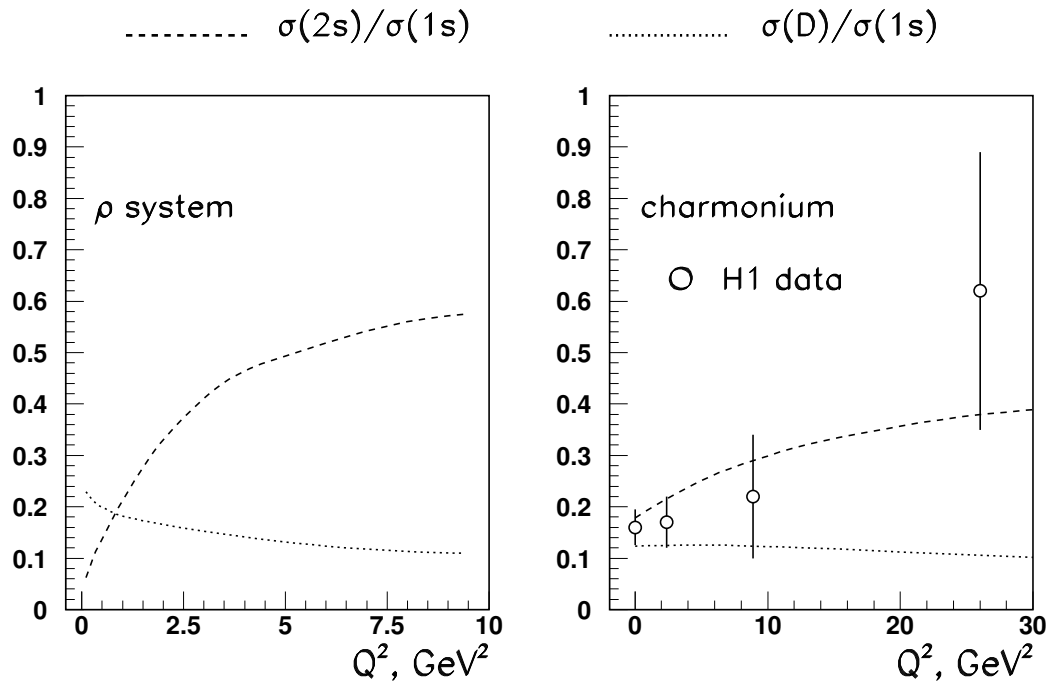


Figure 10.26: The  $Q^2$  behavior of the ratio of excited to ground state vector meson production cross sections in the case of  $\rho$  system and charmonium. Dashed and dotted lines represent  $\sigma(2s)/\sigma(1s)$  and  $\sigma(D)/\sigma(1s)$  ratios respectively. In all calculations, oscillator wave function was used.

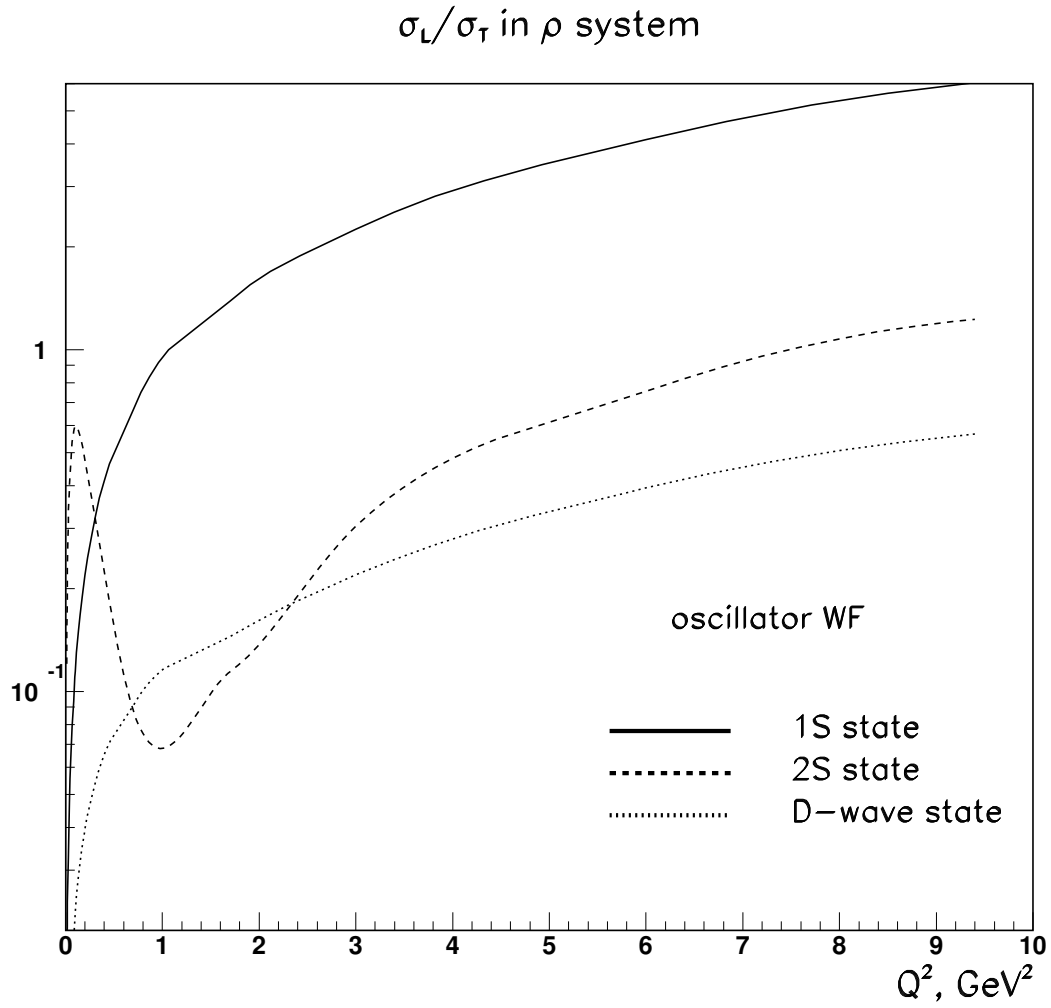


Figure 10.27: The  $Q^2$  behavior of the  $\sigma_L/\sigma_T$  ratio for 1S (solid line), 2S (dashed line) and D wave (dotted line) states in the  $\rho$  system. In all calculations, oscillator wave function was used.

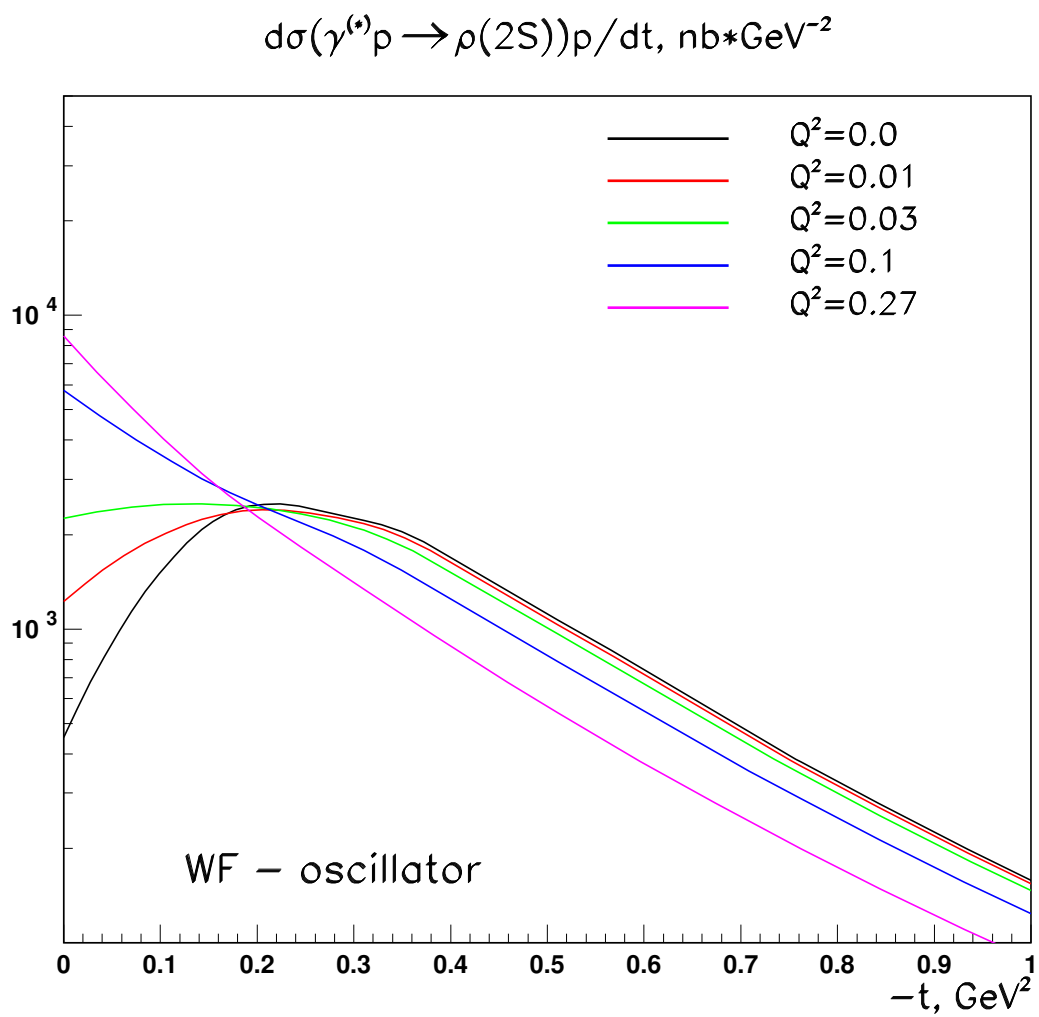


Figure 10.28: Strong forward dip for 2S state in system : the change in  $t$  profile of the differential cross section within narrow  $Q^2$  region.

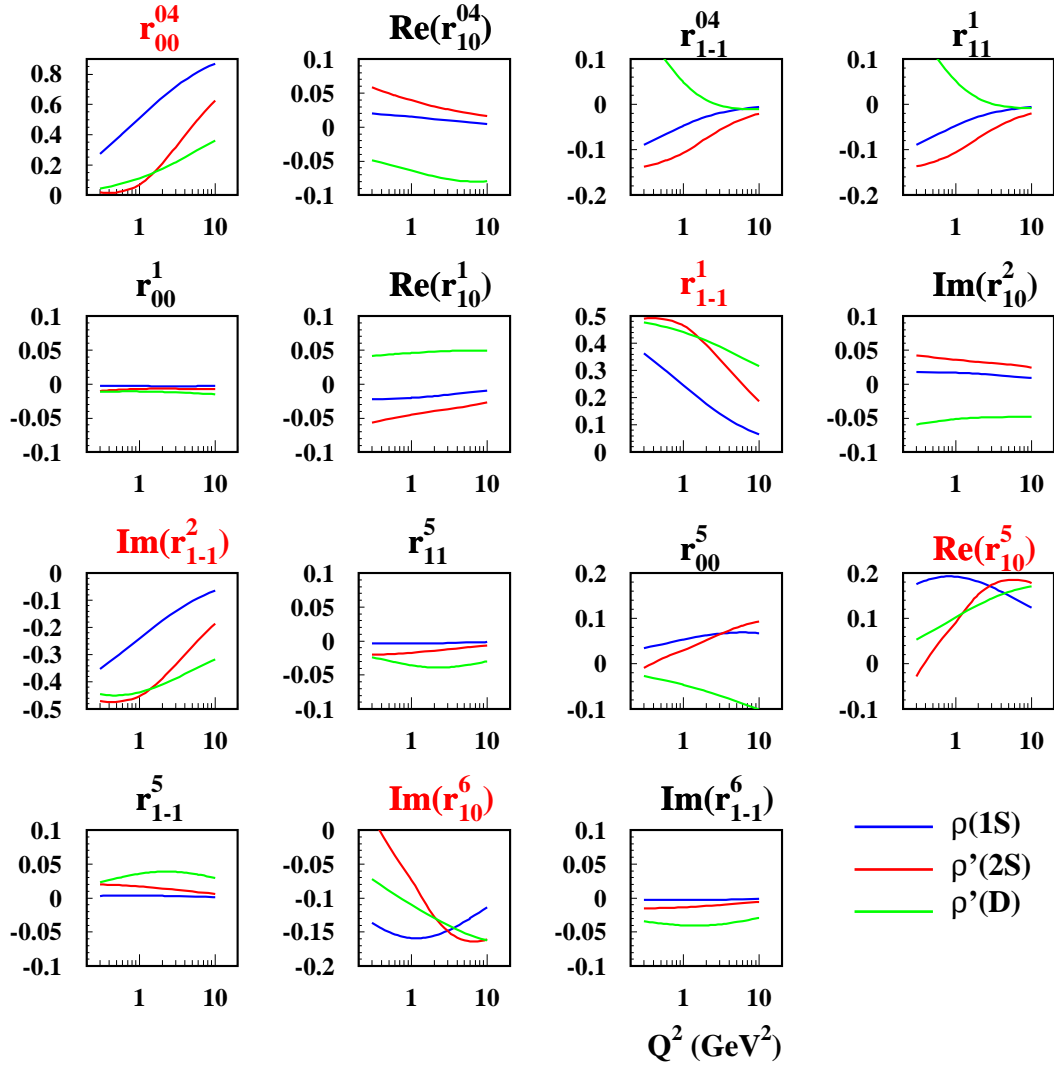


Figure 10.29: The  $Q^2$  behavior of the spin density matrix for 1S, 2S, and D wave states in the system.



# Chapter 11

## The $\sigma_T$ puzzle

The detailed comparison of the numerical results for meson production obtained in the  $k_t$ -factorization approach with the experimental data shows that the scheme used fails to reproduce the correct  $Q^2$  behavior of the transverse cross section  $\sigma_T$ , which was dubbed by us as  $\sigma_T$  puzzle. In this chapter we explore two possible causes of this mismatch. Namely, we explore the effect of color Coulomb interaction of qq pair and show that it leads to  $\sigma_T$  increase in respect to  $\sigma_L$ . Then we analyze the issue of possible S=D wave mixing in the system and try to obtain a better description of the  $\sigma_L = \sigma_T$ .

As we will see, the first method might turn out the remedy for the  $\sigma_T$  puzzle, but even an accurate formulation of this method forces us to go beyond the lowest Fock state, thus making only rough estimates of the effect possible. The second mechanism will be shown indeed to decrease the  $\sigma_L = \sigma_T$  ratio at higher  $Q^2$  down to an acceptable values, but this happens at the expense of too low values of  $\sigma_L$ , not increased values of  $\sigma_T$ . Therefore, this mechanism does not provide the solution to the  $\sigma_T$  puzzle, at least in its pure form.

### 11.1 The Coulomb tail of the wave function

As we discussed before, the major source of ambiguity in our approach is the vector meson wave function. Without accurate knowledge of the radial wave function, one is bound only to an educated guess.

In our treatment we stuck everywhere to the soft wave function Ansatz, that is, we assumed that any integrals involving the wave function would be saturated by small- $p$  region ( $p \ll 1/R_V$ ). This implies that at large- $p$  the wave function must vanish fast enough, or to be precise, faster than any  $p^2$  power present in numerators of the above formulas. Since the highest momentum power is  $k^2$ , which appears, for instance, in the transverse amplitudes, we conclude that the "softness" of the wave function means that

$$(z; \vec{k})_{k^2 \rightarrow 1} = o \left( \frac{1}{k^4} \right) : \quad (11.1)$$

The Gaussian wave function Ansatz used everywhere above certainly satisfies this requirement.

It turns out, however, that the above requirement is violated when the true short-range Coulomb-like interquark potential is taken into account. As well known, if the color Coulomb potential were the only source of the quark-antiquark interaction, the resulting Coulomb-type

wave function of the vector meson would look like

$$\langle p \rangle \sim \frac{1}{(p^2 + a^2)^2} : \quad (11.2)$$

In reality, the interquark forces are much more complicated. However, without any need to know the precise form of interquark forces, one can assert that at short distances there must be some resemblance of the Coulomb-like wave high- $p^2$  tail.

### 11.1.1 The strategy

Certainly, there is a multitude of approaches that claim to account for the color Coulomb interaction at short distances. One of them would consist in obtaining an accurate numeric solution of a given potential model. If one prefers to use a fully QFT-based approach, one must deal then with a set of diagrams. Ideally, one should start with free quarks and then, by taking their interaction into account, arrive at the physical vector meson with a (presumably) uniquely defined qq wave function.

Realizing such a program is still an unresolved task and attempts to accomplish it would certainly go far beyond this study. Moreover, even if we were capable of doing it, we would still run into interpretational difficulties, at least in the framework of our scheme. Indeed, when calculating the diagrams, we will see the higher Fock states intrude into our qq description of the vector meson. So, even if we still wanted to follow only quark-antiquark distribution in a meson, we will be forced to switch from the wave function to the density matrix description. Another problem would be the presence of higher angular momenta of the qq pair due to gluon radiation. This will leave no room for our simple S wave/D wave description of the vector meson. Finally, the qq wave function (or density matrix) will have no unique, process independent definition. Indeed, in order to preserve the gauge invariance at any given order of perturbation theory, we will have to include corrections to the rest of a diagram (the kernel) as well as corrections that entangle the kernel with the wave function. As a result, the two particle irreducibility of the process will be lost.

The conclusion is that we cannot expect a reasonable answer to the question "how to account for short range Coulomb interaction" and still stay within the framework of our approach.

Nevertheless, the mere formulation of this question does not force us to go beyond our lowest Fock state, two-particle irreducible approach. So, it can be reiterated as "The Coulomb tail of the wave function must be there; given that, can we develop a reasonable understanding of its impact on dynamics of the vector meson production?" In this formulation, we now ask for a QFT-inspired model that would produce an estimate of the hard tail without forcing us to run into problems just mentioned.

We suggest the following procedure that would satisfy this need. We start with the soft wave function Ansatz and perform a sort of evolution procedure, that will generate the hard tail. This evolution will basically consist in allowing for gluon exchange between the quark and the antiquark. The result will be interpreted as the hard piece of the vertex function, and eventually as the hard piece of the wave function itself.

### 11.1.2 The quantum mechanics of the Coulomb tail

Suppose that our potential is a sum of an oscillator and Coulomb potential, the latter being a "perturbation" and bearing an intrinsic small parameter:

$$V(p) = V_{\text{osc}}(p) + V_{\text{coul}}(p);$$

$$V_{\text{osc}}(p) = \frac{1}{2} \frac{12}{p^2} \omega(p); \quad V_{\text{coul}}(p) = \frac{4}{p^2 + \frac{2}{G}} s(p^2) C_F; \quad (11.3)$$

Here coupling constant is supposed to be the small parameter. Effective parameter  $G$  accounts for confinement.

The total wave function is represented as sum of the soft part  $s = c \exp(-\frac{1}{2}k^2 a^2)$ , which is the solution of Schrodinger equation with oscillator potential only, and the hard part  $h$ , determined via:

$$\frac{p^2}{2} - E - h(p) = \frac{1}{(2\pi)^3} \int dk V_{\text{coul}}(k) s(p-k) \quad (11.4)$$

Let's for a moment neglect running of the coupling constant. Then,

$$h(p) = \frac{1}{\frac{p^2}{2} - E} \frac{4}{(2\pi)^3} s C_F \int dk V_{\text{coul}}(k) s(p-k); \quad (11.5)$$

so that

$$s(p) = \exp\left(-\frac{k^2 a^2}{2}\right) + \frac{1}{\frac{p^2}{2} - E} \frac{4}{(2\pi)^3} s C_F \int dk V_{\text{coul}}(k) s(p-k); \quad (11.6)$$

Here

$$\begin{aligned} I(p) &= \int \frac{d^3 k}{(p-k)^2 + \frac{2}{G}} \exp\left(-\frac{k^2 a^2}{2}\right) = 2 \int_0^1 k^2 dk \frac{1}{2pk} \log \frac{(p+k)^2 + \frac{2}{G}}{(p-k)^2 + \frac{2}{G}} \exp\left(-\frac{k^2 a^2}{2}\right) \\ &= 2 \int_0^1 \frac{k^2 dk}{k^2 + \frac{2}{G}} \frac{e^{\frac{(k-p)^2 a^2}{2}} - e^{\frac{(k+p)^2 a^2}{2}}}{k p a^2}; \end{aligned} \quad (11.7)$$

This function cannot be evaluated exactly. One can, however ask for its the asymptotic large- $p$  behavior, which can be evaluated directly from (11.4) by replacing  $k \rightarrow p-k$  and taking  $V_{\text{coul}}(p-k) \rightarrow V_{\text{coul}}(p)$  out of the integral:

$$h(p \rightarrow 1) = 4 C_F s \frac{2}{p^4} \quad (r=0); \quad (11.8)$$

Note, however, that one should not use this simple analytic form because it spoils the large distance behavior of the wave function. The wave function (11.8), even when regularized as  $p^2 \rightarrow p^2 + \frac{2}{G}$ , leads to exponential decrease of the wave function as  $\sim \exp(-r/G)$ , while the honest wave function exhibits gaussian decrease  $\sim \exp(-\frac{1}{2}r^2 a^2)$ .

### 11.1.3 Derivation of Coul

The diagrammatical representation of this procedure is shown in Fig. 11.1. Instead of implementing soft vertex function  $\Gamma_{\text{soft}}$ , we use properly normalized

$$\Gamma_{\text{total}} = \frac{1}{N} (\Gamma_{\text{soft}} + \dots); \quad (11.9)$$

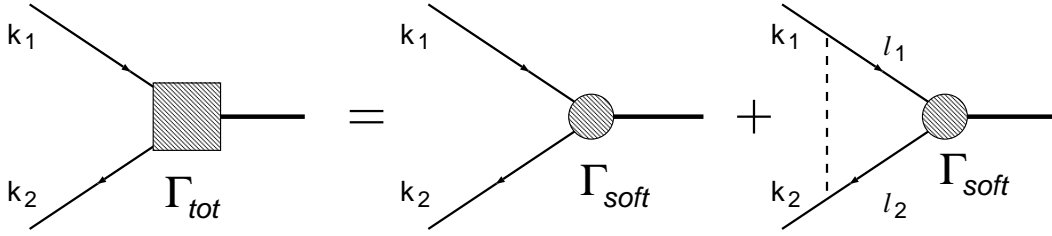


Figure 11.1: Diagrammatic representation of the effect of Coulomb tail at small distances

where  $1 = \frac{P}{N}$  factor accounts for the proper normalization. The Coulomb correction reads then

$$(z; \mathbf{k}) = i \frac{d^4 l}{(2\pi)^4} \mathcal{G}_F \frac{(\hat{l}_2 + m)_{\text{soft}} (\hat{l}_1 + m)}{(\hat{l}_1^2 - m^2 + i'')(\hat{l}_2^2 - m^2 + i'')[(k_1 - l)^2 - \frac{2}{G} + i'']} : \quad (11.10)$$

The Sudakov decomposition of the momenta of the initial and intermediate particles' reads

$$\begin{aligned} k_1 &= y p^0 + z q^0 + k_\perp ; \\ k_2 &= (1-y)p^0 + (1-z)q^0 - k_\perp ; \\ l_1 &= y^0 p^0 + z^0 q^0 + l_\perp ; \\ l_2 &= (1-y^0)p^0 + (1-z^0)q^0 - l_\perp ; \\ (k_1 - l) &= (y - y^0)p^0 + (z - z^0)q^0 + (k_\perp - l_\perp) : \end{aligned} \quad (11.11)$$

We already know from the above analysis that one of the initial particles is on-mass shell. Therefore, one of the two conditions

$$y = \frac{\mathbf{k}^2 + m^2}{z m_V^2} \quad \text{or} \quad y = 1 - \frac{\mathbf{k}^2 + m^2}{(1-z)m_V^2}$$

is fulfilled.

The numerator constitutes the most challenging part. Certainly, there is absolutely no problem to perform gluon index summation:

$$(\hat{l}_2 + m)(\hat{l}_1 + m) = 2m^2 - 2\hat{l}_1 \cdot \hat{l}_2 - 4(l_\perp - l_\perp) : \quad (11.12)$$

The problem however is that this spinorial structure cannot be reduced to the scalar multiplicative renormalization of the original structure. Moreover, after integration the spinorial structure cannot be expressed in terms of S and D waves only. Finally, the resulting spinorial structure will lead to not gauge invariant correction to the wave function.

In order to go as far as we can in trying to obtain a reasonable estimate for the Coulomb tail and avoid trouble, we propose the following procedure. First, we look at the transverse vector meson production. Since the vector meson polarization vector  $V$  possesses only transverse components ( $\nabla$ ), only transverse terms

$$2m^2 \sim + 2\hat{l}_1 \cdot \hat{l}_2 - 2[z(1-y^0)p^0 \cdot q^0 + y^0(1-z^0)q^0 \cdot p^0] \quad \& : \quad (11.13)$$

will survive from the whole expression (11.12). Then, in order to simplify life, we will proceed for the meson as if it were a heavy quarkonium. That is, we will neglect  $\mathbf{l}^2$  in comparison

with  $m^2$  and put  $z^0 = \frac{1}{2}$ . Finally, the last stroke will be to put  $m_V^2 = 4m^2$  in numerator, so that  $y^0$  can be replaced by  $1=2$  as well. The result of this procedure will give

$$(\hat{l}_2 + m) \sim (\hat{l}_1 + m) \quad ! \quad 4m^2 \sim ;: \quad (11.14)$$

Finally, we postulate that the same scalar renormalization holds for longitudinal vector mesons as well.

The denominator is calculated in the same way as before. We note that the numerator in our calculation does not depend on  $y^0$ , and therefore, the pole structure on the  $y^0$  plane comes from the propagators only. The position of poles, however, changes with  $z^0$ : at  $z^0 < 0$  or  $z^0 > 1$  all poles lie in the same half-plane, and thus by closing the contour we can nullify the contribution of these  $z^0$  regions to the integral. Then, the interval  $0 < z^0 < 1$  naturally breaks into two parts:  $z^0 < z$  and  $z^0 > z$  intervals. In the former region we prefer to close the contour from below and take the residue at the position of pole 1. The two other propagators become

$$\begin{aligned} \text{pole 2} & ! \quad (1 - z^0) (m_V^2 - M^2) + i''; \\ \text{pole 3} & ! \quad (z - z^0) e y m_V^2 \frac{k^2 + m^2}{z^0} A \quad k^2 \quad 1^2 \quad \frac{2}{G} + i''; \end{aligned} \quad (11.15)$$

In the second  $z^0$  region we close the contour from above and take residue at  $y^0 = 1 - \frac{k^2 + m^2}{m_V^2} = [(1 - z^0)m_V^2]$ , so that the other poles become

$$\begin{aligned} \text{pole 1} & ! \quad z^0 (m_V^2 - M^2) + i''; \\ \text{pole 3} & ! \quad (z^0 - z) (M^2 - m_V^2) \quad (z^0 - z) e y m_V^2 \frac{k^2 + m^2}{z^0} A \quad k^2 \quad 1^2 \quad \frac{2}{G} + i''; \end{aligned} \quad (11.16)$$

Note that in both cases the familiar  $M^2 - m_V^2$  appears in the denominator, which fuses with  $\text{soft}(M^2)$  to produce  $\text{soft}(M^2)$ . Thus, the result of the  $y^0$  integration is

$$\begin{aligned} & \int_{-1}^1 dy^0 \frac{\text{soft}(M^2)}{(l_1^2 - m^2 + i'')(l_2^2 - m^2 + i'')[(k_1 - l)^2 - \frac{2}{G} + i'']} \\ & = (z - z^0) \frac{1}{1 + (k^2 - 1)^2 + \frac{2}{G}} + (z^0 - z) \frac{1}{2 + (k^2 - 1)^2 + \frac{2}{G}} \end{aligned} \quad (11.17)$$

with

$$\begin{aligned} 1 & = (z - z^0) \frac{k^2 + m^2}{z} \frac{k^2 + m^2}{z^0} \geq k_1 \text{ on mass shell;} \\ 2 & = (z^0 - z) \frac{k^2 + m^2}{z} \frac{k^2 + m^2}{z^0} + (z^0 - z) (M^2 - m_V^2) \geq \\ 1 & = (z - z^0) \frac{k^2 + m^2}{1 - z} \frac{k^2 + m^2}{1 - z^0} + (z^0 - z) (M^2 - m_V^2) \geq k_2 \text{ on mass shell.} \\ 2 & = (z^0 - z) \frac{k^2 + m^2}{1 - z} \frac{k^2 + m^2}{1 - z^0} \geq \end{aligned}$$

The analysis of the positive definiteness of the gluon propagator reveals that in one case the positiveness indeed holds due to inequality

$$\frac{z - z^0}{z} k^2 + \frac{z - z^0}{z^0} 1^2 + (k^2 - 1)^2 = e \frac{z^0}{z} k^2 \quad r \frac{1}{z^0} 1^2 > 0;$$

while in the other case the gluon pole can in principle arise in the allowed kinematical region. Such a pole would correspond to the situation when both quark and gluon are simultaneously on mass shell. However, in the case of mesons such configurations are avoided due to small enough mass of the vector meson ( $m_V^2 < 2 \frac{s}{G}$ ).

So, the expression for  $\phi(z; \mathbf{k})$  takes form

$$\begin{aligned} \phi(z; \mathbf{k}) = & C_F \frac{s(\mathbf{k}^2)}{4} 4m^2 \int_0^1 \frac{dz^0}{z^0(1-z^0)} d^2 \mathbf{l}_{\text{soft}}(M^2) \\ & \left( (z - \frac{z^0}{2}) \frac{1}{1 + (\mathbf{k} - \mathbf{l})^2 + \frac{z^0}{2}} + (z^0 - z) \frac{1}{2 + (\mathbf{k} - \mathbf{l})^2 + \frac{z^0}{2}} \right) : \quad (11.18) \end{aligned}$$

With  $\phi(z; \mathbf{k})$  calculated according to (11.10), we can now construct the hard part of the wave function  $\psi(z; \mathbf{k})$ . However, the straightforward answer  $\psi = \phi(M^2 - m_V^2)$  will not be a satisfactory option due to unphysical pole at  $M^2 = m_V^2$ . We remember that when constructing the soft wave function, we forced the corresponding vertex function  $\Gamma_{\text{soft}}$  to have zero at  $M^2 = m_V^2$  in order to cancel the unphysical pole. Here we do not have such a freedom in manipulation with  $\psi$ , which is, by the way, always positive. However, we can again tune the soft vertex function  $\Gamma_{\text{soft}}$  so that the entire expression  $\psi_{\text{soft}} + \psi$  does have zero at the required point. This can be achieved by shifting the node position of the soft vertex function

$$\Gamma_{\text{soft}}(z; \mathbf{k}^2) \rightarrow \Gamma_{\text{soft}}(M^2) 4M^2 - m_V^2 - \frac{(z; \mathbf{k}_0^2)}{\Gamma_{\text{soft}}(m_V^2)} ; \quad (11.19)$$

where  $\frac{k_0^2 + m^2}{z(1-z)} = m_V^2$ . The total wave function will then turn into

$$\begin{aligned} \psi_{\text{total}}(z; \mathbf{k}^2) = & \frac{\Gamma_{\text{soft}}(M^2) M^2 - m_V^2 - \frac{(z; \mathbf{k}_0^2)}{\Gamma_{\text{soft}}(m_V^2)} + \phi(z; \mathbf{k}^2)}{M^2 - m_V^2} \\ = & \Gamma_{\text{soft}}(M^2) + \frac{1}{M^2 - m_V^2} \left( \phi(z; \mathbf{k}^2) - \phi(z; \mathbf{k}_0^2) \frac{\Gamma_{\text{soft}}(M^2)}{\Gamma_{\text{soft}}(m_V^2)} \right) : \quad (11.20) \end{aligned}$$

The wave function constructed in this manner is regular at  $M^2 = m_V^2$  and does have the expected large  $M^2$  behavior.

#### 11.1.4 The large $Q^2$ asymptotics of $\psi_T$ : analytical result

The honest integration in (11.18) cannot be done analytically, but in order to grasp the asymptotics, a simple estimate can be performed.

For  $\mathbf{k}^2 \gg \frac{s}{G}; \frac{s}{G}; m^2$  the denominators turn into  $\mathbf{k}^2 z^0 = z$  and  $\mathbf{k}^2(1-z^0) = (1-z)$  for on mass shell initial quarks 1 or 2 respectively. If we then suppose that the soft wave function is given by the Gaussian Ansatz with  $R_V^2 m^2 \ll 1$ , we can put  $z^0 \rightarrow 1/2$  and do the integration completely. The answer reads

$$\psi(z; \mathbf{k}^2) = C_F \frac{s(\mathbf{k}^2)}{2} \frac{m^2 2z}{m \mathbf{k}^2} \int d^2 \mathbf{l}_{\text{soft}}(M^2) = \frac{z}{\mathbf{k}^2} C_F \frac{s(\mathbf{k}^2)}{2} 4m^2 \frac{2}{R_V^2} : \quad (11.21)$$

We see that the hard tail of the wave function falls off as  $1/k^4$  at large  $k^2$ , in accordance with our expectations.

The Coulomb tail of the vector meson wave function being finally obtained, we are now ready to estimate the expected change in the  $A_{\text{hard}}/A_{\text{soft}}$  ratio for high- $Q^2$  production of mesons. Before we take a look at the numerical values, let us make an analytical estimate of the  $Q^2$  asymptotics. We plug the hard tail of the wave function  $\psi(z; k^2)$  into the leading twist expression for  $A_{\text{hard}}/A_{\text{soft}}$ , which we write as

$$\begin{aligned} \text{Im } A_T &= \frac{C_V}{4} \frac{p_{\text{em}}}{4} \int_0^1 \frac{dz}{z(1-z)} d^2k_{\text{total}}(z; k^2) \frac{z}{\sim^4} \frac{d^2\sim}{\sim^4} s(\sim^2) F(x_g; \sim^2) \\ &\quad \frac{2\sim^2}{[z(1-z)Q^2 + \sim^2 + k^2]^2} \frac{m^2 + 2[z^2 + (1-z)^2]k^2}{[z(1-z)Q^2 + \sim^2 + k^2]^2} \\ &= \frac{C_V}{4} \frac{p_{\text{em}}}{4} \int_0^1 \frac{dz}{z(1-z)} d^2k_{\text{total}}(z; k^2) \frac{m^2 + 2[z^2 + (1-z)^2]k^2}{[z(1-z)Q^2 + \sim^2 + k^2]^2} \\ &\quad \frac{2}{[z(1-z)Q^2 + \sim^2 + k^2]^2} J_{\text{total}}(Q^2) : \end{aligned} \quad (11.22)$$

The integral

$$J_{\text{total}}(Q^2) = \int_0^1 \frac{dz}{z(1-z)} d^2k_{\text{total}}(z; k^2) \frac{m^2 + 2[z^2 + (1-z)^2]k^2}{[z(1-z)Q^2 + \sim^2 + k^2]^2}$$

is naturally split into  $J_{\text{soft}}(Q^2)$  and  $J_{\text{hard}}(Q^2)$ . The former is calculated in the heavy-quarkonium approximation with Gaussian wave function and yields

$$J_{\text{soft}}(Q^2) = \int d^3k_{\text{soft}} \frac{4m_V^2}{Q^4} = \frac{16m_V}{Q^4} a \frac{2}{R_V^2} : \quad (11.23)$$

The hard piece is calculated as

$$\begin{aligned} J_{\text{hard}}(Q^2) &= \int_0^1 \frac{dz}{z(1-z)} \int d^2k_{\text{hard}} \frac{32[z^2 + (1-z)^2]k^2}{Q^4} \frac{z(1-z)}{k^2} \\ &\quad \frac{1}{2k^2} C_F \frac{s(k^2)}{2} 2m_V a \frac{2}{R_V^2} \\ &= 2m_V a \frac{2}{R_V^2} \frac{C_F}{Q^4} \int_0^1 dz [z^2 + (1-z)^2] \int d^2k_{\text{hard}} \frac{d^2k^2}{k^2} s(k^2) \end{aligned} \quad (11.24)$$

The ratio  $A_{\text{hard}}/A_{\text{soft}}$  is then

$$\frac{A_{\text{hard}}(Q^2)}{A_{\text{soft}}(Q^2)} = \frac{4C_F}{3} \int d^2k_{\text{hard}} \frac{d^2k^2}{k^2} s(k^2) = \frac{64}{81} \log \frac{s(\sim^2)}{s(\frac{1}{4}Q^2)} : \quad (11.25)$$

This expression represents the asymptotic large- $Q^2$  behavior of the  $A_{\text{hard}}/A_{\text{soft}}$  ratio. As it could be expected, it is governed by  $\log \frac{s(\sim^2)}{s(\frac{1}{4}Q^2)}$ , which rises with  $Q^2$  growth, but extremely slowly. Within the experimentally studied region of  $Q^2$  (not higher than  $100 \text{ GeV}^2$ ), this logarithm, which is supposed to be large, is still less than unity (basically  $0.5 - 0.7$ ). This indicates that the asymptotic regime is not reached at HERA, and the estimate just derived

seems to be irrelevant to the real magnitude of the hard tails effects. Nevertheless, this estimate tells us that no abnormally suppressing factors appear in our problem.

The numerical analysis of the Coulomb tail impact on the production amplitudes will be given elsewhere.

## 11.2 The S=D wave mixing

The presence of tensor forces in two-fermion bound states is always a natural consequence of relativistic corrections. They lead mixing of states with definite angular momentum, which in the case of a vector particle translates into S wave { D wave mixing.

The most famous example is provided by the Breit potential in a hydrogen atom. Such forces are present in a deuteron, where they lead to about 5% admixture of D wave state, and they can be present in vector mesons as well. Review [89] provides further examples.

How are we going to mix S and D wave? When calculating the normalization or decay constant for a vector meson, we observed a two-fold dependence on the vector meson state: in the spinorial structure and in the particular form of the radial wave function. In all cases, the rest was absolutely insensitive to the vector meson state. Therefore, the two quantities we should mix, are  $S_s(p^2)$  and  $D_D(p^2)$ :

$$j(p^2)_i = \mathcal{J}_s(p^2)_i \cos \theta + \mathcal{J}_D(p^2)_i \sin \theta: \quad (11.26)$$

If mixing angle  $\theta$  is constant, then this vector meson state satisfies automatically the normalization condition:

$$h_j^2 = h_s^2 \mathcal{J}_s^2 \cos^2 \theta + h_D^2 \mathcal{J}_D^2 \sin^2 \theta = g^2: \quad (11.27)$$

There can be several types of S=D mixing. First, we can mix D state with 1S, 2S or even higher S states. It is not clear a priori which mixing should be stronger. Therefore in our analysis below we accounted for possible 1S=D and 2S=D mixing on the equal foot. Second, the mixing angle  $\theta$  can be an explicit function of  $p^2$ . This case is a bit more complicated but nothing seems to rule out such possibility.

### 11.2.1 Cooking up vertex

The first issue we want to elaborate is how to construct the vertex from accurate S and D spinorial structures. This question arises when one tries to check how the naive u u treatment of the quark-antiquark-vector meson vertex differs from the accurate one. To do so, in the expression

$$j(p^2) = \frac{2p}{M + 2m} S_s(p^2) \cos \theta(p^2) + p^2 + (M + m)p D_D(p^2) \sin \theta(p^2): \quad (11.28)$$

all terms with  $p$  must be banished by properly adjusting mixing angle  $\theta = \theta(p^2)$ . Assuming for simplicity, that we use oscillator ansatz wave functions with all  $a_i$  equal, one obtains for 1S=D mixing

$$\tan \theta(p^2) = \frac{2}{(M + 2m)(M + m)} \frac{c_1}{c_0} = \frac{p \frac{p}{30}}{(M + 2m)(M + m)a^2}: \quad (11.29)$$



A very rough estimate for  $\rho$  system gives  $\tan \delta \approx 0.2$ . For  $2S=D$  mixing one has

$$\tan \delta(p^2) = \frac{p \sqrt{\frac{45}{(M+2m)(M+m)a^2}}}{(1-2p^2a^2=3)} : \quad (11.30)$$

This time the mixing angle even swings with  $p^2$  growth. After  $p$  terms are canceled in (11.28), the residual expression is proportional only to  $p$  and has slightly modified  $p^2$  dependence via explicitly  $p^2$  dependent mixing angle. However, this modification is completely inessential. Moreover, for  $2S=D$  mixing this modification does not shift the position of the node. Therefore, it seems that the impact of this specific mixing on the radial wave function is minimal. The magnitude of this mixing can be also described with only one number — the integrated mixing angle:

$$\tan^2 \delta = \frac{h \sin^2 \delta(p^2) i_D}{h \cos^2 \delta(p^2) i_S} \quad (11.31)$$

where  $h i_{S,D}$  mean the normalization integral for  $S=D$  state. For  $1S=D$  and  $2S=D$  types of mixing,  $\tan^2 \delta$  is equal to 0.027 ( $\delta = 9.3^\circ$ ) and 0.062 ( $\delta = 14^\circ$ ) respectively.

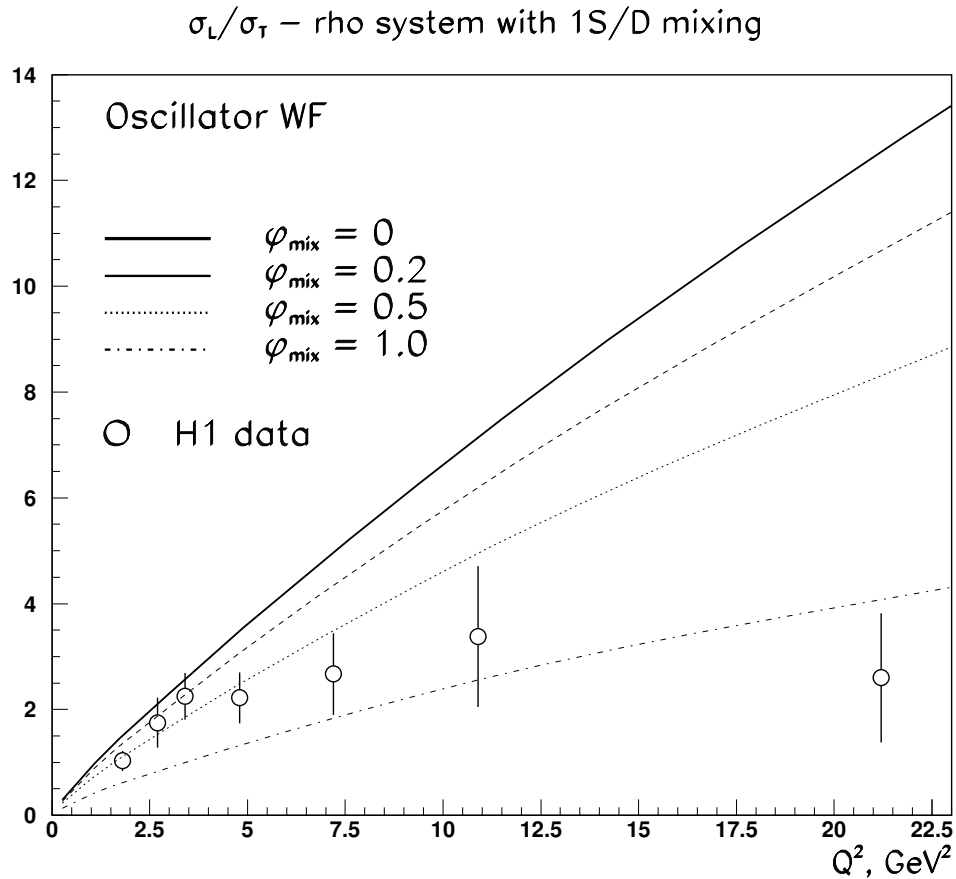


Figure 11.2: The impact of  $1S=D$  mixing in the  $\rho$  system on the  $\sigma_L/\sigma_T$  ratio for the lowest energy state production.

### 11.2.2 Impact of S=D wave mixing on meson production

For the simplicity, we will restrict ourselves to the constant-angle variant of S=D wave mixing. Since our primary motivation here is to check how mixing alters the  $\sigma_L = \sigma_T$  ratio in production, we will focus only on meson.

Since a generic meson production amplitude is linear in the meson wave function (understood in its complete sense, i.e. spinorial structure times the scalar wave function), one immediately has

$$A = A_S \cos \varphi + A_D \sin \varphi : \quad (11.32)$$

With this expression in mind, we can now predict the effect of S=D wave mixing by simply looking at the pictures for pure S and D wave states production.

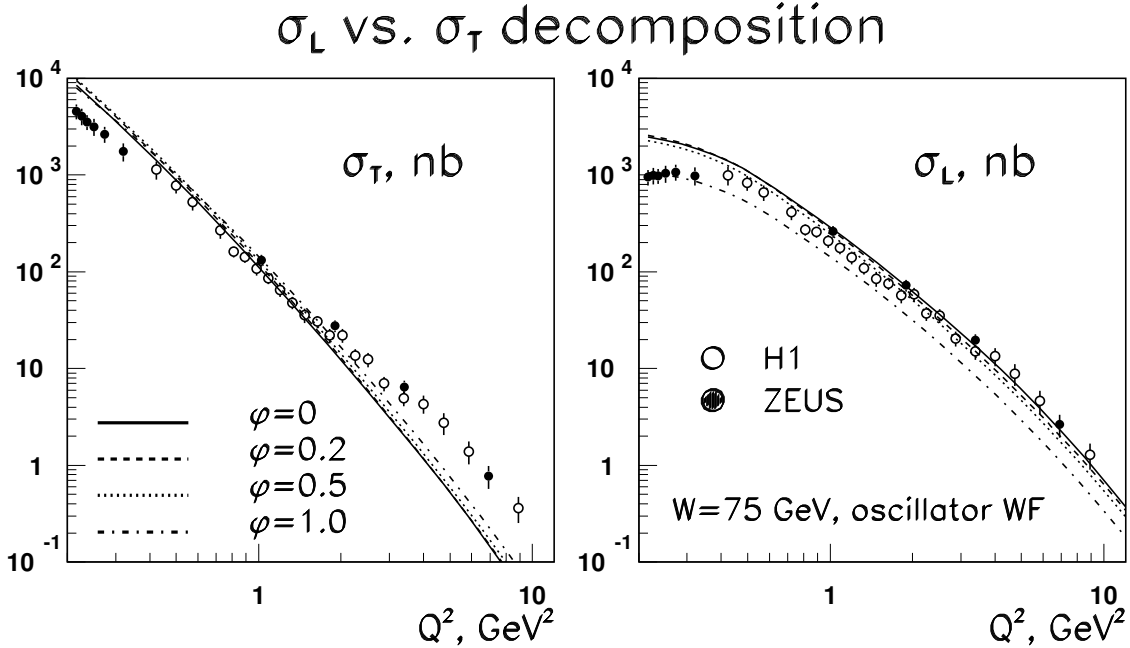


Figure 11.3: Changes in  $Q^2$  profiles of  $\sigma_T$  and  $\sigma_L$  cross sections for system ground states caused by 1S=D mixing.

Fig. 11.2 and Fig. 11.3 show the changes in the longitudinal and transverse meson cross sections caused by the 1S=D mixing. One sees that at  $\varphi_{mix} > 0$  grows, the ratio  $\sigma_L = \sigma_T$  decreases. Fig. 11.2 implies that  $\varphi = 0.7$  would do the best job in describing the data points. Note however that the shape of  $\sigma_L = \sigma_T$  ratio remains the same and does not significantly attenuate, which would be needed for a better description of the experimental points. Even more problems come from separate analysis of  $\sigma_L$  and  $\sigma_T$  cross sections. One sees that decrease of  $\sigma_L = \sigma_T$  arises not from making  $\sigma_T$  higher, but at the expense of making  $\sigma_L$  significantly lower than the data. Thus, although the ratio  $\sigma_L = \sigma_T$  can indeed be corrected in a simple mixing scenario, the cross sections themselves still deviate at large  $Q^2$  from the measured values.

This analysis lead us to a conclusion that the  $\rho$  puzzle in  $\rho$  production still persists in our approach.

Although the S=D wave mixing failed to completely resolve the  $\rho$  puzzle, it is still an interesting issue on its own. In contrast to all previous calculations of the vector meson production amplitudes, our approach allows for a clear formulation and detailed analysis of this phenomenon.

# Chapter 12

## Conclusion

In the present work we formulated the  $k_t$ -factorization approach to the calculation of the diffractive production of vector mesons in DIS. Since this approach is organically linked to the BFKL dynamics, no requirements on the value of  $Q^2 + m_V^2$  was placed, which allowed us to investigate the production cross sections from the photoproduction limit up to highest  $Q^2$  values attainable in the experiment.

When describing the vector meson, we limited ourselves to the lowest Fock state only, that is we treated a vector meson as a bound state of quark-antiquark pair only. Being of course an approximation, this limitation allowed for the strict construction of the pure S-wave and D-wave states of the qq pair sitting inside the meson, which was then applied to the corresponding production amplitudes.

On the other side of the reaction, we related the production amplitudes to the unintegrated gluon structure function of the proton. We undertook an extensive study of the differential gluon density, which included its first ever extraction from the experiment and detailed investigation of its properties. This was then used in the vector meson production calculations and yielded reliable numerical results.

Here we give a detailed list of main results of the present work.

### 1. Differential gluon structure function of the proton

- First ever extraction of the unintegrated gluon structure function and casting it into a form of simple and ready-to-use parametrizations;

- detailed analysis of the soft-hard decomposition of various observables and the impact of soft-to-hard diffusion phenomenon on them ;

- observation of self-generated two-reggeon-like structure of  $E_p$  predicted by  $k_t$ -factorization;

- showing by means of  $^2$  analysis that the high-precision experimental data on  $F_{2p}$  suggests rather strong separation of soft and hard parts of the unintegrated gluon density.

### 2. Diffractive vector meson production: analytical study

- Developing for the first time a theory for vector meson spin-angular coupling and using it consistently in the derivation of the meson production amplitudes;

- observing remarkably different  $Q^2$ -dependence of S and D wave type amplitudes, providing thus a way to discern S and D wave states that are indistinguishable at  $e^+e^-$  colliders;

- at large  $Q^2$ , observing a dramatic role of higher twist contributions to the D wave vector mesons, which even forced sign change for  $L \rightarrow L$  amplitude and led to non-monotonous  $L = T$  ratio;

- observation of very large helicity violating effects for D wave vector states, which do not get suppressed even in the case of heavy quarkonia;

- confirmation of the soft dominance of the double spin flip amplitude in the case of both S and D wave states;

- establishing the borders of our approach during discussing the hard Coulomb tail of the wave function.

### 3. D i r a c t i v e v e c t o r m e s o n p r o d u c t i o n : n u m e r i c a l s t u d y

Showing that  $k_t$ -factorization approach leads to a good overall agreement with available experimental data on all types of vector mesons. Namely, we showed that the overall shape of  $Q^2$  dependence, energy growth,  $t$ -dependence, picture of  $s$ -channel helicity violation observed in  $\rho$ ,  $\omega$ , and  $J/\psi$  mesons production are in good agreement with  $k_t$ -factorization prediction.

Recognizing that two particular issues | the transverse cross section  $\sigma_T$  for mesons at higher  $Q^2$  and the magnitude of  $(1s)$  state | still remain unresolved. The causes of this discrepancy and the resolution possibilities are discussed.

Predicting many previously unknown features of the excited vector meson production reactions, including opposite signs for the largest spin flip amplitude  $T \rightarrow L$  for S and D wave vector mesons and dramatically different  $L = T$  ratio;

- investigating  $S=D$  mixing induced phenomena; indicating that large  $S=D$  wave mixing in  $\psi$  system can be the origin of  $\sigma_T$  puzzle.

Since the work contains a large number of predictions on the observables that have not yet been investigated in experiment, I hope that the thesis will serve as a guide to the directions of future experimental research. The dramatic differences between S and D wave vector meson production predicted in this work demand confirmation and offer a novel way to study the structure of hadrons.

Finally, in this work I intended not merely to list the results, but also give a detailed and pedagogical presentation of all steps. In particular, Part I, where I introduced the  $k_t$ -factorization scheme, Chapter 4, where I construct the theory of the vector meson spin-angular coupling, and Appendices contain very detailed intermediate calculations, so that everyone can follow the entire line of derivation. To this end, I hope that the present text can be used as a means of learning as well.

# Bibliography

- [1] N.N. Nikolaev and B.G. Zakharov, "Phenomenology of Diffractive DIS", Talk given at 5th International Workshop on Deep Inelastic Scattering and QCD (DIS 97), Chicago, IL, 14-18 Apr 1997, hep-ph/9706343.
- [2] A.C. Irving, R.P. Worden, Phys.Rept. 34 (1977) 117-231.
- [3] V.S. Fadin, E.A. Kuraev, L.N. Lipatov, Phys.Lett. B 60 (1975) 60; E.A. Kuraev, L.N. Lipatov, V.S. Fadin, Sov. Phys. JETP 44, (1976) 443; 72 (1977) 377; Ya.Ya. Balitskii, L.N. Lipatov, Sov.J.Nucl.Phys. 28 (1978) 822.
- [4] L.N. Lipatov and V.S. Fadin, JETP Lett. 49 (1995); L.N. Lipatov, Phys.Rept. 286 (1997) 131-198.
- [5] for an introductory text see E. Levin, Heavy Ion Phys. 8 265-283, 1998, hep-ph/9808483; E. Levin, "The Pomeron: yesterday, today and tomorrow", Lectures given at 3rd Gleb Wataghin School on High Energy Phenomenology, Campinas, Brazil, 11-16 Jul 1994, hep-ph/9503399
- [6] D.Yu. Ivanov, R.K. Kirschner, Phys.Rev.D 58 (1998), 114026.
- [7] E.V. Kuraev, N.N. Nikolaev, and B.G. Zakharov, JETP Lett. 68 (1998) 667.
- [8] N.N. Nikolaev, Comments on Nucl.Part.Phys. 21 (1992) 41; B.Z. Kopeliovich, J. Nemchik, N.N. Nikolaev and B.G. Zakharov, Phys. Lett. B 309 (1993) 179; Phys. Lett. B 324 (1994) 469.
- [9] D.Yu. Ivanov, Phys. Rev. D 53 (1996) 3564; I. Ginzburg, S. Panfil and V. Serbo, Nucl. Phys. B 284 (1987) 685; B 296 (1988) 569.
- [10] K. Schilling, G. Wolf, Nucl.Phys. B 61 (1973) 381.
- [11] J. Nemchik, N.N. Nikolaev and B.G. Zakharov, Phys. Lett. B 339 (1994) 194-200.
- [12] D.O. Riska, Acta Phys.Poln. B 29 (1998) 2389.
- [13] I.P. Ivanov, N.N. Nikolaev, Pis'ma ZhETF (JETP Lett.) 69 (1999) 268.
- [14] I.P. Ivanov, N.N. Nikolaev, Phys.Rev.D 65 (2002) 054004.

- [15] I.P. Ivanov and N.N. Nikolaev, "Improved determination of the differential gluon structure function of the proton"; I.P. Ivanov and N.N. Nikolaev, "Vector meson production in the  $k_t$ -factorization approach"; I.P. Ivanov and N.N. Nikolaev, "The effects of Coulomb tail on the vector meson production"; I.P. Ivanov and N.N. Nikolaev, "S-D wave mixing in vector mesons and its impact on diffractive vector meson production"; all works in progress.
- [16] I.P. Ivanov and N.N. Nikolaev, Talk given at 8th International Workshop on Deep Inelastic Scattering and QCD (DIS 2000), Liverpool, England, 25-30 Apr 2000. Published in "Liverpool 2000, Deep inelastic scattering", 119-120, hep-ph/0006100.
- [17] I.P. Ivanov and N.N. Nikolaev, Talk given at Low-x Workshop, Krakow, Poland, 27-30 June 2001.
- [18] V.N. Gribov and L.N. Lipatov, Sov. J. Nucl. Phys. 15 (1972) 438; L.N. Lipatov, Sov. J. Nucl. Phys. 20 (1974) 181; Yu.L. Dokshitzer, Sov. Phys. JETP 46 (1977) 641; G. Altarelli and G. Parisi, Nucl. Phys. B 126 (1977) 298, for the review see R.G. Roberts, The structure of the proton. (Cambridge Univ. Press, 1990).
- [19] V.S. Fadin, E.A. Kuraev and L.N. Lipatov Phys. Lett. B 60, 50 (1975); E.A. Kuraev, L.N. Lipatov and V.S. Fadin, Sov. Phys. JETP 44, 443 (1976); 45, 199 (1977).
- [20] J. Nemchik, N.N. Nikolaev, E. Predazzi and B.G. Zakharov, Phys. Lett. B 374 (1996) 199.
- [21] V.M. Budnev, I.F. Ginzburg, G.V. Mel'edin and V.G. Serbo, Phys. Rept. 15, 181 (1974)
- [22] N.N. Nikolaev, B.G. Zakharov, V.R. Zoller, JETP 105 (1994) 1498.
- [23] N.N. Nikolaev and B.G. Zakharov, Phys. Lett. B 327 (1994) 157.
- [24] M.V. Terentev, Sov. J. Nucl. Phys. 24 (1976) 106; Yad. Fiz. 24 (1976) 207; V.B. Berestetskii and M.V. Terentev, Yad. Fiz. 25 (1977) 653; L.A. Kondratyuk and M.V. Terentev, Sov. J. Nucl. Phys. 31 (1980) 561; Yad. Fiz. 31 (1980) 1087.
- [25] J. Bjorken, J. Kogut, D. Soper, Phys. Rev. D 3 (1971) 1382; G.P. Lepage, S.J. Brodsky, Phys. Rev. D 22 (1980) 2157; S. Brodsky, H.-Ch. Pauli, S. Pinsky, Phys. Rept. 301, (1998), 299-486; T. Heinzl, hep-th/9812190, 1998.
- [26] V.V. Sudakov, Sov. Phys. JETP 3, 65 (1956)/Zh. Eksp. Teor. Fiz. 30, 87 (1956).
- [27] V.V. Anisovich et al., Nucl. Phys. A 563 (1993) 549-583; W. Jaus, Phys. Rev. D 41 (1990) 3394; Phys. Rev. D 44 (1990) 2851.
- [28] A.V. Radyushkin, Phys. Rev. D 56, 5524 (1997).
- [29] A.G. Shuvaev, K.J. Golec-Biernat, A.D. Martin, M.G. Ryskin, Phys. Rev. D 60, 014015 (1999).
- [30] Ya.Ya. Balitskii and L.N. Lipatov, Sov. J. Nucl. Phys. 28 (1978) 822
- [31] N.N. Nikolaev and B.G. Zakharov and V.R. Zoller, JETP Letters 59, 8 (1994)
- [32] N.N. Nikolaev and B.G. Zakharov, JETP 78 (1994) 598; Z. Phys. C 64 (1994) 631.

- [33] A.H. Mueller and B. Patel, Nucl. Phys. B 425 (1994) 471
- [34] N.N. Nikolaev and B.G. Zakharov, Phys. Lett. B 332 (1994) 177; Z. Phys. C 53 (1992) 331.
- [35] N.N. Nikolaev, A.V. Pronyaev and B.G. Zakharov, Phys. Rev. D 59 091501 (1999)
- [36] M. Bertini, M. Genovese, N.N. Nikolaev, A.V. Pronyaev and B.G. Zakharov, Phys. Lett. B 422, 238 (1998)
- [37] E.V. Kuraev, N.N. Nikolaev, and B.G. Zakharov, JETP Lett. 68 (1998) 667; I.P. Ivanov, N.N. Nikolaev, Pis'ma ZhETF (JETP Lett.) 69 (1999) 268
- [38] J. Nemchik, N.N. Nikolaev, E. Predazzi, B.G. Zakharov and V.R. Zoller, J. Exp. Theor. Phys. 86, 1054 (1998)
- [39] N.N. Nikolaev, in: Hamburg 1998/1999, Monte Carlo generators for HERA physics, pp. 377-381; hep-ph/9905562.
- [40] S.P. Baranov and N.P. Zotov, Phys. Lett. B 458 (1999) 389; M.G. Ryskin, A.G. Shuvaev and Yu.M. Shabelski, Phys. Atom. Nucl. 64, 1995 (2001)/Yad. Fiz. 64, 2080 (2001)
- [41] J.R. Forshaw and R.G. Roberts, Phys. Lett. B 335 (1994) 494; A.J. Askew, D.G. Raudenz, J. Kwiecinski and A.D. Martin, Phys. Lett. B 338 (1994) 92.
- [42] J. Kwiecinski, A.D. Martin and A.M. Stasto, B 459 (1999) 644.
- [43] M. G. Lueck, E. Reya, A. Vogt, Eur. Phys. J. C 5, 461 (1998)
- [44] H.L. Lai, W.K. Tung, Z. Phys. C 74, 463 (1997)
- [45] A.D. Martin, R.G. Roberts, W.J. Stirling, R.S. Thorne, Phys. Lett. B 443, 301 (1998)
- [46] V. Barone, C. Pascaud and F. Zomer, Eur. Phys. J. C 12, 243 (2000)
- [47] N.N. Nikolaev and V.R. Zoller, JETP Lett. 69, 103 (1999); E. Gotsman, E. Levin, U. Marmor and E. Naffali, Nucl. Phys. B 539, 535 (1999)
- [48] H. Abramowicz and A. Caldwell, Rev. Mod. Phys. 71, 1275 (1999); ZEUS Collab., J. Breitweg et al., Eur. Phys. J. C 7, 609 (1999).
- [49] E.M. Levin, M.G. Ryskin, Yu.M. Shabelski and A.G. Shuvaev, Sov. J. Nucl. Phys. 54 (1991) 867; S. Catani, M. Ciafaloni and F. Hautmann, Nucl. Phys. B 366 (1991) 135; S. Catani and F. Hautmann, Nucl. Phys. B 427 (1994) 475; J.C. Collins and R.K. Ellis, Nucl. Phys. B 360 (1991) 3.
- [50] N.N. Nikolaev, B.G. Zakharov, Phys. Lett. B 327 (1994) 157.
- [51] N.N. Nikolaev, B.G. Zakharov, V.R. Zoller, JETP Letters 66 (1997) 138; N.N. Nikolaev, J. Speth and V.R. Zoller, Phys. Lett. B 473 (2000) 157.
- [52] N.N. Nikolaev and B.G. Zakharov, Phys. Lett. B 332 (1994) 184.



- [53] V Barone, M Genovese, N N Nikolaev, E Predazzi and B G Zakharov, Phys.Lett. B 326 (1994) 161.
- [54] J Nemchik, N N Nikolaev, E Predazzi and B G Zakharov, Z.Phys.C 75 (1997) 71.
- [55] E M eggio, Phys.Lett. B 451 (1999) 414
- [56] N N Nikolaev and B G Zakharov, Z.Phys.C 49 (1991) 607.
- [57] V N Gribov, Eur.Phys.J.C 10 (1999) 71; D V Shirkov, Phys.Atom.Nucl 62 (1999) 1928; Yu L Dokshitzer, G Marchesini and B R Webber, JHEP 07 (1999) 012;
- [58] P V Landsho and O Nachtmann, Z.Phys.C 35 (1987) 405; H G Dosch, T Gousset, G Kulzinger and H J Pimer Phys.Rev.D 55 (1997) 2602.
- [59] A Donnachie and P V Landsho, Phys.Lett. B 437 (1998) 408
- [60] ZEUS coll, M Derrick et al, Z.Phys.C 72 (1996) 399.
- [61] ZEUS coll, J Breitweg et al, EurPhysJ.C 7 (1999) 609.
- [62] ZEUS coll, J Breitweg et al, Phys.Lett.B 407 (1997) 432.
- [63] H1 coll, S Aid et al, Nucl.Phys.B 470 (1996) 3.
- [64] H1 coll, C Adlb et al, Nucl.Phys.B 497 (1996) 3.
- [65] E665 coll, M R Adams et al, Phys.Rev.D 54 (1996) 3006.
- [66] NM C coll, M Amendo et al, Nucl.Phys.B 483 (1997) 3.
- [67] J Nemchik, N N Nikolaev and B G Zakharov, Phys.Lett.B 341 (1994) 228
- [68] J Kwiecinski, A D Martin and A M Stasto, Phys.Rev.D 56 (1997) 3991.
- [69] ZEUS Collab., J Breitweg et al, Eur.Phys.J.C 12 (2000) 35.
- [70] ZEUS Coll., Phys.Lett. B 487, 52 (2000).
- [71] ZEUS Coll., Eur.Phys.J.C 21, 443 (2001).
- [72] H1 Coll., Eur.Phys.J.C 21, 33 (2001).
- [73] H1 Coll., Phys.Lett. B 520, 183 (2001).
- [74] H1 Coll., Nucl.Phys.B 463, 3 (1996).
- [75] ZEUS Coll., Z.Phys.C 73, 253 (1997).
- [76] H1 Coll., Eur.Phys.J.C 13, 371 (2000).
- [77] ZEUS Coll., Eur.Phys.J.C 6, 603 (1999).
- [78] H1 Coll., Phys.Lett. B 483, 360 (1996).

- [79] ZEUS Coll., Phys.Lett. B 377, 259 (1996).
- [80] ZEUS Coll., Phys.Lett. B 380, 220 (1996).
- [81] H1 Coll., Phys.Lett. B 483, 23 (2000).
- [82] H1 Coll., NuclPhys. B 468, 3 (1996).
- [83] ZEUS Coll., Z.Phys. C 75, 215 (1997).
- [84] ZEUS Coll., Phys.Lett. B 437, 432 (1998).
- [85] B. Clerbaux, talk given at Workshop on Low- $x$  Physics, June 1999, Tel-Aviv, Israel; hep-ph/9908519.
- [86] ZEUS Coll., Eur.Phys.J. C 12, 393 (2000).
- [87] H1 Coll., Phys.Lett. B 421, 385 (1998).
- [88] H1 Coll., Eur.Phys.J. C 10, 373 (1998).
- [89] V.A.Novikov, L.B.Okun, M.A.Shifman, A.I.Vainshtein, M.B.Voloshin, V.I.Zakharov, Phys.Rept. 41, 1-133 (1978).

# Appendix A

## Denominator evaluation: details

Below we give a detailed denominator calculus that is used in all  $k_t$ -factorization processes. The major guideline in this derivation will be the analysis of pole positions and setting some of the propagators on mass shell by taking appropriate residues.

### A.1 Forward Compton scattering

#### A.1.1 The s-channel diagram: all details

We first start with the case of forward virtual Compton scattering amplitude. The integral to be calculated is

$$\int_0^1 dy \int_0^1 dz \int_0^1 d\alpha \int_0^1 d\beta \frac{1}{[(q-k)^2 - m^2 + i\epsilon]^2 [(q-k)^2 - m^2 + i\epsilon] [(k+\ell)^2 - m^2 + i\epsilon]} \frac{1}{[s^2 - 2 + i\epsilon] [(p-\ell)^2 - m^2 + i\epsilon]} \quad (\text{A } 1)$$

With Sudakov's decomposition

$$q = q^0 - \frac{Q^2}{s} p^0; \quad p = p^0 + \frac{m^2}{s} q^0; \quad k = y p^0 + z q^0 + \vec{k}; \quad \ell = p^0 + q^0 + \vec{\ell}; \quad (\text{A } 2)$$

one can rewrite all 7 propagators as:

$$\begin{aligned} \text{h1i} \quad (q-k)^2 - m^2 + i\epsilon &= -y \frac{Q^2}{s} (1-z)s - (\vec{k}^2 + m^2) + i\epsilon; \\ \text{h2i;h4i} \quad k^2 - m^2 + i\epsilon &= yzs - (\vec{k}^2 + m^2) + i\epsilon; \\ \text{h3i} \quad (k+\ell)^2 - m^2 + i\epsilon &= (y+\alpha)(z+\beta)s - (\vec{k}+\vec{\ell})^2 + m^2 + i\epsilon; \\ \text{h5i;h6i} \quad s^2 - 2 + i\epsilon &= s^2 - (2 + \frac{m^2}{s}) + i\epsilon; \\ \text{h7i} \quad (p-\ell)^2 - m^2 + i\epsilon &= (1-\alpha) \frac{m^2}{s} - s - (\vec{\ell}^2 + m^2) + i\epsilon; \end{aligned}$$

Let us analyze the position of propagator poles (namely, the sign of  $i$ ) in complex  $y$  plane as functions of  $z$  and  $\sim$ . One gets

$$\begin{aligned} h1i \quad y &= \frac{Q^2}{s} \frac{k^2 + m^2}{(1-z)s} + \frac{i}{1-z}; \\ h2i; h4i \quad y &= \frac{k^2 + m^2}{zs} - \frac{i}{z}; \\ h3i \quad y &= \frac{(k + \sim)^2 + m^2}{(1+z)s} - \frac{i}{z+1}; \end{aligned} \quad (A.3)$$

For the poles on  $\sim$  plane we get

$$\begin{aligned} h3i \quad \sim &= y + \frac{(k + \sim)^2 + m^2}{(1+z)s} - \frac{i}{z+1}; \\ h5i; h6i \quad \sim &= \frac{\sim^2 + m^2}{s} - \frac{i}{\sim}; \\ h7i \quad \sim &= 1 + \frac{\sim^2 + m^2}{s} + \frac{i}{m^2 - s}; \end{aligned} \quad (A.4)$$

Since the function we integrate (namely, the product of propagators) is an analytic function, which vanishes at large  $|y|$  and large  $|\sim|$  fast enough, we can switch from  $(-1; +1)$  integration to the complex plane contour integration both on  $y$  and  $\sim$  planes. This is done by adding half-circle of infinite radius either on the upper or the lower halfplanes. What we now have to do is just to trace how many poles we have inside the contours.

As clearly seen from (A.3) and (A.4), the position of the poles on  $y$  and  $\sim$  planes depends on the values of  $z$  and  $\sim$ . If values of  $z$  and  $\sim$  are such that no poles happen to fall inside the contours, the integral turns zero, and corresponding  $(z; \sim)$  region does not contribute to the total integral. So, our task now transforms into searching for such  $(z; \sim)$  regions that both  $y$  and  $\sim$  contour integrations result in non-zero values.

A convenient way to perform this analysis is to do it graphically. Figure illustrates the sign of  $i$  in  $y = \dots - i$  (left pane) and  $\sim = \dots - i$  (right pane) for all values of  $(z; \sim)$ . Each shaded line here corresponds to a propagator from (A.3) and (A.4), the shaded side indicating the halfplane with positive value of  $i$ . For example, propagator  $h1i$  from (A.3) has positive  $i$  when  $z < 1$ .

If we now take a closer look at each of possible regions  $(z; \sim)$ , we see that the only  $(z; \sim)$  pairs that result in a non-zero expression lie inside a triangle. For convenience, we break up the whole area into three sub-regions A, B, and C. For each of these regions, we get only one pole inside  $y$  and one pole inside  $\sim$  contours:

$$\begin{aligned} \text{Region A:} \quad & \begin{aligned} & 0 < z < 1 \\ & \sim < 0 \end{aligned} & \text{pole } h1i \text{ for } y; \text{ pole } h3i \text{ for } \sim. \\ \text{Region B:} \quad & \begin{aligned} & 0 < z < 1 \\ & 0 < \sim < m^2 - s \end{aligned} & \text{pole } h1i \text{ for } y; \text{ pole } h7i \text{ for } \sim. \\ \text{Region C:} \quad & \begin{aligned} & z < 0 \\ & \sim < m^2 - s \end{aligned} & \text{pole } h3i \text{ for } y; \text{ pole } h7i \text{ for } \sim. \end{aligned} \quad (A.5)$$

Thus, the integrals over  $y$  and  $z$  turns into taking the residues at certain poles. Let us write the result of this procedure for each of the three regions.

Region A .

Here we get

$$y = \frac{Q^2}{s} \frac{k^2 + m^2}{(1-z)s}; \quad = \frac{Q^2}{s} + \frac{k^2 + m^2}{(1-z)s} + \frac{(k+\sim)^2 + m^2}{(z-j)j} : \quad (A.6)$$

We know that  $\sim < 0$ , so we explicitly switch for more clear notation  $j-j$ . The other two propagators turn now into

$$\begin{aligned} h2i; h4i &= \frac{1}{1-z} [k^2 + m^2 - z(1-z)Q^2] + \text{if} ; \\ h5i; h6i &= \sim^2 + \sim^2 + 4Q^2 + \frac{k^2 + m^2}{1-z} + \frac{(k+\sim)^2 + m^2}{z-jj}^3 + \text{if} ; \\ h7i &= \sim^2 + m^2 + 4s - Q^2 \frac{k^2 + m^2}{1-z} - \frac{(k+\sim)^2 + m^2}{z-jj}^3 - \frac{m^2}{s} + jj + i : (A.7) \end{aligned}$$

Here symbol  $\text{if}$  means that the rule for pole passing is not needed since the propagator has definite sign for the physical values of the parameters.

Thus, the honest result of the integration equals

$$\begin{aligned} \int_0^z dy dz d \frac{1}{\text{propagators}} &= \frac{2-i}{s} \int_0^z dz \int_0^z dj j \frac{1-z}{z-jj} \frac{1}{[k^2 + m^2 + z(1-z)Q^2]^2} \\ &\frac{1}{\sim^2 + \sim^2 + jj Q^2 + \frac{k^2 + m^2}{1-z} + \frac{(k+\sim)^2 + m^2}{z-jj}^2} \\ &\frac{1}{\sim^2 + m^2 - (m^2 + jj)s - 1 - \frac{Q^2}{s} - \frac{k^2 + m^2}{1-z} - \frac{(k+\sim)^2 + m^2}{z-jj} - i} : \quad (A.8) \end{aligned}$$

Now comes the last step. The result (A.8) has both real and imaginary part. Since we are hunting for the imaginary part only, we extract it by using

$$\frac{1}{X-i} = \text{V.P.} \frac{1}{X} + i \quad (X)$$

and killing the integral with the means of  $\delta$  function. The value of  $\delta$  is

$$jj = \frac{\sim^2}{s} - 1 \quad (A.9)$$

and therefore it can be neglected everywhere else in (A.8). The result reads:

$$\text{Im} \left( \int_0^z \frac{dy dz d}{\text{propagators}} \right) = \frac{4-i}{s^3} \int_0^z dz \frac{1-z}{z} \frac{1}{[k^2 + m^2 + z(1-z)Q^2]^2} \frac{1}{[\sim^2 + \sim^2]^2} : \quad (A.10)$$

Of course, the  $z$  integration limits in (A.10) should not be understood literally as 0 and 1. In fact, when  $z$  is close enough to 0 or 1 (by a typical value of  $m^2=s$ ),  $z$  can no longer be neglected in comparison with  $1-z$ . Therefore, the integrand in (A.10) does not have the correct small  $z$  and small  $1-z$  asymptotics. Nevertheless, since the physical quantities will have regular  $z \rightarrow 0$  and  $z \rightarrow 1$  behavior, the impact of this difference will be suppressed by  $m^2=s$  simply due to small integration measure.

Regions B and C.

Although region B has much smaller area than region A, one cannot guarantee a priori that the third pole, which produces the imaginary part of the integral, does not happen to lie inside it. However, one can check that it is not the case.

One extracts first the values of  $y$  and  $z$  according to (A.5)

$$y = \frac{Q^2}{s} \frac{k^2 + m^2}{(1-z)s}; \quad z = \frac{s + \tilde{s}^2}{m^2}; \quad (\text{A.11})$$

We remind that  $0 < \tilde{s}^2 < m^2=s$ , so that no singularity arises here. The remaining propagators are

$$\begin{aligned} h_{2i}; h_{4i} &= \frac{1}{1-z} [k^2 + m^2 - z(1-z)Q^2] + i\epsilon; \\ h_{5i}; h_{6i} &= \frac{s^2 + m^2 \tilde{s}^2}{m^2 s} + i\epsilon; \\ h_{3i} &= [k + \tilde{s}]^2 + m^2 = Q^2 + \frac{k^2 + m^2}{1-z} \frac{1}{s} (z + \tilde{s}) \frac{\tilde{s}^2 + s}{m^2} (z + \tilde{s}) + i\epsilon \quad (\text{A.12}) \end{aligned}$$

We see that throughout the whole phase space of the remaining kinematic parameters all the propagators keep definite sign, which makes the answer purely real.

The similar picture occurs in region C as well. Therefore, regions B and C do not contribute to the imaginary part of our integral.

## A.1.2 The other three s-channel diagrams

The evaluation scheme just described can be applied to the other three diagrams. There will be slight modifications in quark propagators, but the strategy is unchanged.

For example, consider diagram (b) in Fig. 5.2. The only difference is the expression for propagator  $h_{4i}$ :

$$\begin{aligned} h_{4i} &= (q - k - \tilde{s})^2 + m^2 + i\epsilon = (1-z) \frac{Q^2}{s} y + [k + \tilde{s}]^2 + m^2 + i\epsilon; \\ y &= \frac{Q^2}{s} \frac{(k + \tilde{s})^2 + m^2}{(1-z)s} + \frac{i}{1-z}; \\ &= y \frac{Q^2}{s} \frac{(k + \tilde{s})^2 + m^2}{(1-z)s} + \frac{i}{1-z}; \quad (\text{A.13}) \end{aligned}$$

The graphic representation of the pole position on  $y$  and  $z$  planes is shown in Figure. Again, one can check that the main nonzero contribution comes from the same region A and the same

residues. So, if one again calculates the imaginary part of the integral, one finds

$$\begin{aligned} \text{Im} \left( \int \frac{dy dz d^4 d}{\text{propagators}} \right) &= \\ &= \frac{4}{s^3} \int_0^1 dz \frac{1}{[k^2 + m^2 + z(1-z)Q^2][(k+\tilde{\gamma})^2 + m^2 + z(1-z)Q^2]} \frac{1}{[\tilde{\gamma}^2 + \tilde{\gamma}^2]} \quad (\text{A.14}) \end{aligned}$$

Again, one can make sure that the small regions B and C do not contribute to the imaginary part as well, although the proof might not appear as clean as before. Namely, one can find that regions B or C will contain a propagator (namely, propagator h4i) that can change its sign, and therefore will contribute to the real part. However, this can happen at abnormally small  $\tilde{m}^2$

$$\tilde{m}^2 \sim \frac{m^4}{s} :$$

Therefore the contribution of this configuration is  $1/s$ -suppressed, and we cannot take it into account at our level of accuracy.

Finally, the answers for the remaining two diagrams are

$$\begin{aligned} \frac{4}{s^3} \int_0^1 dz \frac{1}{[(k+\tilde{\gamma})^2 + m^2 + z(1-z)Q^2][k^2 + m^2 + z(1-z)Q^2]} \frac{1}{[\tilde{\gamma}^2 + \tilde{\gamma}^2]} &\quad \text{diagram C;} \\ \frac{4}{s^3} \int_0^1 dz \frac{1}{[(k+\tilde{\gamma})^2 + m^2 + z(1-z)Q^2]^2} \frac{1}{[\tilde{\gamma}^2 + \tilde{\gamma}^2]} &\quad \text{diagram D.} \end{aligned}$$

### A.1.3 The u-channel diagrams

We claimed before that the u-channel diagrams do not contribute to the imaginary part. Here we show that it is indeed so.

The only difference between diagrams t-channel and u-channel diagrams is that in the u-channel case we switch the direction of particle p. Propagator h7i will be now

$$\begin{aligned} h7i &= (p+\tilde{\gamma})^2 - m^2 + i = (1+\tilde{\gamma}) \frac{m^2}{s} + \frac{1}{s} (\tilde{\gamma}^2 + m_p^2) + i : \\ &= 1 + \frac{\tilde{\gamma}^2 + m^2}{m^2 + s} - \frac{i}{m^2 + s} : \quad (\text{A.15}) \end{aligned}$$

Following the same line as before, we recognize three regions A, B, and C. In region A ( $1 < \tilde{\gamma} < m^2/s$ ;  $0 < z < 1$ ) the last propagator turns into

$$h7i \sim \frac{1}{s} \frac{m^2}{m^2 + s} \frac{1}{4s + Q^2 + \frac{k^2 + m^2}{1-z} + \frac{(k+\tilde{\gamma})^2 + m^2}{z}} \sim \frac{1}{s} \frac{m^2}{s} + \mathcal{O}(\frac{1}{s^2}) ; \quad (\text{A.16})$$

which means we do not get any contribution to the imaginary part. One can check that no contribution to the imaginary part arises from the other regions on  $(z; \tilde{\gamma})$  plane (except for abnormal cases when  $\tilde{m}^2 = m^4/s$ ). The conclusion is that the u-channel diagram gives no leading  $\frac{1}{s}$  contributions to the imaginary part of the process.

#### A.1.4 The same integral in the $\alpha$ -representation technique

Here, for the purpose of completeness, we show an alternative way to do the integrations over  $y$  and  $z$ . Sure enough, the underlying meaning of all manipulations will be absolutely the same as before. However, in a certain sense this way might appear simpler, since it does not require one to perform any graphic analysis or to think what propagator should be put on mass shell. Everything is done automatically here. It seems that this method is similar to the so-called  $\alpha$ -representation of the loop integrals.

We start with expression (A.1) and use the following representation for each of the seven propagators

$$\frac{1}{X - i} = \frac{i}{+ iX} = i \int_0^1 dt \exp[ -t (X - i)] : \quad (A.17)$$

The integral (A.1) transforms into

$$\begin{aligned} & \int_0^1 dy \int_0^1 dz \int_0^1 dt_1 \dots \int_0^1 dt_7 \exp[ -t_1 (ys + Q^2)(1-z) - it_2 (K^2 + m^2)] \\ & \exp[ -it_3 (K^2 + m^2) - it_4 (y + z + 1)s - it_5 ((K + \tilde{K})^2 + m^2)] \\ & \exp[ -it_6 (K^2 + m^2) - it_7 s - it_8 (\tilde{K}^2 + m^2)] \\ & \exp[ -it_9 s - it_{10} (\tilde{K}^2 + m^2) - it_{11} (m^2 - s)(1-z) - it_{12} (\tilde{K}^2 + m^2)] \end{aligned} \quad (A.18)$$

Since the total integral is convergent and thanks to the factorization of  $y$  and  $z$  dependencies, we can do the  $y$  and  $z$  integration first and obtain

$$\begin{aligned} & \int_0^1 dy e^{iys[t_1(1-z) + t_2 z + t_3(z+1) + t_4 z]} \int_0^1 dz e^{is[t_3(z+1) + t_5 + t_6 + t_7(m^2=s)]} = \frac{2}{s} \frac{i}{s} \\ & [t_1(1-z) + t_2 z + t_3(z+1) + t_4 z] \int_0^1 dz e^{is[t_3(z+1) + t_5 + t_6 + t_7(m^2=s)]} \end{aligned} \quad (A.19)$$

Since all parameters  $t_i$  are positive, the two delta-functions can be simultaneously non-zero only for certain  $(z; y)$  pairs. As should be expected, these pairs lie precisely within the allowed regions.

Now we can take two of  $t_1 :: t_7$  integrations to kill the two delta-functions. Let them be  $t_1$  and  $t_3$  (of course, one can take other pairs as well). We get

$$\begin{aligned} t_3 &= \frac{1}{z+1} (t_5 + t_6 + t_7) + t_7 \frac{m^2}{(z+1)s}; \\ t_1 &= \frac{z}{1-z} (t_2 + t_4) - \frac{1}{1-z} (t_5 + t_6 + t_7) + t_7 \frac{m^2}{(1-z)s}; \end{aligned} \quad (A.20)$$

Since the integrations in  $t_i$  remain factorized, we easily obtain

$$\begin{aligned} & \int_0^1 dt_2 e^{-t_2} e^{-it_2 (K^2 + m^2) - \frac{z}{1-z} (K^2 + m^2) - zQ^2} = \frac{i}{\frac{1}{1-z} [K^2 + m^2 + z(1-z)Q^2] - i}; \\ & \int_0^1 dt_4 e^{-t_4} e^{-it_4 (K^2 + m^2) - \frac{z}{1-z} (K^2 + m^2) - zQ^2} = \frac{i}{\frac{1}{1-z} [K^2 + m^2 + z(1-z)Q^2] - i}; \\ & \int_0^1 dt_5 e^{-t_5} e^{-it_5 (\tilde{K}^2 + m^2) + it_5 \frac{m^2}{z+1} [K^2 + m^2 + Q^2(1-z) + (K + \tilde{K})^2 + m^2]} \end{aligned}$$



$$\begin{aligned}
&= \frac{i}{\tilde{s}^2 + \tilde{t}^2 - i \frac{1}{z_+} [Q^2(1-z) + K^2 + m^2 + (K + \tilde{m})^2 + m^2]} ; \\
\int_0^1 dt_6 e^{it_6} e^{it_6(\tilde{s}^2 + \tilde{t}^2) + it_6 \frac{1}{z_+} [K^2 + m^2 + Q^2(1-z) + (K + \tilde{m})^2 + m^2]} \\
&= \frac{i}{\tilde{s}^2 + \tilde{t}^2 - i \frac{1}{z_+} [Q^2(1-z) + K^2 + m^2 + (K + \tilde{m})^2 + m^2]} ; \\
\int_0^1 dt_7 e^{it_7} e^{it_7(\tilde{s}^2 - s) + it_7(\tilde{s}^2 + m^2) + it_7 \frac{m^2 - s}{z_+} [K^2 + m^2 + Q^2(1-z) + (K + \tilde{m})^2 + m^2]} \\
&= \frac{i}{\tilde{s}^2 + \tilde{t}^2 - s - i \frac{m^2 - s}{z_+} [Q^2(1-z) + K^2 + m^2 + (K + \tilde{m})^2 + m^2]} : \quad (A 21)
\end{aligned}$$

If one now brings all pieces together, one will arrive at already familiar expression.

## A.2 Vector meson production: the fully on-forward case

Since this case is done similarly to the Compton scattering, we do all calculations in less details and pay special attention only to distinctions.

Strictly speaking, the (virtual) photoproduction of vector mesons is always an on-forward process, even though the final state might have no transverse momentum. The reason is that when the initial and final states have different masses, the exchange Pomeron must carry a non-zero longitudinal momentum. In the language of two-gluon exchange it means that the momenta of the gluons are not identical, in contrast to what we had in previous section.

The integral we deal with is

$$\begin{aligned}
&\int dy dz d\alpha d\beta \frac{(M^2)}{[(q - k)^2 - m^2 + i][(k - \tilde{m})^2 - m^2 + i][(k + \tilde{m})^2 - m^2 + i]} \\
&\frac{1}{[(\tilde{s}_1^2 - \tilde{t}_1^2 + i)[(\tilde{s}_2^2 - \tilde{t}_2^2 + i)[(p - \tilde{m}_1)^2 - m^2 + i]}] \quad (A 22)
\end{aligned}$$

With Sudakov decomposition and notation  $\tilde{s}_1 + \tilde{t}_1 = 2$ ;  $\tilde{s}_2 + \tilde{t}_2 = 2$ , we have following seven propagators:

$$h1i \quad (q - k)^2 - m^2 + i = -y \frac{Q^2}{s} (1 - z)s [K^2 + m^2] + i ;$$

$$h2i \quad (k + \tilde{m})^2 - m^2 + i = (y + \tilde{z})s [K^2 + m^2] + i ;$$

$$h3i \quad (k + \tilde{m}_1)^2 - m^2 + i = (y + \frac{1}{2})(z + \frac{1}{2})s [K^2 + m^2 + 2] + i ;$$

$$h4i \quad k^2 - m^2 + i = yzs [K^2 + m^2] + i ;$$

$$h5i \quad \tilde{s}_1^2 - \tilde{t}_1^2 + i = (\tilde{s} + \frac{1}{2})(\tilde{t} + \frac{1}{2})s [(\tilde{s} + \frac{1}{2})^2 + \tilde{t}^2] + i ;$$

$$h5i \quad \tilde{s}_2^2 - \tilde{t}_2^2 + i = (\frac{1}{2})(\frac{1}{2})s [(\frac{1}{2})^2 + \tilde{t}^2] + i ;$$

$$h7i = (p_1)^2 m^2 + i = (1 - \frac{1}{2}) \frac{1}{2} s [(\tilde{\kappa} + \frac{1}{2}\tilde{\gamma})^2 + m^2] + i :$$

One can write now poles on the  $y$  and  $p$  plane, draw the regions of positivity of the corresponding  $i$ 's on the  $(z; )$  plane, and select the regions that leads to non-zero contributions (there will be ve of them this time). One can again make sure that the leading  $1=s$  contribution to the imaginary part comes from the main region. Another thing that helps avoid extra poles is the presence of  $^2$  (namely,  $^2 > m_v^2 - 4m^2$  for all vector mesons).

Setting propagators h1i and h3i on mass shell, we obtain

$$y = \frac{Q^2}{s} \frac{\kappa^2 + m^2}{(1-z)s}; \quad = \frac{Q^2}{s} \frac{1}{2} + \frac{\kappa^2 + m^2}{(1-z)s} + \frac{(\kappa + \tilde{\gamma} + \tilde{\gamma}=2)^2 + m^2}{(z + + =2)s} : \quad (A 23)$$

The resulting quark propagators read

$$h4i = \frac{1}{1-z} \frac{h}{z} \kappa^2 + m^2 + z(1-z)Q^2 + i ;$$

$$h2i = (z + )s - (z + )sQ^2 - (z + ) \frac{\kappa^2 + m^2}{1-z} [(\kappa + \tilde{\gamma})^2 + m^2] + i : \quad (A 24)$$

Note that since the invariant mass of the produced  $q\bar{q}$  state is equal

$$M^2 = \frac{\kappa^2 + m^2}{1-z} + \frac{(\kappa + \tilde{\gamma})^2 + m^2}{z + } \sim^2 ;$$

propagator h2i turns into  $(z + ) (m_v^2 - M^2)$ . Together with the vertex factor  $(M^2)$ , this propagator gives rise to the wave function.

The gluon propagators are

$$h5i = ( + \frac{1}{2})^0 Q^2 + \frac{\kappa^2 + m^2}{1-z} + \frac{(\kappa + \tilde{\gamma} + \tilde{\gamma}=2)^2 + m^2}{z + + =2} A^1 [(\tilde{\kappa} + \frac{1}{2})^2 + ^2] + i ;$$

$$h6i = ( - \frac{1}{2})^0 m_v^2 - \tilde{\gamma}^2 + \frac{\kappa^2 + m^2}{1-z} + \frac{(\kappa + \tilde{\gamma} + \tilde{\gamma}=2)^2 + m^2}{z + + =2} A^1 [(\tilde{\kappa} - \frac{1}{2})^2 + ^2] + i :$$

In the case of gluon h5i the absence of pole was a trivial thing (due to negativity of both and ), in the case of the second gluon the pole can in principle arise. In our case however this is avoided due to large enough  $^2$  (namely,  $^2 > m_v^2 - 4m^2$  for all vector mesons).

Finally, the propagator h7i acquires the form

$$h7i = ( + \frac{1}{2})^4 s - Q^2 \frac{\kappa^2 + m^2}{1-z} - \frac{(\kappa + \tilde{\gamma} + \tilde{\gamma}=2)^2 + m^2}{z + + =2}^3 [(\tilde{\kappa} + \frac{1}{2})^2 + ^2] + i : \quad (A 25)$$

This propagator, as usual, is used to extract the imaginary part of the integral, which leads to

$$\frac{(\tilde{\kappa} + \frac{1}{2}\tilde{\gamma})^2}{s} 1 :$$

With all these manipulations done, one nally obtains

$$\text{Im} \int dy dz d \int d \overline{[\text{all propagators}]}$$

$$= \frac{i}{s} \frac{2}{s} i^2 \int^z \frac{dz}{z(1-z)} v(z; \kappa^2) \frac{1}{[\kappa_1^2 + m^2 + z(1-z)Q^2]} \frac{1}{(\tilde{\kappa}^2 + ^2)^2} \quad (A 26)$$

## Appendix B

### Helicity amplitude technique

Here we give the derivation of expression for traces of the following type

$$\text{Sp} \hat{e} (\hat{k}_4 + m) \hat{p}^0 (\hat{k}_3 + m) \hat{V} (\hat{k}_2 + m) \hat{p}^0 (\hat{k}_1 + m) \quad (\text{B.1})$$

in full detail. Though one can calculate this trace covariantly, a particularly convenient way to do so is given by light cone helicity amplitude technique [25]. We emphasize that both ways are absolutely equivalent. In the helicity amplitude approach, we recall that all fermion lines in (B.1) can be taken on mass shell (see detailed derivation of LCWF normalization in Sect.4.5) and decomposed into a sum of light cone helicities

$$\begin{aligned} (\hat{k} + m) &= \sum_u u \bar{u} \quad \text{for quark lines;} \\ (\hat{k} + m) &= - \sum_v [\bar{v} (\hat{k} - m)] &= \sum_v v \bar{v} \quad \text{for antiquark lines.} \end{aligned}$$

Since the specific choice of this decomposition does not affect the final result, we are free to take the most convenient choice of spinors (see [25] for details), namely,

Here are the spinors we use:

$$\begin{aligned} u(p; \lambda) &= \frac{1}{\sqrt{2p^+}} \begin{pmatrix} p_- \\ 2p^+ + m + \not{p} \end{pmatrix} \quad \begin{matrix} (") = +1 \\ (\#) = -1 \end{matrix} \\ v(p; \lambda) &= \frac{1}{\sqrt{2p^+}} \begin{pmatrix} p_- \\ 2p^+ - m + \not{p} \end{pmatrix} \quad \begin{matrix} (\#) = +1 \\ (") = -1 \end{matrix} \end{aligned} \quad (\text{B.2})$$

where

$$(") = \frac{1}{2} \begin{pmatrix} 0 & 1 \\ 1 & 0 \end{pmatrix} \begin{matrix} B \\ C \\ A \end{matrix}; \quad (\#) = \frac{1}{2} \begin{pmatrix} 0 & 1 \\ 1 & 0 \end{pmatrix} \begin{matrix} B \\ C \\ A \end{matrix}$$

We stress that we use here our normal convention for + components of 4-vectors. For convenience, we also give the explicit expressions for all these spinors in the Dirac representation of matrices:

$$\begin{aligned} \gamma^0 &= \begin{pmatrix} I & 0 \\ 0 & -I \end{pmatrix}, \quad \gamma^k = \begin{pmatrix} 0 & \sigma^k \\ \sigma^k & 0 \end{pmatrix}, \quad \gamma^5 = \begin{pmatrix} 0 & I \\ I & 0 \end{pmatrix} \end{aligned} \quad (\text{B.3})$$

The explicit expressions for all spinors  $u^+(\mathbf{p})$ ;  $u(\mathbf{p})$ ;  $v(\mathbf{p})$ ;  $v^+(\mathbf{p})$  read:

$$\begin{aligned} u^+(\mathbf{p}) &= \frac{1}{\sqrt{2p^+}} \begin{pmatrix} 1 \\ 0 \\ \frac{p_x + ip_y}{2p^+} \\ \frac{p_x - ip_y}{2p^+} \end{pmatrix}, \quad u(\mathbf{p}) = \frac{1}{\sqrt{2p^+}} \begin{pmatrix} 0 \\ 1 \\ \frac{p_x + ip_y}{2p^+} \\ \frac{p_x - ip_y}{2p^+} \end{pmatrix}, \\ v^+(\mathbf{p}) &= \frac{1}{\sqrt{2p^+}} \begin{pmatrix} 0 \\ 1 \\ \frac{p_x + ip_y}{2p^+} \\ \frac{p_x - ip_y}{2p^+} \end{pmatrix}, \quad v(\mathbf{p}) = \frac{1}{\sqrt{2p^+}} \begin{pmatrix} 1 \\ 0 \\ \frac{p_x + ip_y}{2p^+} \\ \frac{p_x - ip_y}{2p^+} \end{pmatrix}. \end{aligned} \quad (\text{B.4})$$

Using these explicit formulas, one can do straightforward calculations and indeed prove that comply with orthonormality and completeness rules:

$$\begin{aligned} u_X(\mathbf{p}; \lambda) u_X(\mathbf{p}; \lambda') &= \delta_{\lambda\lambda'}, \quad v_X(\mathbf{p}; \lambda) v_X(\mathbf{p}; \lambda') = -\delta_{\lambda\lambda'}, \\ u(\mathbf{p}; \lambda) u(\mathbf{p}; \lambda') &= \delta_{\lambda\lambda'}, \quad v(\mathbf{p}; \lambda) v(\mathbf{p}; \lambda') = -\delta_{\lambda\lambda'}. \end{aligned} \quad (\text{B.5})$$

For  $\lambda = 1$  we define

$$a(\mathbf{p}) = \frac{1}{\sqrt{2p^+}} (a_x + ia_y), \quad (\text{B.6})$$

Cross product is defined as

$$[\mathbf{a}\mathbf{b}] = a_x b_y - b_x a_y. \quad (\text{B.7})$$

Moreover every matrix element should be multiplied by common factor  $\sqrt{\frac{p^+}{p^+ q^+}}$ .  
Some useful relations:

$$\begin{aligned} {}^5v(\mathbf{q}) &= u(\mathbf{q}), \quad {}^5u(\mathbf{q}) = v(\mathbf{q}), \\ a(\mathbf{p}) b(\mathbf{q}) &= \frac{1}{2} + i [\mathbf{a}\mathbf{b}], \quad a(\mathbf{p}) b(\mathbf{q}) = \frac{1}{2} - i [\mathbf{a}\mathbf{b}], \\ a(\mathbf{p}) \tilde{a} + i [\mathbf{p}\mathbf{a}] &= b(\mathbf{q}) \tilde{a}^2. \end{aligned} \quad (\text{B.8})$$

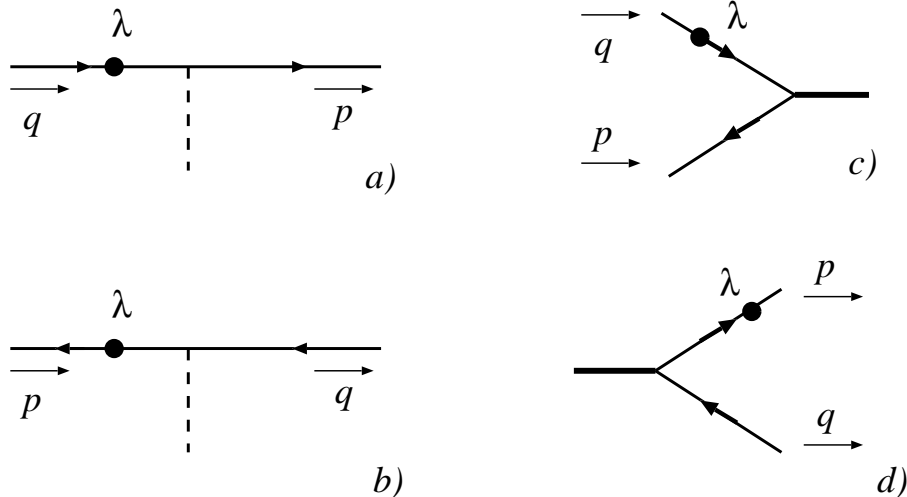


Figure B.1: Four types of transitions, for which we give the amplitudes. Dot with label indicates the spinor whose helicity is used as  $\lambda$ .

Straight line elements

For line in Fig B.1a, one has

$$\begin{aligned}
 u(p) &::: u(q) & u(p) &::: u(q) \\
 + & & 0 \\
 & \frac{1}{p_+ q_+} (m^2 + p q + i [p q]) & \frac{m}{p_+ q_+} (p( ) - q( )) \\
 a & \sim \frac{ap}{p_+} + \frac{aq}{q_+} + i \frac{[ap]}{p_+} - \frac{[aq]}{q_+} & m a( ) \frac{1}{p_+} - \frac{1}{q_+} ! \\
 1 & m \frac{1}{p_+} + \frac{1}{q_+} & \frac{p( )}{p_+} - \frac{q( )}{q_+} \\
 + & \sim a \frac{2}{p_+} (ap - i [ap]) & \frac{2m}{p_+} a( ) \\
 a & \sim + \frac{2}{q_+} (aq + i [aq]) & \frac{2m}{q_+} a( ) \\
 a & \sim + \sim b \frac{2}{+ 5} (ab + i [ab]) & 0 \\
 & & 0
 \end{aligned}$$

For line in Fig B.1b, one has

$$\begin{aligned}
 v(p) &::: v(q) & v(p) &::: v(q) \\
 + & & 0 \\
 & \frac{1}{p_+ q_+} (m^2 + p q - i [p q]) & \frac{m}{p_+ q_+} (p( ) - q( )) \\
 a & \sim \frac{ap}{p_+} + \frac{aq}{q_+} + i \frac{[ap]}{p_+} - \frac{[aq]}{q_+} & m a( ) \frac{1}{p_+} - \frac{1}{q_+} ! \\
 1 & m \frac{1}{p_+} + \frac{1}{q_+} & \frac{p( )}{p_+} - \frac{q( )}{q_+} \\
 + & \sim a \frac{2}{p_+} (ap + i [ap]) & \frac{2m}{p_+} a( ) \\
 a & \sim + \frac{2}{q_+} (aq - i [aq]) & \frac{2m}{q_+} a( ) \\
 a & \sim + \sim b \frac{2}{+ 5} (ab - i [ab]) & 0 \\
 & & 0
 \end{aligned}$$

Vertex lines

For vertex in Fig B 1c, one has

$$\begin{aligned}
 & v(p) \cdots u(q) \quad v(p) \cdots u(q) \\
 & + \quad 0 \quad 2 \\
 & \frac{m}{p_+ q_+} (p(\ ) + q(\ )) \quad \frac{1}{p_+ q_+} m^2 + p q + i [p q] \\
 & a \sim m a(\ ) \frac{1}{p_+} + \frac{1}{q_+} \quad \frac{ap}{p_+} + \frac{aq}{q_+} i \frac{[ap]}{p_+} \frac{[aq]}{q_+} ! \\
 & 1 \quad \frac{p(\ )}{p_+} \quad \frac{q(\ )}{q_+} \quad \frac{m}{p_+} + \frac{m}{q_+} \\
 & + \sim a \quad \frac{2m}{p_+} a(\ ) \quad \frac{2}{p_+} (ap - i [ap]) \\
 & a \sim + \quad \frac{2}{q_+} a(\ ) \quad \frac{2}{q_+} (aq + i [aq]) \\
 & a \sim + \sim b \quad 0 \quad 2 (ab + i [ab]) \\
 & + \quad 5 \quad 0 \quad 2 \\
 & 5 \quad \frac{p(\ )}{p_+} \quad \frac{q(\ )}{q_+} \quad m \frac{1}{p_+} + \frac{1}{q_+} !
 \end{aligned}$$

For vertex in Fig B 1d, one has

$$\begin{aligned}
 & u(p) \cdots v(q) \quad u(p) \cdots v(q) \\
 & + \quad 0 \quad 2 \\
 & \frac{m}{p_+ q_+} (p(\ ) + q(\ )) \quad \frac{1}{p_+ q_+} m^2 + p q + i [p q] \\
 & a \sim m a(\ ) \frac{1}{p_+} + \frac{1}{q_+} \quad \frac{ap}{p_+} + \frac{aq}{q_+} i \frac{[ap]}{p_+} \frac{[aq]}{q_+} ! \\
 & 1 \quad \frac{p(\ )}{p_+} \quad \frac{q(\ )}{q_+} \quad \frac{m}{p_+} \quad \frac{m}{q_+} \\
 & + \sim a \quad \frac{2m}{p_+} a(\ ) \quad \frac{2}{p_+} (ap - i [ap]) \\
 & a \sim + \quad \frac{2m}{q_+} a(\ ) \quad \frac{2}{q_+} (aq + i [aq]) \\
 & a \sim + \sim b \quad 0 \quad 2 (ab + i [ab]) \\
 & + \quad 5 \quad 0 \quad 2 \\
 & 5 \quad \frac{p(\ )}{p_+} \quad \frac{q(\ )}{q_+} \quad m \frac{1}{p_+} + \frac{1}{q_+} !
 \end{aligned}$$

Transverse photon polarization

As we see from the table, neither of gluon legs can flip quark helicity. Therefore, there are 4 combinations of all possible helicity assignments.

In the case both qq helicities are the same, one gets

$$\begin{aligned}
 2zq_+p_- &= 2zq_+p_- \frac{\overline{q}(1-z)q}{z(1-z)q} m e(+) \frac{\overline{q}(1-z)q}{z(1-z)q} (-m)e(+) \\
 &= \frac{z}{1-z} s^2 (m^2) e(+) e(+) \quad (B.9)
 \end{aligned}$$

In the case quark and antiquark helicities are opposite, one obtains

$$\begin{aligned}
 2zq_+p_- &= 2zq_+p_- \frac{\overline{q}(1-z)q}{z(1-z)q} [(e_k)z + (e_k)(1-z) - i(\not{k}z - \not{k}(1-z))] \\
 &\quad \frac{\overline{q}(1-z)q}{z(1-z)q} [(e_k)(1-z) - (e_k)z - i(\not{k}(1-z) + \not{k}z)] \\
 &= \frac{z}{1-z} s^2 [(e_k)(1-2z) + i\not{k}] [(e_k)(1-2z) - i\not{k}] \quad (B.10)
 \end{aligned}$$

Thus, performing summation over qq helicities, one obtains

$$2s^2 \frac{z}{1-z} \sum_h m^2 (e e) + (e_k)(e_k)(1-2z)^2 + [\not{k}]\not{k}^i$$

Finally, averaging over azimuthal angle, omitting factor  $2s^2$  and including  $(-1)$  due to one antiquark propagator reveals

$$\frac{1}{z} I^{(a)} = \frac{h}{m^2 + (z^2 + (1-z)^2)k^2}^i \quad (B.11)$$

Note that the expression for Diagram (d) can be instantly obtained from the above expressions by replacement  $k \rightarrow \tilde{k}$ ;  $z \rightarrow 1-z$ . In this case 3 antiquark propagators also give factor  $(-1)^3 = -1$ . So, the answer for this diagram is

$$\frac{z}{1-z} I^{(d)} = \frac{h}{m^2 + (z^2 + (1-z)^2)k^2}^i \quad (B.12)$$

Finally, one has

$$\begin{aligned}
 &m^2 + (z^2 + (1-z)^2)(k; k+) \\
 &m^2 + (z^2 + (1-z)^2)(k; k-)
 \end{aligned}$$

for Diagrams (b) and (c) respectively.

With all these results, Eq.(2.21) turns into

$$\begin{aligned}
 A^T &= i s \frac{32}{(2)^2} e_f^2 \frac{2}{s_{em}} \int_0^1 dz \frac{d^2 \tilde{k}}{k^2 + m^2 + z(1-z)Q^2} \frac{d^2 \sim V(+)}{(\sim^2 + \sim^2)^2} \\
 &\quad \frac{m^2 + (z^2 + (1-z)^2)k^2}{k^2 + m^2 + z(1-z)Q^2} + \frac{m^2 + (z^2 + (1-z)^2)(k^2 + (\tilde{k} \sim))^\#}{[(k + \sim)^2 + m^2 + z(1-z)Q^2]} : \quad (B.13)
 \end{aligned}$$

Note that we changed  $\tilde{k}$  in Diagram (c), so that it became identical to Diagram (b).

Scalar photon polarization

The virtual photon scalar polarization is described by

$$e_0 = \frac{1}{Q} (q^0 + x p^0) = \frac{1}{Q} (q_+ n_+ + x p_- n_-) \quad (B.14)$$

One notes that in this case only qq states with opposite helicities do contribute. For Diagram (a) an amplitude reads

$$\begin{aligned} 2z q_+ p_- &= 2z q_+ p_- \left[ \frac{1}{Q} \frac{z(1-z)q_-^2}{Q} + 2xp_-^2 \frac{1}{Q} \frac{z(1-z)q_-^2}{Q} + 2xp_-^2 \right] \\ &= s^2 \frac{1}{Q^2} \frac{z}{1-z} \frac{h}{z} m^2 + K^2 - z(1-z)Q^2 i_2 : \end{aligned} \quad (B.15)$$

Therefore,

$$\frac{1}{z} I^{(a)} = \frac{1}{Q^2} \frac{h}{z} m^2 + K^2 - z(1-z)Q^2 i_2 : \quad (B.16)$$

Obviously, for Diagram (d) one has

$$\frac{z}{1-z} I^{(d)} = \frac{1}{Q^2} \frac{h}{z} m^2 + K^2 - z(1-z)Q^2 i_2 : \quad (B.17)$$

The expressions for Diagrams (b) and (c) can be obtained in the same way and give

$$\begin{aligned} I^{(b)} &= \frac{1}{Q^2} \frac{h}{z} m^2 + K^2 - z(1-z)Q^2 i_2 m^2 + (K + \sim)^2 - z(1-z)Q^2 i_1 ; \\ I^{(c)} &= \frac{1}{Q^2} \frac{h}{z} m^2 + K^2 - z(1-z)Q^2 i_2 m^2 + (K - \sim)^2 - z(1-z)Q^2 i_1 : \end{aligned} \quad (B.18)$$

Therefore Eq.(2.21) now reads

$$\begin{aligned} A^0 &= i s \frac{32}{(2)^2} e_f^2 \frac{2}{s} e_m \int_0^1 dz d^2 K \frac{[m^2 + K^2 - z(1-z)Q^2]}{K^2 + m^2 + z(1-z)Q^2} \frac{d^2 \sim V(\sim)}{(\sim^2 + \sim^2)^2} \\ &\quad \frac{2}{Q^2} \left[ \frac{[m^2 + K^2 - z(1-z)Q^2]}{K^2 + m^2 + z(1-z)Q^2} + \frac{[m^2 + (K - \sim)^2 - z(1-z)Q^2]}{[(K - \sim)^2 + m^2 + z(1-z)Q^2]} \right] : \end{aligned} \quad (B.19)$$

In fact, this expression in brackets can be greatly simplified. First, trivial algebra leads to

$$\begin{aligned} &\frac{[m^2 + K^2 - z(1-z)Q^2]}{K^2 + m^2 + z(1-z)Q^2} + \frac{[m^2 + (K - \sim)^2 - z(1-z)Q^2]}{[(K - \sim)^2 + m^2 + z(1-z)Q^2]} \\ &= 1 + \frac{2z(1-z)Q^2}{K^2 + m^2 + z(1-z)Q^2} + 1 - \frac{2z(1-z)Q^2}{[(K - \sim)^2 + m^2 + z(1-z)Q^2]} \\ &= 2z(1-z)Q^2 \frac{1}{K^2 + m^2 + z(1-z)Q^2} - \frac{1}{[(K - \sim)^2 + m^2 + z(1-z)Q^2]} : \end{aligned}$$

Second, if we replace  $e_0 = (q^0 + x p^0)/Q$  by  $q = (q^0 - x p^0)/Q$ , we will get zero due to the gauge invariance of the total sum of all diagrams. Effectively, it means that residual  $[m^2 + K^2$



$z(1-z)Q^2]$  can be replaced by  $2z(1-z)Q^2$ . Of course, it does not mean that these two expressions are identical by themselves. Only after integration over quark momenta they give the same answer. Thus, the final answer for scalar photons reads

$$A^0 = \frac{128Q^2}{(2)^2} e_f^2 \frac{1}{s_{em}} \int_0^1 dz z^2 (1-z)^2 d^2k \frac{1}{k^2 + m^2 + z(1-z)Q^2} \frac{d^2 \tilde{V}(\tilde{k})}{(\tilde{k}^2 + \tilde{m}^2)^2} \quad (B\ 20)$$

## B.1 Photon vertex amplitudes

Notation is given in Fig 5.3. We start with transverse photon.

$$u^0 \hat{e}_T v = u^0 (\tilde{m} \mathbf{e}) v :$$

Equal qq helicities give

$$\frac{q}{z(1-z)q} \frac{1}{z(1-z)q} (\tilde{m}) e(\tilde{k}) \frac{1}{z(1-z)} m e(\tilde{k}) \quad (B\ 21)$$

Opposite qq helicities give

$$\begin{aligned} & \frac{q}{z(1-z)q} \frac{1}{z(1-z)q} (\tilde{e}k_1)(1-z) (\tilde{k}_1)z - i [\tilde{e}k_1](1-z) + [\tilde{k}_1]z \\ &= \frac{1}{z(1-z)} (\tilde{e}k_1)(1-2z) - i [\tilde{k}_1] \end{aligned} \quad (B\ 22)$$

In the case of scalar photon

$$u^0 \hat{e}_0 v = u^0 \frac{1}{Q} (q_+ + xp_+) v$$

the same helicities give exactly zero while opposite helicities result in

$$\begin{aligned} & \frac{q}{z(1-z)q} \frac{1}{Q} \frac{q_+}{q_+} (\tilde{m}^2 + k_1^2) + x2z(1-z)p_+ q_+ \\ &= \frac{1}{z(1-z)Q} (\tilde{m}^2 + k_1^2 - z(1-z)Q^2) \end{aligned} \quad (B\ 23)$$

## B.2 Vector meson vertex amplitudes

This case is more tricky due to the nonzero vector meson transverse momentum  $\tilde{p}_\perp$ . We start with the transverse vector meson polarization:

$$\hat{V}_T = \tilde{\mathcal{V}} + \frac{2(\tilde{\mathcal{V}} \cdot \tilde{p})}{s} p_+ :$$

The same qq helicities give again

$$\frac{q \frac{z(1-z)q}{z(1-z)q}}{z(1-z)q} m V( ) = \frac{1}{z(1-z)} m V( ) \quad (\text{B } 24)$$

while opposite helicities give

$$\begin{aligned} & \frac{q \frac{z(1-z)q}{z(1-z)q}}{z(1-z)q} \left( [\nabla \cdot \mathbf{k}_3]z + (\nabla \cdot \mathbf{k}_2)(1-z) + i [\nabla \cdot \mathbf{k}_3]z - \nabla \cdot \mathbf{k}_2](1-z) \right) \\ & + \frac{2(\nabla \cdot \mathbf{p})}{s} \frac{z(1-z)q}{2z(1-z)q} \\ & = \frac{1}{z(1-z)} \left( (\nabla \cdot \mathbf{k})(1-2z) + i [\nabla \cdot \mathbf{k}] \right) \end{aligned} \quad (\text{B } 25)$$

Here we used definitions and properties (see also Fig.5.3):

$$\begin{aligned} \mathbf{k}_2 &= \mathbf{k} + z\tilde{\mathbf{p}}; \quad \mathbf{k}_3 = \mathbf{k} + (1-z)\tilde{\mathbf{p}} \\ (1-z)\mathbf{k}_2 - \mathbf{k}_3 &= \mathbf{k}; \quad (1-z)\mathbf{k}_2 + z\mathbf{k}_3 = (1-2z)\mathbf{k} + 2z(1-z)\tilde{\mathbf{p}}; \\ (\mathbf{k}_2 \cdot \mathbf{k}_3) &= \mathbf{k}^2 + (1-2z)\mathbf{k} \cdot \tilde{\mathbf{p}} + z(1-z)\tilde{\mathbf{p}}^2 \\ M^2 + \tilde{\mathbf{p}}^2 &= \frac{\mathbf{k}_2^2 + m^2}{z} + \frac{\mathbf{k}_3^2 + m^2}{(1-z)} = \frac{\mathbf{k}^2 + m^2}{z(1-z)} + \tilde{\mathbf{p}}^2; \end{aligned} \quad (\text{B } 26)$$

For the longitudinal vector mesons one has for equal quark-antiquark helicities

$$\frac{q \frac{z(1-z)q}{z(1-z)q} \frac{1}{M}}{z(1-z)q} m \tilde{V}( ) + m \frac{q_{\parallel}}{q_{\perp}} [\mathbf{k}_2( ) + \mathbf{k}_3( )] = 0 \quad (\text{B } 27)$$

and for opposite helicities

$$\begin{aligned} & \frac{q \frac{z(1-z)q}{z(1-z)q} \frac{1}{M}}{z(1-z)q} \left( [(\nabla \cdot \mathbf{k}_3)z + (\nabla \cdot \mathbf{k}_2)(1-z) + i [(\nabla \cdot \mathbf{k})]] + \frac{q_{\parallel}}{q_{\perp}} [m^2 + (\mathbf{k}_2 \cdot \mathbf{k}_3) + i [\mathbf{k}_3 \cdot \mathbf{k}_2]] \right) \\ & + \frac{\tilde{\mathbf{p}}^2}{s} \frac{M^2}{2z(1-z)q} \\ & = \frac{1}{z(1-z)} 2z(1-z)M \end{aligned} \quad (\text{B } 28)$$

### B.3 Final trace calculation

Once we have the expressions for vertex amplitudes, the rest is done quickly. We first note that each gluon vertex attached to the lower or upper line gives factor

$$2zq_{\perp} \cdot \mathbf{p} = sz; \quad 2(1-z)q_{\perp} \cdot \mathbf{p} = s(1-z) \quad (\text{B } 29)$$

correspondingly.

So, let's start with  $T \rightarrow T$  amplitude and calculate it for Diagram (c) at Fig.52.  
Equal qq helicities give

$$s(1-z) = s \frac{1}{z(1-z)} m V(\dots) \frac{1}{z(1-z)} m e(\dots) = 2s^2 m^2 e(\dots) V(\dots) \quad (B.30)$$

Summing over gives

$$2s^2 m^2 (e\bar{V}) : \quad (B.31)$$

The opposite helicities yield

$$s^2 (\bar{V} \bar{K})(1-2z) + i \bar{V} \bar{K} (\epsilon \bar{K}_1)(1-2z) - i [\bar{K}_1] \quad (B.32)$$

Summing over helicities and making use of identity

$$[ab][cd] = (ac)(bd) - (ad)(bc) \quad (B.33)$$

one obtains

$$2s^2 (\bar{V} \bar{K})(\epsilon \bar{K}_1)(1-2z)^2 + (e\bar{V})(\bar{K} \bar{K}_1) - (\bar{K})(\bar{V} \bar{K}_1) : \quad (B.34)$$

Since we factored out  $2s^2$  when deriving (5.18), we finally get

$$I_{T \rightarrow T}^{(c)} = (\epsilon\bar{V})(m^2 + \bar{K} \bar{K}_1) + (\bar{V} \bar{K})(\epsilon \bar{K}_1)(1-2z)^2 - (\bar{K})(\bar{V} \bar{K}_1) : \quad (B.35)$$

We included factor  $(-1)$  since in this diagram we have one antiquark propagator.

An important observation here is that all other integrands, namely  $I^{(a)}(1-z)=z I^{(c)}$ ;  $I^{(d)}(z)=(1-z) I^{(c)}$  give absolutely the same result (with their own definitions of  $\bar{K}_1$  of course). The only thing one should not forget is that diagrams (a,d) enter with sign  $-$  while diagrams (b,c) enter with sign  $+$ :

$$\frac{1}{z} I^{(a)} = I^{(b)} = I^{(c)} = \frac{z}{1-z} I^{(d)} :$$

For  $L \rightarrow L$  amplitude one has immediately

$$I_{L \rightarrow L}^{(c)} = \frac{1}{Q} [m^2 + \bar{K}_1^2 - z(1-z)Q^2] \frac{1}{M} 2z(1-z)M^2 \quad (B.36)$$

In fact, using simple relation

$$\frac{m^2 + \bar{K}_1^2 - z(1-z)Q^2}{m^2 + \bar{K}_1^2 + z(1-z)Q^2} = 1 + \frac{2z(1-z)Q^2}{m^2 + \bar{K}_1^2 + z(1-z)Q^2} \quad (B.37)$$

and noting that all unity terms will eventually cancel out in (5.24), one can rewrite (B.36) as

$$I_{L \rightarrow L}^{(c)} = 4QM^2 z(1-z)^2 : \quad (B.38)$$

For  $T \rightarrow L$  amplitude one has

$$I_{T \rightarrow L}^{(c)} = 2z(1-z)M (\bar{K}_1)(1-2z) \quad (B.39)$$

and for  $L \rightarrow T$  amplitude one has

$$I_{L \rightarrow T}^{(c)} = \frac{1}{Q} [m^2 + \bar{K}_1^2 - z(1-z)Q^2](1-2z)\bar{V} \bar{K} : \quad (B.40)$$

The same transformation as in  $L \rightarrow L$  amplitude, leads to

$$I_{L \rightarrow T}^{(c)} = 2z(1-z)Q^2(1-2z)\bar{V} \bar{K} : \quad (B.41)$$

Note that in the last three amplitudes only opposite qq helicities contributed.

## A cknow ledgem ents

It is an honor for me to thank Prof. J. Speth for his perpetual desire to see me as a member of Julich theory group and for making my entire stay at Forschungszentrum so comfortable and scientifically fruitful.

Million of thanks must undoubtedly go to Kolya Nikolaev for pulling me in the midst of his turbulent scientific activity and making me immediately start contributing, for infecting me with his desire to look for a clear physical meaning behind every formula, and for innumerable discussions we have had during these years.

I want to thank all my colleagues at IKP and in Novosibirsk, in particular, Ilya Ginzburg, who discussed with me details of my work, or just listened to what I've been saying.

I wish to thank all members of the wonderful company that grew up in Julich | Vadim, Ashot, Pasha, Fedya, Dmitro, Lena, Tanya and many others. Thanks for all those parties and journeys together!

Anuta! Thanks to you too! For your continuous and many-sided help and support. Well, most of time it actually looked rather like distracting from studies than supporting them, but thanks anyway! Without relaxing at home, I would get completely crazy with all these vector mesons!

Finally, I want to collectively thank all those people who have helped me in various ways during my work, but whom I failed to recollect in this acknowledgment due to my innate forgetfulness.

# Curriculum Vitae

1. Name: Igor P ierovich Ivanov

2. Date of birth: 26 October 1976

3. Place of birth: Petropavlovsk-K am chatsky, Russia

4. Nationality: Russian

5. Education outline:

Sept. 1983 { May 1991: secondary school 7, Kam chatka, Russia

Aug. 1991 { June 1993: Physics and Mathematics School at Novosibirsk University,  
Novosibirsk, Russia

Sept. 1993 { July 1997: undergraduate studies at Novosibirsk State University,  
Physics Dept.; BSc diploma defended in July 1997

Sept 1997 { July 1999: graduate studies at Novosibirsk State University, Physics  
Dept.; M Sc thesis defended in July 1999.

from Aug. 1999 { postgraduate studies at Institut für Kernphysik, Forschungszentrum  
Jülich